Geological Evaluation of Posidonia and Wealden Organic-Rich Shales: Geochemical and Diagenetic Controls on Pore System Evolution

Eliza J. Mathia

Submitted in fulfilment for the degree of Doctor of Philosophy in the Faculty of Science

School of Civil Engineering and Geoscience
Newcastle upon Tyne

December 2014

Declaration

I hereby certify that this is my own work, except where otherwise acknowledged, and that it has not been submitted for a degree at this, or any other university.

Eliza J. Mathia

Abstract

Free gas in shales occurs mainly in larger mesopores (width >6 nm) and macropores (width >50 nm) and is likely to be the first or even main contributor to gas production. Because evaluation of the storage capacity and final recovery of gas depends on distribution and connectivity of these pores, their correct quantification has become a focus point of advanced research. A major step for understanding pore systems in organic rich shales was made by recognition that under increasing thermal stress, decomposition of kerogen should progressively lead to development of organic porosity. Despite this, many questions concerning fate of organic porosity in organic rich rocks still remain unresolved. To date, several important attempts to link evolution of organic pores with maturation and organic matter content gave inconclusive and contradictory results. In this study, pore systems of the Lower Jurassic Posidonia and Lower Cretaceous Wealden shale, representing different mudrock types and covering a range of maturities, have been characterised. By integrating geochemical and petrophysical measurements, and with a detailed analysis of microscopic images we offered a unique approach for measuring porosity and pore characteristics on micrometre and centimetre scales with thorough understanding for a micrometer lithological variation. Key aims were to quantify the evolution of porosity associated with both organic matter and inorganic rock matrix as a function of maturity, and address the influence of mudrock heterogeneity on porosity change.

Our experiments revealed a non-linear trend of porosity change with maturity in pores of all sizes, with an initial drop in the oil window as a result of mechanical compaction, chemical diagenesis, as well as pore-filling oil and bitumen. At comparable maturities, porosity and distribution of pores depend on the content of clays, organic matter, microfossils, silt grains and pore filling cement. In both Posidonia and Wealden, macropores (> 50 nm) account for merely up to 20% of total porosity physically measured, with the lowest percentage in the least mature samples. It was also demonstrated that gas sorption micropores are controlled by the amount of organic matter and clay minerals, and thus their microporous nature was confirmed. In terms of organic porosity development, we provided evidence that organic matter content and the path of its thermal decomposition control total porosities of the gas window shale. Importantly, neoformed intraorganic porosity is highly heterogeneous with 35% of organic particles containing visible pores (> 6 nm in diameter), and porosities of individual particles ranging from 0–50%. As a key result, we confirmed that porous zones in the gas window are associated with sites of bitumen retention and degradation. That indicates

that the location of potential reservoirs of free gas should be linked to rigid zones, such as fossiliferous faecal pellets, or compaction shadows of mineral grains. Combined mercury injection and SEM data also showed that visible but potentially isolated macropores are connected, but only through throats below 20 nm. With the evolution of the porous network of bitumen saturating the shale matrix in the gas window, connectivity of the system changes from inorganic to organic dominated. The size of the pore throats, and the connectivity of the organic system in shales are likely key controls on the delivery of gas from pore to fracture and then to wellbore.

Acknowledgements

I am grateful to prof. Andrew C. Aplin for giving me the opportunity to pursue this degree, for supervising my work, providing the advice, constructive criticism, encouragement and most importantly, for the support, both purely academic and personal. I would like to express my deepest gratitude to prof. K. Mark Thomas, for his guidance, advice, support and invaluable help in completing this degree. I would like to acknowledge Mr Philip Green for his precious help and guidance in conducting the experimental part of my work. I am thankful to Mr Leon Bowen for his co-operation, his involvement, his invaluable contribution towards the experimental part of my research, his constant support and encouragement. Kind words go to my mom, my dad, and my boyfriend who always believed in me. Finally, I would like to thank all the parties participating in the Gas Shales in Europe project, for funding this research.

Table of Contents

List of Figures

List of Tables

Chapter 1: Introduction

Background

Mudstones constitute up to 70% of volume of sedimentary basins (Aplin and Macquaker, 2011) and due to their unique properties, they have been a target of detailed research. The interest in mudstones was driven by their source rock potential (Bohacs *et al.*, 2005; Hill *et al.*, 2007), their excellent sealing capacities (Neuzil, 1994; Schowalter, 1979; Watts, 1987), their role as depositional and stratigraphic markers (Macquaker, 1994; Macquaker *et al.*, 1998; Schieber, 1999) as well as their capacity to provide clues about environmental and chemical conditions during sediment deposition and diagenesis (Bloch and Hutcheon, 1992; Hicks *et al.*, 1996; Macquaker, 2014; Sageman *et al.*, 2003; Tribovillard *et al.*, 2006). More recently, the boom in oil shale and shale gas exploration revived interest in mudstones and focused on their potential to act as direct reservoirs for oil and gas (Alexander *et al.*, 2011, Bowker, 2007; Curtis, 2002).

Mudstones constitute a basic component of the shale reservoirs, where they interbed with carbonate rocks, siltstones, or even sandstones. Therefore, the name "shale" is more in practical use as it encompasses thick sequences with lithologies deviating from the strict definition of a mudstone (rocks with > 50% of grains in a size < 0.065 mm), and with a wider range of grain sizes (including coarser-grained or carbonate-bearing sections). On the other hand, in the narrower sense, the term shale may imply lithologies which entail dominance of the silicate (silt and clay) grains as opposed to calcareous mudstones dominated by the authigenic component (chalks) (Macquaker *et al.*, 1994). As exemplified by the complex nomenclature of the fine-grained rocks, it is not surprising that the origin and composition of the fine-grained component of the shale sequences differs both vertically and spatially, and may include detrital and/or authigenic clays, autochthonous silica, biogenic carbonates and detrital quartz. Despite the fact that mudstones/shales are usually linked to relatively quiescent conditions of sediment deposition, typical for overbank delta settings, basinal depths, distant lobes of turbidites, or even periodically current or wave swept shelf floors, complex shale sequences may represent a range of depositional environments over the geological time. This vertical and lateral relationship between shale sequences may be placed into broad sequence stratigraphic framework to help predict a distribution of rock formations and accumulations of organic carbon (Bohacs, 2005; Passey *et al.*, 2010).

The physical heterogeneity of shales is reflected by their variable composition, textures and fabric (Macquaker, 1994). Despite being originally controlled by the depositional environment, all these feaures can be syngenetically altered or obliterated during post-depositional diagenesis (Hower *et al.*, 1976; Pedersen and Calvert, 1990). In the first meters of a sediment column, bacterial activity may result in dissolution and precipitaton of new minerals, and depending on the specific setting, and the availability of reactive clays, iron, biogenic silica or organic matter, it may lead to progressive cementation of the pore space (Coleman, 1985; Curtis, 1995, Macquaker *et al.*, 2014). During the progressive burial and increase in temperatures and pressures, further mineralogical and textural changes are induced by transformation of smectite-to-illite (Inoue *et al.*, 1988; Peltonen *et al.*, 2009, Środoń, 1999) A-opal to CT-opal and to quartz (Hesse, 1990; Williams and Crerar, 1985) as well as selective dissolution, precipitation and recrystallization of carbonate phases (Fabricius *et al.*, 2007). Moreover, because of the presence of clay minerals and high initial water saturation, mudstones are sensitive to compaction, progressively expelling water and thus reducing their volume (Bjørlykke and Høeg, 1997; Chaika and Dvorkin, 2000). It was established that over the first 3-4 kilometers of burial, total porosities can drop down to 10% of the rock volume as compared to 90% of original values found in freshly deposited muds (Loucks *et al.*, 2012).

Due to the vast heterogeneity of mudstones, it has long been of interest to establish the link between the genesis of mudstones and their physiochemical properties important from the reservoir standpoint (Bustin *et al.*, 2008; Chalmers and Bustin, 2012; Passey *et al.*, 2010). For instance, in the shale gas exploration, correct evaluation of shale porosities and its linkage to bulk lithologies and rock texture characteristics could help predict the potential gas storage capacity, pin point the best locations of hydrocarbon microreservoirs and estimate final gas recovery. The establishment of the porosity-lithology link, with other factors unchanged, may be somewhat hindered by the low-scale heterogeneity of the shale formations, rapidly changing mineral composition and a grain size. Rine *et al.* (2010) showed that for different high maturity shale reservoirs with non-uniform and distinct composition, porosities change in a manner broadly related to the content of organic carbon but differentiated from each other by the varied slope of the covariation.

Specific settings for mudstone and shale deposition favour them to be enriched in organic matter derived directly from the water column and efficiently buried in the sediment (Algeo and Ingall, 2007; Sageman *et al.*, 2003). Presence of the organic matter significantly adds to the complexity of the mineral-water system, potentially interacting with the mineral

phases and affecting effective shale porosities. The effect of adsorption of organic molecules on mineral grains has been recognized in oil reservoir, where fatty acids and carboxylated polymers inhibit dissolution of carbonates by forming carbonate surface coatings (Thomas and Clouse, 1990). Interestingly, such an effect is noticeable at TOC concentrations as low as 0.1 wt.%. Due to different water saturations of source rocks, presence of both kerogen, bitumen, and oil molecules, narrowness of pore throats and finally different nature of carbonate grains, it is not certain to what extent and via what mechanisms organic maturation affects dissolution or recrystallization of carbonates in mature shales (Lewan *et al.*, 1997).

Presence of kerogen has also major implications for the creation of secondary organic porosity at hydrocarbon generation temperatures (Jarvie *et al.*, 2007; Modica and Lapierre, 2012). Models show that the amount of organic carbon lost during thermal conversion to petroleum is controlled by a kerogen type and thus the structural composition of the organic moieties (Romero-Sarmiento *et al.*, 2013). It has been hypothesized that as lacustrine kerogen has potential to lose higher carbon mass (80%) in comparison to kerogen type II (50%) and III (20%), the evolving porosity will strongly depend on the shale organofacies (Jarvie, 2012). Such estimations do not take into account any porosity loss due to compaction or post-depositional diagenesis, and therefore were shown not to be valid for less mature or consolidated shales (Jarvie *et al.*, 2007). Interestingly, it was emphasized that the direct carbon mass-porosity conversion is neither valid for shales in the peak oil window where the residual oil blocks evolved pores (Curtis *et al.*, 2013; Fishman *et al.*, 2012; Jarvie *et al.* 2007; Romero-Sarmiento *et al.*, 2013). Those studies propose that in order to correctly evaluate shale porosities, the retention of petroleum should be integrated in the organic porosity prediction models (Modica and Lapierre, 2012).

Despite obvious differences between organic matter and its precursors (aquatic kerogen, terrestrial macerals, high molecular weight bitumen compounds directly derived from kerogen and trapped in the shale network, bitumen migrated from adjacent rocks), it is not certain to what extent organic matter composition controls the evolution of the organic pores, their morphologies, and most importantly, the timing of the pore growth. Unfortunately, there are no studies that would directly compare porosities of the marine and lacustrine shales. Moreover, such direct comparisons may be hindered by varied maturities, organic content and lithologies of the rocks, obliterating the influence exerted by the organic phase itself. As far as the terrestrial kerogen is concerned, previous research accentuated its different behaviour under increasing thermal stress, and thus allowing its visual differentiation, still with a considerable level of uncertainty, from the organic matter sourced from the marine

algea (Loucks *et al.*, 2009; Milliken *et al.*, 2013). Such differentiation was facilitated by its arcuate shapes and a lack of nanometer-scale porosity normally observed in the marine and lacustrine shales at sufficiently high resolutions.

Variation between porosities of different organic molecules in shales is a subject of ongoing and extensive research (Bernard *et al.*, 2011, Bernard *et al.*, 2012). The vast amount of experimental work on porosity in organic mater can be found in the coal and char studies. Those studies provided evidence for the extensive degasification of coals during artificial pyrolysis, with the final porosity increase closely linked to a maceral type and the coal rank (Loison *et al.*, 1989). Hence, it is expected that similar distinction should be valid for chemically and structurally distinct kerogens as well as products of their thermal decomposition. The synchrotron-based transmission spectromicroscopy method allowed direct observation of visually porous (> ~20-50 nm) organic molecules present in shales of gas window maturities, and identified by Bernard *et al.* (2011) as oil-spent pyrobitumen. This finding emphasized the significance of the bitumen retention and its pore-blocking effect and its positive role for the porosity increase at gas window maturities. The degasification of bituminous polymer upon thermal cracking is currently the prevailing theory about the origin of the nanometer organic pores (Bernard *et al.*, 2011; Jarvie *et al.*, 2007, Loucks *et al.*, 2009). Though, the exact timing of cracking, and the link between the composition of organic molecules and the morphologies of pores left behind are uncertain. In Woodford shale, Curtis *et al.* (2012) found that a change in porosities quantified from the Scanning Electron Microscope micrographs in wet and gas window shales do not show a linear covariation either with the content of organic matter or a level of the thermal maturity. Moreover, the observed pore morphologies differed on a nano- and micrometer scale, spanning from round, and oval, on the order of nanometers to irregular, up to hundreds of nanometer large (Curtis *et al.*, 2012). Discrepancies are also observed when comparing total porosity-TOC covariations between gas mature shales from different formations. Despite a noticeable positive relationship between the two variables, varied slope of the respective regression lines suggests varied impact of the organic matter, and/or the inorganic framework on the evolution of pores. Constraining these relationships is thus a way to help predict porosity occurrence at different levels of maturity and its relation to the organic matter abundance and type.

Because the pore sizes of the consolidated mudstones span from a micropore < 2 nm, through mesopore (2-50 nm) to macropore (> 50 nm) range (Nelson *et al.*, 2009, Chalmers and Bustin, 2012), their detection will much depend on a specific measuring method

implemented. In the past studies, while some authors concentrated on quantification of microporosity using gas sorption and mercury techniques (Bustin *et al.*, 2008; Chalmers *et al.*, 2012; Chalmers and Bustin, 2007; Kuila and Prasad, 2013; Ross and Bustin, 2009), others implemented mainly microscopic techniques targeting pores in the order of > 10s nm. The latter, although limited by the resolution of the microscopic images, proved to bring important spatial information for the porosity distribution and provided an essential geological background for the interpretation of the experimentally measures porosities (Curtis *et al.*, 2011; Curtis *et al.*, 2013; Fishman *et al.*, 2012; Loucks *et al.*, 2009; Loucks *et al.*, 2012; Milliken *et al.*, 2013; Milner *et al.*, 2010; Schieber, 2011; Slatt and O'Brien, 2011). Still, only a few studies directly quantified image porosities in a statistically meaningful way (Klaver et al., 2013; Milliken *et al.*, 2013) and therefore more extensive data is needed to assess the variability in a distribution of macropores in shales. Finally, mercury porosimetry was deployed in many studies to quantify open clay porosity and determine a distribution of pore throat sizes (Hildenbrand and Urai, 2003; Kuila and Prasad, 2013). This technique, although useful in determining connected porosity held or accessed by pores with a diameter exceeding 2-5 mm, imposes high uncertainties regarding the magnitude of the compressibility of the shale framework and the pores (Bergins *et al.*, 2007). Most of the past studies accentuated that in order to better understand the complexity of the pore systems in shales, a deployment of a combination of different techniques is essential (Bustin *et al.*, 2008; Chalmers and Bustin, 2012; Chalmers *et al.*, 2012; Clarkson *et al.*, 2013; Strapoc *et al.*, 2010).

Motivation and thesis structure

In this study we examined a set of shale samples of different maturities and lithologies originating from two sediment sequences, the Lower Toarcian Posidonia Shale formation, and the Beriassian German Wealden, both from the Lower Saxony Basin, Germany. Our main aim was to track the impact of the variation in lithologies, the composition of the organic macerals, diagenetic alteration, and thermal maturity on shale porosity, and distribution of pore sizes. Although the main rationale behind such work lies in the growing demand for the exploration of the shale gas and therefore the need to understand the evolution of the sub-micrometer and potentially gas containing pores, our results are expected to contribute largely to more generic knowledge about the kerogen maturation and its thermal transformation. In order to quantify pore characteristics not only in a bulk sample, but also on a smaller scale, with thorough understanding for a micrometer lithological variation, our

unique approach consists of an integration of the geochemical and petrophysical measurements with a detailed analysis of the microscopic images.

This work is composed of 3 technical chapters (Chapters 2-4), written in a publication style. To provide a larger picture, the technical chapters are preceded by the general Introduction (Chapter 1), and summarized in the Summary and Conclusions chapter (Chapter 5). In the Chapter 2 we examined a set of calcareous, organic-rich, type II kerogen shale samples of three different maturities spanning from 0.53% to 1.45% Ro, originating from the Posidonia Shale formation. Due to little variance in the mineralogical composition between wells of different maturity, our aim was to track the diagenetic changes within the inorganic framework, the variability in the organic macerals composition and total porosity change upon increasing thermal stress. The petrophysical and geochemical investigations were conducted on core samples with the vertical sampling resolution > 1 m. The analysis of the microtextures was conducted in the petrographic and scanning electron microscope micrographs, and was followed by an analysis of the pore systems using highly polished thin sections.

The Chapter 3 builds on the first chapter, with the main focus placed on the quantification of porosities of the Posidonia Shale with the mercury porosimetry, gas adsorption and image analysis. Our main aim was to investigate the change of the porosity and the pore size distribution as the maturity of the shale changed from the early oil window to the gas window conditions. With two main lithologies, calcareous shale and marlstone, we also addressed the impact of a lithological variation, compaction and diagenesis for the disappearance and reappearance of pores as the maturity progressed. Finally, we tested to what extent the observed gas window pores are related to processes of the hydrocarbons cracking.

In the Chapter 4, the petrophysical and geochemical investigations were carried out on three cores of the German Wealden with predominantly type I kerogen. The bulk measurements were supplemented by the analysis of microtextures both in the petrographic and scanning electron microscope micrographs, and were followed by the quantification of the pores observed in highly polished thin sections. The main aim of our work was to address the issue of a small scale variation of the lithologically heterogeneous clay- and carbonate-rich units, and its effect on the porosity evolution in shales of radically different maturity. Moreover, in the gas window maturity rocks, we paid special attention to development and connectivity of the organic pores and its relation to the content and type of the organic matter.

References

ALEXANDER, T. 2011. Shale gas revolution. *Oilfield review*, **23**, 40-55.

ALGEO, T.J., INGALL, E. 2007. Sedimentary Corg:P ratios, paleocean ventilation, and Phanerozoic atmospheric pO_2. *Palaeogeography, Palaeoclimatology, Palaeoecology*, **256**, 130–155.

APLIN, A.C., MACQUAKER. H.S. 2011. Mudstone diversity: Origin and implications for source, seal, and reservoir properties in petroleum systems. *Association of Petroleum Geologists Bulletin*, **95**, 2031–2059.

BERGINS, C., HULSTON, J., STRAUSS, K., CHAFFEE, A.L. 2007. Mechanical/thermal dewatering of lignite. Part 3: Physical properties and pore structure of MTE product coals. *Fuel*, **86**, 3–16.

BERNARD, S., HORSFIELD, B., SCHULTZ, H.M., WIRTH, R., SCHREIBER, A., SHERWOOD, N. 2011. Geochemical evolution of organic-rich shales with increasing maturity: A STXM and TEM study of the Posidonia Shale (Lower Toarcian, northern Germany). Marine and Petroleum Geology, 31, 70-89.

BERNARD, S., WIRTH, R., SCHREIBER, A., SCHULZ, H.-M., HORSFIELD, B. 2012. Formation of nanoporous pyrobitumen residues during maturation of the Barnett Shale (Fort Worth Basin). *International Journal of Coal Geology*, **103**, 3–11.

BJØRLYKKE, K. 1999. Principal aspects of compaction and fluid flow in mudstones. *Geological Society Special Publications*, **158**, 73-78.

BLOCH, J., HUTCHEON, I.E. 1992. Shale diagenesis: a case study from the Albian Harmon Member (Peace River Formation), Western Canada. *Clays and Clay Minerals*, **40**, 682-699.

BOHACS, K.M., GRABOWSKI, G. J., CARROLL, A. R., MANKIEWICZ, P. J., MISKELL-GERHARDT, K. J., SCHWALBACH, J. R. 2005. Production, destruction, and dilution: The many paths to source rock development. In: HARRIS, N. B. (Ed.)., The deposition of organic carbon-rich sediments: Models, mechanisms, and consequences: Society for Sedimentary Geology Special Publication **82**, 61–101.

BOWKER. K.A. 2007. Barnett Shale gas production, Fort Worth Basin: Issues and discussion. *American Association of Petroleum Geologists Bulletin*, **91**, 523-533.

BUSTIN, R.M., BUSTIN, A.M.M., CIU, X., ROSS, D.J.K., MURPHY PATHI, V.S. 2008. Impact of shale properties on pore structure and storage characteristics. SPE Shale Gas Production Conference, 16-18 November 2008, Fort Worth, Texas, USA.

CHAIKA, C., DVORKIN, J. 2000. Porosity reduction during diagenesis of diatomaceous rocks. *American Association of Petroleum Geologists Bulletin*, **84**, 1173–1184.

CHALMERS, G.R.L., BUSTIN, R.M. 2007. On the effects of petrographic composition on coalbed methane sorption. *International Journal of Coal Geology*, **69**, 288–304.

CHALMERS, G.R.L., BUSTIN, R.M. 2012. Geological evaluation of Halfwaye-Doige-Montney hybrid gas shale-tight gas reservoir, northeastern British Columbia. *Marine and Petroleum Geology*, **38**, 53-72.

CHALMERS, G.R.L., ROSS, D.J.K., BUSTIN, R.M. 2012. Geological controls on matrix permeability of Devonian Gas Shales in the Horn River and Liard basins, northeastern British Columbia, Canada. *International Journal of Coal Geology*, **103**, 120-131.

CLARKSON, C.R., SOLANO, N., BUSIN, R.M, BUSTIN, A.M.M., CHALMERS, G.R.L., HE, L., MELNICHENKO, Y.B., RADLINSKI, A.P., BLACH, T.P. 2013. Pore structure characterization of North American shale gas reservoirs using USANS/SANS, gas adsorption, and mercury intrusion. *Fuel*, **103**, 606–616.

COLEMAN, M.L., BERNER, R.A., DURAND, B., MEADOWS, P.S., EGLINTON, G. 1985. Geochemistry of Diagenetic Non-Silicate Minerals Kinetic Considerations [and Discussion]. *Philosophical Transactions of the Royal Society*, **315**, 39-56.

CURTIS, C.D. 1995. Post-depositional evolution of mudstones l: early days and parental influences. *Journal of the Geological Society*, **152**, 577-586.

CURTIS, J. 2002. Fractured shale-gas systems. *American Association of Petroleum Geologists Bulletin*, **86**, 1921–1938.

CURTIS, M.E., AMBROSE, R.J., SONDEGELD, C.H., RAI, C.S. 2011. Investigation of the relationship between organic porosity and thermal maturity in the Marcellus Shale.

SPE North American Unconventional Gas Conference and Exhibition, 14-16 June 2011, The Woodlands, Texas, USA.

CURTIS, M.E., SONDERGELD, C.H., AMBROSE, R.J., RAI, C.S. 2012. Microstructural investigation of gas shales in two and three dimensions using nanometer-scale resolution imaging. *American Association of Petroleum Geologists Bulletin*, **96**, 665-677.

CURTIS, M.E., SONDERGELD, C.H., RAI, C.S. 2013. Relationship between organic shale microstructure and hydrocarbon generation. SPE Unconventional Resources Conference-USA, 10-12 April 2013, The Woodlands, Texas, USA.

FABRICIUS, I.L., RØGEN, B., GOMMESEN, L. 2007. How depositional texture and diagenesis control petrophysical and elastic properties of samples from five North Sea chalk fields. *Petroleum Geoscience*, **13**, 81–95.

FISHMAN, N.S., HACKLEY, P.C., LOWERS, H.A., HILL, R.J., EGENHOFF, S.O., EBERL, D.D., BLUM, A.E. 2012. The nature of porosity in organic-rich mudstones of the Upper Jurassic Kimmeridge Clay Formation, North Sea, offshore United Kingdom. *International Journal of Coal Geology*, **103**, 32–50.

HESSE, R. 1990. Origin if chert: diagenesis of biogenic siliceous sediments. In: McIlreath, I.A., Morrow, D.W. (Eds.), Diagenesis. Geosci. Can. Reprin Ser., **4**, 227-251.

HICKS, K.S., COMPTON, J.S., McCRACKEN, S., VECSEI, A. 1996. Origin of diagenetic carbonate minerals recovered from the New Jersey continental slope. In: Mountain, G.S.,Miller, K.G.,Blum, P., Poag, C.W., Twichell, D.C. (Eds.), *Proceedings of the Ocean Drilling Program, Scientific Results*, vol. **15**.

HILDENBRAND, A., URAI, J.L. 2003. Investigation of the morphology of pore space in mudstones—first results. *Marine and Petroleum Geology*, **20**, 1185–1200.

HILL, R.J., JARVIE, D.M., ZUMBERGE, J., HENRY, M., POLLASTRO, R.M. 2007. Oil and gas geochemistry and petroleum systems of the Fort Worth Basin. *American Association of Petroleum Geologists Bulletin*, **91**, 445-473.

HOWER, J., ESLINGER, E.V., HOWER, M.E., PERRY, E.A. 1976. Mechanism of burial metamorphism of argillaceous ssediment: 1. Mineralogical and chemical evidence. *American Association of Petroleum Geologists Bulletin*, **87**, 725–737.

INOUE, A., VELDE, B., MEUNIER, A., TOUCHARD, G. 1988. Mechanism of illite formation during smectite-to-illite conversion in a hydrothermal system. *American Mineralogist*, **73**, 1325-1334.

JARVIE, D.M., HILL, R.J., RUBLE, T.E., POLLASTRO, R.M., 2007. Unconventional shale-gas systems: the Mississippian Barnett Shale of north-central Texas as one model for thermogenic shale gas assessment. *American Association of Petroleum Geologists Bulletin*, **91**, 475–499.

JARVIE, D.M, JARVIE, B.M., MAEDE, A. 2012. Components and processes affecting producibility and commerciality of shale oil resource systems. Shale Oil Symposium, 16-17 April 2012, Wuxi, China.

KLAVER, J., DESBOIS, G., URAI, J.L., LITTKE, R. 2012. BIB-SEM study of the pore space morphology in early mature Posidonia Shale from the Hils area, Germany. *International Journal of Coal Geology*, **103**, 12-25.

KUILA, U., PRASAD, M. 2013. Specific surface area and pore-size distribution in clays and shales, *Geophysical Prospecting*, **61**, 341–362.

LEWAN, M.D., 1997. Experiments on the role of water in petroleum formation. *Geochimica et Cosmochirnica Acta*, **61**, 3691-3723.

LOISON R., FOCH P., BOYER A., 1989. Coke: Quality and Production, Butterworths, London, pp. 353.

LOUCKS, R.G., REED, R.M., RUPPEL, S.C., JARVIE, D.M. 2009. Morphology, genesis and distribution of nanometer-scale pores in siliceous mudstones of the Mississippian Barnett Shale. *Journal of Sedimentary Research*, **79**, 848–861.

LOUCKS, R.G., REED, R.M., RUPPEL, S.C., HAMMES, U. 2012. Spectrum of pore types and networks in mudrocks and a descriptive classification for matrix-related mudrock pores. *American Association of Petroleum Geologists Bulletin*, **96**, 1071-1098.

MACQUAKER, J.H.S. 1994. A lithofacies study of the Peterborough Member, Oxford Clay Formation (Jurassic), UK: an example of sediment bypass in a mudstone succession: *Journal of the Geological Society of London*, **151**, 161-172.

MACQUAKER, J.H.S., GAWTHORPE, R.L., TAYLOR, K.G., OATES, M.J. 1998. Hetrogeneity, stacking patterns and sequence stratigraphy in distal mudstone successions; examples from the Kimmeridge Clay Formation, UK. In: Schieber, J., Zimmerle, W., Sethi, P.S., eds., Shales and Mudstones, vol. 1, Stuttgart, Schweizerbart'sche Verlagsbuchhandlung, p. 163-186.

MACQUAKER, J.H.S., TAYLOR, K.G., KELLER, M., POLYA, D. 2014. Compositional controls on early diagenetic pathways in fine-grained sedimentary rocks: Implications for predicting unconventional reservoir attributes of mudstones. *American Association of Petroleum Geologists Bulletin*, **98**, 587–603.

MILLIKEN, K.L., RUDNICKI, M., AWWILER, D.N., ZHANG, T. 2013. Organic matter–hosted pore system, Marcellus Formation (Devonian), Pennsylvania. *American Association of Petroleum Geologists Bulletin*, **97**, 177-200.

MILNER, M., MCLIN, R., PETRIELLO, J., TEK, T. 2010. SPE Canadian Unconventional Resources and International Petroleum Conference, 19-21 October 2010, Calgary, Alberta, Canada.

MODICA, C.J., LAPIERRE, S.G. 2012. Estimation of kerogen porosity in source rocks as a function of thermal transformation: Example from the Mowry Shale in the Powder River Basin of Wyoming. *Association of Petroleum Geologists Bulletin*, **96**, 87-108.

NELSON, P.H. 2009. Pore-throat sizes in sandstones, tight sandstones, and shales. *American Association of Petroleum Geologists Bulletin*, **93**, 329–340.

NEUZIL, C.E. 1994. How permeable are clays and shales? *Water Resources Research*, **30**, 145-150.

PASSEY, Q. R., BOHACS, K. M., ESCH, W. L., KLIMENTIDISS, R., SINHA, S. 2010. From Oil-Prone Source Rock to Gas-Producing Shale Reservoir – Geologic and petrophysical characterization of unconventional shale-gas reservoirs. *Proceedings of the North American Unconventional Gas Conference and Exhibition. Society of Petroleum Engineers*, Paper 131350, 29p.

PEDERSEN, T.F., CALVERT, S.E. 1990. Anoxia vs. Productivity: What controls the formation of organic-carbon-rich sediments and sedimentary rocks? *American Association of Petroleum Geologists Bulletin*, **74**, 454–466.

PELTONEN, C., MARCUSSEN, Ø., BJØRLYKKE, K., JAHREN, J. 2009. Clay mineral diagenesis and quartz cementation in mudstones: The effects of smectite to illite reaction on rock properties. *Marine and Petroleum Geology*, **26**, 887–898.

RINE, J.M., DORSEY, W., FLOYD, M., LASSWELL, P. 2010. A comparative SEM study of pore types and porosity distribution in high to low porosity samples from selected gas-shale formations. *Gulf Coast Association of Geological Societies Transactions*, v. **60**, p.825.

ROMERO-SARMIENTO, M.-F., DUCROS, M., CARPENTIER, B., LORANT, F., CACAS, M.-C., PEGAZ-FIORENT, S., WOLF, S., ROHAIS, S., MORETTI, I. 2013. Quantitative evaluation of TOC, organic porosity and gas retention distribution in a gas shale play using petroleum system modeling: Application to the Mississippian Barnett Shale. *Marine and Petroleum Geology*, **45**, 315-330.

ROSS, D.J.K, BUSTIN. 2009. The importance of shale composition and pore structure upon gas storage potential of shale gas reservoirs. *Marine and Petroleum Geology*, **26**, 916–927.

SAGEMAN, B.B., MURPHY, A.E., WERNE, J.P., VER STRAETEN, C.A., HOLLANDER, D.J., LYONS, T.W. 2003. A tale of shales: the relative roles of production, decomposition, and dilution in the accumulation of organic-rich strata, Middle–Upper Devonian, Appalachian basin. *Chemical Geology*, **195**, 229-273.

SCHIEBER, J. 1999. Distribution and deposition of mudstone facies in the Upper Devonian Sonyea Group of New York. *Journal of Sedimentary Research*, **69**, 909-925.

SCHIEBER, J. 2011. Shale microfabrics and pore development – an overview with emphasis on the importance of depositional processes. In: Gas Shale of the Horn River basin, D.A. Leckie and J.E. Barclay (Eds.), Canadian Society of Petroleum Geologists, Calgary, p. 115-119.

SCHOWALTER, T.T. 1979. Mechanics of secondary hydrocarbon migration and entrapment. *American Association of Petroleum Geologists Bulletin*, **63**, 723–760.

SLATT, R.M., O'BRIEN, N.R. 2011. Pore types in the Barnett and Woodford gas shales: Contribution to understanding gas storage and migration pathways in fine-grained rocks. *American Association of Petroleum Geologists Bulletin*, **95**, 2017–2030.

STRAPOC, D., MASTALERZ, M., SCHIMMELMANN, A., DROBNIAK, A., HASENMUELLER, N.R. 2010. Geochemical constraints on the origin and volume of gas in the New Albany Shale (Devonian–Mississippian), eastern Illinois Basin. *American Association of Petroleum Geologists Bulletin*, **94**, 1713-1740.

ŚRODON, J. 1999. Nature of mixed-layer clays and mechanisms of their formation and alternation. *Annual Review of Earth Planetary Science*, **27**, 19-53.

THOMAS, M.M., CLOUSE, J.A. 1990. Primary migration by diffusion through kerogen: II. Hydrocarbon diffusivities in kerogen. *Geochimica et Cosmochimica Acta*, 54, 2781-2792.

TRIBOVILLARD, N., ALGEO, T.J., LYONS, T., RIBOULLEAU, A. 2006. Trace metals as paleoredox and paleoproductivity proxies: An update. *Chemical Geology*, **232**, 12–32.

WATTS, N.L. 1987. Theoretical aspects of cap-rock and fault seals for single- and two-phase hydrocarbon columns. *Marine and Petroleum Geology*, **4**, 274-307.

WILLIAMS, L.A., CRERAR, D.A. 1985. Silica diagenesis, II. General mechanisms. *Journal of* Sedimentary Petrology, **55**, 312-321.

Chapter 2: Microscopic and petrophysical characterization of the Posidonia Shale – implications for porosity development in organic rich, calcareous shales

Introduction

Mudstones constitute up to 70% of volume of sedimentary basins (Aplin and Macquaker, 2011) and due to their unique properties, they have been a target of detailed research. The interest in mudstones was driven by their source rock potential (Bohacs *et al.*, 2005; Hill *et al.*, 2007), their excellent sealing capacities (Neuzil, 1994; Schowalter, 1979; Watts, 1987), their role as depositional and stratigraphic markers (Macquaker, 1994; Macquaker *et al.*, 1998; Schieber, 1999) as well as their capacity to record chemical conditions of sedimen deposition and diagenesis (Bloch and Hutcheon, 1992; Hicks *et al.*, 1996; Macquaker, 2014; Sageman *et al.*, 2003; Tribovillard *et al.*, 2006). Most recently, the boom in oil shale and shale gas exploration revived interest in mudstones and focused on their potential to act as direct reservoirs for oil and gas (Alexander *et al.*, 2011).

Mudstones are extremely heterogeneous and their original composition may vary from clay-dominated, through silica-rich, to calcareous. Although the original composition of mudstones is controlled by the depositional environment, their original mineral assemblage usually changes during diagenesis (Hower *et al.*, 1976; Pedersen and Calvert, 1990). Mineral dissolution and precipitation may accompany bacterial activity and lead to precipitation of carbonate phases, apatite or pyrite in the first meters of a sediment column (Curtis, 1995). Availability or absence of reactive clays is crucial in that matter and influences not only the alkalinity of the environment (through reaction of HS^- anions with detrital iron), but also sulphurization of organic matter (most pronounced in settings with limited delivery of terrigenous material) (Macquaker *et al.*, 2014). The progressive burial leads to numerous mineral transformations including smectite-to-illite (Inoue *et al.*, 1988; Peltonen *et al.*, 2009, Środoń, 1999) and opal A to opal CT and quartz (Hesse, 1990; Williams and Crerar, 1985). The recognition of conditions controlling those diagenetic reactions in shales is crucial to help predict their properties interesting from the production point of view.

Presence of organic matter in organic-rich shales (Total Organic Content > 2 wt.%) increases their complexity and modifies their behaviour under increasing temperatures and pressures. Depending on the kerogen type, thermal decomposition of accumulated organic matter can significantly reduce Total Organic Content (TOC) of the bulk rock and potentially

add new porosity (Jarvie et *al.*, 2007). Instead, in shales of maturities equivalent to oil window a drop in porosities due to bitumen and oil filling is observed (Curtis *et al.*, 2013). Microscopic observations, although cannot provide direct answers regarding physochemical evolution of kerogen and bitumen, when coupled with geochemical and petrophysical measurements, can help understand distribution and heterogeneity of the organic material in the shale matrix. Such heterogeneity may reflect varied organic precursors, a degree of kerogen transformation, petroleum migration and expulsion, as well as evolution of residual material under oil-to-gas cracking conditions.

In this paper we examined a set of calcareous, organic-rich shale samples of three different maturities spanning from 0.53% to 1.45% Ro, from the Posidonia Shale formation, Lower Saxony Basin. Due to little variance in mineralogical composition between wells of different maturity, our aim was to track the evolution of the inorganic framework, the macerals composition and porosity change upon increasing thermal stress. We also addressed the issue of small scale heterogeneity on potential for development of organic porosity as potential sites for storage of gas.

Samples and Methodologies

Posidonia Shale of the Lower Saxony Basin, North Germany is a calcareous fine-grained rock deposited in the epicontinental sea during the Lower Toarcian second-order sea level rise (e.g. Littke et al., 1991; Röhl and Schmid-Röhl, 2005). The Lower Toarcian transgression was a global event that induced worldwide shelf anoxia and produced excellent source rocks (Bachmann *et al.*, 2008). The vertical heterogeneity of the Posidonia Formation mudstones is then regarded as being controlled by higher order sea level changes, coupled with subtle climatic fluctuations (Röhl *et al.*, 2001). Based on macro- and microscopical observations, the formation is sub-divided into three units: lower marlstone (I), middle calcareous clay-shale (II) and upper calcareous clay-shale (III) (Figure 2.1b). While marlstone differs from the overlying shales in higher carbonate contents, units II and III are lithologically similar and were distinguished based on the common occurrence of bivalves in the middle (II) shale (Littke, 1991). All three units contain well-preserved Type II marine organic matter with minor contribution from terrestrial macerals (Bour *et al.*, 2007; Littke, 1991; Röhl *et al.*, 2001). For this study, samples were taken from the stratigraphically equivalent sections of three boreholes in the Hils syncline: Wickensen (0.53% R_o), Harderode (0.89% R_o) and Haddessen (1.45% R_o) (Figure 2.1a). The Hils half-graben forms a part of a

series of horst and graben structures evolved during the Late Jurassic and Cretaceous tectonic movements (Bruns *et al.*, 2014; Radke *et al.*, 2001). Partly due to the complex tectonic and thermal history within the area, the genesis of a distinct maturity gradient across wells in the Hils area was a subject of dispute. While a source of the heat was often ascribed to a hypothetical Cretaceous intrusive body, the Vlotho Massif (Schaefer and Littke, 1988), other studies suggest the maturity gradient is a function of differential burial and high temperature regime (Mackenzie *et al.*, 1988; Munoz *et al.*, 2007). Recent 3D modelling studies confirmed that the region experience complex burial and thermal history with differential heat flow associated with the Mesozoic rifting episodes (Bruns *et al.*, 2014).

26 samples were selected for bulk analyses including Rock-Eval, TOC, grain density and total porosity (Figure 2.1b). Total Organic Carbon was measured with the LECO carbon analyzer equipped with a HF-100 Induction Furnace on a carbonate-free aliquot. Standard Rock-Eval was performed according to Espitalié *et al.* (1977) using Delsi Rock Eval OSA. To correct for an oil-in-kerogen peak, 4 shale samples were solvent extracted with a mixture of dichloromethane (93%) and methanol (7%) and subsequently analysed for its remaining hydrocarbon potential.

The X-ray diffraction was performed by Macaulay Scientific Consulting Ltd. The bulk samples were wet ground (in ethanol) in a McCrone mill and spray dried to produce random powders with the optimum distribution of grains. X-ray powder diffraction (XRPD) patterns were recorded from 2-75°2θ using Cobalt Kα radiation. Quantitative analysis was done by a normalised full pattern reference intensity ratio (RIR) method. Expanded uncertainty using a coverage factor of 2, i.e. 95% confidence, is given by $\pm X^{0.35}$, where X = concentration in wt.%, e.g. 30 wt.% ±3.3.

Shale grain density was measured on samples dried at 105°C using the "Small Pycnometer Method" and yielding density values within an error ± 0.02 g/cm^3. In this method, 3 g of dry powdered shale sample was added to a pre-weighed pycnometer of a nominal value 50 mL, immersed in the 10 mL of surfactant (5% Teepol) and gently shaken. The slurry was outgassed in a dessicator overnight, filled with the outgassed deionized water up to the total volume of the pycnometer and weighed at temperature 25°C. The grain density was calculated from the Equation 1:

$$\delta g = \frac{\delta w\ (m2-m1)}{(m4-m1)-(m3-m2)} \qquad \text{(Equation 1)}$$

where δg (g/cm^3) is the shale grain density, δw (g/cm^3) is the density of water at 25°C, m1 (g) is the pycnometer mass, m2 (g) is the mass of the pycnometer plus dry sample, m3 (g) is the mass of the pycnometer plus dry sample plus water, and m4 (g) is the mass of the pycnometer plus water.

Total shale porosity was determined from the measured grain density and bulk density when immersed in mercury at the pressure 25 psia using the Equation 2:

$$\rho = 1 - \frac{\delta b}{\delta g} \qquad \text{(Equation 2)}$$

where ρ (%) is the calculated shale total porosity, δb (g/cm^3) is the measured bulk density at 25 psia, and δg (g/cm^3) is the predetermined grain density.

For microscopic studies, 20 highly-polished thin sections and 3 resin covered blocks, cut perpendicular to bedding, were prepared. Thin sections were first scanned using an Epson Perfection V500 scanner with a 9600 dpi resolution. Subsequently, each thin section was examined with a Nikon Eclipse LV100 POL transmitted light petrographic microscope with an attached Nikon Digital Sight DS-U3 camera. Polished blocks were examined in reflected and UV light using an Oil Zeiss Immersol 518N oil immersion microscope. The fluorescence of organic matter was determined qualitatively using UV light with an HXP 120C accessory.

Carbon-coated polished thin sections were examined using a Hitachi SU-70 High Resolution Analytical SEM, equipped with an Oxford Instrument Energy Dispersive X-ray microanalysis system (INCA Energy 700). Samples were viewed in Back Scattered Electron (BSE) mode using the YAG detector with the following conditions: 15-8 mm WD, 15keV accelerating voltage, 2-4 nA filament current. To reduce the shale topography, prior to the SEM imaging, selected samples were polished with an argon broad ion beam (BIB) in the GATAN 691 Precision Ion Polishing System (PIPS^{TM}). In order to fit into a chamber, the sample size was reduced to a 3 mm in diameter disc with GATAN 601 Ultrasound Disc Cutter using water emulsion of boron nitrate powder as a saw. Such prepared discs were inserted into the PIPS^{TM} chamber and bombarded with Ar ions in a vacuum (10^{-2} Pa) for 6 hours (angle 3°, 5kV, 1-20 μA). The images of shale porosity were captures in Secondary Electron (SE) mode using through-the-lens detector (TLD) at magnification 6000x (pixel size 15 nm). The total image porosity was quantified on image mosaics covering a total area 6000 μm^2 with the point counting method (10000 counts) in the image analysis software JMicroVision 1.2.7. (Roduit, 2008).

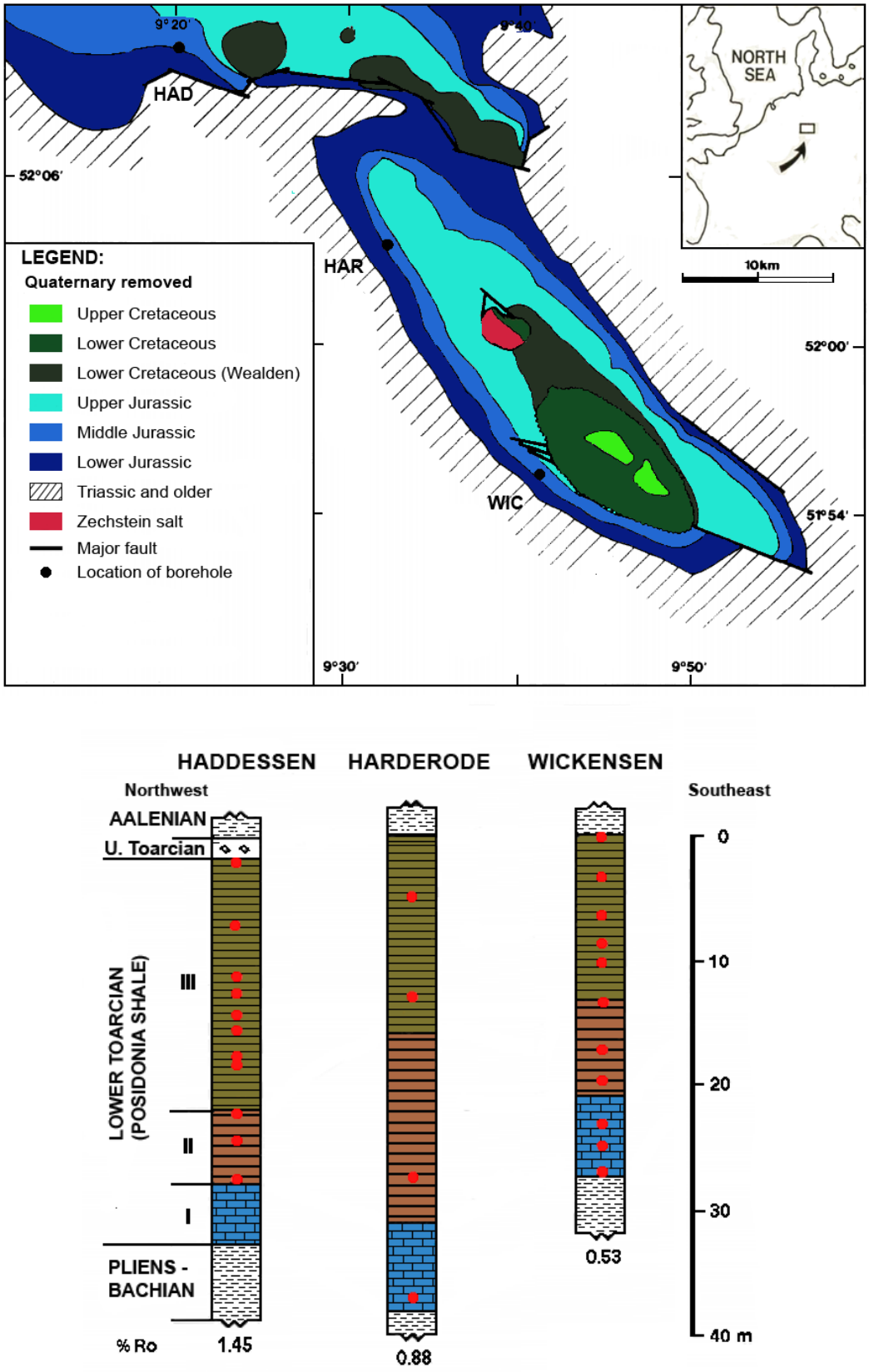

Figure 2. 1. *Location of Hils syncline, Northern Germany and three boreholes: WIC (R_o 0.53%), HAR (0.89%) and HAD (1.45%) (after Mann and Müller (1988) and Horsfield et al. (2010)). b) Lithological profile of the Posidonia Shale from the three boreholes with a marlstone unit (I) and two calcareous shale units (II and III); red dots represent sample locations (after Littke et al. (1991)).*

For selected areas, an Energy Dispersive X-ray (EDX) mode was implemented. With this technique maps of elements distributions are generated due to emission of characteristic x-rays by atoms as a result of the de-excitation of core electron holes created by a high energy electron beam. Microanalysis settings for the EDX collection were set at 300 µm dwell time, 15kV accelerating voltage and 4 nA filament current.

For high resolution imaging, three samples were milled, polished and imaged with Gallium (Ga) focused ion beam (FIB) in the FEI Helios Nanolab 600 with FEG source. The trenches 15 µm x 5 µm were cut at 1-30kV accelerating voltage and 3.3nA beam current. Samples were viewed in BSE Immersion or secondary electron mode with the following conditions: 4.1 mm WD, 1.5-3.0 kV accelerating voltage, 2-4 nA beam current, using through-the-lens detector for better spatial resolution. The images were captured at magnifications between 10,000-200,000x, corresponding to pixel sizes 25-1.2 nm.

Results

Shale composition and texture

Low maturity Posidonia shale from the Wickensen (WIC) borehole (Ro = 0.53%) is a medium grey, fine-grained calcareous mudstone, showing variation both on a formation as well as a lamina scale (Figure 2.1, Figure 2.2). The XRD bulk mineralogy (Table 2.1) shows equal proportion (30-40 wt.%) of both calcite and clays in the upper shale units, but higher content of calcite to clays in the lower marlstone (~50% and ~25% respectively). The calcite and phyllosilicate abundance are inversely correlated, indicating a mutually exclusive mechanism of their deposition. The size of the visible calcareous fraction varies across the core (Figure 2.2), and is much coarser in the lowest marlstone unit (up to 0.6 mm) in comparison to both shale-rich units (<0.1-0.3 mm) (Figure 2.3). While the finest particles constituting the shale matrix cannot be resolved with the standard petrographic methods, the microcrystalline nature of the microscopically distinguishable carbonate aggregates suggest that they are compacted faecal pellets (Bour *et al.*, 2007; Littke *et al.*, 1987; Röhl *et al.*, 2001; Röhl and Schmid-Röhl, 2005; Schieber, 1999). Their distribution varies from sparse, occasionally aligned into discontinuous layers or horizons in the calcareous shale, to densely packed in the marlstone unit.

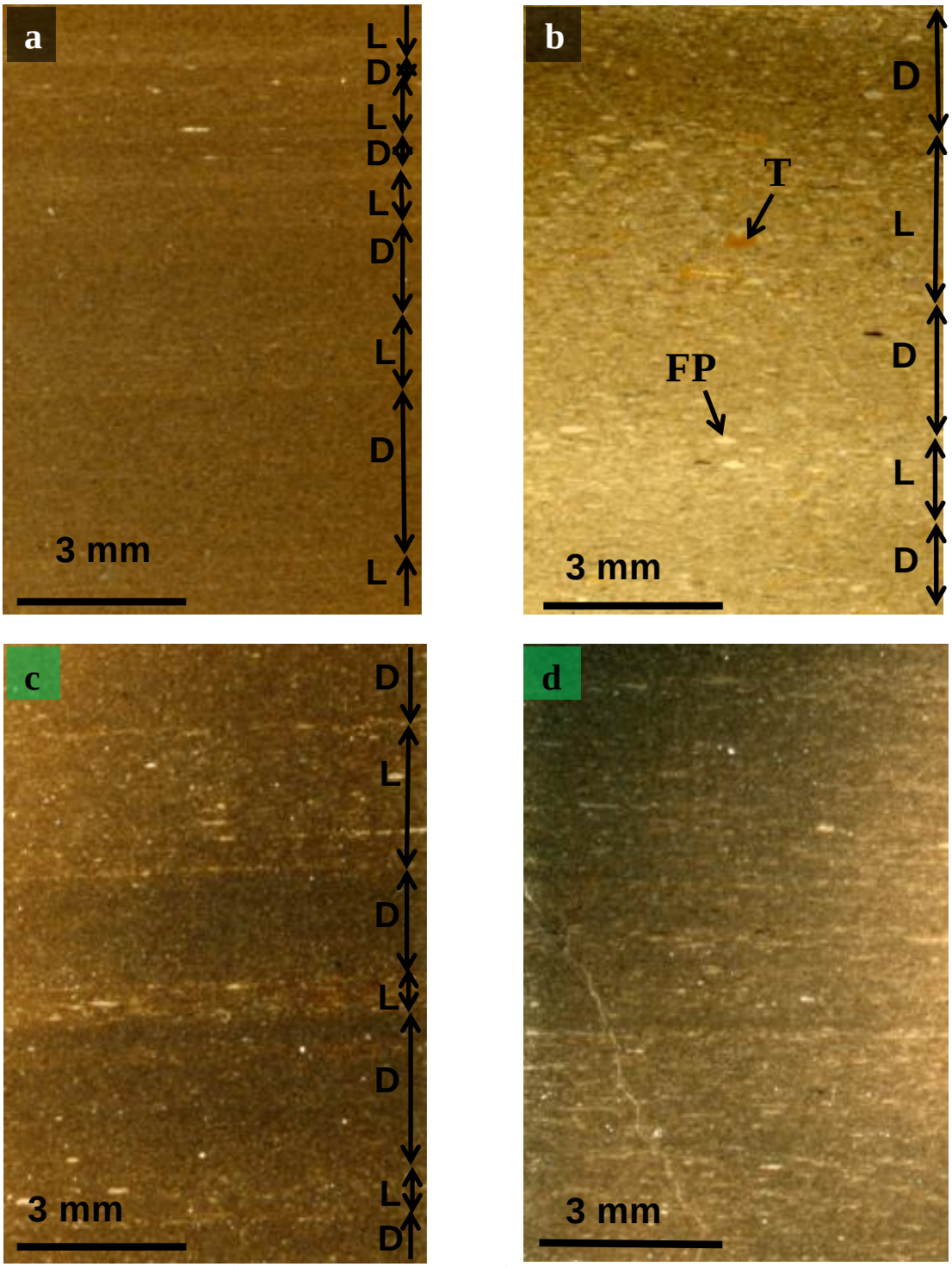

Figure 2. 2. *Scans of polished thin sections of Posidonia Shale. The bedding plane is horizontal. Vertical arrows denote thickness of distinguishable lamina. a) (WIC 7129): Well visible horizontal lamination marked by the alternation of more calcite- and clay-rich horizons. The thickness of the individual lamina reaches up to 3 mm. b) (WIC 7153): Well pronounced lenticular lamination with large faecal pellets up to 0.6 mm. Faecal-pellet diluted horizons alternate with horizons with higher proportion of background clay sedimentation (darker lamina). c) (HAD 7101): Alternating dark and light lamina due to varied content of the carbonate and clay component are still visible in this higher maturity shale. The original lamination is visibly modified by the recrystallization of the matrix components. d) (HAD 7119): The original lamination is obliterated in this higher maturity marlstone sample. D – dark clay-rich lamina, L – light carbonate-rich lamina, FP – faecal pellet, T – terrestrial organic matter.*

Table 2. 1. *The TOC-normalized XRD mineralogical composition of the Posidonia shale in wt.% for WIC (Ro 0.53%), HAR (Ro 0.89%) and HAD (Ro 1.45%). The TOC content (in wt.%) was determined with LECO.*

	WIC 7129	WIC 7135	WIC 7145	WIC 7147	WIC 7155	HAR 7038	HAR 7046	HAR 7060	HAR 7070	HAD 7083	HAD 7090	HAD 7110	HAD 7119
Quartz	12.4	15.1	11.8	14.0	7.8	14.6	16.4	12.2	10.8	11.1	14.8	14.1	7.6
Plagioclase	1.0	0.2	0.9	0.6	1.3	1.9	2.0	2.6	3.7	2.4	2.8	3.2	4.5
K-Feldspar	0.7	0.0	0.0	0.0	0.0	0.5	0.4	0.4	0.5	0.5	0.1	0.7	0.6
Calcite	32.4	35.8	41.5	38.1	50.0	40.1	39.5	28.7	42.2	49.5	36.8	28.5	46.3
Dolomite	0.3	0.0	0.3	0.2	0.5	0.6	1.0	6.0	2.0	0.6	1.7	3.7	2.5
Siderite/ Ankerite	0.4	0.0	0.8	1.8	0.5	0.2	0.3	0.3	0.3	0.1	0.8	0.4	0.6
Aragonite	na	na	1.2	na	1.2	na	na	na	na	na	0.6	na	1.4
Pyrite	4.8	4.5	3.5	3.7	4.9	5.2	4.8	8.6	5.2	6.9	4.6	6.6	4.2
Marcasite	0.7	na	na	na	na	0.6	0.2	0.9	1.2	na	na	0.2	na
Anatase	0.3	0.1	na	0.1	na	0.3	0.2	0.2	0.3	0.2	na	0.4	na
Muscovite	2.3	2.2	0.0	1.2	0.1	2.9	2.8	3.5	3.0	2.4	1.2	4.4	0.0
Illite + I/S	21.7	22.0	20.0	25.4	17.5	17.0	18.9	24.7	18.3	13.3	22.1	23.5	18.1
Kaolinite	10.4	6.0	4.5	7.1	2.0	8.2	6.8	6.2	4.0	6.1	3.6	8.1	1.0
Dickite	na	na	1.1	na	0.9	na	na	na	na	na	1.2	na	0.0
Chlorite	na	0.4	1.8	0.2	1.6	na	na	na	na	0.0	0.6	na	2.5
Gypsium	na	0.3	2.0	0.4	2.2	na	na	na	na	0.4	1.7	na	3.5
Halite	na	0.1	na	0	na	na	na	na	na	0.1	na	na	na
TOC	12.6	13.3	10.9	7.3	9.7	7.9	6.8	5.8	8.7	6.4	7.4	6.4	7.2
Total	100	100	100	100	100	100	100	100	100	100	100	100	100

Within all units the shale matrix is arranged into sub-centimetre light and dark laminae, reflecting differences in the proportion of carbonate and clay components (Figure 2.2). This sub-centimetre lamination is most pronounced in the upper shale unit, with a typical thickness of single lamina up to 3 mm (Figure 2.2a, Figure 2.3a). In both the lower calcareous shale (Figure 2.3b) and marlstone horizons (Figure 2.3c, d) the sub-centimetric lamination is less pronounced. In the marlstone unit, horizontal lamination is partly imparted by the abundant faecal pellets (Figure 2.2b, Figure 2.3c, d). Here, due to the large size of individual pellets (exceeding 0.5 mm), lenticular lamination is common (Figure 2.2b, Figure 2.3d) and convoluted lamination occurs sporadically. In all units, contacts between laminae are parallel and vary between sharp to gradual (Figure 2.2a, b; Figure 2.3). The regular character of the lamination suggests that it is primary, reflecting changes in the supply of the clastic and biogenic components. Very sporadically, the laminae boundaries are marked by an erosional contact or presence of a thin layer of silt carbonates or quartz (Figure 2.3a, b).

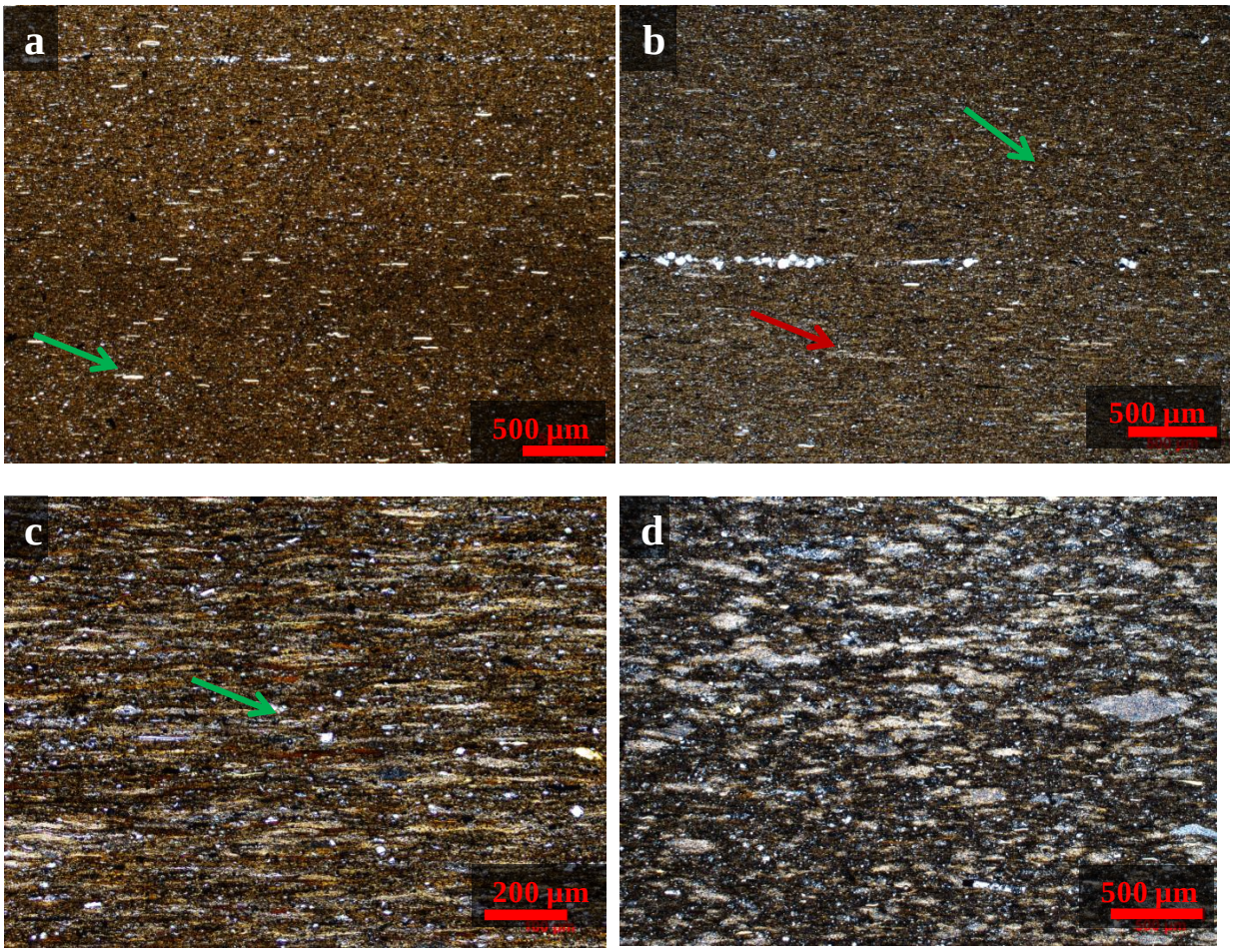

Figure 2. 3. *Plane-polarized-light optical micrographs of Posidonia Shale Formation samples. a) (WIC 7129): Fine microlamination marked by varied abundance of matrix calcite. Dark unit (centre) is relatively enriched in a clay component and impoverished in a calcite component. No visible faecal pellets present at this horizon. A single quartz layer can be observed at the top. Flattened algal bodies constitute well oriented components in the fabric (green arrow). b) (WIC 7145): A layer of silt-sized carbonates separating two lamina. Horizontal faecal pellets (red arrow) and flattened algal cysts (green arrow) show signs of compaction. The shale below the silt layer has larger accumulation of faecal pellets and is lighter in plain light. c) (WIC 7151): An example of lenticular microlamination in a clay- and organic matter-rich matrix. The bright horizontal lenses are composed of well-defined faecal pellets. Flat organic-rich clay aggregates marked with a green arrow. d) (WIC 7153): Well-developed lenticular lamination. The top half contains faecal pellets up to 0.5 nm, forming a distinguishable horizon in a sample. The bottom half contains faecal pellets of a smaller size with a greater proportion of the clay and organic matter in the matrix.*

Most of the organic matter remains unresolved in the petrographic sections. However, darker colour of the calcite-depleted laminae may imply relatively higher content of disseminated organic matter in the clayish horizons. Resolved organic matter is present both as flat, up to 0.3 mm long, organo-clay aggretates (Figure 2.3c) and as highly compacted, discrete cysts (Figure 2.3a). Large terrestrial organic particles (up to 500 µm) are scarce, but relatively more common in the marlstone unit (Figure 2.2b).

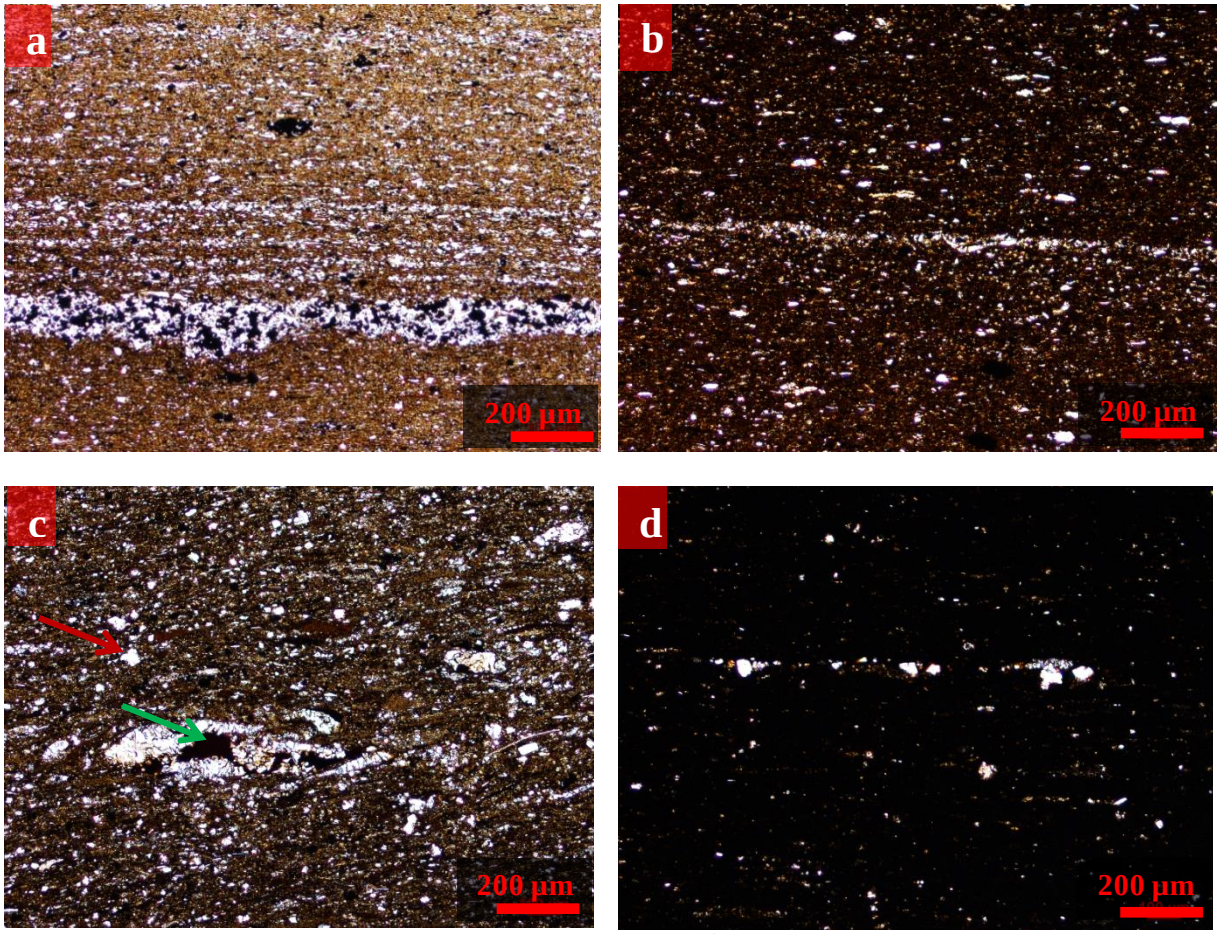

Figure 2. 4. *Plane-polarized-light optical micrographs of Posidonia Shale Formation samples. a) (HAR 7038): The visible lamination is due to presence of diagenetic layers composed of quartz and authigenic pyrite. An uneven surface below the bottom silt layer may be erosive or diagenetic in origin. b) (HAR 7046): The original lamination is mostly obliterated. A silt-sized quartz grain layer of unknown origin visible in the middle. c) (HAR 7060): Sub- and euhedral carbonate crystals (red arrow) are widely disseminated in the shale matrix. Some parts of the shale are cemented. Green arrow denotes an authigenic pyrite nodule. d) (HAR 7070): Recrystallized carbonates are aligned in a single layer.*

Moving towards higher maturities (Ro > 0.9%), we observed a slight change in the shale composition and fabric. While the bulk clay and carbonate content do not differ from those encountered in the immature section, there is a relative increase in the proportion of dolomite to calcite, irrespective of the unit (Table 2.1). This, along with a higher content of Na-rich plagioclase, suggests that diagenetic processes were active at oil window maturities. The effect of these processes can be seen in the thin section scale. In both Harderode and Haddessen the primary sub-centimetre lamination is modified (Figure 2.2c) or obliterated (Figure 2.2d) due to recrystallization of the matrix calcite (Figure 2.4, 2.5). The authigenic carbonate is common, reaching up to 0.05-0.1 mm, and is usually present as oval pelloids (Figure 2.4b, 2.4d, 2.5b, 2.5c). Some layers are more affected by diagenetic recrystallization (Figure 2.4a) and may reflect differences in the original composition, e.g. higher calcite or

quartz content. Consistently with the observations from the low maturity well, faecal pellets are more abundant in the marlstone unit (Figure 2.5d).

At all maturities, macrofossils were rarely observed except for single occurrences of bivalves, calcareous shells and fish-bone fragments.

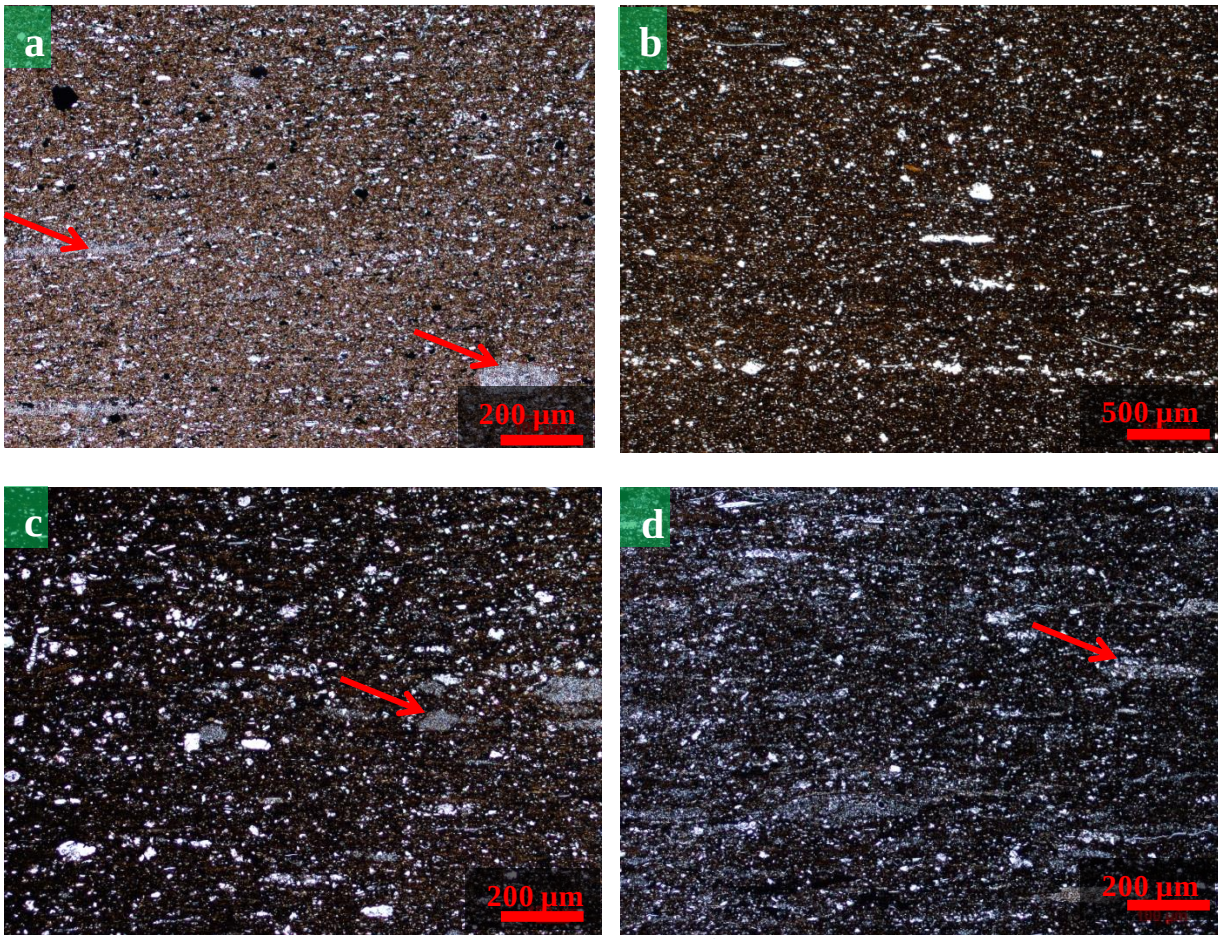

Figure 2. 5. *Plane-polarized-light optical micrographs of Posidonia Shale Formation samples. a) (HAD 7083): Small-scale heterogeneity is imparted by the presence of flattened and oval faecal pellets (red arrows). The unit at the top has more silty material (carbonates and quartz), and more pyrite. b) (HAD 7101): Diagenetic carbonates are found in layers, in an otherwise recrystallized shale matrix. c) (HAD 7110): Large faecal pellets (red arrow) coexist with discrete carbonate crystals and carbonate pelloids. d) (HAD 7119): Shale matrix is strongly recrystallized with a large volume occupied by faecal pellets (red arrow) and cements.*

Small-scale shale heterogeneity in the SEM micrographs

High-resolution BSEM micrographs show that most of the carbonate fraction in the early mature Wickensen samples is of biogenic origin, and was deposited as faecal pellets (Figure 2.6b, d). Nannofossils, mostly coccoliths and schizospheres, form debris dispersed in the shale matrix or concentrated in microlayers or ellipsoidal aggregates (Figure 2.6c). Although individual particles are often mechanically broken (Figure 2.6b), some samples still contain a high proportion of less disarticulated material. The size of nannofossil aggregates varies from ~10 µm (Figure 2.6b), up to 100-200 µm in the calcareous shale units to over 300 µm in the marlstone samples. In all units, microlamination is typical, but its pattern is different in the sub-centimetre light and dark laminae. While in the first the nannofossil material tends to form continuous, <100 µm thick layers (Figure 2.6a), in the dark laminae isolated faecal pellet islands surrounded by the clay-rich matrix are common (Figure 2.6b). The biogenic fraction shows signs of diagenesis, but its intensity is different in the marlstone and calcareous shale units. In the marlstone unit (Figure 2.6d) calcite redistribution was more prominent, and involved precipitation of the calcite cement in intrafossil porosity and recrystallization of the accumulated coccoliths and schizospheres. The advanced recrystallization is reflected by a nearly equant shape of some of the calcite particles. In the two more clay-rich Posidonia units, carbonate cement is present, but the intensity of the calcite redistribution processes was much smaller. Still, we observed syntaxial overgrowths on single biogenic fragments, signs of recrystallization and cementation within biogenic aggregates, as well as the presence of small microcarbs of unknown origin infilling porosity. Overall, the calcite redistribution was stronger in the sub-centimetre, light laminae, with more concentrated nannofossil material, and much weaker in the clay-rich zones with more dispersed biogenic fragments.

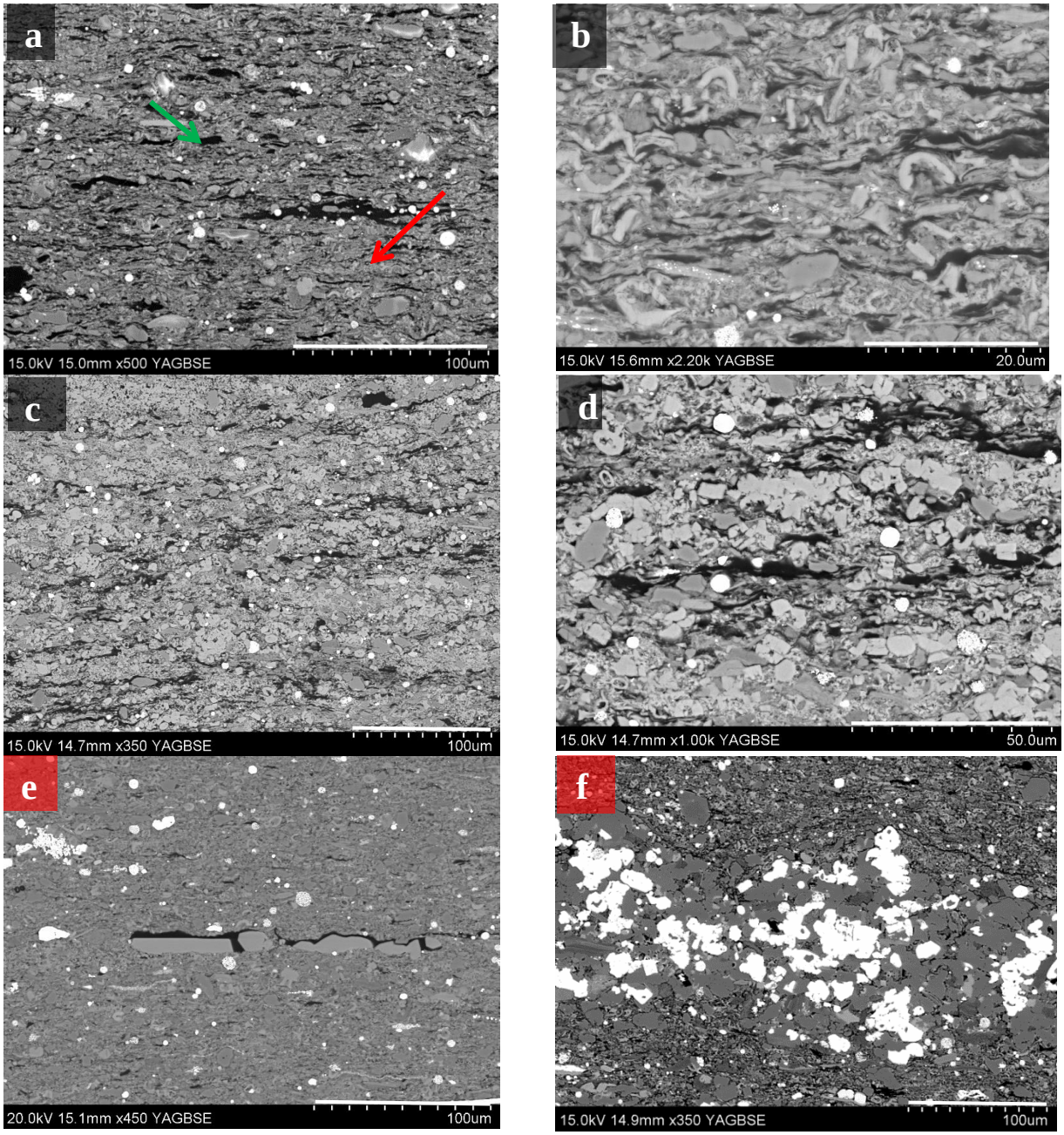

Figure 2. 6. *Backscattered electron micrographs. The bedding plane in all images is horizontal. a) (WIC 7129): Microlaminated calcareous shale (light lamina) with faecal pellet rich layers (red arrow) alternating with clay material (green arrow). Visible organic matter is mostly associated with the last but may also fill cavities within fossil fragments. Silt-sized quartz and pyrite are common, widely disseminated in the matrix. b) (WIC 7129): Details of the nannofossil enrichment in a dark lamina of the calcareous shale. Biogenic calcite is surrounded by clays. Coccoliths are mostly broken, some show signs of diagenetic recrystallization. c) (WIC 7155): Recrystallized nannofossil-rich pellets in a marlstone sample. The silt-size components include quartz, pyrite and organic matter. Clay laminae are volumetrically less abundant than in the calcareous shale. d) (WIC 7155): Strongly recrystallized coccoliths as a product of intensive diagenesis of biogenic calcite in a marlstone sample. e) (HAR 7046): Calcareous shale of at peak oil window maturity. The nannofossil rich matrix is visibly recrystallized. Authigenic cement present as dolomite and calcite crystals with uniform crystal lattice, as well as newly precipitated kaolinite. Calcite cement precipitated in an algal cyst locally prevented the shale from compaction. f) (HAR 7046): A lamina of quartz associated with authigenic minerals. Quartz grains are strongly recrystallized, with the interstices filled by authigenic pyrite and kaolinite.*

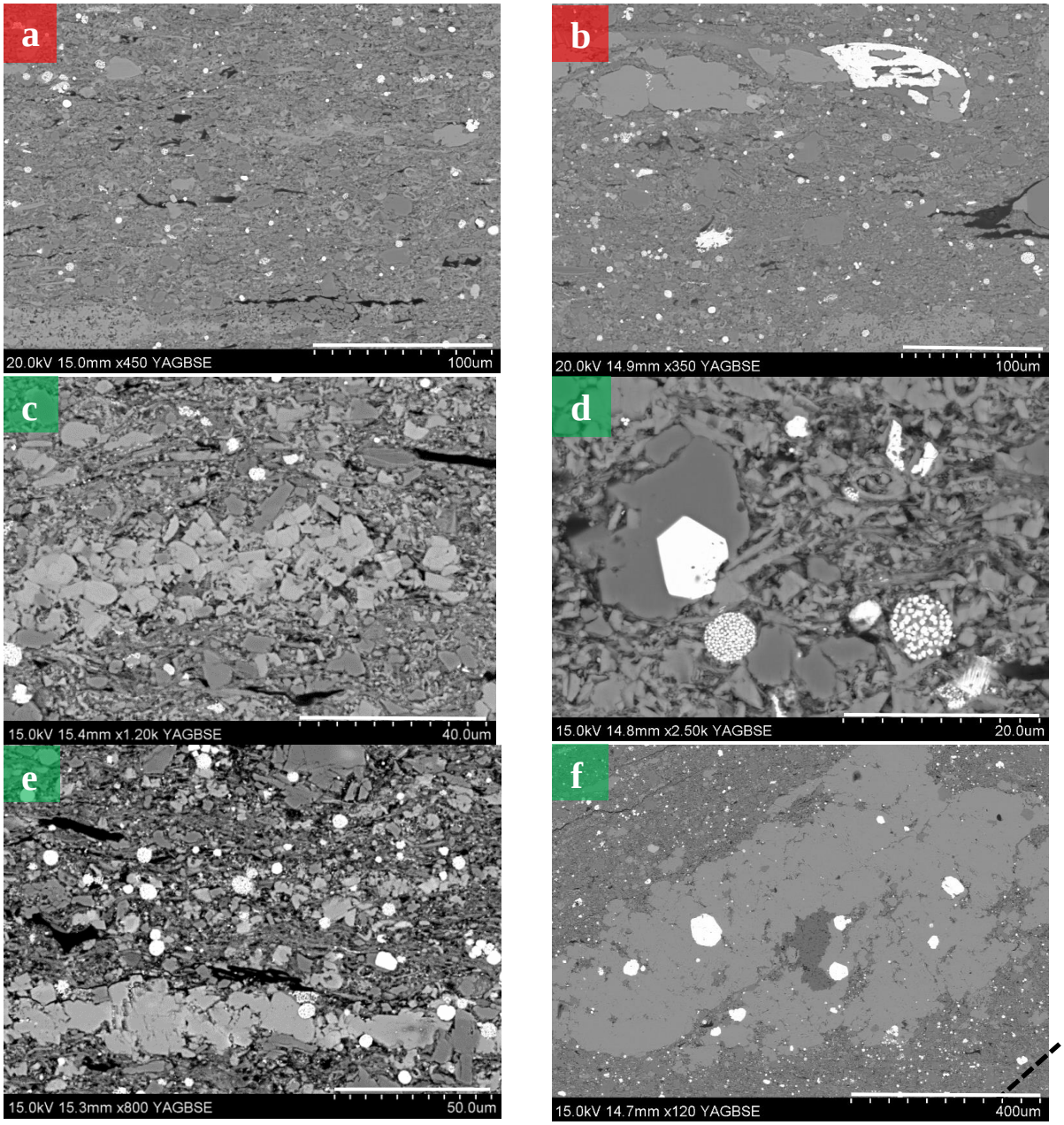

Figure 2. 7. *Backscattered electron micrographs. The bedding plane in all images is horizontal except for image f). a) (HAR 7046): Calcareous shale with recrystallized carbonate matrix. The biogenic material in fecal pellets shows signs of both advanced recrystallization and local cement precipitation. Algal bodies remain mostly collapsed or filled by carbonate cement (bottom right). b) (HAR 7060): Calcite and pyrite cement (top) may replace significant portion of original shale fabric. c) (HAD 7083): Carbonate-rich shale with cement precipitated within coccolith canals. Most of the carbonate material in the matrix is recrystallized and dolomite cement is common. d) (HAD 7083): Authigenic pyrite may form small euhedra, oval framboids or directly replace biogenic calcite. The recrystallization of biogenic calcite led to significant fusing of calcite crystals. Small authigenic calcite (microcarbs) is closely admixed with organic matter. e) (HAD 7115): Well visible microlamination with alternating clay- and calcite-rich lamina. Calcite cement at the bottom is either filling a fracture or cementing a faecal pellet. Biogenic fragments in the centre present strong syntaxial overgrowths acquiring an equant crystal shape. New dolomite phases are cementing the original fabric. f) (HAD 7115): Large calcite cementation zone is replacing the original shale fabric. Authigenic kaolinite is filling centre of the calcite cementation zone, possibly evolved due to dissolution of the grain framework. Bedding plane is marked with a dash line.*

Redistribution of the original shale components and precipitation of new authigenic phases was more advanced in samples of maturity 0.9% Ro and higher. In both HAR and HAD, calcite cement filling coccolith canals is ubiquitous (Figure 2.7c). All biogenic fragments present syntaxial overgrowths (Figure 2.7c), and the fusing due to recrystallization of single crystals is common (Figure 2.7a). The sub- and euhedral crystals of authigenic calcite often preserve uniform crystal lattice and reach a size up to tens of microns (Figure 2.7e). Occasionally, calcite cement is filling algal cysts (Figure 2.6e), preventing them from mechanical compaction. Some zones are fully cemented, and their size can reach up to 100 µm in length in HAR (Figure 2.7b) and 1000 µm in HAD (Figure 2.7f). The authigenic, fabric replacement dolomite is common, and can be observed either as small discrete assemblages, from a few µm up to 20-40 µm in size (Figure 2.7d), or large cemented zones up to 100 microns in length.

Unlike carbonates, the composition of the clay fraction does not vary between maturities. Detrital clays are K enriched at all maturities. Authigenic kaolinite is present and usually fills algal cysts, cements cavities in fossil canals, or occludes pores developed due to dissolution of the framework (Figure 2.6e, 2.7f). The detrital silt fraction is dominated by quartz, which similarly to clays, is more abundant in the shale-rich units. It forms anhedral, rounded to subangular grains of a size varying from under 1 µm up to 20 µm (Figure 2.7a). Occasionally, recrystallized quartz forms part of diagenetically changed layers in samples of higher maturities (Figure 2.6f). Finally, authigenic pyrite is present at all maturities, forming small euhedra (Figure 2.7d), oval framboids (Figure 2.7f), nodules (Figure 2.4c), or directly replacing biogenic calcite (Figure 2.7b, 2.7d).

Posidonia shale shows signs of physical compaction, reflected by the horizontal arrangement of its components (Figure 2.8). The horizontal flattening visibly affected algal cysts, clay aggregates, and faecal pellets. The collapse of the shale structure can be seen adjacent to rigid shale components associated with compaction shadows. The shortening of the matrix in the vertical direction visibly progressed between 0-5-0.9% Ro, often related to the collapse of algal cysts (Figure 2.7a).

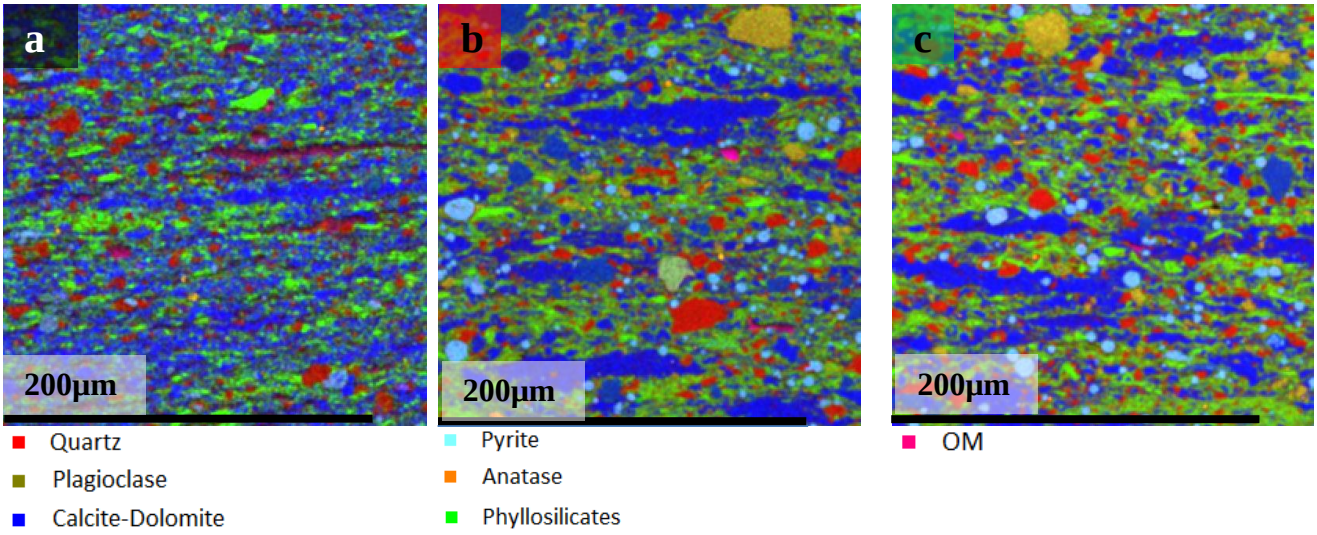

Figure 2. 8. *A mix of X-ray maps displaying well-defined microlamination of shale components at all maturities (a) WIC 7129, b) HAR 7060, c) HAD 7110). The microlamination is marked by the alternating pattern of calcite- and clay lamina, and in the lower maturity samples, also organic wisps. The bedding plane in all images is horizontal.*

Change of organic matter upon maturation

Posidonia Shale is an organic-rich rock with the TOC variability controlled by the mineral composition (e.g. carbonates more strongly dilute OM than clays) as well as the degree of the thermal maturation (Table 2.2). In the least mature shale at 0.53% R_o (WIC) TOC varies between ~7-15 wt.% (mean 10 wt.%), and gradually decreases to an average ~7% in the peak oil window (HAR 0.89% R_o) and down to ~6% in the gas window (HAD 1.45% R_o). RockEval data confirms the maturation pathway typical for the Type II marine kerogen. We also observed a consistent drop in both S1 and S2 yields, resulting in a decrease in HI from ~650 to ~60 mg/gTOC. A significant drop in yield, from 10 to 1 mg/g, was observed for the amount of organic matter pyrolizable under standard RockEval conditions, but extracted with organic solvents ($S2_a$). For all samples, $S2_a$ is consistently higher than RockEval measured free bitumen S1, significantly reducing the yield of the pyrolizable organic matter $S2_b$ of the solvent extracted shale (Table 2.3). Calculated oil saturation indices vary from 105 mg/gTOC for the early oil window sample, 66 and 102 for the two peak oil window samples and 27 mg/gTOC for the gas window sample.

Table 2. 2. *Leco, Rock-Eval, grain density and total porosity results for selected Posidonia samples from wells WIC (Ro 0.53%), HAR (Ro 0.89%) and HAD (Ro 1.45%).*

Sample	TOC	S1	S2	HI	T_{max}	Grain density	Total porosity
WIC 7129	12.59	3.02	90.25	717	427	2.254	0.098
WIC 7133	8.71	2.57	54.90	630	434	2.392	0.128
WIC 7135	13.27	4.62	84.63	638	427	2.249	0.101
WIC 7137	10.25	3.18	68.10	665	427	2.343	0.106
WIC 7139	9.36	2.81	64.95	694	428	2.375	0.135
WIC 7142	10.43	3.52	72.37	694	426	2.346	0.122
WIC 7145	10.92	4.18	72.03	660	425	2.331	0.129
WIC 7147	7.28	2.26	47.76	656	434	2.458	0.114
WIC 7151	14.75	5.85	89.61	608	429	2.236	0.105
WIC 7153	7.34	2.45	48.37	659	431	2.489	0.139
WIC 7155	9.67	3.87	69.41	718	428	2.361	0.126
HAR 7038	7.905	3.29	30.17	382	449	2.493	0.031
HAR 7046	6.75	2.93	26.03	386	450	2.526	0.046
HAR 7060	5.78	1.47	19.72	341	447	2.592	0.045
HAR 7070	8.71	2.26	31.27	359	449	2.463	0.035
HAD 7083	7.35	0.75	4.10	56	465	2.589	0.137
HAD 7090	7.41	0.94	4.16	56	463	2.572	0.114
HAD 7094	5.21	0.845	3.52	68	459	2.608	0.121
HAD 7097	5.40	0.75	3.15	58	458	2.609	0.119
HAD 7099	6.51	0.98	3.86	59	463	2.576	0.106
HAD 7101	5.88	0.92	3.1	53	457	2.624	0.118
HAD 7104	5.04	0.72	3.385	67	459	2.620	0.116
HAD 7105	5.85	0.77	3.28	56	461	2.621	0.112
HAD 7110	6.36	1.07	3.79	60	462	2.600	0.094
HAD 7115	6.49	1.12	3.80	59	460	2.614	0.093
HAD 7119	7.15	1.23	3.16	44	458	2.607	0.115

Table 2. 3. *Rock-Eval evaluation after solvent extraction for four Posidonia samples, wells WIC (0.53% R_o), HAR (0.89% R_o) and HAD (1.45% R_o).*

Sample	S2a (mg/g)	S1 + S2a		S2b (mg/g)	Oil saturation index (mg/gTOC)	Grain density (g/cm^3)	Total porosity (%)	Estimated bitumen content (%)
		(mg/g)	% TOC					
WIC 7129	10.4	13.20	10.5	79.89	104.8	2.236	na	na
HAR 7060	4.5	5.89	10.2	15.25	101.9	2.682	7.8	2.8
HAR 7070	3.5	5.71	6.6	27.79	65.6	2.533	6.3	3.4
HAD 7110	0.7	1.74	2.7	3.05	27.4	2.618	10.1	0.7

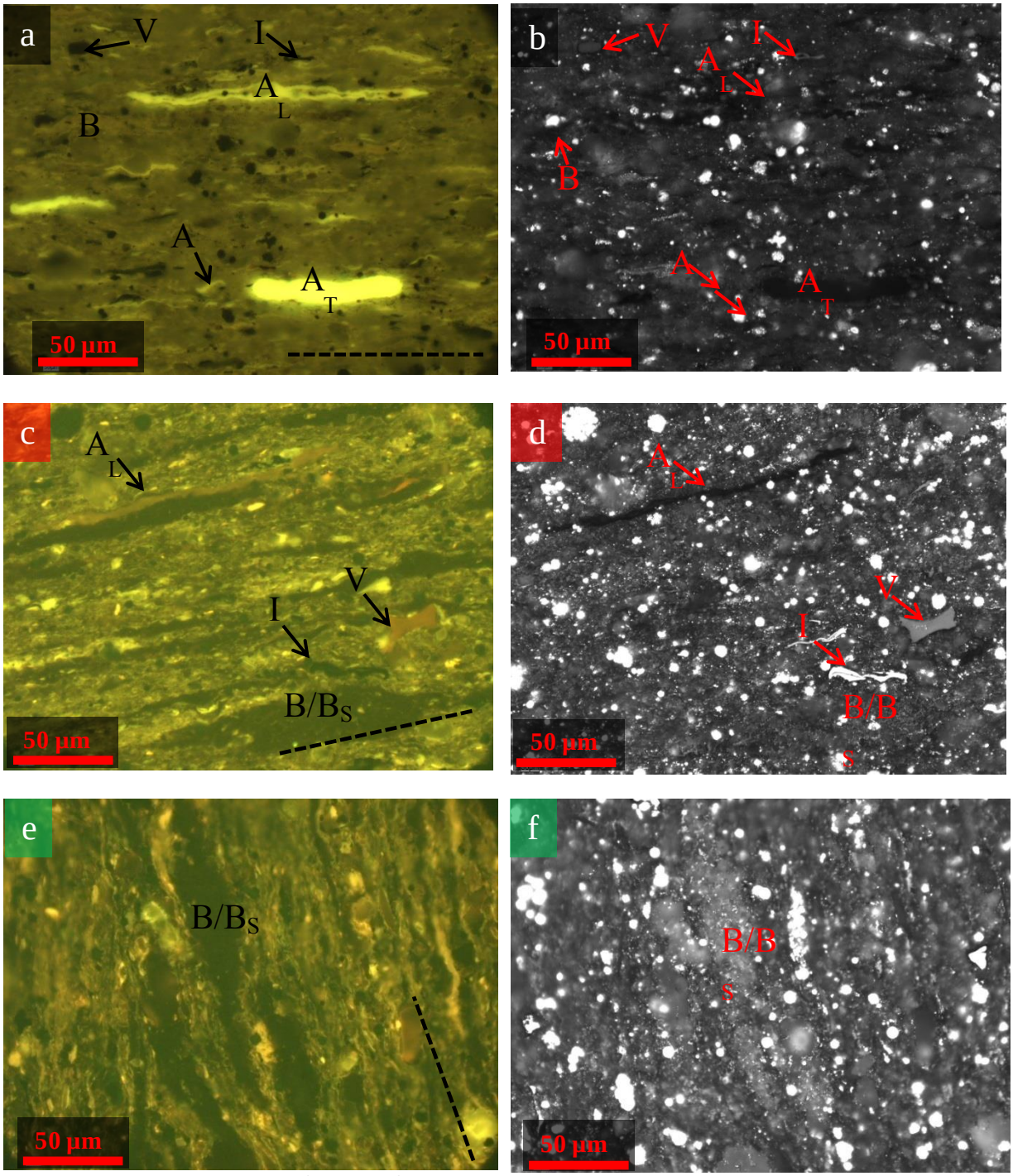

Figure 2. 9. *Oil immersion (left) and reflected light (right) micrographs. Horizontal scale bar denotes 50 µm. Dashed line indicates direction of a bedding plane. a, b) (WIC 7129): Wisps and oval bodies of algal cysts (A_T Tasmanales, A_L Leiosphaeridales) constitute the most prominent organic component. Other macerals include: unidentified alginates (A), bituminite (B), vitrinite (V), inertinite (I). Strong fluorescence of the matrix is due to the presence of the matrix bituminite. The contrast in this micrograph has been subdued due to strong yellow fluorescence. c ,d) (HAR 7060): Algal bodies are mostly collapsed (A_L). Matrix bituminite shows much weaker fluorescence. Solid bitumen (B_S) is present in the matrix, concentrating in the fossiliferous zones. e, f) (HAD 7110): No alginate is present and the matrix is only marginally fluorescent. Solid bitumen (B_S) forms a dense network in the shale matrix and within recrystallized fossiliferous units.*

The macerals found in shales of different maturities show gradual change in type, volume and colour. At Ro = 0.53%, structured algal liptinite (e.g. Tasmanales, Leiosphaeridales) is common, forming well-preserved laminae or thick bodies (Figure 2.9a, b), and co-existing with less pronounced lamellar bituminite. The shale matrix is strongly fluorescing, composed of the bituminous-mineral groundmass, with its organic component, the so-called matrix bituminite, representing a non-structured degradation product of marine phytoplankton and zooplankton (Tao *et al.*, 2012), forming the most abundant organic component of the shale. In low maturity Posidonia, the bituminous groundmass is primarily associated with clays, but may also fill the interstices within fossils (Figure 2.7d). Terrestrial macerals, including vitrinite and inertinite, are dispersed and are present in low abundances. Both structured liptinite and terrestrial macerals show presence of sulphur typically incorporated into organic structure as a by-product of bacterial sulfate reduction processes taking place in anoxic waters under iron-limited conditions (Kenig *et al.*, 2004).

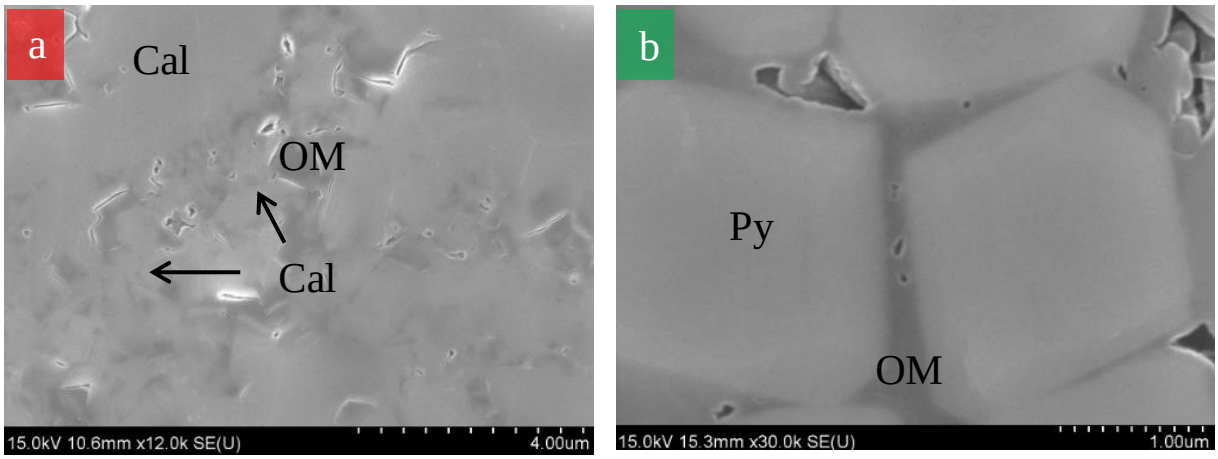

Figure 2. 10. *Secondary Electron micrographs of BIB polished samples after solvent extraction. a) (HAR 7060): Non-extractable organic matter (dark) in an oil window sample fills up spaces between calcite crystals (black arrows) in a fossiliferous domain. b) (HAD 7110): Non-extractable organic matter (dark) in a gas window sample fills the space between pyrite crystallites (light grey) in a pyrite framboid. Note very fine pores (< 100 µm) within the OM.*

At the peak oil window maturity, structured algal liptinite is volumetrically less abundant with only weak brownish fluorescence (Figure 2.9c). The bodies of Tasmanales are collapsed, or locally filled with diagenetic carbonates (Figure 2.6e). The bituminous groundmass is much less fluorescent and instead, a dense network of non-solvent extractable, solid bitumen is filling the intergranular space (Figure 2.9d, 2.10a). The increased concentration of solid bitumen within faecal pellets is a strong contrast to typical organo-clay associations observed

at lower maturity. Solid bitumen can also be found within microfractures, often in the association with diagenetic carbonates.

At the gas window maturity, the bituminous groundmass exhibits only very weak fluorescence and no structured algal liptinite is present (Figure 2.9e). A tight network of irregularly-shaped, non-extractable, solid bitumen is a dominant feature (Figure 2.9f, Figure 2.10b). The bitumen phase homogeneously fills in a tight clay-carbonate matrix and microfractures.

Characterization of shale porosity

Total Porosity

The average grain density of the Posidonia mudstone increases gradually as a function of maturity from ~2.3 g/cm^3 at 0.53% R_o, to ~2.5 at 0.89% R_o and ~2.6 at 1.45% R_o (Table 2.2). When accounted for this grain density change (see Equation 2), measured total porosities show a non-linear trend with increasing maturity of the shale (Table 2.2 and Figure 2.11). At 0.53% R_o porosities vary between 10-14% and, despite an observed decrease in TOC, decline to 2.5-4.5% in the peak oil window (0.89% R_o). In contrast, at gas window maturities, with further reduction of the carbon content, a rise in total porosity is observed. Porosities oscillate here between 9-14% reaching values similar to those at 0.53% R_o. Due to a small range in TOC values at any single maturity, porosities are not directly related to TOC, and only at the early oil window maturity do porosities and organic content show a weak negative covariation (Figure 2.11). For both peak oil window and gas window samples, the porosity values scatter over the measured range of TOC with no apparent trend.

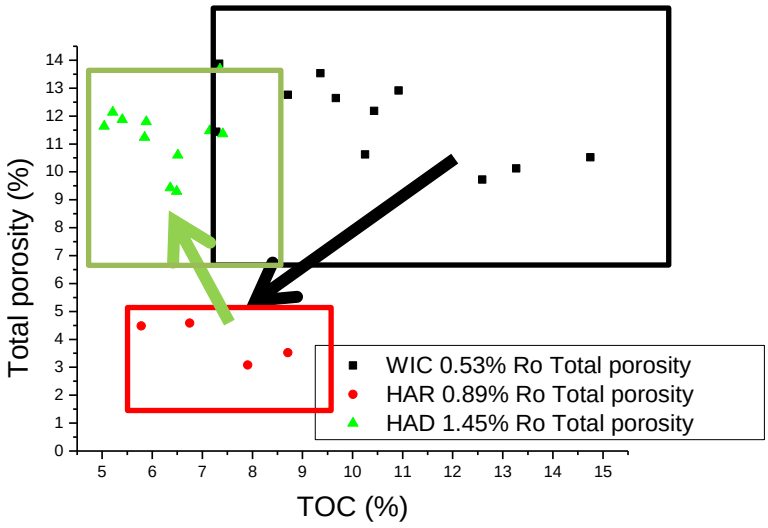

Figure 2. 11. *Total porosity as a function of maturity and organic carbon content.*

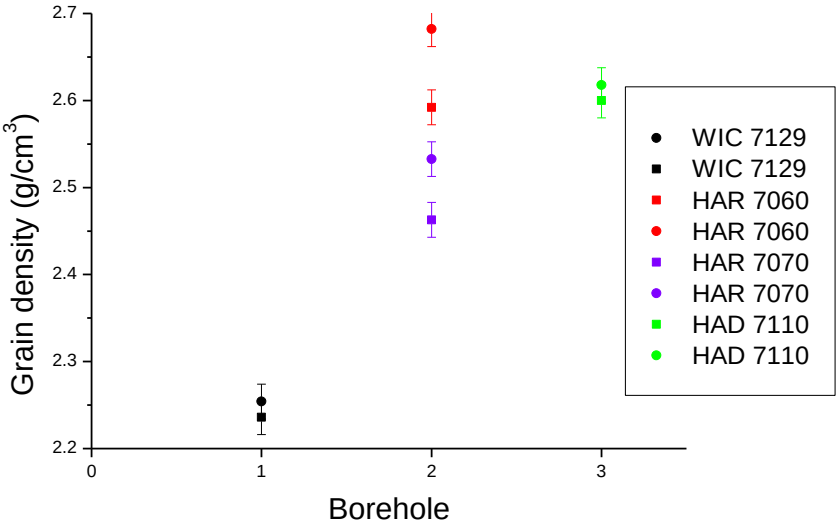

Figure 2. 12. *Grain density change with maturation as measured on "pre-extracted" (squares) and "post-extracted" (circles) shale. Solvent extraction significantly increased density of the peak oil window maturity shale (HAR 7060 and HAR 7070, 0.89% Ro) with little change in the early oil window (WIC 7129, 0.53% Ro) and gas window (HAD 7110, 1.45% Ro).*

Upon extraction of soluble bitumen, both grain densities and total porosities of the shale changed. The most significant increase in the grain density was measured for the peak oil window sample, with only little increase in the gas window shale and a slight decrease in the early mature shale, both within the method error (Table 2.3 and Figure 2.12). On the basis of a change in the grain density of a bulk shale "pre-" and "after extraction" we estimated the amount of the extractable bitumen and thus the "minus-soluble bitumen" total porosity for the three samples of medium (HAR 7060, 7070) and high maturity (HAD 7110). Our calculation assumed that the extractable bitumen occludes porosity, and therefore its amount is equivalent to the fraction of porosity additionally available after this bitumen bitumen was removed from the sample. The results show that the amount of the extractable bitumen present in samples decreases from 2.8% in the marlstone and 3.4% in the calcareous shale at the peak oil window maturities to 0.68% (calcareous shale) in the gas window (Table 2.3), accounting for oil saturations ca. 35%, 54% and 7% correspondingly. The estimated total porosities after solvent extraction are higher than those measured in the as-received shale (Table 2.2), amounting to 6.3-7.8% and 10.1% in the peak oil window and gas window samples respectively (Table 2.3).

SEM observation of Meso- and Macroporosity

Porosity point counted from BIB images does not show significant difference between samples of different maturity, amounting to 1.3% (light lamina) in the Wickensen sample, and 1.1% and 1.5% in the Harderode and Haddessen samples respectively (Figure 2.13a). Due to the limited image resolution (pixel size equals 15 nm) almost all point-counted pores lie within the macropore size range (> 50 nm). Under such conditions, the mesoporosity (2-50 nm) stays greatly underestimated or, along with the microporosity (< 2 nm), unresolved. Consequently, the point counted image porosity is only 14-25% of the experimentally measured total porosity, with the highest fraction of resolved porosity found in the oil window shale (Figure 2.13b).

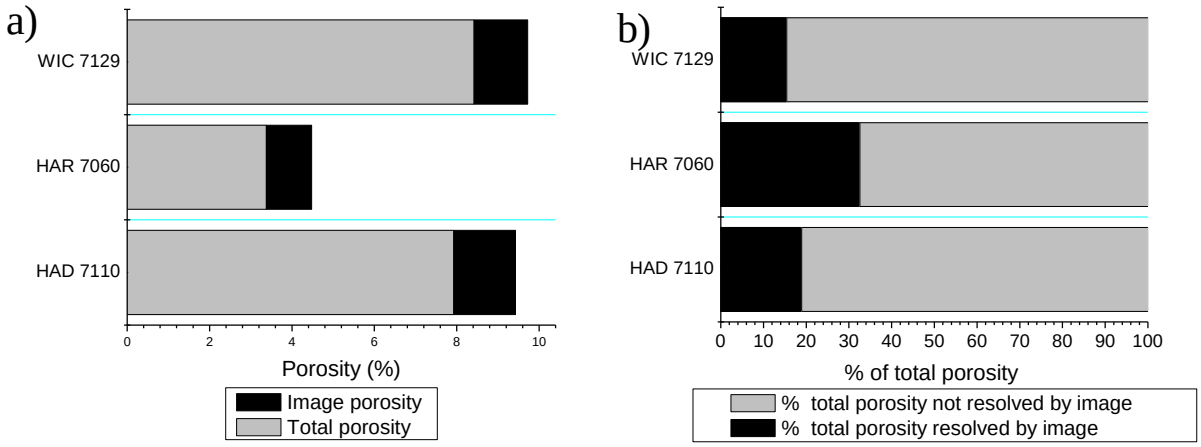

Figure 2. 13. *Point counted image porosity in % (a) and as a fraction of total porosity (b).*

Pores were classified using the general classification of Loucks *et al.* (2009) into interparticle, intraparticle and organic. Our division is based on the spatial relation of pores with respect to mineral phases and organic matter, and not on the origin of pores. Due to the nature of Posidonia Shale minerals and porosity, the following definitions of different pore types were adapted for this study:

- Interparticle: 1) pores between detrital grains, authigenic minerals, nannofossils and clay flakes; 2) pores (in 2 or 3D space) associated with the interface of the organic matter and mineral matrix that do not visibly extend into an organic particle, and that are either irregularly shaped or acquiring shape of the adjacent mineral phase;
- Intraparticle: 1) pores within single mineral grains or fossil bodies; 2) pores within well-defined faecal pellets and pyrite framboids; 3) moldic pores formed due to dissolution of

mineral phases; 4) pores at the interface of inorganic matrix and organic macerals that do not visibly extend into an organic particle, contained within a fossil body, faecal pellet or pyrite framboid;

- Organic: 1) discrete, round, bubble-like pores in the organic matter; 2) sponge-like pores within the organic matter, often interconnected and grouped; 3) pores usually at the interface of the organic matter and mineral matrix, irregular in shape, but visibly extending in 3D into the organic particle; 4) visible cracks within OM particles, often with jagged edges and extending into the particle edge.

Pore network types estimated by a point-counting technique change throughout the maturity sequence from exclusively inter- and intraparticle in the low maturity sample (light lamina), to inter- and intraparticle dominated in the peak oil window and finally, to inter- and intraparticle-rich with moderate proportion of organic pores in the sample of the gas window maturity (Figure 2.14). The visual observations of different pore types using high-resolution SEM micrographs show a varied assemblage of pores with the size as small as a 5 nanometers (x 200,000), up to a few µm.

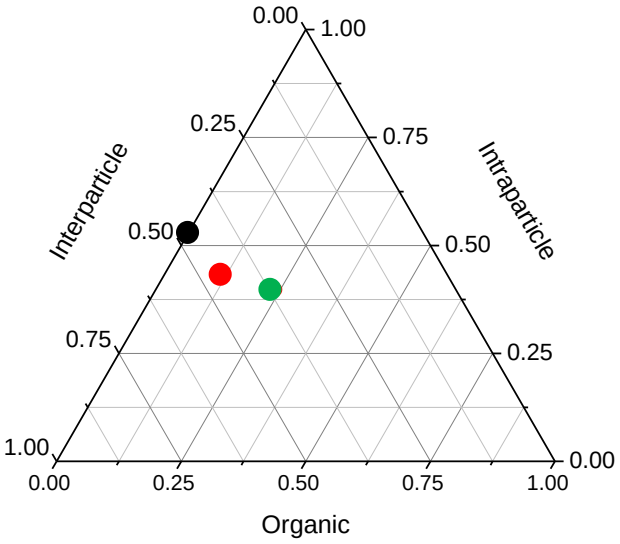

Figure 2. 14. *A ternary diagram showing distribution of visible SEM porosity (pixel size 15 nm) in three Posidonia samples: WIC 7129 (0.53% Ro)(black circle), HAR 7060 (0.89% Ro) (red circle) and HAD 7110 (1.45% Ro) (green circle).*

In the least mature sample (Figure 2.15), visible pores are associated mainly with the biogenic calcite, with no significant porosity within the clay matrix. The typical intraparticle, calcite related pores are found within fully-open coccolith canals, coccolith canals partly

cemented with authigenic calcite, within fragments of Schizosphaerella as well as between fragmented or crushed nanofossils and authigenic calcite phases within well-defined faecal pellets (Figure 2.15a-e). Intraparticle pores are also found within zones cemented with authigenic calcite, between cements, and within discrete calcite crystals as a result of carbonate dissolution (Figure 2.15h). On some occasions, those pores are lined with organics, imparting a smooth, pendular shape to pore edges. (Figure 2.15e). As opposed to the intraparticle pores, the interparticle, carbonate-associated pores are found mostly between carbonate phases and the organo-clay matrix (Figure 2.15i, j). The size and shape of the inter- and intraparticle pores is strongly associated with a degree of recrystallization of diagenetic carbonates (Figure 2.17i). The size of visible, calcite-associated pores ranges between tens of nm to ~3 µm. Pores found in the fossil bodies of Schizopheralles are usually equant and straight edged, up to 500 nm in diameter. Large inter- and intraparticle pores associated with recrystallized nanofossils can be straight edged or spheroidal, reaching up to 3 µm.

Non-calcite porosity is relatively minor but small amount of interparticle pores occur between flocculated clays, or adjacent to quartz, or pyrite, often at the interface with organic matter. These pores can reach 2-5 µm in diameter but also may form narrow < 100 nm rims around or adjacent to mineral phases or organic matter (Figure 2.15k). Elongated intraparticle pores occur within mica group minerals, more pronounced where pyrite has precipitated between mica platelets (Figure 2.15f). Large intraparticle pores, usually lined with organic matter, can also be sporadically found within pyrite framboids (Figure 2.15g).

The majority of organic matter at the maturity 0.5% Ro is not internally porous, and occurrences of intraparticle organic pores are very rare. Those include remnant porosity within walls of not fully compacted Tasmanales bodies (Figure 2.15l) or well-defined, round or angular, < 1 µm pores found within arcuate-shaped, terrestrial organic particles.

In the oil window shale, most of the pore types previously observed is absent, lost due to compaction or occluded by solid bitumen (Figure 2.10). Instead, several new types of pores are present of both intra- and interparticle nature (Figure 2.16). Typical oil window pores are associated with organic matter and/or authigenic phases. Microfracture-resembling pores, elongated and with jagged edges, cross-cut organic particles (Figure 2.16a) often up to their edges (Figure 2.16b). Many pores are found at the organo-mineral interface, with complex shapes resembling shapes of the surrounding mineral phases (Figure 2.16e). Most of those interface pores are associated with diagenetic calcite, and are occasionally filled with the authigenic phases (Figure 2.16f). Pores found directly within organics are always linked in 3D space to particle edges (Figure 2.16 c, d).

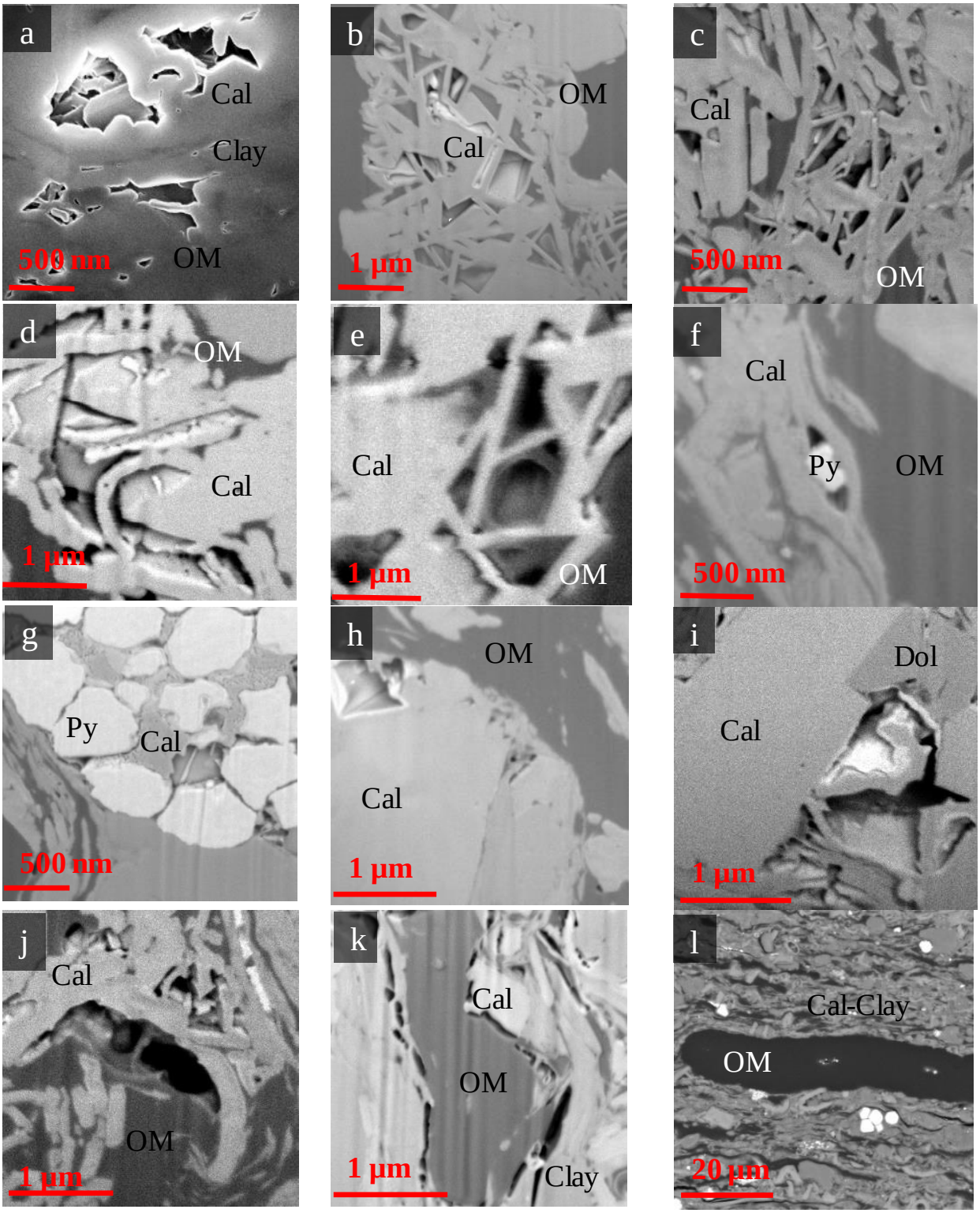

Figure 2. 15. *FIB-BIB-SEM micrographs of the WIC 0.53% R_o shale. The bedding is perpendicular to the view plane. a) Intraparticle pores within a coccolith canal; b) Intraparticle pores in a fragment of Schizophaerella; c) Intraparticle pores in a crushed faecal pellet; d) Intraparticle pore in a strongly recrystallized faecal pellet; e) Intraparticle pores lined with the organic material in a fragment of Schizophaerella; f) Intraparticle pore in clay. The pore formed after pyrite precipitated within the clay material; g) Intraparticle pore within a pyrite framboid; h) Intraparticle calcite dissolution pore; i) Interparticle pore associated with recrystallizing calcite; j) Interparticle pore associated with biogenc calcite; k) Organic associated pores at the interface with the mineral matrix; l) Organic pore within an algal body. Cal – calcite, Dol – dolomite, Py – pyrite, Qtz – quartz, OM – organic matter.*

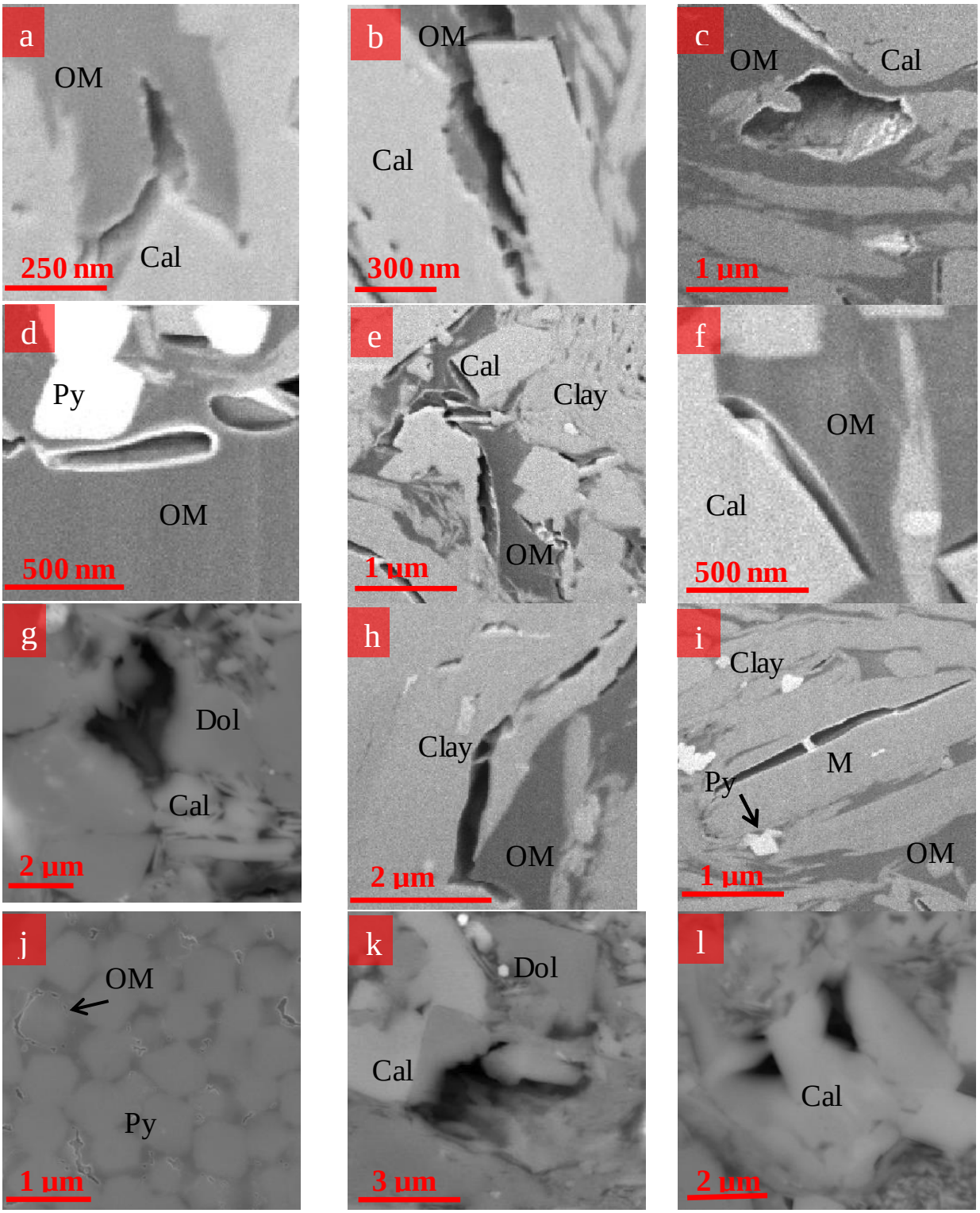

Figure 2. 16. *FIB-BIB-SEM micrographs of the HAR Ro 0.89% shale. The bedding is perpendicular to the view plane. a) Fracture within the OM; b) Fracture at the interface of the OM and calcite; c) Interparticle pore at the interface with the OM and calcitte; d) Interparticle pores within the OM; e) Interparticle pores at the interface of the OM and diagenetic calcite; f) Interparticle crack-like pore from the interface of the OM with diagenetic calcite. An authigenic calcite crystal precipitated within the pore; g) Interparticle pore between dolomite grains/crystals and the shale matrix; h) Fracture within clay; i) Intraparticle, cleavage associated pore in mica; j) Intraparticle pores within a pyrite framboid; k) Intraparticle dolomite dissolution pore; l) Intraparticle pore associated with recrystallized calcite. Cal – calcite, Dol – dolomite, M – mica, Py – pyrite, Qtz – quartz, OM – organic matter.*

Despite the prevalence of organic-associated porosity, pores are also hosted by inorganic domains (Figure 2.16g). Clay-mineral platelets break away yielding fracture or cleavage-related porosity (Figure 2.16 h, i), occasionally partially filled with authigenic phases. Crack-like pores are also observed at clay-carbonate interfaces. In 3D Slice and View reconstructions cracks often follow the shape of underlying or overlying organic particles. Within carbonate minerals, intraparticle dissolution pores can be found (Figure 2.16k) ranging from < 100 nm up to 2 μm. Rare intraparticle porosity, not clogged by bitumen, is also encountered within recrystallized authigenic calcite domains (Figure 2.16l) and pyrite framboids (Figure 2.16j).

Gas window shale, as opposed to the shale samples of lower maturities, shows presence of pores contained *within* organic particles (Figure 2.17). The visible intraorganic porosity is highly heterogeneous, with values ranging between 0-40%, and 65% of point counted organic particles showing no sign of porosity at all. Although the shape and size of organic pores form a continuum, we distinguished several end-members.

Isolated, bubble-like pores are limited in size, often < 100 nm in diameter, and their visualization requires higher magnifications. Although they are present in all shale domains, their distribution within organic particles is varied. They can be uniformly distributed within an organic particle (Figure 2.17a), occupy only a fraction of a particle (Figure 2.17c) or be concentrated at the particle margins (Figure 2.17f).

Similar to round, 'bubble' pores, but usually clustered in groups, are sponge-like pores (Figure 2.17b). They are very often visibly interconnected in 2D and 3D Slice and View images, and thus they have elongated shapes with the size exceeding 100 nm. The elongation often follows the phase margin if developed at the boundary of a visibly porous and non-porous organic area or near the organic-inorganic interface. Similarly to discrete pores, sponge-like pores may be evenly distributed or occupy only a fraction of an organic particle.

With the increase in size and connectivity of individual pores, sponge-like pores may be replaced by irregularly shaped or speroidal organic pores. Although often present directly within organic particles (Figure 2.17d), in 3D they are usually associated with the organic-inorganic interface (Figure 2.17e). In the 3D Slice and View images, the interiors of complex pores branch out into numerous spongy-pores, penetrating the organic mass (Figure 2.17e). Depending on the size of a host organic particle, a diameter of the single complex pore may reach even ~500 nm.

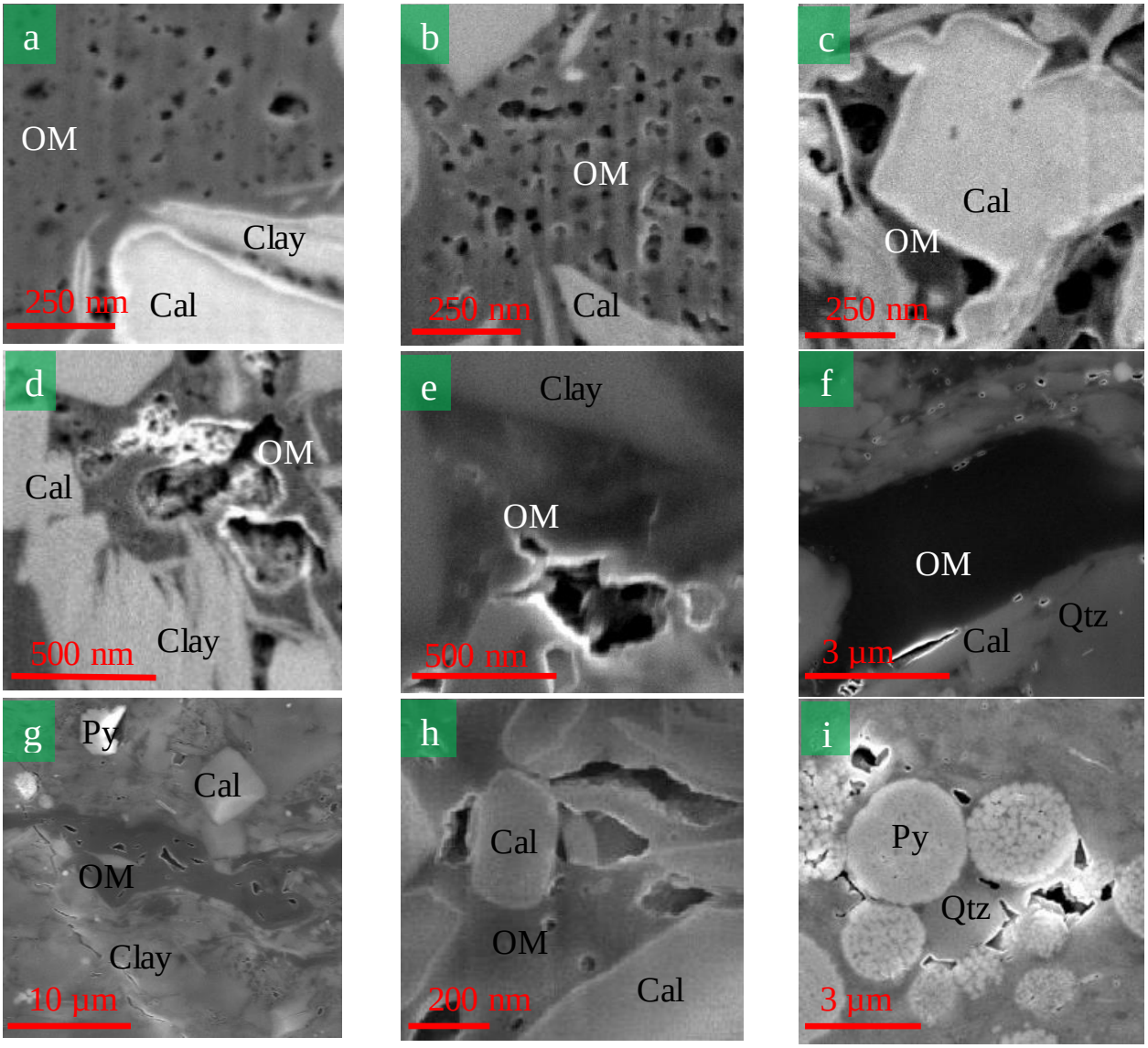

Figure 2. 17. *FIB-SEM and BIB-SEM micrographs of the HAD 1.45% R_o sample. The bedding is perdendicular to the view plane. a) Discrete, bubble-like pores within an organic particle; b) Spongy-organic pores, often visibly interconnected and grouped; c) Pendular-organic pores; Discrete pores are also present; d) Complex organic pore at the interface with the mineral matrix; e) Complex organic pore partly contained within the organic particle, occupying the interface with the mineral matrix in the 3D space; f) Organic pores bordering a terrestrial maceral ; g) Partly compacted organic pores within a terrestrial maceral; h) Interparticle pore at the interface of an organic partcle with diagenetic calcite and clays; i) Interparticle pores between clusters of pyrite framboids, partly contained in the OM. Cal – calcite, Py – pyrite, Qtz – quartz, OM – organic matter.*

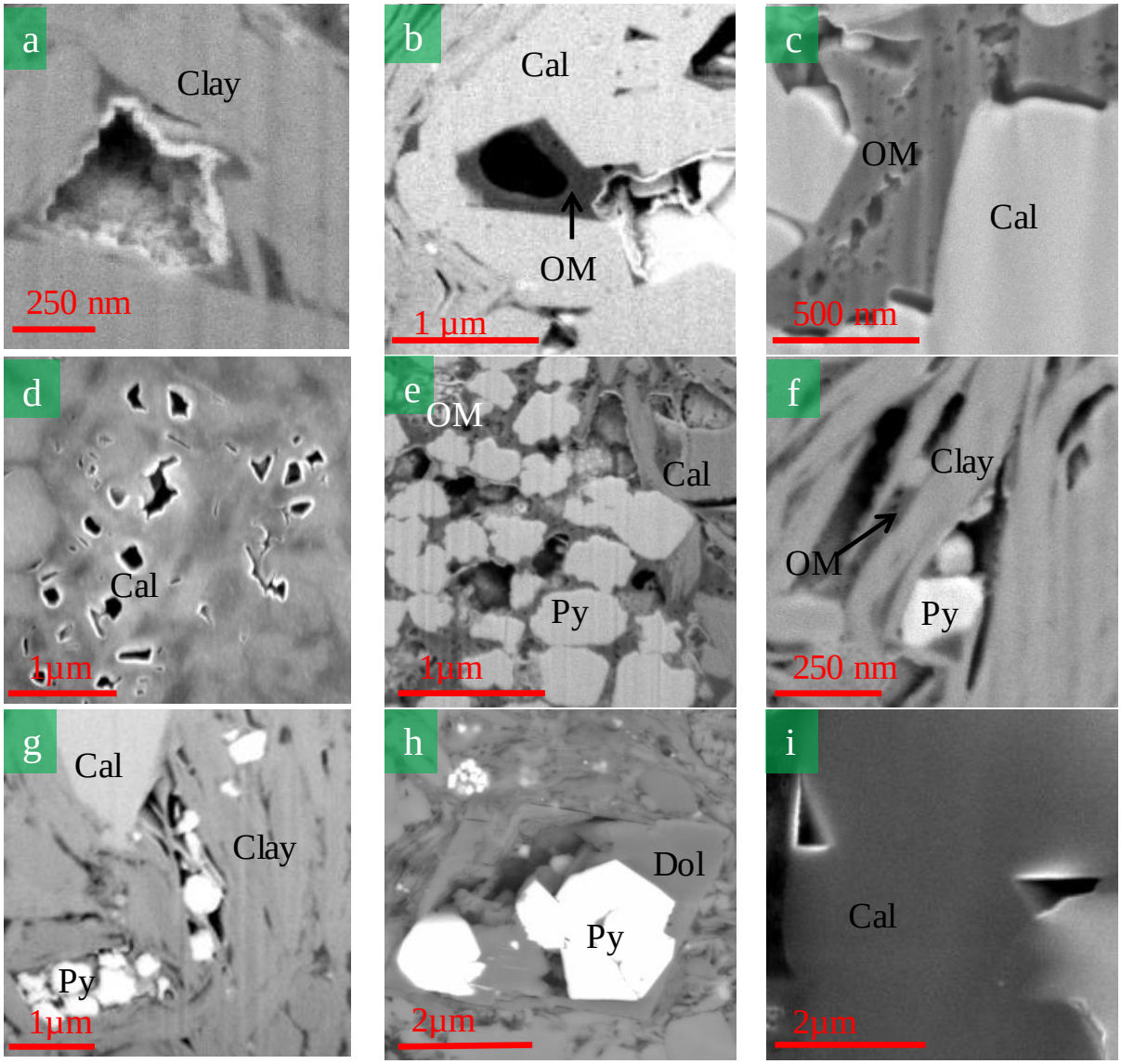

Figure 2. 18. *FIB-SEM and BIB-SEM micrographs of the HAD 1.45% R_o sample. The bedding is perpendicular to the view plane. a) Interparticle pore between flocculated clays; b) Interparticle pore between diagenetic calcite crystals. The pore is lined with organics and thus may resemble organic porosiy; c) Interparticle pores at the interface of the OM and diagenetic calcite. Note discrete and spongy pores within the organic particle; d) Intraparticle pores found in a fossil fragment; e) Intraparticle, complex organic and spongy pores in a pyrite framboid; f) Intraparticle pores between clay platelets. Note close association of the porosity with the OM; g) Intraparticle pores within clays evolved due to precipitation of diagenetic pyrite; h) Intraparticle dolomite dissolution pore; i) Intraparticle pores within recrystallized calcite. Cal – calcite, Dol – dolomite, Py – pyrite, OM – organic matter.*

Also similar in shape to sponge-like pores, but usually associated with particle margins and less likely to agglomerate into complex pores, are oval 'pendular' pores (Figure 2.17c). Ranging in diameter from a few tens to a few hundreds of nanometers, a single 'pendular' pore can occupy a large fraction of a particle or alternatively, it may be located only at the particle interface. Within an organic particle, 'pendular' pores can co-exist with other organic pore types.

The last type of intraparticle organic pores is found with terrestrial macerals (Figure 2.17g). The shape of those pores varies from angular to oval, and their size may reach up to 1 µm in diameter.

Although intraorganic pores are the most characteristic feature of the gas window Posidonia shale, at the magnifications used in this study it is the inorganic-hosted porosity that predominates. However, this may be only an artifact resulting from the limited image resolution, and, with only small % of total porosity resolved in images, the real percentage of the organic pores may be dominating. Similarly to the irregular and complex organic pores, inorganic-hosted pores are usually present at the organic-inorganic interface, but as opposed to the first, they visibly do not branch out into an adjacent organic mass (Figure 2.17h, Figure 2.18a, Figure 2.18 d-f). The interface pores can be jagged edged, with the irregularly shaped organic face (Figure 2.17h), or remain smooth (Figure 2.18b, c), much resembling the smooth interface pores already present in the oil window (Figure 2.16e). Depending on their relation to the surrounding inorganic phases, the inorganic-hosted pores can be classified either as intraparticle or interparticle. The locations of the highest density of the interface pores include faecal pellet domains and pyrite framboids, but the jagged-shaped pores can also be found in vicinity of detrital grains and clay packages (Figure 2.18f). The interface pores are the largest pores present in the gas window Posidonia, and their size may exceed 2 µm in diameter.

Other inorganic pores types in the gas maturity sample are relatively uncommon. Those include: intraparticle pores within mica group minerals (Figure 2.18g), intracrystal carbonate dissolution pores (Figure 2.18h) or possibly blind, remnant pores within recrystallized carbonate phases (Figure 2.18i).

Discussion

Sedimentological controls on mineralogy and texture

A laminated texture of the Posidonia shale is the result of variations in the relative amounts of biogenic calcite and detrital clay-rich material. This variation can be observed both at a sub-centimetre scale, mainly in the low maturity shale, and a micron scale at all maturity levels. Littke (1991) ascribed the vertical variations in the amount of carbonate and clay minerals to relative changes in the rate of nutrient-dependent primary production in surface waters as compared to the supply of terrigeneous clays. Similarly, increased nutrient supply and higher primary production due to flooding of large shelf areas would account for higher carbonate content in the marlstone unit. Our data supports the interchangeable relationship between the clay and calcite content and points to moderate dilution of organic matter by the biogenic material. Similar vertical laminations were observed in the Posidonia Shale deposited in the Southwest German Basin and ascribed both to longer-term variations in sea-levels and short-term climatic changes (Röhl *et al.*, 2001). According to Bour *et al.* (2007) and Röhl *et al.* (2001), relative rise in the sea level could enhance sea water circulation, destabilize the water column and therefore explain episodes of bottom colonization and presence of only indistinct lamination in some shale intervals. Alternatively, distinct type of lamination, found in the upper portion of the Posidonia sequence, could point to long-term anoxic conditions in the benthic environment (Röhl and Röhl, 2005). Prolonged sea water stratification and high rates of primary production as indicated by Röhl *et al.* (2001) could be responsible for high TOC values and the lack of bioturbation in our samples. Predominantly concordant contacts between laminae as observed in this study confirm the primary nature of the lamination in the low maturity shale. As opposed to Trabucho-Alexandre *et al.* (2012) who investigated Posidonia Shale from the Dutch Central Graben characterized by a higher clastic input, apart from rare layers of silt-sized material of unknown origin we did not encounter evidence of wave or current activity in the LSB Posidonia mudstone.

Carbonate diagenesis

The sub-centimetre lamination pattern is largely obliterated in shales of the oil and gas window maturities, and based on the high-resolution SEM micrographs, could be explained by the intense diagenesis of the shale components. For instance, lack of distinct fossil shapes in the oil and gas window shale, and even low maturity carbonate-rich lower Posidonia, reflects their diagenetic transformation and rerystallizaion. Similar behavior was commonly reported for diagenetically changed sediments originally rich in biogenic calcite (e.g.; Hicks *et al.*, 1996). One of the proposed mechanisms for early calcite precipitation involves an increase in carbonate alkalinity of the pore waters due to bacterial organic matter degradation (Dix and Mullins, 1987). Early precipitation of cement in the pore space of Posidonia is indicated by the presence of calcite-filled uncompacted coccolith canals and thus high minus-cement porosity (Hesse, 1990; Macquaker *et al.*, 2007). Presence of this early carbonate cement is consistent with the possibility that biogenic gas formed in the early mature Posidonia as reported by Schultz *et al.* (2013). However, taking into account a constant ratio between clay and carbonate phase regardless of the maturity level, it is plausible that other and less temperature-limited processes remained vital for the net redistribution of the carbonate phase. For instance, recrystallization of carbonates may result from the interexchange of ions with the pore water solutions and their transfer from less to more stable calcite surfaces with no net gain or loss of solid phase (Fabricius, 2003). This type of recrystallization will lead to more equant shape of calcite particles even when not in direct contact with other inorganic grains. The recrystallization of carbonates may further proceed as a pore stiffening effect due to development of contact cement, but may also involve pressure solution and calcite cement precipitation in pores away from the stress point (Fabricius *et al.*, 2008; Scholle and Halley, 1985).

Although usually observed in carbonate-dominated mudstones and limestones, pressure solution and calcite recrystallization also occurs in organic rich, clay-bearing limestones or clay-bearing chalks (Marshak and Engelder, 1985). The diagenesis of calcite in organic- and clay-rich shales has not been studied in detail, but our observations suggest that it is different to that observed in carbonate rocks. Chemical processes such as pressure solution commence in chalk at temperatures as low as 20°C, with dissolution seams and stylolites common at temperatures around 30-40°C (e.g. Mallon and Swarbrick, 2002). Carbonate recrystallization in chalk is very advanced by 100-120°C, similar to the temperature experienced by our lowest maturity sample. In contrast, calcite cementation and recrystallization in Posidonia are

limited at Ro = 0.53%, becoming increasingly evident at 0.9% (ca. 140°C) and 1.45% (ca 170°C). Whilst we do not have sufficient information to be conclusive about the apparently retarded carbonate diagenesis in the Posidonia compared to chalk, experimental data suggest that argillaceous chalks, due to the inhibition of carbonate precipitation, are less prone to chemical compaction than pure chalk (Baker *et al.*, 1980). This is consistent with our observations that calcite diagenesis is more advanced in the more carbonate-rich Posidonia marlstone compared with the more clay-rich middle and upper Posidonia units. It has also been observed that diagenesis and cementation can be retarded in oil-filled carbonate and quartzose reservoirs as a result of alterations in the wetting state of the reservoir from water-wet to oil-wet and a concomitant reduction of the amount of water available for solution transfer (e.g. Worden et al., 1998; Heasley *et al.*, 2000; Scholle, 1977). It is certainly plausible that in an organic-rich shale like the Posidonia carbonate surfaces become oil-wet even prior to oil generation, as a result of sorption of polar organic molecules, and the arrest in the transfer of solutes (van Duin and Larter, 2001; Aplin and Larter, 2005).

Without further support from the isotopic or petrophysical data, we cannot be conclusive about which diagenetic process was a dominant factor in the redistribution of calcite in Posidonia. As observed in SEM images, recrystallization features and contact-cement structures appear as early as 0.53% Ro, and are significantly better developed in the more calcite-rich laminae. The recrystallization of calcite as a major process could explain lack of dissolution or etching on nanofossils as reported by Bour *et al.* (2007) from the immature Posidonia from the Southwest German Basin. It could also account for the high minus-cement porosity and crystal fusing features as seen in the oil and gas window samples under the oil-wet conditions. In contrast, presence of cements with a uniform crystal lattice as well as fracture filling calcite may suggest that pressure solution occurred at some point. The dissolution may have been followed by the precipitation from carbonate ions-rich pore waters of both calcite and dolomite. As significant dolomitization occurred at oil window temperatures, it is unlikely that Mg required for dolomite formation was released due the smectite to illite transformation reaction (cf McHargue and Price, 2006). For instance, Kanitpanyacharoen *et al.* (2012) found that degree of preferred orientation in Posidonia clays between 0.68-1.45% R_o is not significantly different and concluded that the fabric evolved early in the history. Likewise, it is unlikely that the dolomite precipitation was induced by anaerobic oxidation of biogenic methane. The SEM micrographs (Figure 2.6 and 2.7) evidently demonstrate that the intensity of dolomite formation increased at oil window temperatures (> 100-120°C), too extreme to sustain the bacterial activity (Berner, 1968;

Raiswell and Fisher, 2000). An alternative source of magnesium was suggested by Bernard *et al.* (2013) and linked to the circulation of brines (Munoz *et al.*, 2007).

Porosity loss through compaction

SEM visible porosity associated with faecal pellets and recrystallized biogenic fragments in the low maturity Posidonia constitutes only ca. 10% of total porosity and its further change with maturity is minor. The remaining porosity, especially that associated with clays and kerogen, is not resolved with the microscopic methods applied in this study. An overview of the < 6 nm meso-and microporosity, along with its distribution in the Posidonia shale, is provided by Rexer *et al.* (2014). A clear division between resolved and unresolved porosities and their attribution to specific domains points to the importance of original rock fabric as a starting point to model the behaviour of porosity retention, loss and development.

The loss of porosity in shales is driven primarily by compactional processes, both mechanical (Aplin and Yang, 2005) and chemical (Bjørlykke, 1999). Although mechanical compaction is significant for muds at shallow burial (Dræge *et al.*, 2006), according to Emmanuel and Day-Stirrat (2012) it may have a negligible impact on pore size distributions of the smallest pores once it is established that the magnitude of preferred orientation of clays ceases to change. As already mentioned, Kanitpanyacharoen *et al.* (2012) found that a degree of the preferred orientation in clays in Posidonia between 0.68-1.45% R_o is not significantly different and therefore, their further compaction within this interval might have been minor. However, we found clear evidence for the physical compaction of the shale fabric between 0.53-0.89% Ro, as associated with the collapse of the algal bodies (Figure 2.7a. Taking into account the loss of the organic matter volume upon maturation, it is more difficult to assess the overall effect of compaction on porosity loss in organic rich shales without taking into account a degree of the kerogen transformation and bitumen retention. Without this knowledge, it is also impossible to verify to what degree the chemical compaction affected the porosities. Recrystallization of calcite without porosity modification is already known from chalks (Fabricius *et al.*, 2008) and it might have been important in the lower maturity Posidonia. Presence of uniform calcite and dolomite cements (Figure 2.7) points that at later stages of diagenesis porosity loss definitely occurred, most likely due to pressure solution. However, the large scale pressure solution and pore cementation might have been mostly arrested by bitumen migrating into fossiliferous zones and occluding the pore space. Still, it is plausible that, similarily to oil-saturated chalks, minor recrystallization of calcite continued

even under oil-wet conditions (Fabricius, 2003). Similarly, the presence of cement within algal cysts suggests that local cementation was active even under oil generation conditions. Therefore, we cannot preclude, that in the organic rich shales diagenetic processes may partly continue in the peak oil window, taking advantage of the kerogen volume loss upon thermal conversion to hydrocarbons. That also indicates that the impact of compaction may be underestimated when taking into account merely the absolute change in the visible SEM porosity and the change of volume in the organic component must be quantified.

Evolution of organic matter with maturation

Although much research was already dedicated to the composition of different kerogen types and their decomposition paths under increasing thermal stress (e.g. Behar and Pelet, 1986; Behar and Vanderbroucke, 1987; Behar *et al.*, 1992; Behar *et al.*, 2010; Bernard *et al.*, 2011; Dieckmann *et al.*, 1988; Guo *et al.*, 2009; Hill *et al.*, 2003; Leythaeuser *et al.*, 1988; Lewan *et al.*, 1997; Lorant and Behar, 2002; Mann *et al.*, 1991; Mao *et al.*, 2010; Michelis *et al.*, 1996; Putschew *et al.*, 1998; Rullkötter and Michaelis, 1990; Rullkötter *et al.*, 1988; Schenk *et al.*, 1997; Vanderbroucke *et al.*, 1993), the mechanisms of primary migration, phase behaviour, bitumen entrapment and organic porosity evolution are still a subject of discussion. In this study, we showed a consistent decrease in TOC, S1, S2 and Hydrogen Index from early oil window to gas window conditions, consistently with observations reported in Posidonia by Leythaeuser *et al.* (1988) and ascribed to the processes of petroleum generation, expulsion and cracking. The net effect of the generation and expulsion processes in Posidonia was documented therein between maturities 0.48 to 1.45% Ro as a progressive increase of the rock extract composition in aliphatic compounds and a decrease in the heavier polar fraction. In this study, direct observations of the Posidonia organic matter under the microscope confirm its progressive thermal degradation, reflected as a change in the volume and composition of macerals (Rullkötter et *al.*, 1988). Specifically, a general change in the UV light response (Khavari-Khorasani, 1987; Khavari-Khorasani and Michelsen, 1992) is consistent with the increasing aromaticity of the maturing Posidonia kerogen (Bernard *et al.*, 2011). Thermal degradation of organic matter is also corroborated by a measured grain density rise between 0.53-1.45% Ro, driven by condensation and aromatization of the carbon structure. Degradation of organic matter accounts then for a major TOC loss with progressive maturity, and overprints primary differences in the organic content inherited from marginally

varied environmental conditions during deposition of the Posidonia Shale sequence (e.g. varied degree of dilution by the biogenic carbonates).

Tissot and Welte (1984) recognized that the composition of petroleum generated during the thermogenic conversion of the accumulated organic matter is a function of kerogen type and maturity. To understand the mechanisms of kerogen decomposition in the subsurface, open and close pyrolysis experiments were performed by various authors and general models of the organic matter transformation were developed (e.g. Behar *et al*. 1992, 1995, 2008; Guo et al., 2009; Horsfield *et al.*, 1992; Lewan, 1997). Behar *et al.* (2008) proposed a kinetic scheme where kerogen decomposes, mainly through depolymerization reactions, into very viscous liquid rich in NSO (nitrogen, oxygen and sulphur) compounds, followed by decomposition of the last into more soluble non-hydrocarbon compounds and finally, cracking into hydrocarbons. The presence of the heavy, intermediate bitumen phase was also proposed by Michelis *et al.* (1996) and Lewan (1997). Our experiments on unextracted and extracted samples confirm the presence of a substantial amount of a non-volatile bitumen phase residing in kerogen of the low maturity Posidonia shale (Clementz, 1978; Wilhelms *et al.*, 1990). Consistent with little change in the bulk shale grain density after the organic extract was removed (Figure 2.12), we presume that this early bitumen is most likely composed of high molecular weight compounds, imparting its viscous nature and low mobility in the shale matrix. Dominance of the heavy bitumen over total extract substantiates that relatively few light compounds are generated directly from kerogen. The nature of petroleum changes in the oil window, and at the peak window maturity it is dominated by lighter compounds responsible for a measurable decrease in grain density of the bulk shale. Similar density reduction was recently reported by Rexer *et al.* (2014) on Posidonia kerogen, implying high adsorptive capabilities of the organic matter leading to retention of oil (Jarvie *et al.*, 2007). Presence of lighter oil at higher maturities likely reflects breakage of C-C bonds (Dieckmann *et al.*, 1988; Rullkötter *et al.*, 1988; Schenk et al., 1997) and in Posidonia it is paralleled by the formation of an insoluble high molecular weight residue, often described as prechar. Occlusion of shale porosity by this insoluble heavy bitumen indicates that a fraction of the early generated petroleum remained entrapped in the shale matrix (Figure 2.10) (Hill *et al.*, 2003; Lewan 1997). Similar solid bitumen, although of different genesis, is known not only for clogging the pore space and closing pore throats in oil and gas reservoirs (Hwang *et al.*, 1998; Lomando, 1992) but is also found as a product of solidification of heavy oil in coals (Mastalerz and Glikson, 2000). Whilst we do not have information on the exact chemo-physical nature of the organic particles occupying porosity in the oil window maturity

Posidonia shale, it is plausible that its precursor was a heavy, viscous non-hydrocarbon or hydrocarbon phase that migrated within the source rock, progressively developing more aromatic and condensed structure upon cracking to hydrocarbons (Behar *et al.*, 1997; Horsfield *et al.*, 1992; Michelis *et al.*, 1996). Such conclusion is consistent with Pelet *et al.* (1986), who analyzing residual but soluble phase demonstrated preferential retention of the heaviest and most polar molecules in the source rock. If our solid bitumen is indeed a spent residue of the viscous bitumen generated from kerogen, it could be classified as post-oil (Curiale, 1986) or secondary (Curiale, 1983; Stasiuk, 1997). Indeed, EDX analyses on solid bitumen found in a fracture in the oil window sample, quite in agreement with extract analyses performed by Leythaeuser *et al.* (1988), still show the presence of sulphur originally incorporated in the marine kerogen.

Primary migration of petroleum

The occlusion of porosity by residual bitumen phase in the oil window validates the processes of micromigration and trapping as a mechanism leading to an increased small-scale heterogeneity of the organic matter. The micromigration of the generated petroleum was already demonstrated by Leythaeuser *et al.* (1988) as a mechanism leading to a fractionation of the soluble bitumen phase, and its progressive enrichment in a non-eluted residue towards macrofractures. It is therefore reasonable to assume that the bitumen phase in Posidonia became mobile and started filling pores once enriched in relatively smaller and lighter compounds. Vanderbroucke at al. (1993) argue that compounds lighter than C_{14+} may be important for migration of heavier compounds by dissolving them and reducing density of the mobile phase. Alternatively, Lewan (1997) proposes that it is solubility with water and volume increase that enable formation of a continuous bitumen network and migration of the bitumen phase within the source rock. The formation of a continuous bitumen network for effective migration is also recognized by Tissot and Welte (1984). Alternative proposed mechanisms enhancing separation of the heavy bitumen and lighter hydrocarbon phase may include preferential sorption on minerals and organic matter (Sandvik *et al.*, 1992), or phase immiscibility in the presence of water (Lewan, 1997). In our study the micromigration mechanism is corroborated by microscopic observations, revealing highly dispersed nature of the solid bitumen, forming a semi-continuous network (Landis and Castano, 1995). The dispersion of this retained bitumen phase might be traced back to the dispersion of the amorphous organic matter in the immature shale, likely the main contributor to the petroleum

generated, here partly sulphurized as a result of the limited availability of the reactive iron in the biogenic-rich intervals (Hutton, 1994; Tao *et al.*, 2012) (Figure 2.9a). Moreover, as opposed to the immature kerogen, mainly associated with the clays (also Littke, 1991), the peak oil window organic matter shows a close spatial association with fossiliferous domains, indicating that the micromigration indeed occurred. It is plausible, that analogous to reservoir oil (Hwang *et al.*, 1998), the source rock bitumen followed the path of the least resistance and relatively quickly filled calcite-pores as zones of the lowest capillary pressure. The highest concentrations of solid bitumen in the zones of recrystallization of biogenic calcite show that the migration might have been inhibited once a migrating or in-situ generated phase became trapped in a porous, rigid zone. The lack of driving force to push the petroleum out of the system, despite the presence of light hydrocarbons, would have therefore accounted for the large amount residual bitumen accumulated.

Further evidence for the small scale heterogeneity of organic matter as a result of the bitumen flow and entrapment is provided by the FIB polished SEM micrographs of the overmature shale sample. The distinction between porous and non-porous organic regions has been already observed by several authors and ascribed to differences in structural composition of organic particles (Bernard *et al.*, 2010; Loucks *et al.*, 2009). For instance, the internally porous organic regions were identified by Bernard *et al.* (2010) and Bernard *et al.* (2012) as pyrobitumen, a residue after thermal cracking of oil, and opposed to kerogen, asphaltene and NSO-rich bitumen showing no signs of visible porosity. If different organic compounds behaved differently upon increasing thermal stress, then their distribution can reveal clues about their possible genetic association and migration mechanisms. In Posidonia, close association of porous and non-porous particles, often remaining in direct vicinity, suggests that pyrobitumen-like, porous phases might have directly evolved from the neighbouring non-porous particles, and at higher temperatures, with the limited scope to flow, underwent further thermal cracking. In this case, the visible pore structure likely marks a boundary between two different organic compounds. This scenario may also apply to non-porous arcuate-shaped terrestrial macerals, often with a rim of porous organic phase.

The role of organic matter on porosity modification in the oil window

It is experimentally proven that substantial amount of porosity in organic rich rocks may be created during the conversion of kerogen to petroleum (Kanitpanyacharoen *et al.*, 2013; Oberlin and Villey, 1980). In Posidonia Shale, despite significant loss of TOC, porosities do

not show a consistent increase, but instead reach minimum values at the peak oil window maturity (Figure 2.11). Relatively high porosity was found in the early mature sample characterized by the largest content of the extractable bitumen. We presume that this early bitumen did not enter the mass migration stage, remaining associated with kerogen (Sandvik *et al.*, 1992) and thus physically immobile to flow (Hwang *et al.*, 1998). According to Landis and Castano (1995), bitumen, as a product of the thermal conversion of kerogen, may start filling porosity of the shale as early as at 0.4% R_o. In Posidonia, early signs of migration may be reflected by the presence of pendular pores, with organics lining mineral walls. As opposed to the early stages of petroleum generation, the loss of porosity was substantial in the peak oil window Posidonia, and although partly related to compactional processes, it was closely associated with the generation and micromigration of petroleum (Lewan, 1997). Jarvie (2012) suggested that the lack of visible organic porosity at the peak oil generation maturities is due to solubility of oil in kerogen and consequent kerogen swelling. Selective absorption of petroleum compounds, reflected by swelling of the organic polymers, was also proposed by Sandvik *et al.* (1992) to govern yield of petroleum expelled from a source rock. Our experiments showed that oil extracted from the peak oil window Posidonia shale has a strong affinity for organic matter and is equivalent to 2-3% of porosity. Assuming that this oil is homogeneously distributed within organics, the volumetric ratio of the soluble/insoluble organic matter would reach 1.2-1.3. This value is consistent with swelling ratios, varying between 1.1-1.7, measured by Larsen and Li (1992) on type II Albany kerogen using a set of solvents of different polarity. While we do not know if in the peak oil window kerogen physically expanded (Lewan, 1997), our results show that organic matter can accommodate oil and it is therefore not unreasonable to assume that light oil was a driving force for petroleum migration, and porosity loss (Pelet *et al.* 1986). Still, a variety of pores associated with organic matter exists in the peak oil window Posidonia shale. For instance, the appearance of pores accumulated primarily at the interface of organic and inorganic phases might indicate not only volume loss due to exsolution of lighter hydrocarbons (Kanitpanyacharoen *et al.*, 2013), but also provide evidence for the low mobility of the bitumen phase. Although those pores are commonly interpreted as dessication, depressurization or post-coring phase alteration features (Milliken *et al.*, 2013), it is not unreasonable to think that similar pores could be a product of dissolution and limited recrystallization of carbonate phases within viscous and 'plastic' organic polymer susceptible to shrinkage after initial swelling (Simons, 1979). Curtis *et al.* (2013) who analyzed pores in the Avalon Shale suggested that oil window porosity might be related to pressure build up

during petroleum generation and fracture formation. Indeed, fracture-like pores with jagged edges developed in Posidonia Shale, but they are relatively scarce and subordinate to microscale, calcite or bitumen filled fractures. The general scarcity of the organic porosity in the oil window Posidonia shale, despite major loss of the organic carbon, may be also considered in terms of the phase behavior. It is reasonable to expect that in the type II kerogen like Posidonia bitumen phase was undersaturated to gas before the onset of the oil-to gas cracking. Consequently, any gas molecules generated early from kerogen or NSO-rich bitumen were most likely dissolved in the liquid phase and expelled (Pepper and Dodd, 1995; Schenk *et al.*, 1997; Tan *et al.*, 2013; Waples, 2000).

Organic porosity in the gas window

RockEval experiments performed on Posidonia shale show decrease in the content of both total oil and organic carbon between 0.89-1.45%, coinciding with the formation of the microscopically visible, isolated, spongy and complex organic pores, similar to those reported by Milliken *et al.* (2013) from the overmature Marcellus Shale. Such clear relation in HI and porosity appearance suggests that the evolution of the gas window porosity should be interpreted in the light of the thermal cracking of the kerogen and residual hydrocarbons (Behar *et al.*, 2008). Apart from the synchrotron-based study by Bernard *et al.* (2011) and thorough SEM petrographic analysis by Milliken *et al.* (2013), there are no sufficient studies explaining what governs the appearance and distribution of organic porosity in overmature organic-rich shales. Bernard *et al.* (2011) and Bernard *et al.* (2012) linked intraorganic pores encountered both in the Barnett and Posidonia Shale with residual pyrobitumen. Such association is consistent with Loucks *et al.* (2009) who suggested that the appearance of organic pores may be related to exsolution of thermogenic gas molecules. Indeed, pyrolytic experiments performed by Horsfield and Dueppenbecker (1991) on the Posidonia kerogen revealed increased ratio of C_2-C_5/C_{6+} of pyrolysate at high temperatures, ascribed by them to the secondary breakdown of naphthenoaromatic units and gas generation. In our study and at the scale of the BIB/SEM images, only ~25% porosity is contained directly within organics, with ~75% remaining mineral associated. As these pseudo-interparticle and -intraparticle pores were to a large extent occluded by the solvent insoluble bitumen phase in the peak oil window, we presume that their evolution, similarly to the intraorganic pores, is the result of a thermal decomposition of the organic material. A variety of organic pores that evolved between 0.89-1.45% Ro points to the small-scale heterogeneity of the organic material in the

shale matrix at the onset of cracking, and raises questions about the phase of the cracked hydrocarbons. For instance, to explain accumulation of pores in the fossiliferous zones and pyrite framboids one may have to recall primary migration mechanisms already discussed in this chapter, dissolution of oil in initially heavy bitumen and fractionation of bitumen into polar and lighter compounds of different mobility. The prevalence of calcite zones or pyrite framboids as locations of bitumen entrapment and secondary porosity development is reasonable considering a large amount of potential pore space physically protected against compaction, that could be filled with the migrating and in-situ generated bitumen, the lack of driving force to expel petroleum from the rigid framework, and also high retention capability of residual bitumen for the generated oil (Pepper and Dodd, 1995).

Although we cannot be conclusive about the exact role of bitumen heterogeneity on a distribution of organic porosity, many authors point to the importance of hydrogen donor compounds such as asphaltenes or hydroaromatics as preventing cross-linking during cracking reactions (Behar and Pelet, 1988; Michelis, 1996; Schenk *et al.*, 1997) and therefore delaying the conversion and aromatization of the organic polymers (Lewan, 1997). On the other hand, Tiem *et al.* (2008) believed that although the absence of hydrogen donors may enhance cross-linking and reduce oil potential of an organic molecule, it will increase its gas potential at higher temperatures. Therefore, we presume that the heterogeneity of the organic phase in terms of porosity development in Posidonia could mimic different chemophysical properties of the organic molecules at the time of cracking, their association with unexpelled oil and their potential to release different hydrocarbon fractions including wet gas and methane. Pyrolysis experiments on various coals revealed different potential for porosity development depending on the maceral composition, their plastic properties as well as coal rank, with the viscosity and the advance in cross-linking shown to control an extent of the coal devolatilization (Alvarez *et al.*, 1997). Similarly, different pyrobitumen precursors, related to dealkylation of NSO compounds or aromatic condensation reactions were also proposed by Hill *et al.* (1996) and could account for different optical properties of reservoir pyrobitumens as encountered by Stasiuk (1997). In the light of this discussion, the bubble-like nature of some pores may indeed represent the last step in gas exsolution from already polycondensed aromatic molecules (Tiem *et al.*, 2008), which were not able to release the pressure build up during gas generation but were viscous enough to prevent pore closure.

Despite that demethylation of residual kerogen is often reported from pyrolytic experiments (Guo *et al.*, 2009), it is still debatable whether residual kerogen itself can participate in development of organic porosity at gas window maturities. Bernard *et al.*

(2011) did not find any porosity in the overmature kerogen. Similarly, our SEM micrographs show that in the HAD sample approximately 65% of organic particles are not visibly porous. Recent sorption experiments by Rexer *et al.*, (2014) found that non-soluble bulk organic matter extracted from the overmature Posidonia shale is microporous, but they did not separate kerogen from residual bitumen. It is plausible that the presence of internal microporosity will facilitate diffusive release of gaseous moieties from kerogen and does not favour development of pores (Vanderbroucke and Largeau, 2007).

Summary and conclusions

Posidonia Shale from the Hils syncline is an organic-rich rock following a maturation pathway typical for the Type II kerogen source rocks. Due to its relatively small heterogeneity in terms of facies development between rocks of different maturities, it is a natural laboratory which enables to track evolution of organic and inorganic components under increasing thermal stress. The most volumetrically significant diagenetic changes involve carbonates, both calcite and dolomite. Deposited as biogenic nannofossils, calcite behavior, its recrystallization, dissolution and reprecipitation is controlled by the bulk mineralogy, texture, organic richness and thermal maturity of the shale. We found that both high clay content as well as petroleum generation and retention slow down chemical compaction and irreversible porosity reduction as observed e.g. in chalks. Such behaviour leads to high minus-bitumen porosities as encountered in the peak oil window Posidonia.

Our observations show that small-scale clay-calcite lamination of the Posidonia Shale underlies heterogeneity of the residual organic matter in shales of higher maturities as a result of differential generation and expulsion. The original association of the amorphous organic matter as a major source of petroleum with clays drastically changes with the onset of bitumen migration and filling of microreservoirs within rigid fossiliferous domains. Such petroleum entrapment also occurs in the vicinity of any other rigid grains, where porosity evolved due to the thermal conversion of kerogen is protected in compaction shadows. Petroleum migration may enhance its fractionation, increasing heterogeneity of the residual organic matter in terms of its chemophysical properties and potential for secondary cracking.

Both diagenetic reactions within the mineral matrix and thermal decomposition of the organic material have a major impact on porosity change with maturation and its redistribution between different shale domains. At low maturities, clays and organic matter are not visibly porous, but most likely hold most of the shale porosity. In the oil window,

cement precipitation, bitumen occlusion, and possibly swelling due to retention of the residual oil, lead to reduced total porosities. High bitumen retention capacity of the rigid fossiliferous domains gains in significance in the gas window, and affects the evolution and distribution of the secondary pores. The evolved organic porosity is highly heterogenous and is likely controlled by the chemophysical properties of the residual organic matter at the time of thermal cracking. Specifically, the distribution of the nanometer size 'bubble' pores, analogously to pores found in cokes, suggests that the movement of the gas molecules was constraint by the viscosity of the organic polymer. The evolution and distribution of organic pores is important from the gas storage and production point of view. For instance, the lack of visible connectivity between pore bodies adjacent to and within organic paricles imply that pores may be gas filled in the subsurface. Moreover, high bitumen retention capacity of the rigid fossiliferous zones, followed by the secondary pore evolution, suggests that those are excellent microreservoirs of free gas.

References

ALEXANDER, T. 2011. Shale gas revolution. *Oilfield review*, **23**, 40-55.

ALVAREZ, D., BORREGO, A.G., MENENDEZ, R. 1997. Unbiased methods for the morphological description of char structures. *Fuel*, **76**, 1241-1248.

APLIN, A.C., LARTER, S.R. 2005. Fluid Flow, Pore Pressure, Wettability, and Leakage in Mudstone Cap Rocks. AAPG Special Bulletin**:** *AAPG Hedberg Series*, **2**, 1-12.

APLIN, A.C., MACQUAKER. H.S. 2011. Mudstone diversity: Origin and implications for source, seal, and reservoir properties in petroleum systems. *Association of Petroleum Geologists Bulletin*, **95**, 2031–2059.

APLIN, A.C., YANG, Y. 2005. Assessment of ß the compression coefficient of mudstones and its relationship with detailed lithology. *Marine and Petroleum Geology*, **12**, 955-963.

BACHMANN, G.H., VOIGT, T., BAYER, U., VON EYNATTEN, H., LEGLER, B., LITTKE, R. (2008): Depositional history and sedimentary cycles in the Central European Basin System. In: Littke,R., Bayer, U., Gajewski, D., Nelskamp, S. (Eds), Dynamics of

Complex Intracontinental Basins - The Central European Basin System, Springer-Verlag, Berlin-Heidelberg, pp. 155-169.

BAKER, P.A., KASTNER, M., BYERLEE, J.D., LOCKNER, D.A., 1980. Pressure solution and hydrothermal recrystallization of carbonate sediments—an experimental study. *Marine Geology*, **38**, 185–203.

BEHAR, F., PELET, R. 1985. Pyrolysis-gas chromatography applied to organic geochemistry. Structural similarities between kerogens and asphaltenes from related rock extracts and oils. *Journal of Analytical and AppIied Pyrolysis*, **8**, 173-187.

BEHAR, F., VANDENBROUCKE, M. 1987. Chemical modelling of kerogens. *Organic Geochemistry*, **11**, 15-24.

BEHAR, F., PELET, R. 1988. Hydrogen-Transfer Reactions in the Thermal Cracking of Asphaltenes. *Energy & Fuels*, **2**, 259-264.

BEHAR, F., KRESSMANN, S., RUDKIEWICZ, J.L., VANDENBROUCKE, M. 1992. Experimental simulation in a confined system and kinetic modelling of kerogen and oil cracking. *Organic Geochemistry*, **19**, 173-189.

BEHAR, F., VANDENBROUCKE, M. TEERMANN, S.C., HATCHER, P.G., LEBLOND, C., LERAT, O. 1995. Experimental simulation of gas generation from coals and a marine kerogen. *Chemical Geology*, **126**, 247-260.

BEHAR, F., VANDENBROUCKE, M., TANG, Y., MARQUIS, F., ESPITALIE, J. 1997. Thermal cracking of kerogen in open and closed systems: determination of kinetic parameters and stoichiometric coefficients for oil and gas generation. Organic Geochemistry, 26, 321-339.

BEHAR, F., LORANT, F., LEWAN, M. 2008a. Role of NSO compounds during primary cracking of a Type II kerogen and a Type III lignite. *Organic Geochemistry*, **39**, 1–22.

BEHAR, F., LORANT, F., MAZEAS, L. 2008b. Elaboration of a new compositional kinetic schema for oil cracking. *Organic Geochemistry*, **39**, 764–782.

BEHAR, F., ROY, S., JARVIE, D. 2010. Artificial maturation of a Type I kerogen in closed system: Mass balance and kinetic modelling. *Organic Geochemistry*, **41**, 1235–1247.

BERNARD, S., HORSFIELD, B., SCHULTZ, H.M., SCHREIBER, A., WIRTH, R., TIEM, T.A.V., PERSSEN, F., KÖNITZER, S, VOLK, H., SHERWOOD, N., FUENTES, D. 2010. Multi-scale detection of organic and inorganic signatures provides insights into gas shale properties and evolution. *Chemie der Erde*, **70**, 119-133.

BERNARD, S., HORSFIELD, B., SCHULTZ, H.M., WIRTH, R., SCHREIBER, A., SHERWOOD, N. 2011. Geochemical evolution of organic-rich shales with increasing maturity: A STXM and TEM study of the Posidonia Shale (Lower Toarcian, northern Germany). Marine and Petroleum Geology, 31, 70-89.

BERNARD, S., WIRTH, R., SCHREIBER, A., SCHULZ, H.-M., HORSFIELD, B. 2012. Formation of nanoporous pyrobitumen residues during maturation of the Barnett Shale (Fort Worth Basin). *International Journal of Coal Geology*, **103**, 3–11.

BERNARD, S., WIRTH, R., SCHREIBER, A., BOWEN, L., APLIN, A.C., MATHIA, E.J., SCHULZ, H.-M., HORSFIELD, B. 2013. FIB-SEM and TEM investigations of an organic-rich shale maturation series from the lower Toarcian Posidonia Shale, Germany: Nanoscale pore system and fluid-rock interactions. In: Camp, W., Diaz, E., Wawak, B. (Eds.), Electron microscopy of shale hydrocarbon reservoirs, *AAPG memoir*, **102**, 53-66.

BERNER, R. A. 1968. Calcium carbonate concretions formed by the decomposition of organic matter: *Science*, **159**, 195 - 197.

BJØRLYKKE, K. 1999. Principal aspects of compaction and fluid flow in mudstones. *Geological Society Special Publications*, **158**, 73-78.

BLOCH, J., HUTCHEON, I.E. 1992. Shale diagenesis: a case study from the Albian Harmon Member (Peace River Formation), Western Canada. *Clays and Clay Minerals*, **40**, 682-699.

BOUR, I. MATTIOLI, E., PITTET, B. 2007. Nannofacies analysis as a tool to reconstruct paleoenvironmental changes during the Early Toarcian anoxic event. *Palaeogeography, Palaeoclimatology, Palaeoecology*, **249**, 58–79.

BRUNS, B., LITTKE, R., GASPARIK, M., van WEES, J.-D., NELSKAMP, S. 2014. Thermal evolution and shale gas potential estimation of the Wealden and Posidonia Shale in NW-Germany and the Netherlands: a 3D basin modeling study. *Basin Research*, doi: 10.1111/bre.12096.

CLEMENTZ, D.M. 1978. Effect of oil and bitumen saturation on source-rock pyrolysis. *American Association of Petroleum Geologists Bulletin*, **63**, 2227-2232.

CURIALE, J.A., 1983, Petroleum occurrences and source-rock potential of the Ouachita Mountains, southeastern Oklahoma: Oklahoma Geological Survey, Bulletin 135, 65 p.

CURIALE, J.A. 1986. Origin of solid bitumens, with emphasis on biological marker results. *Organic Geochemistry*, **10**, 559-580.

CURTIS, C.D. 1995. Post-depositional evolution of mudstones l: early days and parental influences. *Journal of the Geological Society*, **152**, 577-586.

CURTIS, M.E., SONDERGELD, C.H., RAI, C.S. 2013. Relationship between organic shale microstructure and hydrocarbon generation. SPE Unconventional Resources Conference-USA, 10-12 April 2013, The Woodlands, Texas, USA.

DIECKMANN, V., SCHENK, H.J., HORSFIELD, B., WELTE, D.H. 1988. Kinetics of petroleum generation and cracking by programmed-temperature closed-systempyrolysis of Toarcian Shales. *Fuel*, **77**, 23-31.

DIX, G.R., MULLINS, H.T. 1987. Shallow, subsurface growth and burial alteration of Middle Devonian calcite concretions. *Journal of Sedimentary Petrology*, **57**, 140–152.

DRÆGE, A., JAKOBSEN, M., JOHANSEN, T.A. 2006. Rock physics modelling of shale diagenesis. *Petroleum Geoscience*, **12**, 49-57.

EMMANUEL, S. DAY-STIRRAT, R. J. 2012. A framework for quantifying size dependent deformation of nano-scale pores in mudrocks. *Journal of Applied Geophysics*, **86**, 29–35.

ESPITALIE, J., LAPORTE, J.L., MADEC, M., MARQUIS, F., LEPLAT, P., PAULET J., BOUTEFEU, A. 1977. Methode rapide de characterisation des roches meres, de leur potential petrolier et de leur degree d'evolution, *Rev. Inst. Franc. Pétrole.*, **32**, 23-42

FABRICIUS, I.L. 2003. How burial diagenesis of chalk sediments controls sonic velocity and porosity. *American Association of Petroleum Geologists Bulletin*, **87**, 1755 – 1778.

FABRICIUS, I.L., GOMMESEN, L., KROGSBØLL, A., OLSEN, D. 2008. Chalk porosity and sonic velocity versus burial depth: Influence of fluid pressure, hydrocarbons, and mineralogy. *American Association of Petroleum Geologists Bulletin*, **92**, 201-223.

GUO, L., XIANMING, X, HUI, T., ZHIGUANG, S. 2009. Distinguishing gases derived from oil cracking and kerogen maturation: Insights from laboratory pyrolysis experiments. *Organic Geochemistry*, **40**, 1074–1084.

HEASLEY, E.C., WORDEN, R.H., HENDRY, J.P. 2000. Cement distribution in a carbonate reservoir: Recognition of a paleo-oil–water contact and its relationship to reservoir quality in the Humbly Grove field, onshore, United Kingdom. *Marine and Petroleum Geology*, **17**, 639–654.

HESSE, R. 1990. Origin if chert: diagenesis of biogenic siliceous sediments. In: McIlreath, I.A., Morrow, D.W. (Eds.), Diagenesis. Geosci. Can. Reprin Ser., **4**, 227-251.

HICKS, K.S., COMPTON, J.S., McCRACKEN, S., VECSEI, A. 1996. Origin of diagenetic carbonate minerals recovered from the New Jersey continental slope. In: Mountain, G.S.,Miller, K.G.,Blum, P., Poag, C.W., Twichell, D.C. (Eds.), *Proceedings of the Ocean Drilling Program, Scientific Results*, vol. **15**.

HILL, R.J., TANG, Y., KAPLAN, I.R., JENDEN, P.D. 1996. The Influence of Pressure on the Thermal Cracking of Oil. *Energy & Fuels*, **10**, 873-882.

HILL, R.J., TANG, Y., KAPLAN, I.R. 2003. Insights into oil cracking based on laboratory experiments. *Organic Geochemistry*, **34**, 1651–1672.

HORSFIELD, B., DUEPPENBECKER, S.J. 1991. The decomposition of Posidonia Shale and Green River Shale kerogens using microscale sealed vessel (MSSV) pyrolysis. *Journal of Analytical and Applied Pyrolysis*, **20**, 107-123.

HORSFIELD, B., SCHENK, H.J., MILLS, N., WELTE, D.H. 1992. An investigation of the in-reservoir conversion of oil to gas: compositional and kinetic findings from closed-system programmed-temperature pyrolysis. *Organic Geochemistry*, **19**, 191-204.

HORSFIELD, B., LITTKE, R., MANN, U., BERNARD, S., TIEM, A.T.V., Di PRIMIO, R., SCHULZ, H.-M. 2010. Shale Gas in the Posidonia Shale, Hils Area, Germany. American

Association of Petroleum Geologists Annual Convention, April 11-14, 2010, New Orleans, LA, USA.

HOWER, J., ESLINGER, E.V., HOWER, M.E., PERRY, E.A. 1976. Mechanism of burial metamorphism of argillaceous ssediment: 1. Mineralogical and chemical evidence. *American Association of Petroleum Geologists Bulletin*, **87**, 725–737.

HWANG, R.J., TEERMAN, S.C., CARLSON, R.M. 1998. Geochemical comparison of reservoir solid bitumens with diverse origins. *Organic Geochemistry*, **29**, 505-517.

HUTTON, A.C. 1994. Organic petrography and oil shales. *Energetica*, **5**, 1-6.

INOUE, A., VELDE, B., MEUNIER, A., TOUCHARD, G. 1988. Mechanism of illite formation during smectite-to-illite conversion in a hydrothermal system. *American Mineralogist*, **73**, 1325-1334.

JARVIE, D.M., HILL, R.J., RUBLE, T.E., POLLASTRO, R.M., 2007. Unconventional shale-gas systems: the Mississippian Barnett Shale of north-central Texas as one model for thermogenic shale gas assessment. *American Association of Petroleum Geologists Bulletin*, **91**, 475–499.

JARVIE, D.M, JARVIE, B.M., MAEDE, A. 2012. Components and processes affecting producibility and commerciality of shale oil resource systems. Shale Oil Symposium, 16-17 April 2012, Wuxi, China.

KANITPANYACHAROEN, W., KETS, F.B., WENK, H.-R., WIRTH, R. 2012. Mineral preferred orientation and microstructure in the Posidonia Shale in relation to different degrees of thermal maturity. *Clays and Clay Minerals*, **60**, 315-329.

KANITPANYACHAROEN, W., VANORIO, T., LIU, Y., XIAO, X., BENMORE, C. 2013. Evolution of mineral fabrics and microstructures in Kimmeridge Shale upon kerogen maturation. Second international Workshop on Rock Physics, 4-9 August 2013, Southampton.

KHAVARI-KHORASANI, G. 1987. Novel development in fluorescence microscopy of complex organic mixtures: Application in petroleum geochemistry. *Organic Geochemistry*, **11**, 157-168.

KHAVARI-KHORASANI, G., MICHELSEN, J.K. 1992. Primary alteration-oxidation of marine algal organic matter from oil source rocks of the North Sea and Norwegian Arctic: new findings. Organic Geochemistry, **19**, 327-343.

LANDIS, C.R., CASTAÑO, J.R. 1995. Maturation and bulk chemical properties of a suite of solid hydrocarbons. *Organic Geochemistry*, **22**, 137-149.

LARSEN, J.W., LI, S. 1994. Solvent swelling studies of Green River kerogen. Energy & Fuels, **8**, 932-936.

LEYTHAEUSER, D., LITTKE, R., RADKE, M., SCHAEFER, R.G. 1988. Geochemical effects of petroleum migration and expulsion from Toarcian source rocks in the Hils syncline area, NW-Germany. *Organic Geochemistry*, **13**, 489-502.

LEWAN, M.D., 1997. Experiments on the role of water in petroleum formation. *Geochimica et Cosmochirnica Acta*, **61**, 3691-3723.

LEYTHAEUSER, D., LITTKE, R., RADKE, M., SCHAEFER, R.G. 1988. Geochemical effects of petroleum migration and expulsion from Toarcian source rocks in the Hils syncline area, NW-Germany. *Organic Geochemistry*, **13**, 489-502.

LITTKE, R., BAKER, D.R., LEYTHAEUSER, D., RULLKÖTTER, J. 1991. Keys to the depositional history of the Posidonia Shale (Toarcian) in the Hils Syncline, northern Germany. In: Tyson, R.V., Pearson, T.H. (Eds.) Modern and ancient continental shelf anoxia. *Geological Society Special Publication*, **58**, 311-333.

LITKE, R., BAKER, D.R., RULLKÖTTER, J. 1987 Deposition of petroleum source rocks. In: Welte, D.H., Horsfield, B., Baker, D.R. (Eds.). Petroleum and Basin Evolution. Springer, Heidelberg, pp. 271-333.

LOMANDO, A.J. 1992. The influence of solid reservoir bitumen on reservoir quality. *American Association of Petroleum Geologists Bulletin*, **76**, 1137–1152.

LORANT, F., BEHAR, F. 2002. Late generation of methane from mature kerogens. *Energy & Fuels*, **16**, 412-427.

LOUCKS, R.G., REED, R.M., RUPPEL, S.C., JARVIE, D.M. 2009. Morphology, genesis and distribution of nanometer-scale pores in siliceous mudstones of the Mississippian Barnett Shale. *Journal of Sedimentary Research*, **79**, 848–861.

MACKENZIE, A.S., LEYTHAEUSER, D., ALTEBÄUMER, F.-J., DISKO, U., RULLKÖTTER, J. 1988. Molecular measurements of maturity for Lias 6 shales in N.W. Germany. *Geochimica et Cosmochimica Acta*, **52**, 1145-1154.

MACQUAKER. J.H.S. 1994. A lithofacies study of the Peterborough Member, Oxford Clay Formation (Jurassic), UK: an example of sediment bypass in a mudstone succession: *Journal of the Geological Society of London*, **151**, 161-172.

MACQUAKER, J.H.S., GAWTHORPE, R.L., TAYLOR, K.G., OATES, M.J. 1998. Hetrogeneity, stacking patterns and sequence stratigraphy in distal mudstone successions; examples from the Kimmeridge Clay Formation, UK. In: Schieber, J., Zimmerle, W., Sethi, P.S., eds., Shales and Mudstones, vol. 1, Stuttgart, Schweizerbart'sche Verlagsbuchhandlung, p. 163-186.

MACQUAKER, J.H.S., TAYLOR, K.G., GAWTHORPE, R.L. 2007. High-resolution facies analyses of mudstones: implications for paleoenvironmental and sequence stratigraphic interpretations of offshore ancient mud-dominated successions. *Journal of Sedimentary Research*, **77**, 324–339.

MACQUAKER, J.H.S., TAYLOR, K.G., KELLER, M., POLYA, D. 2014. Compositional controls on early diagenetic pathways in fine-grained sedimentary rocks: Implications for predicting unconventional reservoir attributes of mudstones. *American Association of Petroleum Geologists Bulletin*, **98**, 587–603.

MALLON, A.J., SWARBRICK, R.E. 2002. A compaction trend for non-reservoir North Sea Chalk. *Marine and Petroleum Geology*, **19**, 527-539.

MANN, U., MÜLLER, P.J. 1988. Source rock evaluation by well log analysis (Lower Toarcian, Hils syncllne). *Organic Geochemistry*, **13**, 109-119.

MANN, A.L., PATIENCE, R.L., POPLETT, I.J.F. 1991. Determination of molecular structure of kerogens using ^{13}C NMR spectroscopy: I. The effects of variation in kerogen type. *Geochimica et Cosmochimica Acta*, **55**, 2259-2268.

MAO, J., FANG, X., LAN, Y., SCHIMMELMANN, A., MASTALERZ, M., XU, L., SCHMIDT-ROHR, K. 2010. Chemical and nanometer-scale structure of kerogen and its change during thermal maturation investigated by advanced solid-state ^{13}C NMR spectroscopy. *Geochimica et Cosmochimica Acta*, **74**, 2110–2127.

MARSHAK, S., ENGELDER, T. 1985. Development and distribution of tectonic cleavage and stylolites in limestones of a fold-thrust belt in eastern New York State, *Journal of Structural Geology*, **7**, 345-359.

MASTALERZ, M., GLIKSON, M. 2000. In-situ analysis of solid bitumen in coal: examples from the Bowen Basin and the Illinois Basin. *International Journal of Coal Geology*, **42**, 207–220.

McHARGUE, T.R., PRICE, R.C. 2006. Dolomite from clay in argillaceous or shale-associated marine carbonates. *Journal of Sedimentary Research*, **52**, 873-886.

MICHELIS, R., LANGLOIS, E., RUAU, O., MANSUY, L., ELIE, M., LANDAIS, P. 1996. Evolution of asphaltenes during artificial maturation: A record of the chemical processes. *Energy & Fuels*, **10**, 39-48.

MILLIKEN, K.L., RUDNICKI, M., AWWILER, D.N., ZHANG, T. 2013. Organic matter–hosted pore system, Marcellus Formation (Devonian), Pennsylvania. *American Association of Petroleum Geologists Bulletin*, **97**, 177-200.

MUÑOZ, Y.A., LITTTKE, R., BRIX, M.R. 2007. Fluid systems and basin evolution of the western Lower Saxony Basin, Germany. *Geofluids*, **7**, 335–355.

NEUZIL, C.E. 1994. How permeable are clays and shales? *Water Resources Research*, **30**, 145-150.

OBERLIN, A., VILLEY, M. 1980. Influence of elemental composition on carbonization. Pyrolysis of kerosene shale and kuckersite. *Carbon*, **18**, 347-353.

PEDERSEN, T.F., CALVERT, S.E. 1990. Anoxia vs. Productivity: What controls the formation of organic-carbon-rich sediments and sedimentary rocks? *American Association of Petroleum Geologists Bulletin*, **74**, 454–466.

PELET, R., BEHAR, F., MONIN, J.C. 1986. Resins and asphaltenes in the generation and migration of petroleum. *Organic Geochemistry*, **10**, 481-498.

PELTONEN, C., MARCUSSEN, Ø., BJØRLYKKE, K., JAHREN, J. 2009. Clay mineral diagenesis and quartz cementation in mudstones: The effects of smectite to illite reaction on rock properties. *Marine and Petroleum Geology*, **26**, 887–898.

PEPPER, A.S., DODD, T.A. 1995. Simple kinetic models of petroleum formation. Part II: oil-gas cracking. *Marine and Petroleum Geology*, **12**, *321-340*.

PUTSCHEW, A., SCHAEFFER-REISS, C., SCHAEFFER, P., KOOPMANS, M.P., DE LEEUW, J.W., LEWAN, M.D., DAMSTE, J.S.S., MAXWELL, J.R. 1998. Release of sulfur- and oxygen-bound components from a sulfur-rich kerogen during simulated maturation by hydrous pyrolysis. *Organic Geochemistry*, **29**, 1875-1890.

RADKE, M., VRIEND, S.P., SCHAEFER, R.G. 2001. Geochemical characterization of Lower Toarcian source rocks from NW Germany: interpretation of aromatic and saturated hydrocarbons in relation to depositional environment and maturation effects. *Journal of Petroleum Geology*, **24**, 287-307.

RAISWELL, R., FISHER, Q. J. 2000. Mudrock-hosted carbonate concretions: a review of growth mechanisms and their influence on chemical and isotopic composition: *Journal of the Geological Society*, **157**, 239 - 251.

REXER, F., MATHIA, E.J., APLIN, A.C., THOMAS, K.M. 2014. High-Pressure Methane Adsorption and Characterization of Pores in Posidonia Shales and Isolated Kerogens. *Energy & Fuels*, **28**, 2886-2901.

RODUIT. 2008. JMicroVision: Image analysis toolbox for measuring and quantifying components of high-definition images. Version 1.2.7. Software available for free download at http://www.jmicrovision.com/ accessed August, 2011.

RÖHL, H.J., SCHMID- RÖHL, A. 2005. Lower Toarcian (Upper Liassic) black shales of the Central European epicontinental basin: a sequence stratigraphic case study from the SW German Posidonia Shale. In: HARRIS, N. B. (Ed.), The deposition of organic carbon-rich sediments: Models, mechanisms, and consequences: Society for Sedimentary Geology Special Publication, **82**, 165-189.

RÖHL, H.J., SCHMID- RÖHL, A., OSCHMANN, W., FRIMMEL, A., SCHWARK, L. 2001. The Posidonia Shale (Lower Toarcian) of SW-Germany: an oxygen-depleted ecosystem controlled by sea level and palaeoclimate. *Palaeogeography, Palaeoclimatology, Palaeoecology*, **165**, 27–52.

RULLKÖTTER, J., LEYTHAEUSER, D., HORSFIELD, B., LITTKE, R., MANN, U., MÜLLER, P.J., RADKE, M., SCHAEFER, H.-J., SCHWOCHAU, K., WITTE, E.G.,

WELTE, D.H. 1988. Organic matter maturation under the influence of a deep intrusive heat source: A natural experiment for quantitation of hydrocarbon generation and expulsion from a petroleum source rock (Toarcian shale, northern Germany). *Organic Geochemistry*, **13**, 847-856.

RULLKÖTTER, J., MICHAELIS, W. 1990. The structure of kerogen and related materials. A review of recent progress and future trends. *Organic Geochemistry*, **16**, 829-852.

SANDVIK, E.I., YOUNG, W.A., CURRY, D.J. 1992. Expulsion from hydrocarbon sources: the role of organic absorption. *Organic Geochemistry*, **19**, 77-87.

SCHAEFER, R.G., LITTKE, R. 1988. Maturity-related compositional changes in the low-molecular-weight hydrocarbon fraction of Toarcian shales. *Organic Geochemistry*, **13**, 887-892.

SCHENK, H.J., DI PRIMIO, R., HORSFIELD, B. 1997. The conversion of oil into gas in petroleum reservoirs. Part 1: Comparative kinetic investigation of gas generation from crude oils of lacustrine, marine and fluviodeltaic origin by programmed-temperature closed-system pyrolysis. *Organic Geochemistry*, **26**, 467-481.

SCHIEBER, J. 1999. Distribution and deposition of mudstone facies in the Upper Devonian Sonyea Group of New York. *Journal of Sedimentary Research*, **69**, 909-925.

SCHOLLE, P. A. 1977. Chalk diagenesis and its relation to petroleum exploration: oil from chalks, a modern miracle? *American Association of Petroleum Geologists Bulletin*, **61**, 982-1009.

SCHOLLE, P. A., HALLEY, R. B. 1985. Burial diagenesis: out of sight, out of mind! In*:* Schneidermann, N., Harris, P.M. (Eds.), Carbonate Cements: Tulsa, OK, *SEPM Special Publication*, **36**, 309-334.

SCHOWALTER, T.T. 1979. Mechanics of secondary hydrocarbon migration and entrapment. *American Association of Petroleum Geologists Bulletin*, **63**, 723–760.

SCHULZ, H.M., BERNARD, S. HORSFIELD, B.KRÜGER, M, LITTKE, R., Di PRIMIO, R. 2013. Shale gas characteristics of the Lower Toarcian Posidonia Shale in Germany: from basin to nanometre scale. EGU General Assembly, 7-12 April, 2013, Vienna, Austria

SIMONS, G.A. 1979. Char gasification: Part I. Transport model. *Combustion Science and Technology*, **20**, 107-116.

STASIUK, L.D., 1997. The origin of pyrobitumens in Upper Devonian Leduc Formation gas reservoirs, Alberta, Canada: an optical and EDS study of oil to gas transformation. *Marine and Petroleum Geology*, **14**, 915-929.

ŚRODON, J. 1999. Nature of mixed-layer clays and mechanisms of their formation and alternation. *Annual Review of Earth Planetary Science*, **27**, 19-53.

TAN, J., HORSFIELD, B., MAHLSTEDT, N., ZHANG, J., DI PRIMIO, R., TIEM, T.A., BOREHAM, C.J., Van GRAAS, G., TOCHER, B.A. 2013. Physical properties of petroleum formed during maturation of Lower Cambrian shale in the upper Yangtze Platform, South China, as inferred from PhaseKinetics modelling. *Marine and Petroleum Geology*, **48**, 47-56.

TAO, S., WANG, Y., TANG, D., WU, D., XU, H., HE, W. 2012. Organic petrology of Fukang Permian Lucaogou Formation oil shales at the northern foot of Bogda Mountain, Junggar Basin, China. *International Journal of Coal Geology*, **99**, 27–34.

TIEM, V.T., HORSFIELD, B., SYKES, R. 2008. Influence of in-situ bitumen on the generation of gas and oil in New Zealand coals. *Organic Geochemistry*, **39**, 1606–1619.

TISSOT, B.P., WELTE, D.H. 1984. Petroleum formation and occurrence. Springer-Verlag, New York, pp. 699.

TRABUCHO-ALEXANDRE, J., DIRKX, R., VELD, H., KLAVER, G., De BOER, P.L. 2012. Toarcian black shales in the Dutch Central Graben: record of energetic, variable depositional conditions during an Oceanic Anoxic Event. *Journal of Sedimentary Research*, **82**, 104–120.

VANDENBROUCKE, M.., BEHAR, F., SAN TORCUATO, A., RULLKÖTER, J. 1993. Kerogen maturation in a reference kerogen Type II series: the Toarcian shales of the Hils syncline, NW Germany. *Organic Geochemistry*, **20**, 961-972.

VANDENBROUCKE, M.., LARGEAU, C. 2007. Kerogen origin, evolution and structure. *Organic Geochemistry*, **38**, 719–833.

VAN DUIN, A.C.T., LARTER, S.R. 2001. A computational chemical study of penetration and displacement of water films near mineral surfaces, Geochemical Transactions 6.

WAPLES, D.W. 2000. The kinetics of in-reservoir oil destruction and gas formation: constraints from experimental and empirical data, and from thermodynamics. *Organic Geochemistry*, **31**, 553-575.

WATTS, N.L. 1987. Theoretical aspects of cap-rock and fault seals for single- and two-phase hydrocarbon columns. *Marine and Petroleum Geology*, **4**, 274-307.

WILHELMS, A., LARTER, S.R., LEYTHAEUSER, D., DYPVIK, H. 1990. Recognition and quantification of the effects of primary migration in a Jurassic clastic source-rock from the Norwegian. *Organic Geochemistry*, **16**, 103-113.

WILLIAMS, L.A., CRERAR, D.A. 1985. Silica diagenesis, II. General mechanisms. *Journal of* Sedimentary Petrology, **55**, 312-321.

WORDEN, R.H., OXTOBY, N.H., SMALLEY, P.C. 1998. Can oil emplacement prevent quartz cementation in sandstones? *Petroleum Geoscience*, **4**, 129–137.

Chapter 3: Porosity of the Posidonia Shale: from a low scale variation to the formation characterization

Introduction

Mudstones are defined as a fine-grained rock with over a half of its components in the clay size fraction (MacQuaker and Adams, 2003). Because of the presence of clay minerals and high initial water saturation, mudstones are sensitive to compaction, progressively expelling water and thus reducing their volume. Over a several kilometer depth, porosities of mudstone sequences can decrease from 90 to 10 % or less, depending on the initial rate of mud deposition, and its initial composition (Loucks *et al.*, 2012). This porosity can be modified via diagenetic processes as early as in a first few centimeters and proceed with further consolidation of a mudstone (Bjørlykke and Høeg, 1997; Chaika and Dvorkin, 2000; Curtis, 1995; Macquaker *et al.*, 2014).

In opposition to organic-lean mudstones, porosities of the organic-rich shales are significantly modified via processes linked to maturation of in-situ organic matter. Recent boom in shale gas and shale oil exploration (Alexander *et al.*, 2011), in order to correctly evaluate potential storage capacity and final recovery of oil and gas, emphasized the necessity to better constrain factors controlling porosities of shales. A major step for understanding the change of shale properties and porosities under increasing thermal stress was made by recognition that thermal decomposition of kerogen should progressively lead to development of organic porosity (Jarvie *et al.*, 2007). So far authors did not find any organic pores in the oil window shales, but widely reported occurrence of secondary pores in the gas window (Loucks *et al.*, 2009). Although several great attempts were made to link organic pores with maturation and the organic matter content, they very often gave inconclusive and contradictory results (e.g. Bernard *et al.*, 2011; Fishman *et al.*, 2012; Loucks *et al.*, 2009; Mastalerz *et al.*, 2013; Milliken *et al.*, 2013; Modica and Lapierre, 2012; Passey *et al.*, 2010).

Pore sizes of consolidated mudstones span from a micropore < 2 nm, through mesopore (2-50 nm) to macropore (> 50 nm) range (Nelson *et al.*, 2009, Chalmers and Bustin, 2012) and therefore their detection will much depend on a specific method implemented. In the past research, while some authors concentrated on estimation of microporosity and gas potential using gas sorption and mercury methods (Bustin *et al.*, 2008; Chalmers *et al.*, 2012; Chalmers and Bustin, 2007; Kuila and Prasad, 2013; Ross and Bustin, 2009), others implemented mainly microscopic techniques to resolve porosities held by various shale domains (Curtis *et*

al., 2011; Curtis *et al.*, 2013; Fishman *et al.*, 2012; Loucks *et al.*, 2009; Loucks *et al.*, 2012; Milliken *et al.*, 2013; Milner *et al.*, 2010; Schieber, 2011; Slatt and O'Brien, 2011). This research experience led to a conclusion that in order to better understand the complexity of pore systems in these extremely heterogeneous and fine-grained rocks, a combination of different techniques is essential (Bustin *et al.*, 2008; Chalmers and Bustin, 2012; Chalmers *et al.*, 2012; Clarkson *et al.*, 2013; Strapoc *et al.*, 2010). It was also recognized that because of the low-scale variations in shales composition, structure and texture, the bulk techniques (gas sorption, mercury injection) yielding bulk values, will always provide different information than when high resolution microscopic methods are implemented. The last, although not representative for the shale reservoir as a whole, are essential for constraining a geological background for porosity occurrence and its spatial variation. The main advantage of the microscopic techniques is the possibility to quantify porosities and pore size distributions within single laminae defined by the specific lithology, organic matter content and texture.

In this study, we provided an example of the Posidonia shale (Northern Germany), a calcareous rock formation with maturities between 0.53% - 1.45% Ro and only little variance in mineralogical composition between wells of different maturity (Figure 3.1a, b). Our main aim was to investigate the change of porosity and pore size distribution as the maturity of the shale changed from the early oil window to the gas window conditions and detect any links between the porosity change and kerogen transformation, hydrocarbon generation and cracking. With two lithologies, middle and upper calcareous shale and bottom marlstone, we also addressed the issue of a lithological variation, compaction and diagenesis for pore development and connectivity. By integrating geochemical and petrophysical measurements, with a detailed analysis of microscopic images we offered a unique approach for measuring porosity and pore characteristics on different scales with thorough understanding for a micrometer lithological variation.

Samples and Methodologies

26 core samples were selected from stratigraphically equivalent sections of the three boreholes: Wickensen (early oil window, Ro 0.53%), Harderode (peak oil window, Ro 0.89%) and Haddessen (gas window, 1.45% R_o) (Figure 3.1). The samples were chosen for bulk analyses including Rock Eval, TOC, grain density and mercury porosimetry.

Total Organic Carbon was measured with the LECO carbon analyzer equipped with a HF-100 Induction Furnace on carbonate-free shale. Standard Rock-Eval was performed according to Espitalié *et al.* (1977) using Delsi Rock Eval OSA on a 100 mg aliquot. To correct for an oil-in-kerogen peak, 4 selected shale samples were solvent extracted with a mixture of dichloromethane (93%) and methanol (7%) and subsequently analysed for its remaining hydrocarbon potential.

The X-ray diffraction was performed by Macaulay Scientific Consulting Ltd. Quantitative analysis was done by a normalised full pattern reference intensity ratio (RIR) method.

Grain density was measured on samples dried at 105°C using the "Small Pyknometer Method" yielding density values within an error ± 0.02 g/cm^3. Mercury injection data was collected on Micrometrics Autopore II via Mercury Injection Capillary Pressure analysis (MICP) on samples previously freeze-dried at -50°C and evacuated to 10^{-4} psia. Total shale porosity was determined from grain density and bulk density when immersed in mercury at the pressure 25 psia. Pore sizes were calculated as a function of applied pressure according to the Washburn equation (Washburn, 1921) with the input parameters as followes: an advancing contact angle of 141°, a receding contact angle 140° and surface tension 485dyn/cm. The maximum pressure (41000 psi) applied allowed to detect pores as small as 5.6 nm. A full intrusion – extrusion cycle was run for selected samples with the final pressure decline to 25 psia.

Low pressure sorption experiments were performed on Intelligent Gravimetric Analyzers (IGA), supplied by Hiden Isochema Ltd., Warrington, UK, on shales (~ 140 mg) dried to a constant weight at 110°C for 4 hours under vacuum (< 10^{-6}). CO_2 was injected stepwise up to a pressure of 1 bar at a constant temperature 195K (dry ice/acetone bath) in order to obtain subcritical conditions for CO_2. All isotherms were run twice to ensure experimental repeatability. Sorption pore volumes (SPV) were calculated from the maximum uptake at 1 mbar, assuming CO_2 density 1.177 g/cm^3. Corresponding sorption porosities were determined using pycnometer shale grain density.

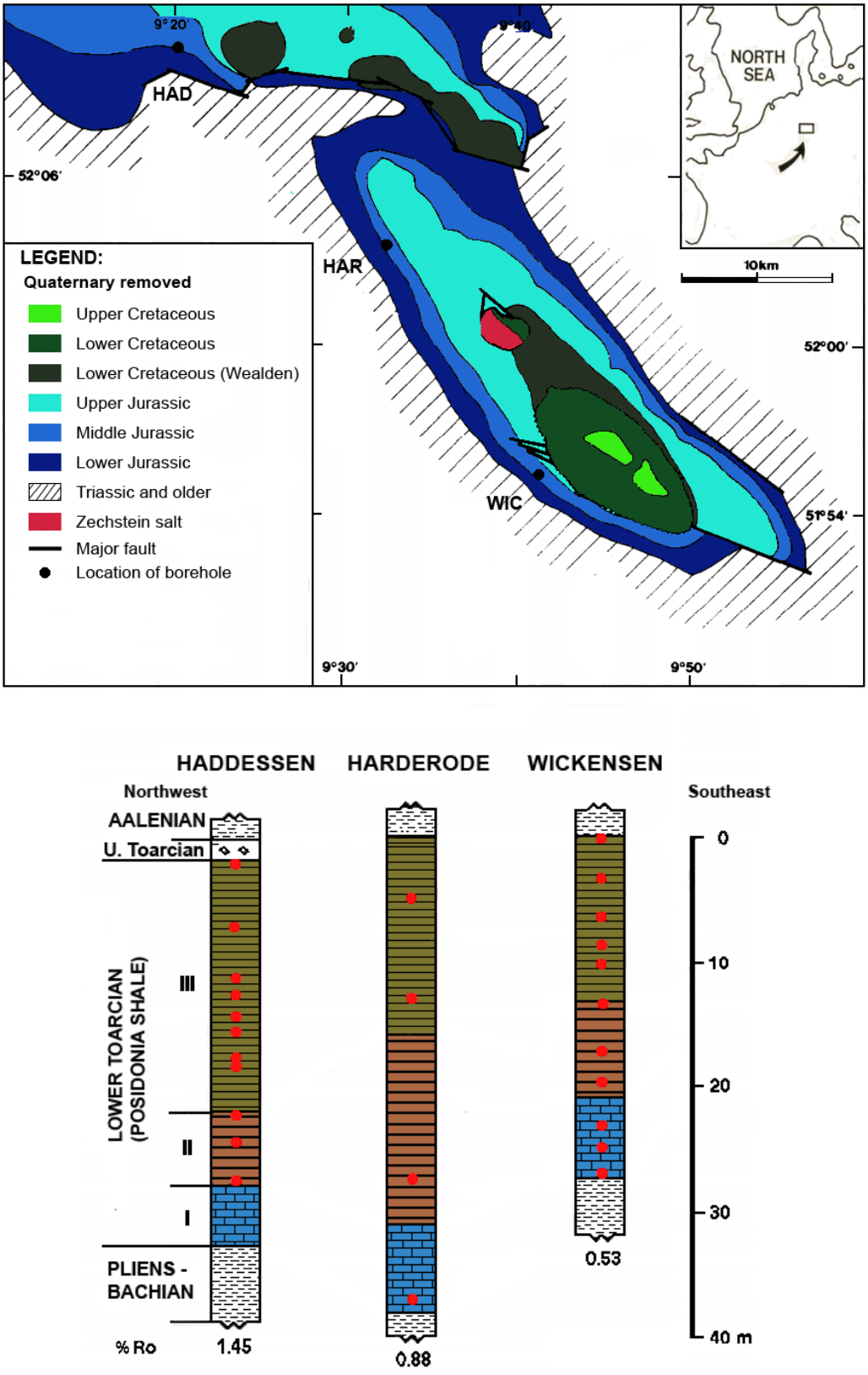

Figure 3. 1. *Location of Hils syncline, Northern Germany and three boreholes: WIC (0.53% Ro), HAR (0.89% Ro) and HAD (1.45% Ro) (after Mann and Müller (1988) and Horsfield et al. (2010)). b) Lithostratigraphic profile of the Posidonia Shale from the three boreholes showing a bottom marlstone unit (I) and two calcareous shale units (II and III); red dots represent sample locations (after Littke et al. (1991).*

For microscopic studies, carbon-coated polished thin sections were examined using a Hitachi SU-70 High Resolution Analytical SEM, equipped with an Oxford Instrument Energy Dispersive X-ray microanalysis system (INCA Energy 700). Samples were viewed in Back Scattered Electron (BSE) mode using the YAG detector with the following conditions: 15-8 mm WD, 15keV accelerating voltage, 2-4 nA filament current. To reduce the shale topography, prior to the SEM imaging, selected samples were polished with an argon broad ion beam (BIB) in the GATAN 691 Precision Ion Polishing System (PIPS^{TM}). In order to fit into the PIPS^{TM} chamber, the sample size was reduced to a 3 mm in diameter disc with GATAN 601 Ultrasound Disc Cutter using water emulsion of boron nitrate powder as a saw. Such prepared discs were bombarded with Ar ions in a vacuum (10^{-2} Pa) for 6 hours (angle 3°, 5kV, 1-20 µA). The images of shale porosity were captured in the Secondary Electron (SE) mode using through-the-lens detector (TLD) at magnifications 10,000 x (pixel size 6 nm) and 6,000 x (pixel size 15 nm), using the Automate mosaic building option. For selected mosaics, an Energy Dispersive X-ray (EDX) mode was implemented, generating maps of elemental and phase distribution. Microanalysis settings for the EDX collection were set at 300 µm dwell time, 15kV accelerating voltage and 4 nA filament current. The areas covered by EDX mapping varied between 4397 and 133023 µm^2. The phase extraction procedure involved conversion of each X-ray map into an RGB colour mode map, its binarization and area quantification with the ImageJ 1.44 software (Abramoff *et al.*, 2004).

To determine a Representative Elementary Area for estimations of image porosity, a modified box counting method described in Houben *et al.* (2013) was applied. With this method, continuous variations of any given property can be established by gradually increasing an area of investigation in a two-dimensional space. The box counting was proceeded for 4 groups of minerals: phyllosilicates, quartz and feldspar, carbonates and pyrite. The phases were extracted from a mix of RGB-converted EDX elemental maps. For the purpose of this study an area was selected as representative if the change in the content of an individual phase in boxes of increasing size did not exceed +/-10% relative to the previous area.

For each representative mosaic, total image porosity was quantified by digitization of pore areas manually outlined in the Adobe Photoshop 8.0. The digitization was followed by binarization and quantification proceeded in the image analysis software ImageJ 1.44 (Abramoff, 2004). Further statistical analysis was performed using statistical and mathematical software: Minitab 15 and Excel 2010. For selected mosaics, organic matter content was quantified with the point counting method using the image analysis software

JMicroVision 1.2.7. (Roduit, 2008). The point counting was proceeded until 300 counts or above until no significant change in the OM percentage was observed. For the gas window sample, the fraction occupied by porous and non-porous particles was additionally point-counted on two high magnification (10,000 x) image mosaics.

As a result of the limited image resolution at any magnification, not all pores could be fully visualized in the BIB image mosaics. To account for the missing pores area and determine the minimum fully resolved pore size in the BIB mosaics at the magnifications used, a method described in Houben *et al.* (2013) and Klaver *et al.* (2012) and based on a concept of a fractal dimension was implemented. According to this method, all pore areas were grouped in bins with subsequent bins increased by a power of two and subsequently, the number of pores were counted and varied as a power of the corresponding pore area. The unique power law equation was determined for pores sizes fully resolved and was graphically represented by a linear regression line(s) defined by a specific slope (D) and interception with the *y* axis (C). The minimum pore size fully resolved in images was determined as the one corresponding to the minimum pore area that does not deviate from the calculated regression line. For the intraorganic pores, the fractal distribution relationship was used for the calculation of a missing pore area after extrapolating the corresponding linear regression equation down to a selected diameter.

The fractal and power law approach was also implemented to scale pore volume as a function of a cross-sectional area of pore throats injected by mercury (Bernal and Bello, 2001). The use of this approach was justified by the fact that a range of pore areas progressively injected by mercury exceeds one order of magnitude. Again, the equation provided by Houben *et al.* (2013) was used to relate injected pore volume to a pore diameter.

Results

Impact of the research methodology used on porosity estimations

To address the issue of shales heterogeneity on different scales, and to overcome the limitations intrinsic to each method on its own, the multi-technique approach is required. In this study all methods were implemented complementarily, probing pores from < 1 nm to 5 µm in diameter. The information about porosity held by pores as small as 6 nm was obtained via CO_2 195K gas sorption (Rexer *et al.*, 2014). A drawback of such analysis is that it does

not differentiate between adsorbing phases unless a separate analysis for bulk shale and kerogen is performed. Mercury injection can be complementary to gas sorption techniques, but one should consider its limited use for estimating the true pore size distribution of shales if pore bodies are connected through narrow pore throats (Schmitt *et al.*, 2013). Moreover, sample compressibility may introduce errors in quantifying porosities (Giesche, 2006). Mercury injection is the basic method to understand distribution of pore throats and a relation of pore bodies to pore throats if both intrusion and extrusion are run on a single sample (Ioannidis *et al.*, 1991). In this study, the minimum size of pores that were intruded by mercury is 5.6 nm, leaving all finer pores, pores accessible through throats < 5.6 nm or any blind pores outside the scope of our experiments (Bustin *et al.*, 2008). To quantify the amount and distribution of macropores not detected neither through mercury injection nor gas adsorption, we resolved to microscopic techniques. With the typical minimum resolution in the order of 100s pixels when analyzing standard polished thin sections under Scanning Electron Microscope, higher resolutions can only be obtained by polishing samples with Ga or Ar ions. But even image-based techniques using highly polished samples have limited use in quantifying total porosities, as they typically only allow to see macropores and larger mesopores. Still, they provide good overview of the sample mineralogy and fabric and with a sufficient area, they allow for a qualitative and quantitative comparison of the abundance and distribution of larger pore bodies between different areas. The most complete pore volumes and (open) porosities in shale samples can be quantified with bulk methods using Archimedes Principle and water as a probing fluid. When combined with mercury immersion, this method detects pores which size exceeds the diameter of water (0.275 nm) and correlates well with He pycnometry (Rexer *et al.*, 2014).

Shale texture and organic abundance from microscopic observations

Low maturity Posidonia shale from the Hils half-graben is a dark grey, calcareous mudstone exhibiting macroscopically visible, subcentimetric lamination, marked by the varied abundance of a carbonate and clay component. Due to the diagenetic phase redistribution within the mineral matrix and progressive maturation of organic matter imparting black colour to shale samples, this sub-centimeter lamination is to a large extent obliterated in rocks of higher maturity. The calcitic component building the shale matrix is composed predominantly of nanofossils, mainly intact or broken coccoliths and disarticulated schizospheres, and bears signs of advanced recrystallization in the bottom marlstone and in

the most calcite-rich laminae of the middle and upper calcareous shale. The majority of nannofossils forms debris concentrated in thin layers or ellipsoidal aggregates (faecal pellets), alternating on a micrometer scale with clay rich laminae. The recrystallization features and the appearance of the carbonate cement are more pronounced both in the low maturity marlstone and in the higher maturity marlstone and calcareous shale. Those features include equant calcite crystals, often fused by a contact cement, and abundant authigenic calcite and dolomite replacing algal cysts, cementing clay and calcite-bearing shale framework and sealing microfractures.

The type and mode of occurrence of organic macerals change throughout the whole maturity sequence. In the early oil window sample, structured algal liptinite is the most distinguishable maceral, but it is volumetrically surpassed by the microscopically unresolved and mineral associated, strongly fluorescing matrix bituminite (Tao *et al.*, 2012). At the peak oil window maturity, structured algal bodies are less abundant, either mechanically collapsed or filled with the carbonate cement. The bituminous groundmass is much less fluorescent and instead, a dense network of non-solvent extractable solid bitumen fills the inerclay pores and the fossilliferous aggregates. At the gas window maturity, no structured alginites are present, and a tight network of irregularly-shaped, non-extractable, solid bitumen is a dominant feature. The solid bitumen fills microfractures, recrystallized faecal pellets, and spaces within clay aggregates.

Bulk properties of the shale

The bulk mineralogical composition of the Posidonia samples suite is relatively constant throughout the whole maturity sequence (Table 3.1 and Figure 3.2). The two most abundant components, calcite and phyllosilicates, present an interchangeable relationship and show more drastic variations within single wells rather than between wells. For instance, in all wells, the lower marlstone unit (Figure 3.1b) shows higher enrichment in calcite in comparison to clays (~50% and ~25 wt.% respectively), while the middle and upper calcareous shale present equal proportions of both (30-40 wt.%). Only two phases, dolomite and sodium rich plagioclase, show increase in abundance while moving towards higher maturity shale. Despite the variation in the calcite and clay content between units, the Posidonia shale is unanimously classified as a calcareous nannoplankton-, (calcite cement-), silt- and clay-bearing mudstone.

Table 3. 1. *The TOC-normalized XRD mineralogical composition of Posidonia shale in wt.% for WIC (0.53% Ro), HAR (0.89% Ro) and HAD (1.45% Ro). The TOC content (in wt.%) was determined with LECO.*

	WIC 7129	WIC 7135	WIC 7145	WIC 7147	WIC 7155	HAR 7038	HAR 7046	HAR 7060	HAR 7070	HAD 7083	HAD 7090	HAD 7110	HAD 7119
Quartz	12.4	15.1	11.8	14.0	7.8	14.6	16.4	12.2	10.8	11.1	14.8	14.1	7.6
Plagioclase	1.0	0.2	0.9	0.6	1.3	1.9	2.0	2.6	3.7	2.4	2.8	3.2	4.5
K-Feldspar	0.7	0.0	0.0	0.0	0.0	0.5	0.4	0.4	0.5	0.5	0.1	0.7	0.6
Calcite	32.4	35.8	41.5	38.1	50.0	40.1	39.5	28.7	42.2	49.5	36.8	28.5	46.3
Dolomite	0.3	0.0	0.3	0.2	0.5	0.6	1.0	6.0	2.0	0.6	1.7	3.7	2.5
Siderite/ Ankerite	0.4	0.0	0.8	1.8	0.5	0.2	0.3	0.3	0.3	0.1	0.8	0.4	0.6
Aragonite	nd	nd	1.2	nd	1.2	nd	nd	nd	nd	nd	0.6	nd	1.4
Pyrite	4.8	4.5	3.5	3.7	4.9	5.2	4.8	8.6	5.2	6.9	4.6	6.6	4.2
Marcasite	0.7	nd	nd	nd	nd	0.6	0.2	0.9	1.2	nd	nd	0.2	nd
Anatase	0.3	0.1	nd	0.1	nd	0.3	0.2	0.2	0.3	0.2	nd	0.4	nd
Muscovite	2.3	2.2	0.0	1.2	0.1	2.9	2.8	3.5	3.0	2.4	1.2	4.4	0.0
Illite + I/S	21.7	22.0	20.0	25.4	17.5	17.0	18.9	24.7	18.3	13.3	22.1	23.5	18.1
Kaolinite	10.4	6.0	4.5	7.1	2.0	8.2	6.8	6.2	4.0	6.1	3.6	8.1	1.0
Dickite	nd	nd	1.1	nd	0.9	nd	nd	nd	nd	nd	1.2	nd	0.0
Chlorite	nd	0.4	1.8	0.2	1.6	nd	nd	nd	nd	0.0	0.6	nd	2.5
Gypsium	nd	0.3	2.0	0.4	2.2	nd	nd	nd	nd	0.4	1.7	nd	3.5
Halite	nd	0.1	nd	0	nd	nd	nd	nd	nd	0.1	nd	nd	nd
TOC	12.6	13.3	10.9	7.3	9.7	7.9	6.8	5.8	8.7	6.4	7.4	6.4	7.2
Total	100	100	100	100	100	100	100	100	100	100	100	100	100

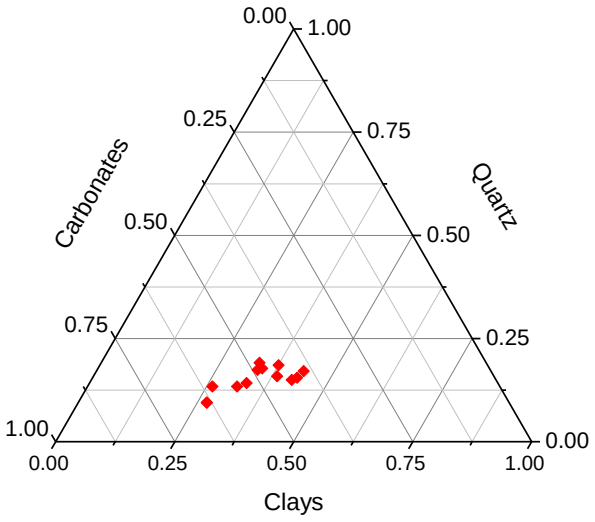

Figure 3. 2. *Ternary diagram showing the basic mineralogy of the Posidonia suite. Samples taken from three cores: WIC 7129 (0.53% Ro), HAR 7060 (0.89% Ro) and HAD 7110 (1.45% Ro). Note a strong alignment of points describing the mutually exclusive relationship between abundance of clays and carbonates.*

Table 3. 2. *TOC, Rock-Eval and grain density measurements for the selected Posidonia samples, wells WIC (0.53% Ro), HAR (0.89% Ro) and HAD (1.45% Ro).*

Sample	TOC (%)	S1 (mgHC/g)	S2 (mgHC/g)	HI (mgHC/ gTOC)	T_{max} (C°)	Grain density (g/cm^3)	Grain density after solvent extraction (g/cm^3)
WIC 7129	12.59	3.02	90.25	717	427	2.254	2.236
WIC 7133	8.71	2.57	54.90	630	434	2.392	-
WIC 7135	13.27	4.62	84.63	638	427	2.249	-
WIC 7137	10.25	3.18	68.10	665	427	2.343	-
WIC 7139	9.36	2.81	64.95	694	428	2.375	-
WIC 7142	10.43	3.52	72.37	694	426	2.346	-
WIC 7145	10.92	4.18	72.03	660	425	2.331	-
WIC 7147	7.28	2.26	47.76	656	434	2.458	-
WIC 7151	14.75	5.85	89.61	608	429	2.236	-
WIC 7153	7.34	2.45	48.37	659	431	2.489	-
WIC 7155	9.67	3.87	69.41	718	428	2.361	-
HAR 7038	7.90	3.29	30.17	382	449	2.493	-
HAR 7046	6.75	2.93	26.03	386	450	2.526	-
HAR 7060	5.78	1.47	19.72	341	447	2.592	2.682
HAR 7070	8.71	2.26	31.27	359	449	2.463	2.533
HAD 7083	7.35	0.75	4.10	56	465	2.589	-
HAD 7090	7.41	0.94	4.16	56	463	2.572	-
HAD 7094	5.21	0.845	3.52	68	459	2.608	-
HAD 7097	5.40	0.75	3.15	58	458	2.609	-
HAD 7099	6.51	0.98	3.86	59	463	2.576	-
HAD 7101	5.88	0.92	3.1	53	457	2.624	-
HAD 7104	5.04	0.72	3.385	67	459	2.620	-
HAD 7105	5.85	0.77	3.28	56	461	2.621	-
HAD 7110	6.36	1.07	3.79	60	462	2.600	2.618
HAD 7115	6.49	1.12	3.80	59	460	2.614	-
HAD 7119	7.15	1.23	3.16	44	458	2.607	-

Posidonia Shale is a kerogen Type II, organic-rich rock with the TOC change linked to the degree of its thermal maturation (Table 3.2). The average organic content gradually decreases from 10 (+/-2) wt.% at 0.53% Ro (WIC), to 7 (+/-1) wt.% in the peak oil window (HAR 0.89% Ro) and 6 (+/-1) wt.% in the gas window (HAD 1.45% Ro). A drop in TOC is accompanied by a consistent decrease in S1 and S2 values, a drop in HI from ca. 662 (+/-33) in WIC to 58 (+/-6) mg/gTOC in HAD, a rise in Tmax from 429 (+/-3) to 460 (+/-3) °C, and a decrease in the solvent soluble bitumen from 13 mg/g to 2 mg/g (Table 3.3). For all samples analyzed, the kerogen-bound but solvent extractable bitumen (S2a) consistently exceeds the amount of RockEval measured free bitumen (S1), and reduces the yield of the pyrolizable, but solvent non-extractable organic matter (S2b). For the 4 solvent washed samples, the corrected oil saturation index decreased from 105 mg/gTOC in the early oil window sample, to 66 and 102 in the peak oil window samples and 27 mg/gTOC in the gas window sample.

Table 3. 3. *Rock-Eval evaluation after solvent extraction for the four selected Posidonia samples, wells WIC (0.53% Ro), HAR (0.89% Ro) and HAD (1.45%Ro).*

Sample	S2a (mg/g)	S1 + S2a		S2b (mg/g)	S1/TOC (mg/gTOC)
		(mg/g)	% TOC		
WIC 7129	10.4	13.20	10.5	79.89	104.8
HAR 7060	4.5	5.89	10.2	15.25	101.9
HAR 7070	3.5	5.71	6.6	27.79	65.6
HAD 7110	0.7	1.74	2.7	3.05	27.4

S1: Free bitumen
S2a: Kerogen bound, solvent extractable bitumen
S2b: pyrolizable, but not solvent extractable organic matter.

The average grain density of the mineral matrix shows minimal variation between samples from different wells. In consequence, the observed spread in the measured shale grain densities is linked to the maturity of the organic matter, organic content and the degree of saturation with free bitumen. In the investigated sample suite, the measured average shale grain densities increased from 2.4 (+/-0.1) g/cm^3 at 0.53% Ro, to 2.5 (+/-0.1) at 0.89% Ro and 2.6 (+/-0.2) at 1.45% Ro (Table 3.2). Upon extraction of the extractable bitumen phase, the density increased significantly only in the peak oil window maturity sample, with little change in samples of two other maturities (Table 3.2).

Total and mercury porosity. Pore throat size distribution

In this study, total porosity and mercury pore size distribution were corrected for pores intersected by the sample surface, responsible for an increase in the volume of mercury at the very start of the injection experiment (Figure 3.3b). In order to estimate a true radius of the onset of Hg intrusion into a porous network within each sample, cumulative mercury volume data were compared with pore volume density data and pore throat fractal distribution (Figure 3.3). To make a comparison effective, calculated areas of pore throats cross-sectioned by a theoretical plane were grouped in bins of an increasing size and plotted as a function of pore volume intruded by mercury (Bernal and Bello, 2001; Houben *et al.*, 2013). The resulting fractal distribution of Posidonia pore throats was fitted with 2-3 linear regression lines (Figure 3.3c). The line with the smallest slope (typically < 1.1) describing the largest pores was interpreted as an artifact, created due to intersection of pores by the sample surface (Figure 3.6d, e, f). A true injection of Hg to pore bodies is described by a regression line with a higher slope reflecting increasing pore volume density of progressively smaller pores, and corresponds to a rise in the pore volume density beyond the background values (Figure 3.3a,

Figure 3.6a, b, c). Consistently with Comisky (2011), the estimated true radius of intrusion is up to 3 orders of magnitude lower than the apparent radius determined by the raw data.

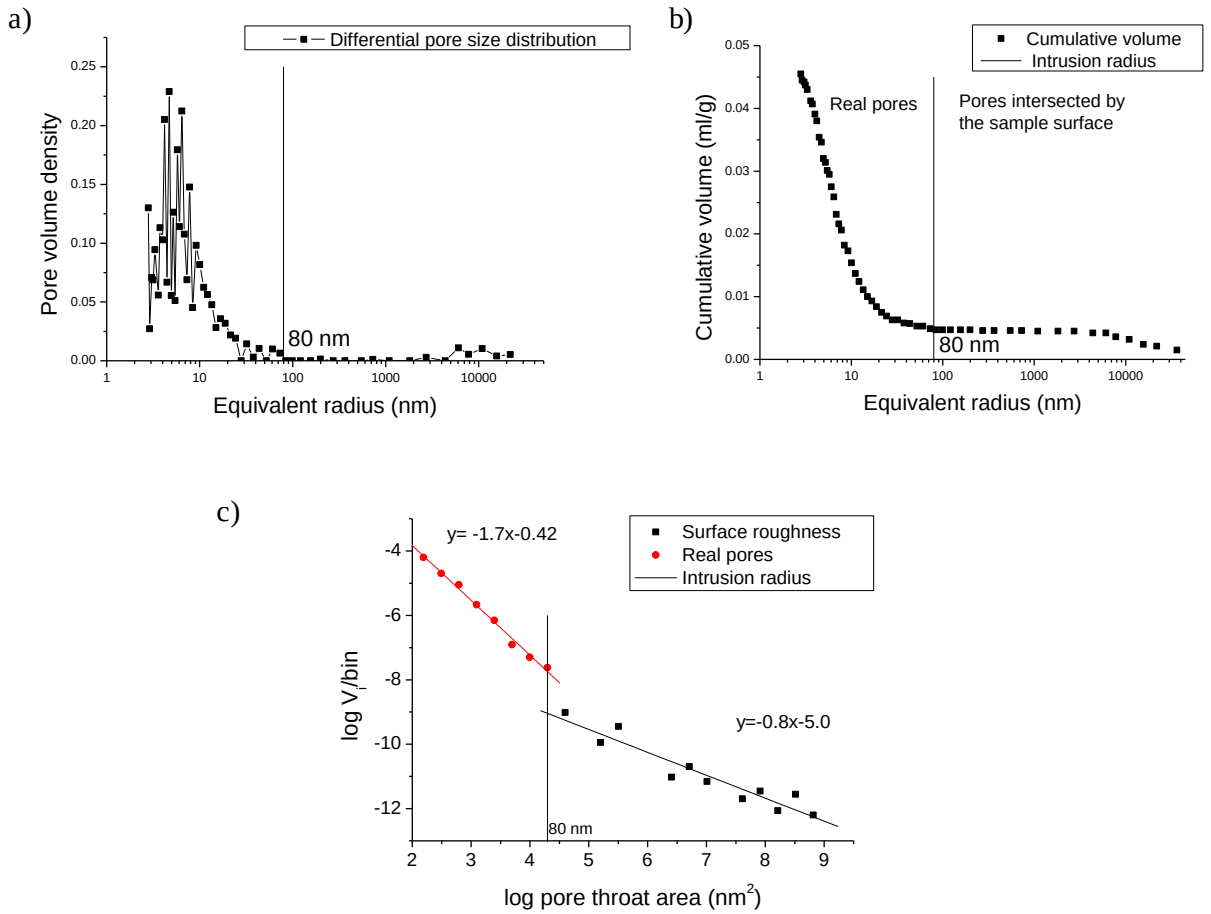

Figure 3. 3. *a) Pore volume density, b) cumulative volume of intruded mercury and c) fractal distribution of pores in the WIC 7151 sample (0.53% Ro). Pores exhibit a non-uniform, fractal distribution with pores > 80 nm (slope -0.8) interpreted as those intersected by the sample surface (surface roughness) and pores < 80 nm (slope -1.7) interpreted as pores accessed through corresponding throats.*

Total porosities, as measured for as-received shale samples, show a significant change with increasing maturity over the whole maturation sequence (Table 3.4 and Figure 3.4). At 0.53 Ro% porosities vary between 10-14% and, despite an observed decrease in TOC, decline to 2.5-4.5% in the peak oil window (0.89% Ro). In contrast, at gas window maturities, with further reduction of the carbon content, a rise in total porosity is observed. Porosities oscillate here between 9-14% reaching values similar to those at 0.53% Ro. As observed in Figure 3.4, with only a small variation in the measured carbon content, porosities are not directly related to TOC, and only in the early oil window maturity shale do porosities and organic content show a weak negative correlation. For both peak oil window and gas window samples, the

porosity values scatter over the measured range of TOC with no apparent trend. Total porosities show varied relation to bulk mineralogy in samples of different maturities. In general, there is a positive relationship between calcite content and total porosity, and the negative relation between porosity and the phyllosilicates content, for both early mature and gas window samples (Figure 3.5). In contrast, no trend exists for the shale bulk composition and porosities measured in the peak oil window

Table 3. 4. *Porosities measured with different techniques for selected Posidonia samples, wells WIC (0.53% Ro), HAR (0.89% Ro) and HAD (1.45% Ro).*

Sample	Total porosity (%)	Mercury Injection			CO_2 195K	
		Hg porosity (%)	Hg access radius (nm)	Porosity < 5.6 nm (%)	Sorption porosity (%)	Sorption pore volume
WIC 7129	9.72	6.98	9.5	2.77	4.08	0.019
WIC 7133	12.76	9.51	13.1	3.27	-	-
WIC 7135	10.12	5.86	8.1	4.28	4.27	0.020
WIC 7137	10.62	8.09	8.3	2.53	-	-
WIC 7139	13.53	8.16	8.6	5.39	-	-
WIC 7142	12.18	8.35	10.7	3.86	-	-
WIC 7145	12.91	9.46	11.1	3.47	3.71	0.017
WIC 7147	11.44	10.41	17.1	1.14	3.57	0.015
WIC 7151	10.52	8.18	15.1	2.35	-	-
WIC 7153	13.87	11.20	30.3	2.68	-	-
WIC 7155	12.64	9.50	18.3	3.11	3.53	0.015
HAR 7038	3.08	1.27	5.2	1.83	2.04	0.008
HAR 7046	4.58	0.68	3.4	3.90	-	-
HAR 7060	4.48	1.96	5.5	2.54	2.08	0.008
HAR 7070	3.52	1.70	5.6	1.83	2.51	0.010
HAD 7083	13.68	10.35	13.9	3.35	3.79	0.015
HAD 7090	11.24	6.00	8.5	5.32	4.15	0.017
HAD 7094	12.13	8.16	10.1	4.00	3.94	0.016
HAD 7097	11.87	5.25	6.7	6.65	-	-
HAD 7099	10.60	3.16	4.2	7.50	-	-
HAD 7101	11.79	7.57	7.00	4.25	-	-
HAD 7104	11.63	4.55	5.0	7.12	-	-
HAD 7105	11.23	6.42	5.7	4.83	-	-
HAD 7110	9.43	3.45	4.8	6.01	3.76	0.015
HAD 7115	9.30	4.68	5.5	4.63	-	-
HAD 7119	11.29	8.34	14.7	2.98	3.29	0.013

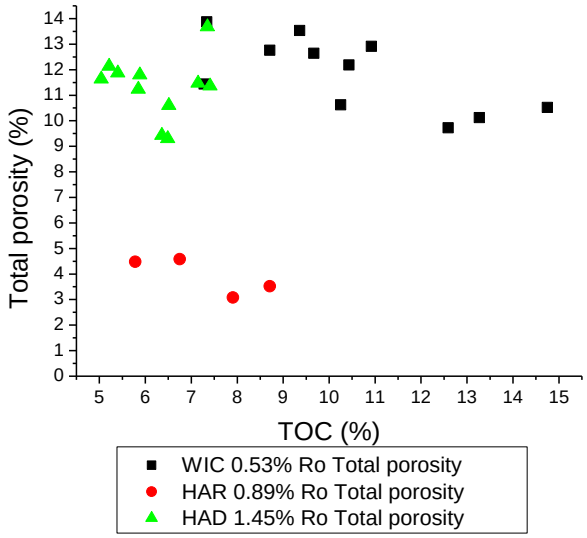

Figure 3. 4. *Plot of total porosity change as a function of maturity and organic carbon content.*

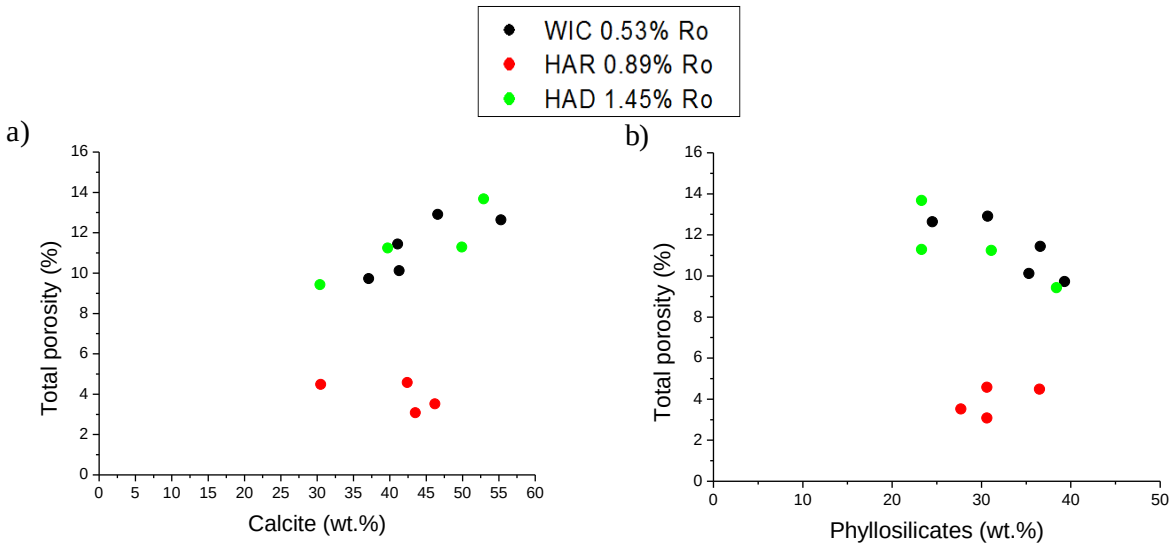

Figure 3. 5. *Cross-plots showing relationship between shale total porosity and its XRD mineralogical composition. Calcite and phyllosilicates contents are not TOC normalized.*

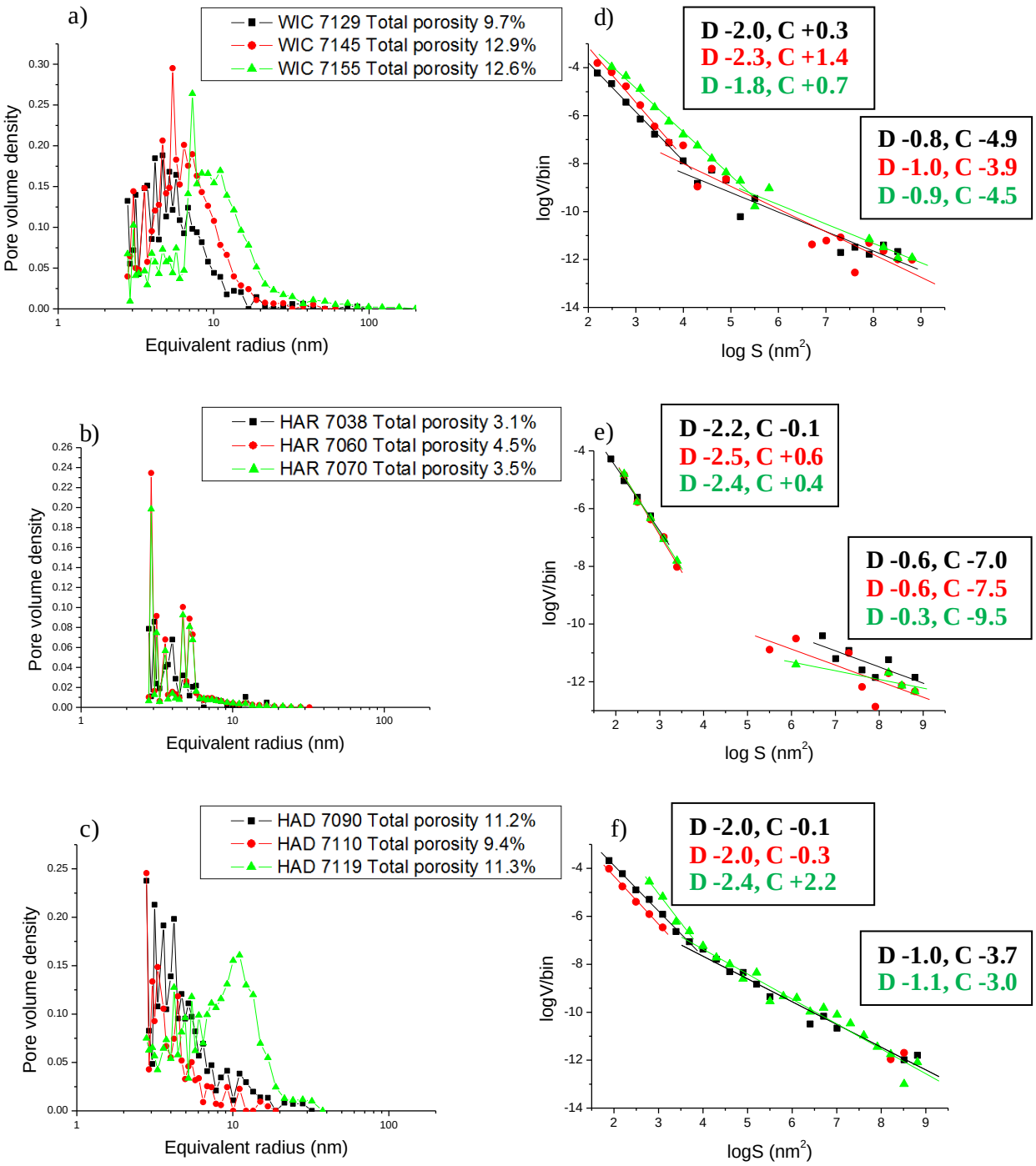

Figure 3. 6. *a), b), c) Pore volume density distribution of true intrusion pores in the selected Posidonia samples, wells WIC (0.53% Ro), HAR (0.89% Ro) and HAD (1.45% Ro). The mercury data was cut off at a radius interpreted as the onset of intrusion into a pore network. This corresponds to a pore radius at which a visible change in the slope of a regression line describing fractal distribution of pore throats occurs (see Fig 3.3). d), e), f) Fractal distibution of pore throats approximated by a linear regression line defined by a slope (D) and point of interception with the y axis. In each sample the regression line characterized by a low slope (<-1.1) defines surface roughness, while the line with a high slope (>1.8) describes real pores intruded by mercury.*

A non-linear pattern of porosity change with maturity, similar to the one described above, is observed for porosities intruded by Hg. Here values decrease from 6-12% to 1-2% between 0.53% and 0.89% Ro (Table 3.4). A subsequent increase in total porosity at gas window maturities is not consistent, with values varying between 3 and 10%. At all maturities, the threshold aperture, defined as an aperture providing access to > 10% of porosity is narrow, and usually does not exceed 40 nm of diameter (Table 3.4 and Figure 3.6). In the Wickensen sample suite, it oscillates between 16 and 37 nm, with the extreme values approaching 60 nm only in the faecal pellet rich marlstone samples. In the gas window samples, the size of the aperture is slightly lower, between 8-20 nm, approaching 30 nm in the most calcite rich shales. The finest pore throats and the narrowest pore throat size distribution characterize the oil window shale, with the pore throat threshold apertures between 7-11 nm and no influence of shale lithology on the measured pore volume density (Figure 3.6 b, e). At all maturities, pore throats show fractal behaviour up to the maximum pore volume density, but its distribution varies between lithologies and maturities. This variation reflects varied spread of pore throat sizes (high D with a smaller spread) for any given slope, and a different amount of porosity contained in the probed pores (high C with higher porosity). In general, pore size distributions are the narrowest in the oil window shales (high D), and describe the lowest porosities (low C for any given D) (Figure 3.6b). A major change between samples of different maturity is seen in the size of pore throats providing the highest differential increase in porosity. Between 0.53% and 0.89% R_o this size decreases from 9-17 nm to 6-7 nm (Figure 3.6a, b). Amongst the lowest maturity shale, only marlstone samples exhibit differential maxima at pores that are much wider, up to 34 nm. Similarly to the low maturity well, at the gas window maturity a size of pore throats contributing the highest porosity value is similar for all calcareous shale samples, oscillating between 6-12 nm, with the exception of the marlstone sample, where this diameter reaches 22 nm (Figure 3.6c). High contribution of pore bodies within the maximum pore volume density intervals of the low and high maturity shale is indicated by the presence of mercury hysteresis (Figure 3.7a, b). Such hysteresis associated with spontaneous imbibition is controlled not by a pore throat radius, like during a drainage stage, but by a pore body/pore throat ratio (Webb, 2001). The increase of this ratio is interpreted as reflecting entrapment of mercury in pore cavities, causing pores to empty at capillary pressures lower than the corresponding intrusion pressures (Padhy *et al.*, 2007). As shown with the curve plotting difference between porosity intruded and emptied during intrusion-extrusion experiments at equivalent pressures, as a function of pore radii (Figure 3.7c), the absolute amount of trapped mercury, due to a small rate of extrusion, initially

increases. When a threshold diameter is reached (here 34 and 27 nm for WIC and HAD samples respectively), the rate of extrusion exceeds the rate of intrusion at equivalent pressures, and mercury starts to recede from pores that could not be emptied before (Padhy et al., 2007). The curve shows that 90% of porosity in the lowest and highest maturity Posidonia is not emptied before pressure equivalent to the threshold diameter is reached. Such high percentage of the trapped mercury reflects either the high volume of the pore bodies, or alternaively, high compressibility of the studied shale and the embedded organic matter (Toda and Toyoda, 1972).

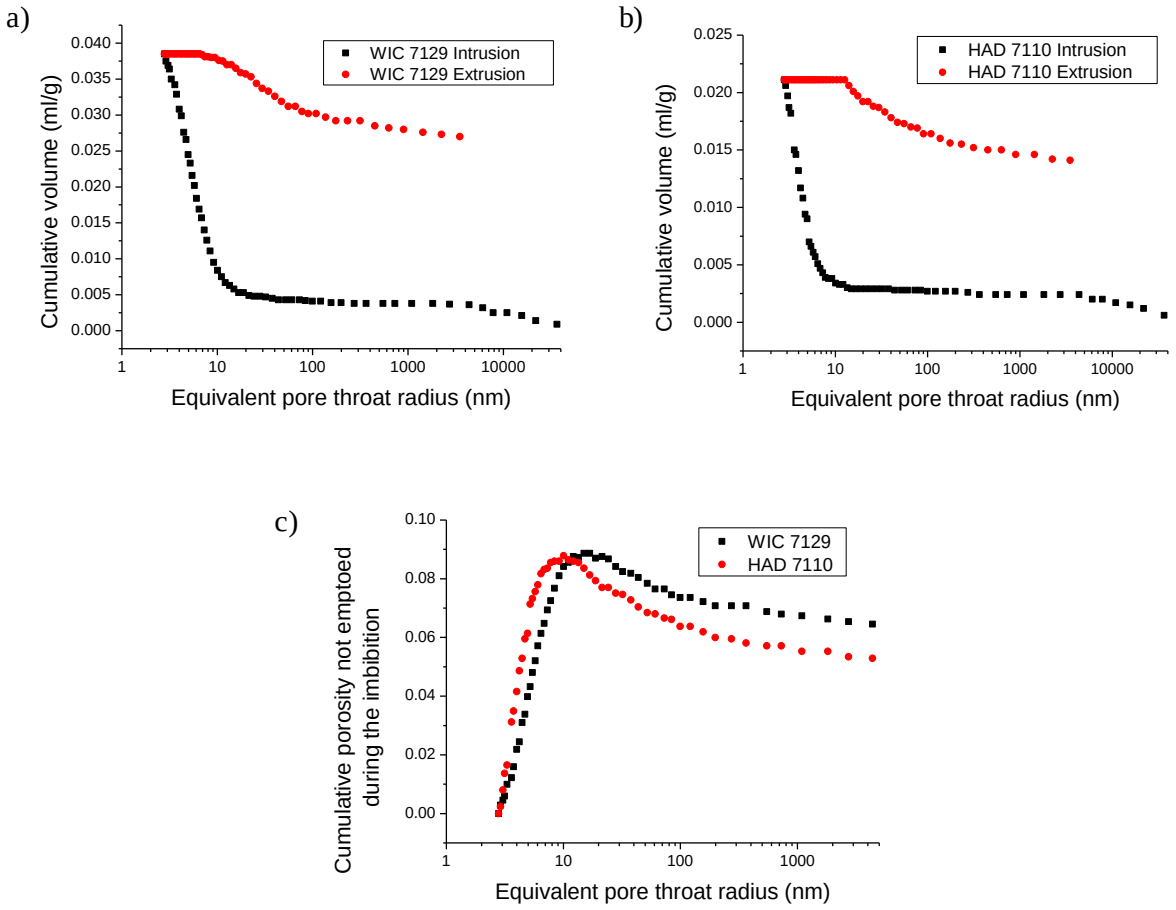

Figure 3. 7. *Cumulative intrusion (black) and extrusion (red) of mercury for a) WIC 7129 0.53% Ro and b) HAD 7110 1.45% Ro shale. The mercury data were normalized to the true volume of intrusion after cutting off the pore volume data interpreted as representing surface roughness. Difference between the two curves is defined as a hysteresis. c) Cumulative porosity that is not emptied from mercury during the imbibition from the WIC 7129 (black) and HAD 7110 (red shale). The curve plots difference between porosity intruded and emptied during the intrusion-extrusion experiments at equivalent pressures as % of a rock. For pores with a radius < 16.8 nm the rate of extrusion < rate of intrusion and thus fraction of mercury is trapped. Note that in during the imbibition process the absolute amount of mercury that is not released at the intrusion pressure initially increases. For pores with a radius > 16.8 nm for WIC and > 13.5 nm for HAD the rate of extrusion > rate of intrusion, causing emptying from the previously trapped mercury at lower pressures attained.*

The amount of total porosity present in the Posidonia shale changes after extraction of the soluble bitumen with organic solvents. Although not measured directly, on the basis of a change in the grain volume of a bulk shale pre- and after solvent extraction we were able to estimate the volume of the soluble bitumen and thus bitumen-free total porosity for three samples of the medium (HAR 7060, 7070) and high maturity (HAD 7110). Because we did not notice any increase in the grain density of the early mature sample after solvent extraction, plausibly due to change in the polymer structure upon interaction with the solvent (Sandvik et *al.*, 1992), we could not estimate bitumen-free porosity in the Wickensen shale. For the peak oil and gas window shale, the amount of the extractable bitumen decreased from 2.8% in the bottom marlstone and 3.4% in the middle calcareous shale at the peak oil window maturities to 0.68% (upper calcareous shale) in the gas window (Table 3.5 and Figure 3.8a). Consequently, the estimated bitumen-free total porosities are higher than those measured in the as-received shale (Table 3.4), amounting to 6.3-7.8% and 10.1% in the peak oil window and gas window maturity samples respectively (Table 3.5). As generation and expulsion of hydrocarbons leads to loss of OC (Raiswell and Berner, 1987), the measured and bitumen-free porosities were compared to potential porosities that would characterize shale of a given maturity stage by assuming perfect expulsion of generated petroleum (Table 3.6). The loss of OC in wt.% was calculated according to Justwan and Dahl (2005) and Jarvie *et al.* (2007) and converted to OM (vol.%) according to Coskey (2001). The calculated Transformation Ratios (TR) of the Posidonia kerogen are as follows: 5% for WIC 7129, 63% for HAR 7060, 73% for HAR 7070 and 96% for HAD 7110. These TR show agreement with a reference kinetic curve for type II kerogen from the Toarcian of Paris Basin as well as TR estimated for other shale formations at an equivalent maturities (Modica and Lapierre, 2012, their Figure 3.8). The conversion of accumulated OM from wt.% to vol.% yielded potential organic porosity values. Those increase from 0.8% in Wickensen to 7-8% in Harderode and further to 13% in Haddessen (Figure 3.8b). Assuming the initial porosity of the low maturity shale 10% (Table 2.4), the estimated increase in total porosity between 0.53-0.89% Ro is inconsistent with a measured drop in oil-free porosities in the oil window (Figure 3.8c). In contrast, the calculated increase in the organic porosity by absolute 4 % between maturities 0.89-1.45% matches an increase experimentally measured in the gas window shale (Figure 3.8d).

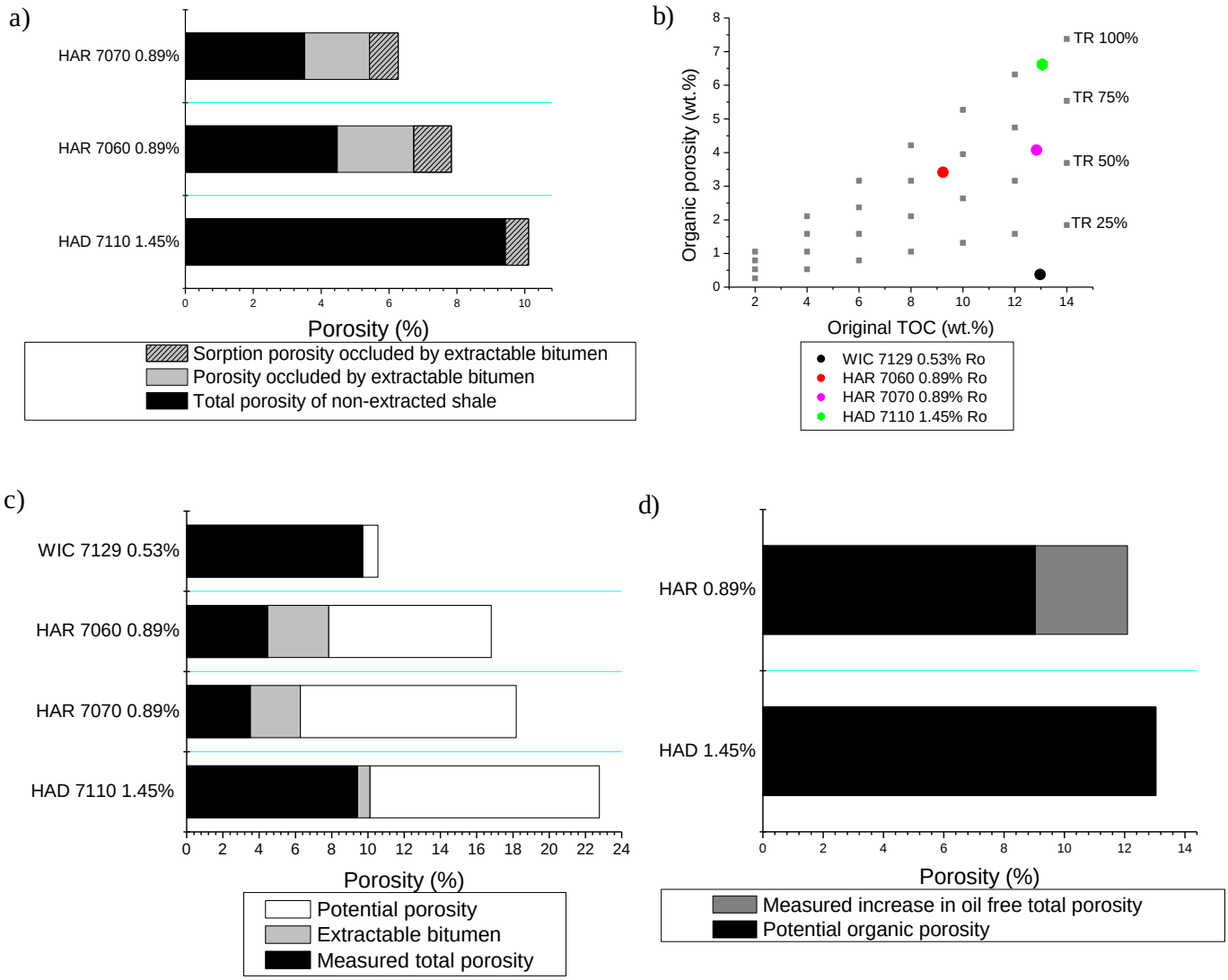

Figure 3. 8. *a) Total porosity prior (black) and after extraction of soluble bitumen (sum of black and grey) in the peak oil window HAR (0.89%) and gas window HAD (1.45%) shale. Post extraction total porosity was estimated on the basis of a change in the grain volume of a bulk shale pre- and after solvent extraction. Sorption porosity occluded by extractable bitumen was measured by comparing gas sorption porosity prior and after solvent extraction. b) A hypothetical organic porosity (in wt.%) present in shale of different maturity as a result of thermal decomposition of organic matter. The organic porosities were calculated according to equations of Jarvie et al. (2007) and Coskey (2001). TOC for each sample was restored to original values according to Justwan and Dahl (2005). c) Potential organic porosity (sum of black, grey and white) for 0.53% Ro (WIC 7129), 0.89% (HAR 7060) and 1.45% R_o (HAD 7110), superimposed on experimentally measured porosities (black). The initial inorganic porosity was assumed 10%, and total porosities were estimated as a sum of the initial porosity and organic porosity characteristic for each maturity step. Difference between potential total porosities and measured total porosities are due to occlusion by solvent extractable bitumen (grey), as well as combined compaction and occlusion by solid bitumen (white). d) Similarity between potential organic porosity for the gas window shale and the sum of the potential organic porosity of the peak oil window shale (black) and measured increase in total porosity between the two shales after accounting for the solvent extractable bitumen occluding pores (grey).*

Table 3. 5. *Estimated total porosities and measured sorption porosities after solvent extraction for the selected Posidonia samples, HAR (0.89% Ro) and HAD (1.45% Ro). Difference between pre- and post-extraction porosities yielded volume of extractable bitumen occluding porosity.*

Sample	Total porosity after solvent extraction (%)	Extractable bitumen occluding porosity (vol. %)	Sorption porosity after solvent extraction (%)	Sorption porosity occluded by extractable bitumen (%)	Fraction of sorption porosity occluded by extractable bitumen	Fraction of total extractable bitumen in sorption pores < 6 nm
HAR 7060	7.84	3.36	3.19	1.11	0.35	0.33
HAR 7070	6.27	2.75	3.35	0.85	0.25	0.31
HAD 7110	10.11	0.68	4.55	0.79	0.17	~1.00

Table 3. 6. *Determination of potential organic porosity at different stages of thermal maturity for selected samples of WIC (0.53% Ro), HAR (0.89% Ro) and HAD (1.45% Ro) using equations of Justwan and Dahl (2005) Jarvie et al. (2007) and Coskey (2001). S2b – hydrocarbon potential of post-extracted shale, TR – Transformation Ratio, GOC – Generative Organic Carbon.*

Sample	S2b (mg/g)	HI o (mg/g)	HI pd (mg/g)[1]	TOCo (%)	TOCpd (%)	TR	GOC	Organic porosity (wt.%)	Organic porosity (vol.%)
WIC 7129	79.9	650	635	12.97	12.59	0.05	0.55	0.37	0.83
HAR 7060	15.3	600	264	9.23	5.78	0.72	0.51	3.41	7.08
HAR 7070	27.8	600	319	12.83	8.71	0.63	0.50	4.07	8.46
HAD 7110	3.0	620	48	13.05	6.36	0.96	0.53	6.62	13.04

[1]*HI pd was estimated on the basis of S2b, after extraction of soluble bitumen.*

Micro- and mesoporosity. Gas adsorption

Significant part of porosity is not detected by Hg and thus might be blind or contained/accessible through pores < 5.6 nm (Table 3.4). This porosity accounts for as much as 10-42% of total porosity in the least mature samples, and 52-59% at the peak oil window. In the gas window, < 5.6 nm porosity shows the highest spread, accounting for 25-71% of total porosity. While in both mature and overmature shale, lower values of the < 5.6 nm porosity are characteristic for the bottom marlstone, in the WIC sample suite we found no porosity difference between lithologies. In order to investigate nature and connectivity of the < 5.6 nm pores, shale porosities were measured with the low pressure CO_2 195K gas sorption. The sorption porosities (SP) showed overall agreement with porosities that lie beneath the resolution of the mercury injection (MP-1) in shales of all maturities (Tab. 3.4 and Figure 3.10). This agreement suggests that the combination of sorption and mercury techniques can account for the total pore volume measured in the Posidonia shale and that the size of the pores fully filled with adsorbing gas at CO_2 195K lies below and close to 5.6 nm.

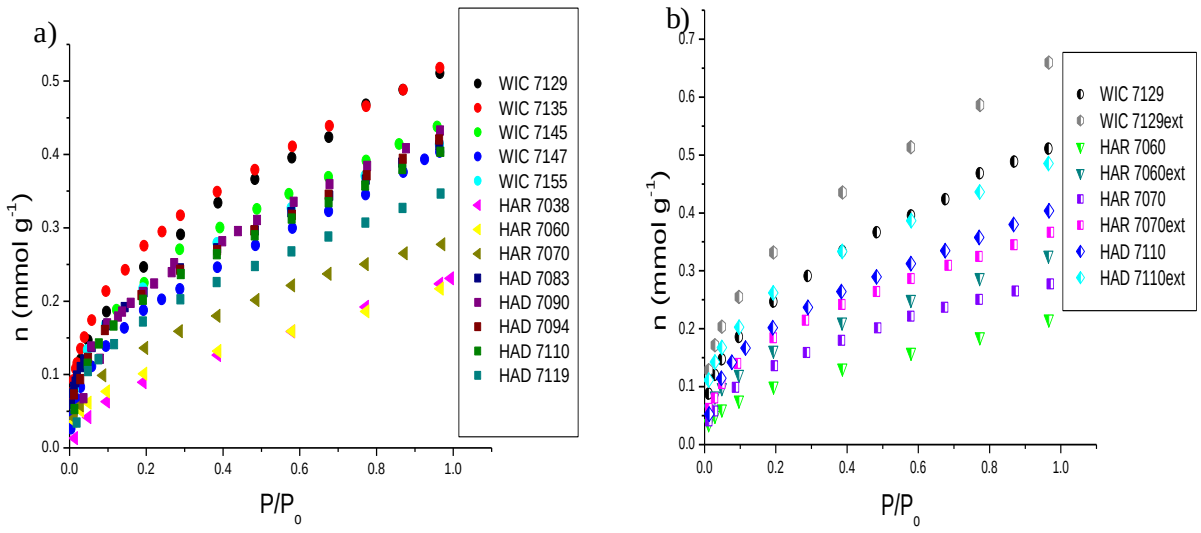

Figure 3. 9. *a) 195K CO_2 isotherms for selected WIC 0.53% Ro (circles), HAR 0.89% Ro (triangles) and HAD 1.45% Ro (rectangles) shales. The x-axis represents the relative pressure, while the y-axis represents concentration (in mmol/g) of CO_2 adsorbed at the temperature of 195K. Samples were not solvent extracted prior to analysis. Peak oil window shales (HAR) show lower sorption than early oil window (WIC) and gas winodw (HAR) counterparts. b) CO_2 195K isotherms for 7129 WIC 0.53% Ro (circles), 7060 HAR 0.89% Ro (triangles), 7070 HAR 0.89% Ro (rectangles) and 7110 HAD 1.45% Ro (diamonds) shales measured prior and after solvent extraction (ext). Non-extracted shales show higher sorption than extracted shales at all maturities.*

All captured CO_2 isotherms are type I (Sing *et al.*, 1985), that is they demonstrate evidence for the presence of microporosity filled at the lowest pressures and little surface for further adsorption at higher pressures (Figure 3.9a). Sorption pore volumes measured at 1 mbar and corresponding sorption porosities (SP) exhibit a non-linear change with the maturation of the shale, similar to the trend observed for measured total (TP) and mercury porosities (MP) (Table 3.4 and Figure 3.10). These volumes decrease from 0.015-0.029 cm^3/g at early oil window maturities to 0.008-0.010 cm^3/g in the peak oil window, followed by a rise to 0.013-0.017 cm^3/g in the gas window samples. Consistently, calculated sorption porosities bottom out in the oil window at 2.0-2.5 %, and amount to 3.5-4.3% and 3.3-4.1% for the early mature Wickensen and the gas window Haddessen samples, respectively. Sorption porosity shows no correlation to TOC between maturities and despite indication for the predictable change of porosity with the TOC change within wells, due to a small sample size we cannot be conclusive about the true nature of this relationship (Figure 3.11a). However, a positive covariation was found for the combined TOC and clay content and sorption porosity for both the early oil window and the gas window shale (Figure 3.11b). After solvent washing, performed for 4 shale samples, the concentration of the adsorbed gas

increased (Figure 3.9b), resulting in an increase in the calculated sorption porosities at all maturities (Table 3.4). For the least mature sample, as the structure of kerogen might have been affected by the solvent, we did not calculate the post-extraction porosity value. In the remaining samples, the calculated sorption porosity occluded by the extractable bitumen oscillates between 0.8-1.1%, constituting 25-35% of the oil-free sorption porosity in the peak oil window samples and 17% in the gas window sample. In total, while only 31-33 vol.% of the extractable oil in the peak oil window shale is contained in sorption pores, in the gas window sorption pores hold all the residual extractable bitumen (Table 3.5 and Figure 3.8a).

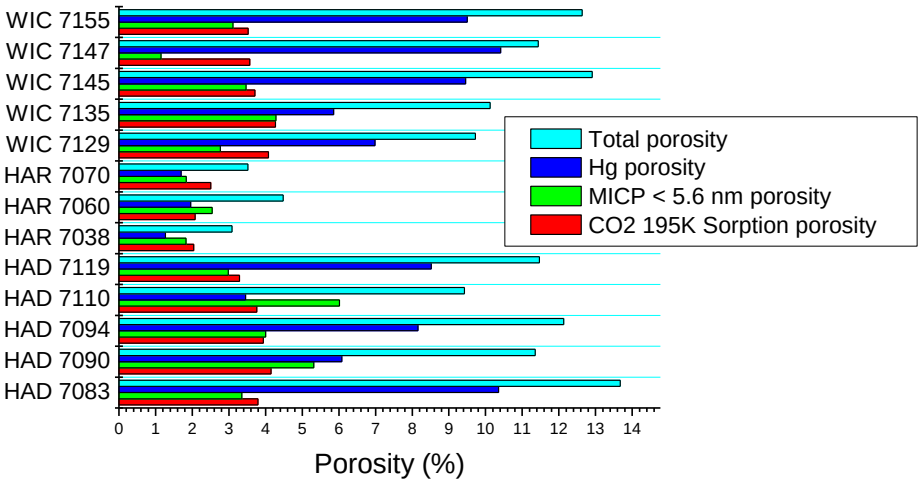

Figure 3. 10. *Comparison of total porosity, Hg porosity, part of total porosity not accessible to mercury (< 5.6 nm) as estimated from the Mercury Injection Capillary Pressure analysis (MICP) and CO_2 195K sorption porosity, for selected samples of three different maturities: 0.53% (WIC), 0.89% (HAR) and 1.45% (HAD). The sum of CO_2 195K sorption and Hg porosities approximate total porosities.*

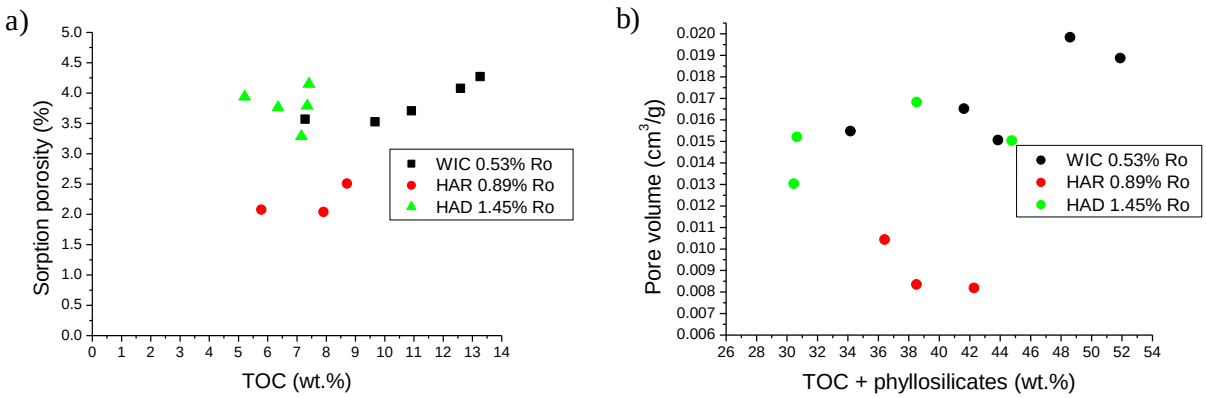

Figure 3. 11. *a) A lack of relationship between TOC and sorption porosity in the Posidonia* WIC 7129 0.53% R_o, HAR 7060 0.89% R_o and HAD 7110 1.45% R_o *shale. b) Positive correlation between sorption pore volume and the content of organic carbon and phyllosilicates in the WIC and HAD shales.*

Meso and macroporosity in FIB- and BIB-SEM images

Mineralogical composition from SEM images. Estimation of the Representative Elementary Area

Acquisition of the elemental composition via EDX mapping provides an important geological background for XRD analyses and enables to cross-check the petrophysical data. Therefore, three samples of different maturity (WIC 7129, HAR 7060, HAD 7110) were selected for both EDX mineralogical assessment and BIB-SEM porosity measurements. Although the samples exhibit a similar clay/phyllosilicate ratio (0.8-0.9) and thus the differences in their mineralogical may be neglected, their texture varies. For the samples selected for the analysis, the higher maturity shales show stronger recrystallization of biogenic calcite and more pronounced presence of large nannofossil-rich aggregates.

To determine the Representative Elementary Area that could yield representative porosity values and distribution of pores in the shale matrix, for each sample, a mix of EDX maps was used (Figure 3.12). The estimation of the REA did not include organic matter grains which remained largely unresolved in the EDX maps. The box counting was performed twice for each sample, starting from a point chosen at random, and proceeded until a relative change in the content of a particular phase did not exceed 10% (VandenBygaart and Protz, 1999). During the analysis it was found that the scale of a change in the content of the mineral phases depends on a thickness of the alternating nannofossil aggregates and clays microlaminae. In the three samples, the calculated change in the content of the three mineral groups taken into account, phyllosilicates, quartz and feldspar, and carbonates, decreased to 10% or below for areas covering 5985 μm^2 or more (Table 3.7 and Figure 3.13). Much larger areas were required to reduce the relative change in the mineral content below 5% - 39577 μm^2 for WIC, 23941 μm^2 for HAR and 35302 μm^2 for HAD. Only for pyrite, relatively scarce and scattered (Figure 3.12), did the change remain significant (> 10% change) for areas smaller than 31271 μm^2 in the HAD sample and 12215 μm^2 in the WIC and HAR samples. For the purpose of this paper, 5985 μm^2 area was established as representative.

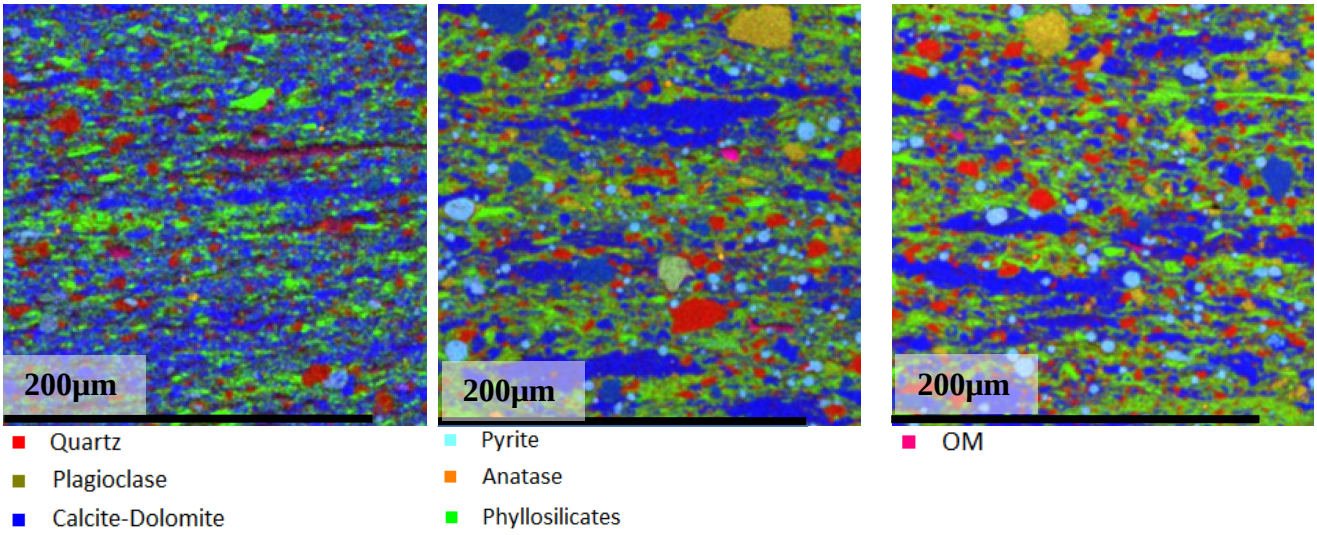

Figure 3. 12. *A mix of X-ray maps (RGB colour mode) displaying distribution of various shale components. The bedding plane in all images is horizontal. a) WIC 7129 0.53 Ro, b) HAR 7060 0.89% Ro, c) HAD 7110 1.45$ Ro. At all maturities samples exhibit visible fabric anisotropy with well-defined microlamination marked by the alternation of calcite- (blue) and clay (green) lamina , and in the lower maturity samples, organic matter wisps (pink).*

Table 3. 7. *Minimum areas for which a relative change in the mineralogical composition does not exceed 5% and 10%. Samples investigated include WIC 7129 0.53% Ro, HAR 7060 0.89% Ro and HAD 7110 1.45% Ro.*

Sample	Area µm^2							
	Variance <10 %				Variance < 5 %			
	Phyllo-silicates	Carbonates	Qtz+Fds	Pyrite	Phyllo-silicates	Carbonates	Qtz+Fds	Pyrite
WIC 7129	1954	4397	5985	12215	14780	9894	39577	53869
HAR 7060	5985	3054	3054	12215	7818	20644	23941	31271
HAD 7110	5985	5985	5985	31271	7818	12215	35302	53869

Table 3. 8. *Comparison of EDX Representative Elementary Area phase composition and bulk mineralogical composition retrieved from XRD. XRD mineral contents were converted to vol.% of rock using standard grain densities of composite minerals. Numbers in brackets show standard deviation for EDX mineral content estimation.*

Phase	Phyllo-silicates (vol.%)		Qtz+Fsp (vol.%)		Carbo-nates (vol.%)		Pyrite (vol.%)	
Method	EDX	XRD	EDX	XRD	EDX	XRD	EDX	XRD
WIC 7129	24 (+/-4)	26.0	6 (+/- 3)	10.9	30 (+/- 6)	24.8	3 (+/- 1)	2.0
HAR 7060	35 (+/- 3)	31.5	10 (+/- 4)	14.3	32 (+/- 9)	31.6	4 (+/- 2)	4.2
HAD 7110	37 (+/- 7)	31.5	11 (+/- 3)	16.1	30 (+/- 10)	28.0	4 (+/- 1)	3.1

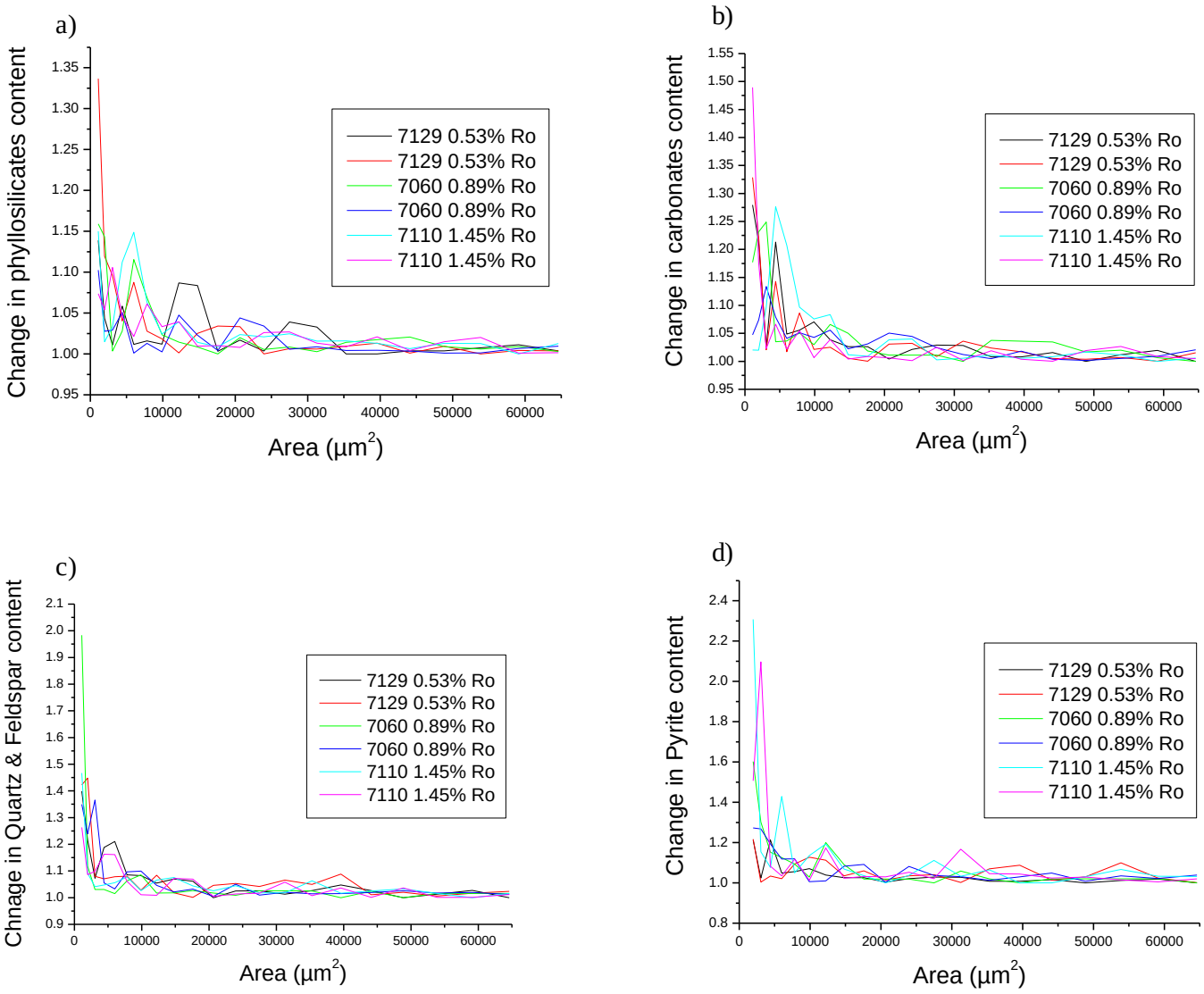

Figure 3. 13. *Change of the mineralogical composition within areas of progressively increasing size as retrieved from EDX maps of three selected shale samples. Measurements reflect % change of a parameter between two successive areas. Phases investigated include phyllosilicates (a), carbonates (b), quartz and feldspar (c) and pyrite (d).*

Because of the laminated character of the Posidonia Shale on a sub-centimetre scale, with a single lamina reaching a few mm, an average EDX composition of the graphically determined Representative Elementary Area is similar but not thoroughly consistent with the volume converted XRD values using standard mineral grain densities. As seen in Table 3.8, the estimated composition shows scatter when calculated for several different areas of the same sample. In general, in the Wickensen shale, where the sub-centimetric lamination is well preserved, light laminae show higher concentration of calcite (34 vol.% ±2) and lower content of clays (22 vol.% ±4), while the dark laminae show more constant proportion of both (24 ±3 and 27 ±2 vol.% respectively). In the two higher maturity samples, despite that

the lamination no longer can be distinguished, higher carbonate values are associated with laminae enriched in fecal pellets. Because the sub-centimetre scale lamination was not captured during standard EDX mapping and probability of introducing errors related to the acquisition and processing stage is high, this technique cannot be considered as a valid quantitative mineral analysis. First, a substantial error may be introduced when quantifying porous phases, not only due to the presence of unresolved micropores (clays, faecal pellets), but also due to a signal sent from pore walls (faecal pellets). Moreover, post-acquisition phase thresholding and extraction may distort the results if the limited image resolution prevents from setting correct threshold values. Finally, limited resolution of EDX maps may introduce additional inaccuracies in calculations of fine phases below or close to the resolution of EDX maps. The largest discrepancy between our EDX and XRD results lies in the Quartz (Qtz) and Feldspar content. Consistently, lower quartz content in the acquired EDX maps may be ascribed both to the low-scale sample heterogeneity (presence of large silt-size quartz grains not sufficiently represented in SEM images), limited resolution of the EDX maps for detecting small authigenic and detrital quartz grains as well as phase extraction errors.

BIB-SEM porosity. Pore size distribution of meso- and macropores

Pore types were point counted on representative elementary areas with a pixel size 15 nm. For the low maturity shale, the quantification was proceeded on a light lamina (Figure 3.12a). All pores resolved by images were classified based on their spatial relation with respect to the mineral phases and organic matter using classification of Loucks *et al.* (2012). For the purpose of this study we adapted the following definitions of pore types:

- Interparticle – 1) pores between detrital grains, authigenic minerals, nannofossils and clay flakes; 2) pores (in 2 or 3D space) associated with the interface of organic matter and mineral matrix that visibly do not extend into an organic particle;
- Intraparticle – 1) pores within single mineral grains or fossil bodies; 2) pores within well-defined faecal pellets and pyrite framboids; 3) moldic pores formed due to dissolution of mineral phases; 4) pores at the interface of the inorganic matrix and organic macerals that do not visibly extend into an organic particle, contained within a fossil body, faecal pellet or pyrite framboid;
- Organic – 1) discrete, round, bubble-like pores in the organic matter; 2) sponge-like pores within the organic matter, often interconnected and grouped; 3) irregularly

shaped pores, often from the interface of the organic matter and mineral matrix, visibly extending in 3D into the organic mass; 4) visible cracks within OM particles, often with jagged edges and extending into the particle edge.

Table 3. 9. Binarized BIB/SEM image porosities and point-counted relative contribution of different pore types of selected Posidonia shales samples: WIC 7129 (0.53% Ro) HAR 7060 (0.89% Ro) and HAD 7110 (1.45% Ro) samples. The minimum fully resolved pore size is 100 nm, except for the intraorganic pores of the HAD sample - 50 nm.

Sample	Area (μm^2)	BIB image porosity (%)	BIB image porosity as fraction of total porosity	Extrapolated intraorganic porosity (>6 nm) (%)	Intraorganic porosity as fraction of total porosity	% of inter-, intraparticle and organic pores
WIC 7129	96x70	0.7	0.07	-	-	47-53-0
HAR 7060	96x70	0.6	0.13	-	-	44-43-13
HAD 7110	96x70	1.1	0.12	-	-	36-40-24
HAD 7110 Intraorganic	153x96	0.2	0.02	1.7-3.1	0.18-0.33	-

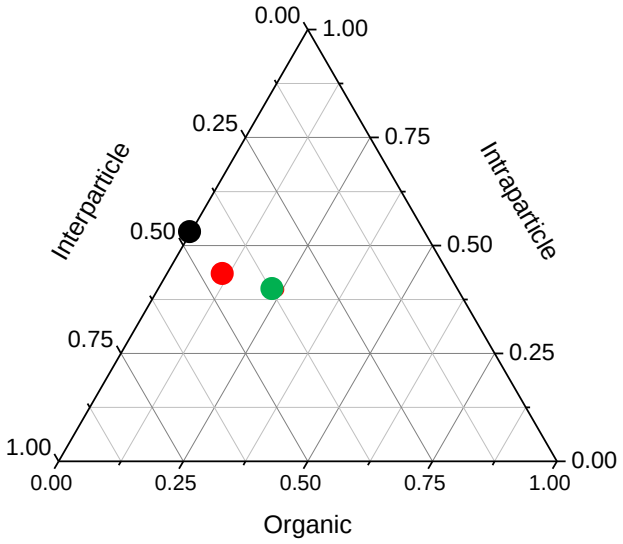

Figure 3. 14. *Ternary diagram showing contribution to porosity of three pore types as resolved in BIB-SEM micrographs (pixel size 15 nm) in three Posidonia shale samples: WIC 7129 (0.53%)(black circle), HAR 7060 (0.89%) (red circle) and HAD 7110 (1.45%) (green circle).*

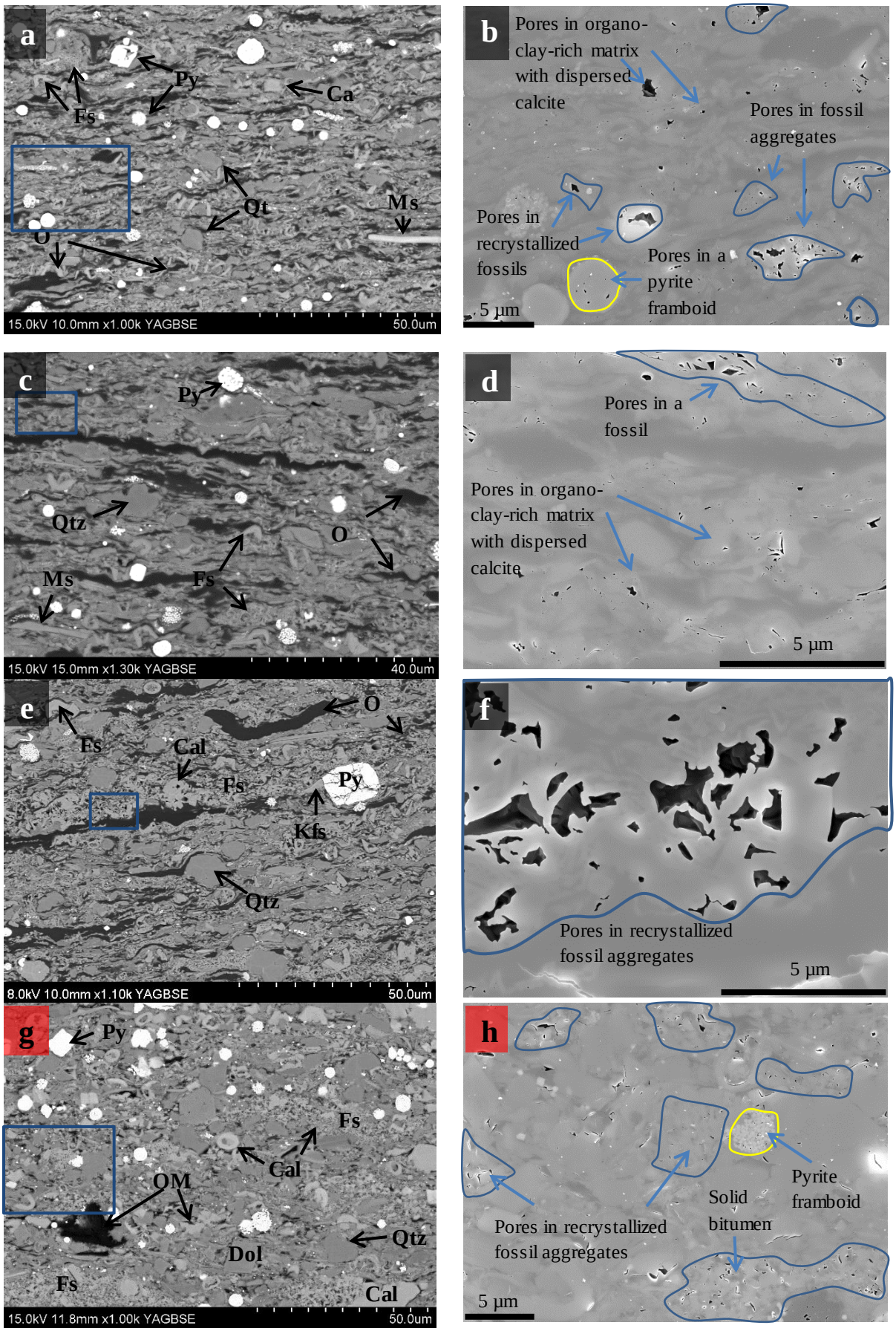
a
Py
Fs
Ca
Qt
Ms
O
15.0kV 10.0mm x1.00k YAGBSE
50.0um
b
Pores in organo-clay-rich matrix with dispersed calcite
Pores in fossil aggregates
Pores in recrystallized fossils
Pores in a pyrite framboid
5 µm
c
Py
Qtz
O
Ms
Fs
15.0kV 15.0mm x1.30k YAGBSE
40.0um
d
Pores in a fossil
Pores in organo-clay-rich matrix with dispersed calcite
5 µm
e
O
Fs
Cal
Fs
Py
Kfs
Qtz
8.0kV 10.0mm x1.10k YAGBSE
50.0um
f
Pores in recrystallized fossil aggregates
5 µm
g
Py
Fs
Cal
OM
Qtz
Dol
Fs
Cal
15.0kV 11.8mm x1.00k YAGBSE
50.0um
h
Pyrite framboid
Solid bitumen
Pores in recrystallized fossil aggregates
5 µm

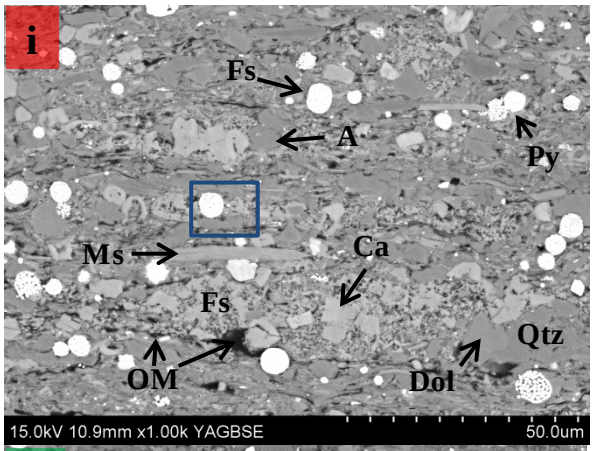
i
Fs
A
Py
Ms
Ca
Fs
Qtz
OM
Dol
15.0kV 10.9mm x1.00k YAGBSE
50.0um

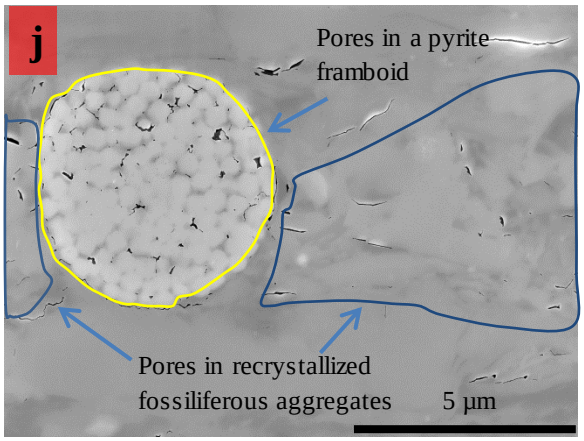
j
Pores in a pyrite framboid
Pores in recrystallized fossiliferous aggregates
5 µm

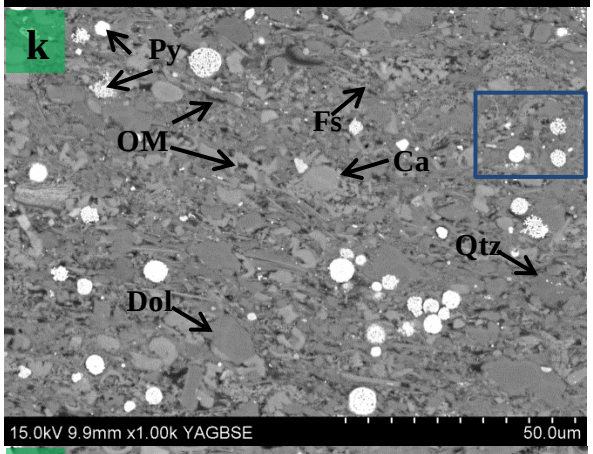
k
Py
OM
Fs
Ca
Qtz
Dol
15.0kV 9.9mm x1.00k YAGBSE
50.0um

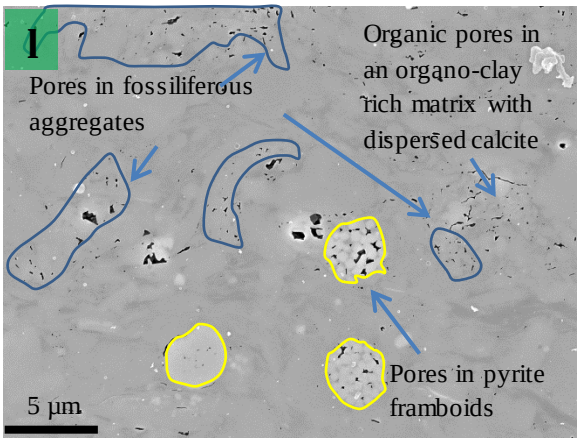
l
Pores in fossiliferous aggregates
Organic pores in an organo-clay rich matrix with dispersed calcite
Pores in pyrite framboids
5 µm

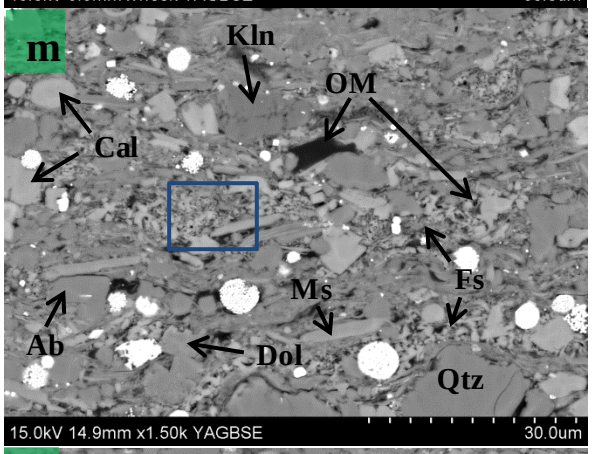
m
Kln
OM
Cal
Fs
Ms
Ab
Dol
Qtz
15.0kV 14.9mm x1.50k YAGBSE
30.0um

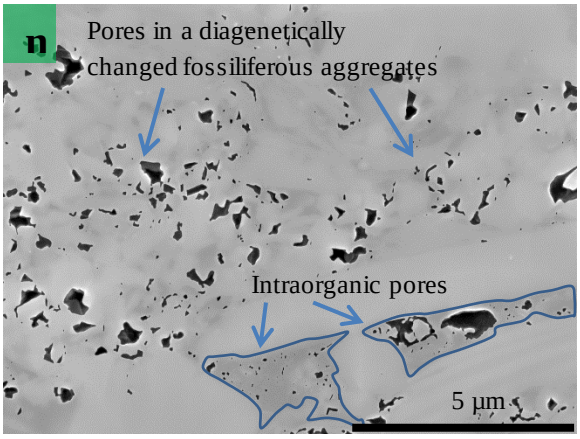
n
Pores in a diagenetically changed fossiliferous aggregates
Intraorganic pores
5 µm

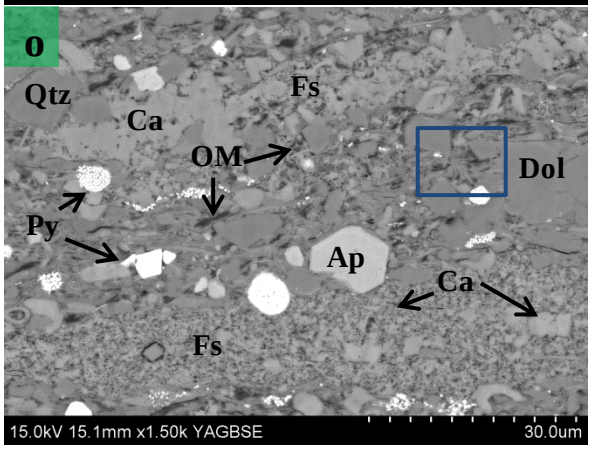
o
Qtz
Fs
Ca
OM
Dol
Py
Ap
Ca
Fs
15.0kV 15.1mm x1.50k YAGBSE
30.0um

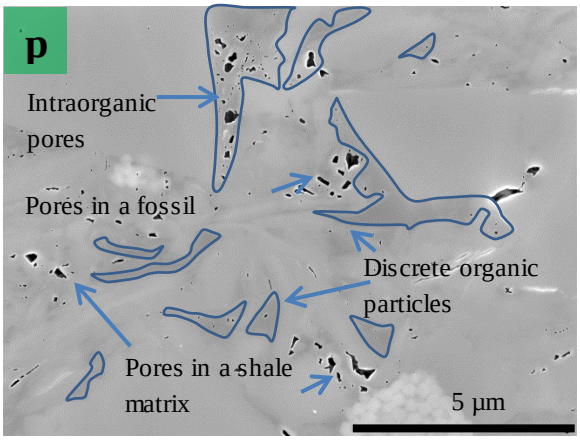
p
Intraorganic pores
Pores in a fossil
Discrete organic particles
Pores in a shale matrix
5 µm

Figure 3. 15. *Backscattered electron micrographs (L) of shale samples polished with the Argon BIB. Secondary electron micrographs (R) show details of porosity distribution within areas outlined with a blue rectangle in BSE micrographs. The bedding plane in all images is horizontal. a)(WIC 7129): Calcareous shale (light lamina) with disseminated faecal pellets alternating with clay material, silt-size quartz, pyrite framboids and sparsely disseminated calcite. b) Pores are found within fossil aggregates, locally within pyrite framboids and in the organoclay-rich matrix with dispersed fossils. c) (WIC 7129): Calcareous shale (dark lamina) enriched in the clay material admixed with organic matter, with disseminated silt-size quartz, pyrite framboids and calcite fossils. d) Pores are dispersed in an organoclay matrix with dispersed calcite grains and accumulated in fossil bodies. e) (WIC 7129): Calcareous shale (light lamina) with recrystallized fossiliferous aggregates alternating with organic and clay laminae. f) Pores in diagenetically changed fossil aggregates can reach 3 µm in diameter. Note lack of organic material lining the pores. g) (HAR 7060): Calcareous shale with densely packed nannofossil aggregates. Partial recrystallization of the nannofossil rich shale matrix and presence of calcite and dolomite cement all indicate diagenetic transformation of the original material. h) Pores in recrystallized fossil aggregates occur at the interface with organic matter filling the intragranular space. i) (HAR 7060): Calcareous shale with alternating calcite-and clay laminae. Fossiliferous aggregates are to a large extent recrystallized and locally cemented. j) Pores are encountered within fossiliferous aggregates as well as within pyrite framboids. k) (HAD 7110): Calcareous shale with recrystallized fossils and authigenic carbonate phases replacing the original fabric. l) The porosity is encountered between pyrite crystallites in pyrite framboids, within well-defined diagenetically changed fossiliferous aggregates as well as within shale matrix. m) (HAD7110): Calcareous shale with a strong diagenetic overprint. n) Typically porous zones include fossiliferous aggregates and organic particles. o) (HAD 7110): Common features of a diagenetic overprint in the Posidonia shale. Biogenic calcite in faecal pellets (top and bottom) is much recrystallized, and locally cemented. New dolomite phases are replacing the original fabric. p) Organic matter (outlined) spans from non-porous to highly porous.*

Pore network types change throughout the maturity sequence from exclusively inter- and intraparticle in the low maturity sample (47 and 53% of the inter- and intraparticle pores respectively), to inter- and intraparticle dominated in the peak oil window (44 and 43% respectively), and finally to inter- and intraparticle-rich with moderate proportion of organic pores in the sample of the gas window maturity (36, 40 and 24% respectively) (Table 3.9 and Figure 3.14). In the least mature sample inorganic porosity is associated mainly with the aggregates of biogenic calcite (Figure 3.15a-f), significantly recrystallized in the carbonate rich laminae and in the lower marlstone (Figure 3.15a, b, e, f). Moreover, pores are found at the interface of mineral phases and the organic matter, within pyrite framboids (Figure 3.15b), and are occasionally lined with organic matter. Moving towards peak oil window maturity, slit-shaped pores from the interface of the organic matter and mineral matrix, mainly found within calcite domains, predominate (Figure 3.15g, h), with rare porosity within pyrite framboids (Figure 3.15i, j) and very rare within organic matter in the form of cracks and fractures. In the gas window sample, intraorganic pores appear in the form of discrete, spongy and irregular pores (Figure 3.15m-p), and interface pores gain in significance. Most of the visible pores are found within inorganic domains, with calcite and pyrite as locations of their highest density (Figure 3.15k-n).

Image extraction and binarization of the visible pores provided information about porosity, pore shapes, pore sizes, and pore size distributions. To compare between mosaics covering a representative area (Figure 3.15a, g, k), and acquired at the magnification 6,000x with a pixel resolution 15 nm, we took into account only fully resolved pores. Their minimum size was estimated after grouping all pore areas into bins of an increasing size and plotting them as a function of pore numbers (Houben *et al.*, 2013; Klaver *et al.*, 2012). At all maturities, fractal distribution of fully resolved pores was approximated by one linear regression line, with a slope varying between -2.38 in WIC, -2.42 in HAD to -2.55 in HAR (Figure 3.16, Figure 3.17a). As pores smaller than 100 nm could not be linearly fitted, this diameter may be interpreted as the minimum pore diameter fully resolved in our REA images (Figure 3.16).

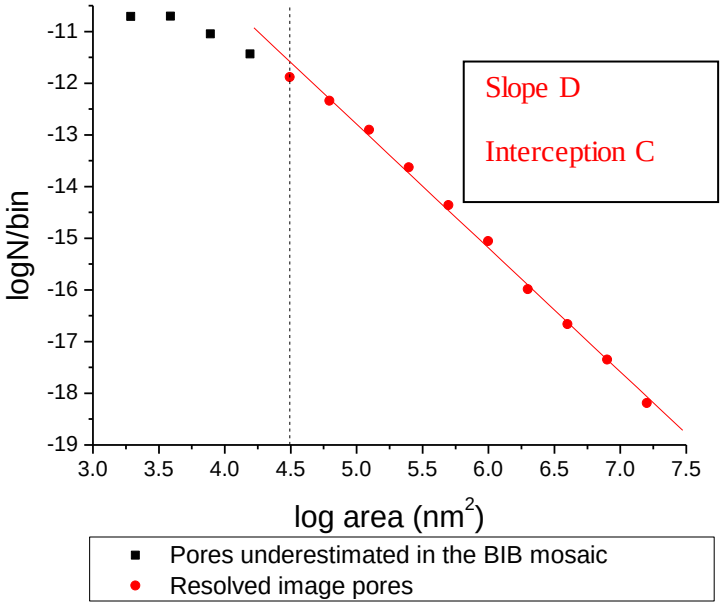

Figure 3. 16. *Typical distribution of pores from BIB-SEM mosaics of the Posidonia shale samples. An area of investigation covers the size of an estimated Representative Elementary Area (96x70 µm^2). Fully resolved pores (red circles) are fitted with a linear regression line defined by a slope (D) and a point of interception with the y axis (C). Pores not fully resolved in mosaics (black squares) deviate from the linear regression line estimated for the fully resolved pores.*

The resolved image porosity does not show significant difference between samples of different maturity, amounting to 0.7% in a light lamina of the Wickensen shale, and 0.6% and 1.1% in Harderode and Haddessen samples respectively (Table 3.9). Although the equivalent median diameter of resolved pores does not vary substantially, reaching 160 nm in WIC and HAD and 150 nm in HAR (Figure 3.18a), pores are twice as elongated in the last (Table 3.10, Figure 3.18b). In each shale a differential distribution of pore sizes shows a single maximum located between 280-400 nm in WIC and HAD and 200-280 nm in HAR (Figure 3.17b). To verify what factors determine the position of this maximum, pores from 4 additional mosaics (Figure 15c, i, m, o) with an area < REA and estimated practical image resolution 50 nm (mag. 10,000 x), were binarized and their differential size distribution was plotted as a function of pores area. From the Figure 3.17c it stems that for the Wickensen sample, a dark lamina characterizes with larger contribution of porosity held by pores < 300 nm and thus their distribution is skewed towards smaller pores. In contrast, in a more recrystallized light lamina, the absolute amount of porosity held by finer pores is smaller, and thus the distribution is skewed towards larger pores. In the peak oil and gas window, the impact of an original texture is obliterated and there is little shift of the maximum pore density between different sample areas.

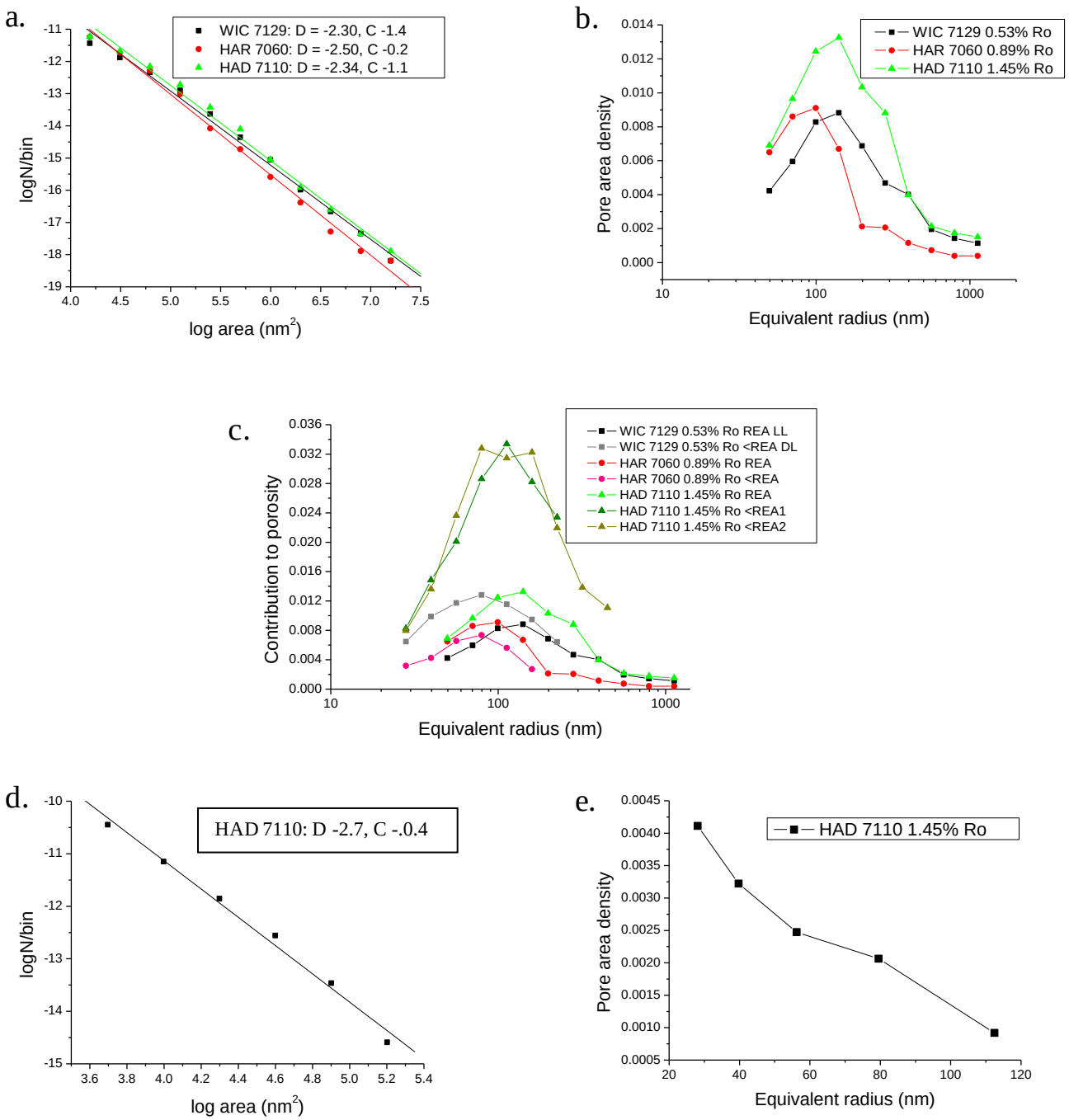

Figure 3. 17. *Distribution of pore sizes of BIB-SEM image pores for three samples WIC 7129 0.53% Ro, HAR 7060 0.89% Ro and HAD 7110 1.45% Ro. a) Fractal distribution of pores > 100 nm with the line of the best linear fit described by a slope (D) and intercept with the y axis (C). The BIB-SEM images were captured at the magnification 6,000x and cover an estimated REA. Note that porosity > 100 nm approximates inorganic hosted porosity in all samples. b) Differential pore size distribution as a function of an equivalent radius. Note descending pore area density of pores < 400 nm diameter. c) Differential pore size distribution as a function of an equivalent radius. The BIB-SEM images were captured at the magnification 10,000x (< REA, >50 nm) or 6,000x (REA, >100 nm) (LL – light lamina, DL – dark lamina).* d) *Fractal distribution of image intraorganic pores (> 50 nm) for the HAD 7110 1.45% Ro shale. The BIB-SEM images were captured at the magnification 10,000x covering the estimated REA. e) Differential size distribution of intraorganic pores as a function of an equivalent radius. Note ascending pore area density of all resolved pores (> 50 nm).*

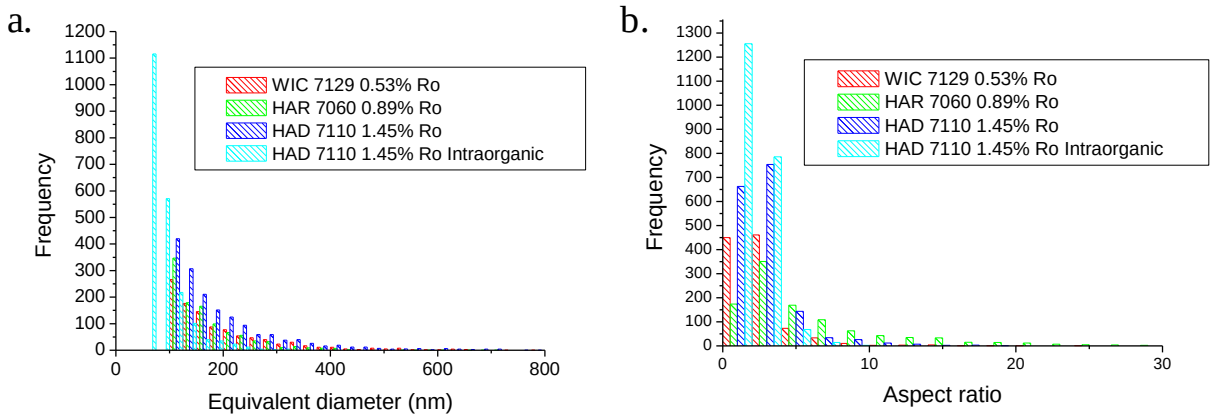

Figure 3. 18. *Distribution of a) equivalent diameters and b) aspect ratios of BIB-SEM image pores for three samples WIC 7129 0.53% Ro, HAR 7060 0.89% Ro and HAD 7110 1.45% Ro. The histograms represent pores with a diameter above the practical image resolution. The magnification of a single image is 6,000x for histograms representing all pores, and 10,000x for a histogram representing intraorganic pores only. Frequency denotes number of pores with the characteristic measured within a specific bin.*

Table 3. 10. *Median equivalent diameter and aspect ratio of pores resolved fully resolved in BIB-SEM images for WIC 7129 (0.53% Ro) HAR 7060 (0.89% Ro) and 7110 HAD (1.45% Ro). The minimum fully resolved pore size is 100 nm, except for intraorganic pores of the HAD sample -50 nm.*

Sample	Median equivalent diameter (nm)	Median aspect ratio
WIC 7129	161	2.2
HAR 7060	148	4.0
HAD 7110	161	2.3
HAD organic	73	1.8

At magnification 6,000x, the majority of resolved image porosity lies within inorganic domains and thus a size distribution of visible pores approximates size distribution of inorganic pores. Such approximation does not include potential clay pores, as those remained unresolved in mosaics at all times. Similarly, little is known about intraorganic pores, which due to their small sizes (< 200 nm) account for merely17% of the image porosity (> 50 nm) in the overmature shale (Table 3.9). To gather information about size distribution of pores contained within organic particles, separate distribution curves were constructed with all the inorganic porosity excluded. The resolved organic pores show fractal distribution, with a slope of the line of the best linear fit approaching 2.7 (Figure 3.17d). In contrast to the inorganic pores, differential pore size distribution of intraorganic pores shows no maximum, and pores of a decreasing size contribute progressively more porosity (Figure 3.17e).

Fully resolved image porosities contained in pores > 100 nm constitute only 7, 11 and 10% of the physically measured total porosity for the investigated WIC, HAR and HAD samples, respectively. Comparison of image and mercury injection derived cumulative and incremental porosity curves show that > 100 nm image pore bodies are 1-3 orders of magnitude larger than pore throats 'seen' by the mercury injection experiments, and thus that they are not directly connected (Figure 3.19a, b). Lack of such connectivity is consistent with a differential distribution of image resolved pores, showing decreasing contribution to porosity of pores below 200 nm (Figure 3.17b). Likewise, due to a limited resolution of the mosaics, we found no quantitative evidence for the connectivity between intraorganic pores or their direct connectivity with the inorganic pores. However, using the fractal relationship of the resolved intraorganic pores with a diameter > 50 nm, we assumed a similar fractal behavior of the unresolved intraorganic pores and extrapolated the log pore area-log N relationship towards finer pore sizes (Figure 3.19c). The limit of our extrapolation was set at the diameter 6 nm, corresponding to the maximum pore volume density in the mercury differential pore size distribution curve (Figure 3.6c). The results show that if the unresolved but extrapolated organic pores follow the same distribution as resolved pores, the intraorganic pores could contribute 1.7-3.1% porosity in the pore size range 6-300 nm, bringing overall 18%-33% to the total porosity in the overmature shale and yielding an average porosity of organic matter 24%. Moreover, because combined inorganic and extrapolated organic porosities approximate experimentally measured mercury porosity (Figure 3.19d), it stems that intraorganic pores could account for the increase in the mercury porosity below < 40 nm and provide connectivity within the overmature shale pore system.

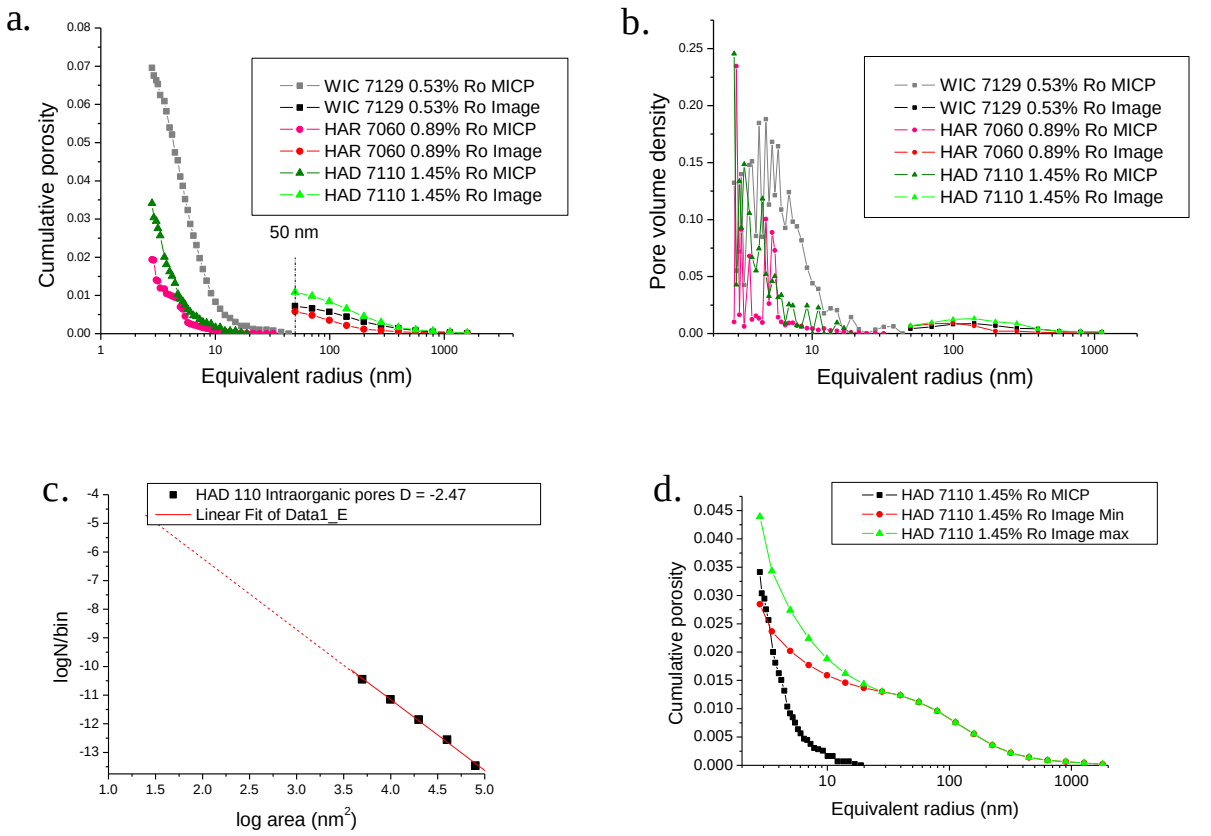

Figure 3. 19. *Comparison of cumulative porosity (a) and pore size distribution (b) obtained from mercury injection (> 5.6 nm diameter) and image analysis (> 100 nm diameter) covering the REA for three samples: WIC 7129 0.53% Ro, HAR 7060 0.89% Ro and HAD 7110 1.45% Ro. c) Extrapolation of a line of the best linear fit describing distribution of intraorganic pores to a diameter 6 nm. d) Comparison of cumulative porosity obtained from mercury injection (> 5.6 nm diameter) (black) and image analysis with inorganic (> 100 nm) and intraorganic (>6 nm) porosities superimposed. The red line denotes the minimum value of the extrapolated image porosity, while the green line – the maximum value.*

Distribution of image porosity in various shale domains

Low maturity Posidonia shale exhibits fine-scale lamination of clay-rich packages, alternating with calcite-rich laminae of biogenic origin, differentiated by varied proportion of both components (Figure 3.12). As clay packages are not visibly internally porous at any maturity (Figure 3.15), we encountered no correlation whatsoever between EDX derived phyllosilicates content and image porosity, regardless of maturity (Figure 3.20a). Likewise, no correlation was found for pyrite, despite porous nature of pyrite framboids in the highest maturity sample. In contrast, we found a moderate covariation between image macroporosity and EDX derived calcite content. To look into this calcite-image porosity relationship in detail, we differentiated between porosity values as captured in the clay-enriched dark (Figure 3.15 c, d) and calcite-enriched light laminae (Figure 3.15e, f) in the low maturity

shale. Despite the compositional variation, a relationship between visible porosity and calcite content in both sample sets is not significantly different and shows the same range of values (0.3-2.4%) with a positive sign of the covariation (Figure 3.20b). Only those regions that show advanced redistribution of the calcite phase, found exclusively within the light lamina, do show relative increase in porosity (up to 10%) at any given calcite content and deviate from the range of values characteristic for areas with more dispersed calcite grains.

For the peak oil window maturity shale (Figure 3.15i, j), we could not differentiate between light and dark laminae, and therefore the micrographs were classified into two groups depending on the content of faecal pellets. The first group includes areas dominated by calcite aggregates of the biogenic origin, with a strong diagenetic overprint, either recrystallization or partial cementation, named here as faecal pellet rich domains. The second group consists of areas rich in clays, quartz, pyrite framboids, or only discrete carbonate crystals, named as matrix rich domains. The results show that, unlike in its lower maturity counterpart, in the peak oil window maturity shale there is no relation between calcite content and image porosity, even when most porous and strongly recrystallized faecal pellet rich domains are excluded (Figure 3.20c). Overall, despite the large variation in calcite content (7-74%), the image porosity values oscillate only within a very small range (0.0-1.5%), showing no relation to change in the mineralogical composition.

The greatest variation of macroporosity values in relation to calcite content was found in the most mature shale. Similarly to the peak oil window maturity shale, the micrographs and the associated porosity were divided into faecal pallet and matrix-rich domains. We found that faecal pellet domains are characterized by higher calcite content (> ~30%) and exhibit higher porosities than the shale matrix domains (Figure 3.20d). Faecal pellet rich domains also show the highest spread in the porosity values encountered in samples of all maturities, with the variability between 3-7%. In general, image gas window porosities are by one order of magnitude higher than porosities found in any domain in the oil window and match porosities encountered in the light lamina of the immature shale.

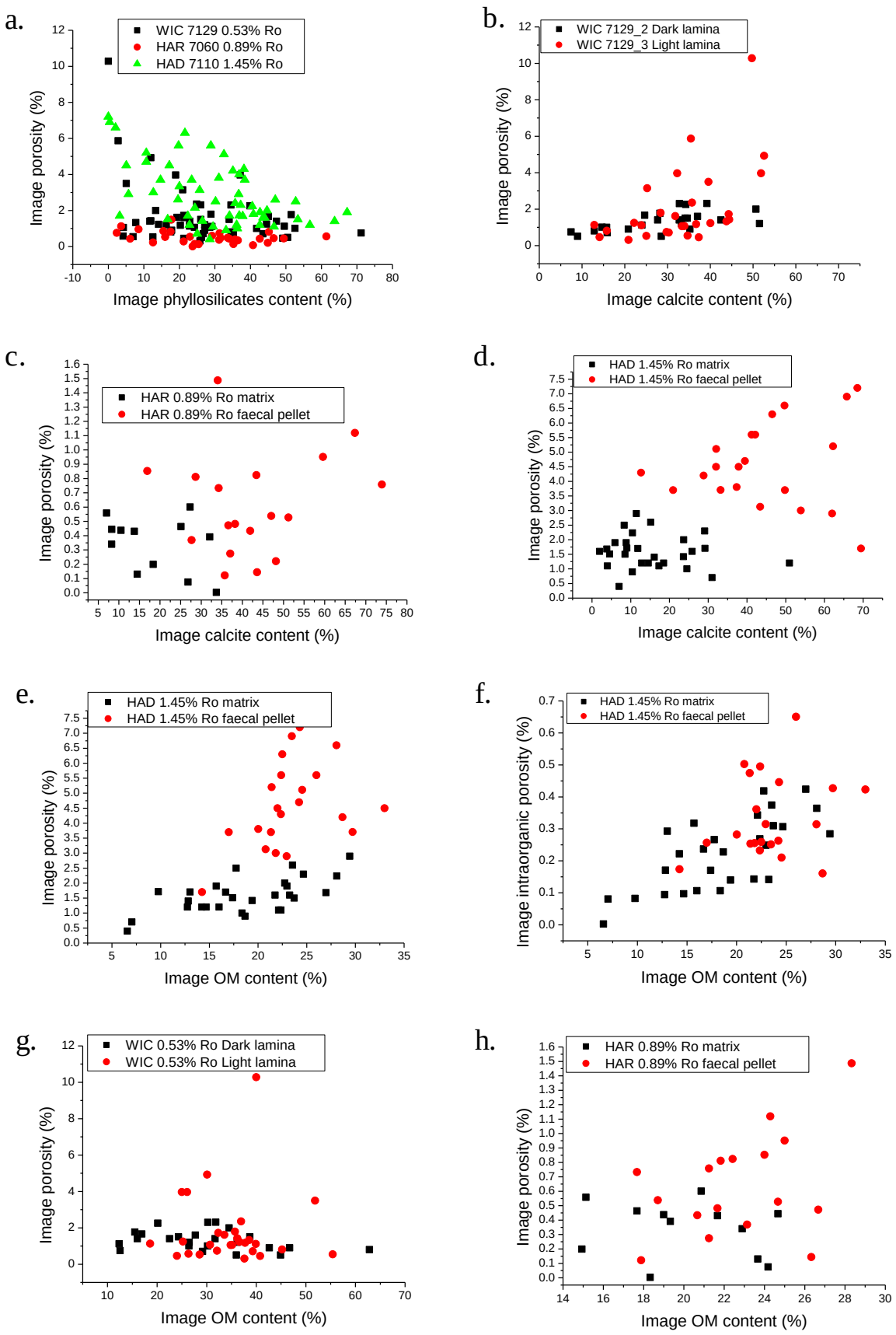

Figure 3. 20. *Relationship of image porosity with EDX maps derived clay and calcite content, and point-counted OM content. Each data point represents one BIB-SEM image captured at magnification 10,000 x and a pixel size 15 nm.*

Similarly to the calcite-porosity relationships, we found varied relation between point counted organic content and image porosity for shales of different maturities. In both the early oil window and peak oil window shale, there is no observable trend beween the two variables (Figure 3.20 g, h). In contrast, in the gas window shale, an analysis of the image porosity with distinction to microfacies showed that despite the fact that the matrix-rich domains are on average less enriched in the organic material (7-30%) in comparison to the faecal pellet domains (20-30%), they show stronger dependence of image porosity on OM content (Figure 3.20e). When accounting for the resolved intraorganic porosity only, its values are quite similar in both matrix and faecal pellet rich domains for a given organic matter content, showing relatively small spread (0.0-0.7%), and slightly higher covariance in the former (Figure 3.20f).

After combining the area occupied by the point counted OM and image porosity for each image (Figure 3.21), we found a similar covariation between this area (10-40%) and the calcite content for the peak oil and gas window shale. In contrast, in the low maturity shale, and at the equivalent calcite content, the values are higher (up to 65%), and show a larger spread.

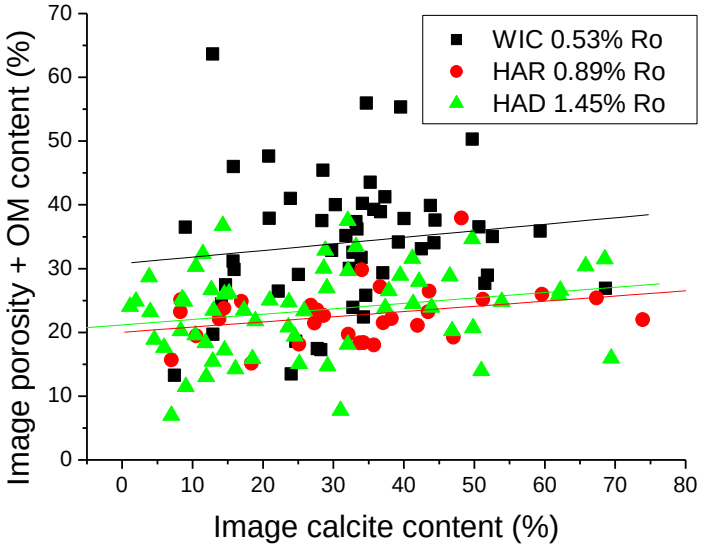

Figure 3. 21. *Combined image porosity and point-counted OM content and its relationship to EDX derived calcite content. Each data point represents one BIB-SEM image captured at magnification 10,000 x (corresponding pixel size 15 nm).*

Discussion

Pattern of porosity change upon burial and diagenesis

Posidonia Shale shows a non-linear pattern of porosity change with maturity observed in pores of all sizes (Figure 3.10, Figure 3.22a). Based on the amount of porosity held by pores grouped according to their size, we observed that the absolute change in total porosity is controlled predominantly by pores between 6-100 nm. Pores in this range exhibit the most radical change in the absolute volume of porosity they hold, with the initial drop by over 3 vol.% of the bulk rock, followed by an almost 2 vol.% increase (Table 3.11, Figure 3.22b). A considerable change in porosity is also observed for pores < 6 nm, and only a small absolute change is observed for pores 100 nm. Such pattern of porosity loss and gain is typical for shales passing through the oil and gas window, respectively, and was reported from other shale formations (e.g. Mastalerz *et al.*, 2013). The non-uniform variation of porosity within different groups of pores is related to the micro-, and millimeter scale heterogeneity of the rock-building components (Table 3.1, Figure 1, Figure 3.12, Figure 3.15), reflected by the varied amount of biogenic calcite, detrital clays and organic matter. A direct result of this heterogeneity is the presence of a network of pores with a different association for the carbonate, clay and organic domains and varied sensitivity for compaction or occlusion by the petroleum phase.

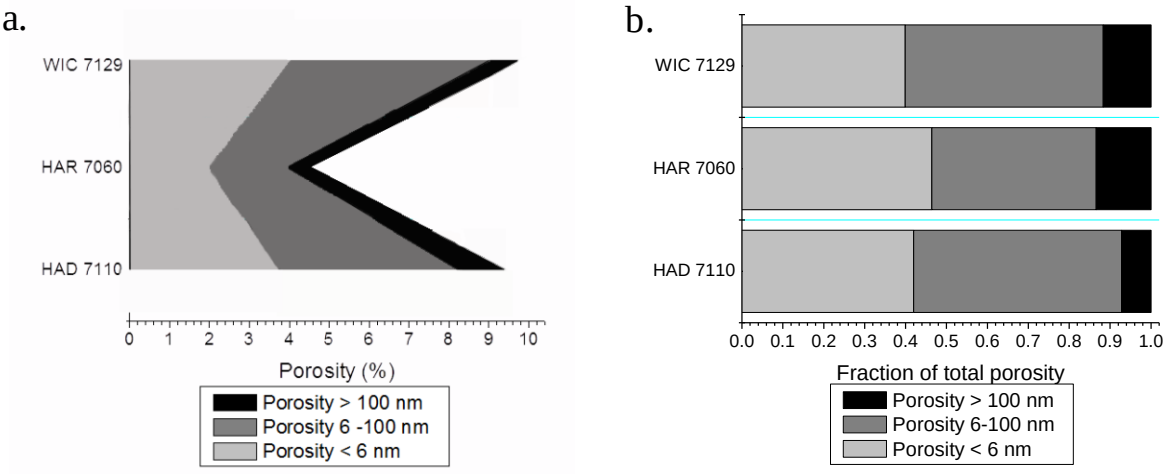

Figure 3. 22. a) *Cumulative porosity contained in pores grouped into three intervals < 6 nm, 6-100 nm, > 100 nm, estimated for three samples: WIC 7129 0.53% Ro, HAR 7060 0.89% Ro and HAD 7110 1.45% Ro. Within all three groups, the change of porosity is non-linear, bottoming out in the peak oil window shale. b) A change in the total porosity with increasing maturity is controlled to the large extent by the pores in the interval 6-100 nm.*

Table 3. 11. The summary of porosities contained in the three selected Posidonia Shale samples: WIC 7129 (0.53% Ro) HAR 7060 (0.89% Ro) and 7110 HAD (1.45% Ro). Pores with diameters < 6 nm were calculated from the gas sorption, pores > 100 nm were quantified from the SEM-BIB images, and pores between 6-100 nm represent a difference between total porosity and the sum of the gas sorption and SEM-BIB porosity.

Sample	Porosity in pores < 6 nm (%)	Porosity in pores 6-100 nm (%)	Porosity in pores >100nm (%)
WIC 7129	4.1	4.9	0.7
HAR 7060	2.1	1.8	0.6
HAD 7110	3.8	4.6	1.1

Micro- and mesoporosity of clays

With the limited resolution of SEM images, only ca. 10% of total porosity is resolved at the magnification 6,000x. As the resolved pores are > 100 nm in size, in our study clays are not visibly porous at any maturity, and therefore little is known about their porosity. While deploying sorption techniques we did detect pores < 6 nm, the analyses were performed on the bulk shale and provided no information about how much porosity is held by the clay phase itself. A strong covariation between the sorption pore volume and the combined content of organic carbon and phyllosilicates in the early oil and gas window shale (Figure 3.11b) suggests that both these phases contribute to the micropore volume. Indeed, detailed work by Rexer *et al.* (2014) showed that only half of the sorption pore volume is in kerogen, and thus inorganic matrix must also contribute to measured porosities. This also agrees with previous studies by Furmann *et al.* (2013), Mastalerz *et al.* (2013), Kuila and Prasad (2013), Chalmers and Bustin (2012) and Schmitt *et al.* (2013). In the early oil window and gas window Posidonia, shales with a higher abundance of clays were shown to have smaller pore throat threshold apertures and higher contribution of finer mesopores in comparison to their calcite richer counterparts. Interestingly, no difference in a distribution of mercury pores between the clay-rich and calcite-rich units was found in the oil-filled peak oil window shale (Figure 3.6). Despite our expectations that part of the mercury porosity should be hosted by clay pores (Chalmers *et al.*, 2012; Chalmers and Bustin, 2008; Ross and Bustin, 2009), the XRD analyses on the lowest and highest maturity Posidonia shale revealed negative correlation between total porosities and the phyllosilicates content (Figure 3.5b). These few results suggest that in the organic-rich and oil-wet calcareous shale, despite that oil coatings inhibit dissolution and reprecipitation of the carbonate cement, local recrystallization of calcite leads to strengthening of the matrix (Fabricius, 2003), arresting compaction, and preventing clays to hold a final control on porosity. Such interpretation could also be valid for

siliceous shales, and explain a lack of a positive correlation between total porosity and clay content as reported by Bustin *et al.* (2008).

Porosity and distribution of pores and pore sizes in the calcareous matrix

In contrast to clays, at all maturities, the calcareous matrix shows presence of visible pores in sizes between << ca. 50 nm – 5000 nm, with pores > 100 nm approximating porosity of pyrite framboids and of the biogenic, microcrystalline calcite. Our micrographs show that upon burial, biogenic calcite experienced intensive diagenetic redistribution, with much stronger intensity in the marlstone unit and relatively small extent of recrystallization in the clay-rich lamina of the calcareous shale. Limited degree of recrystallization in the clay-rich domains is consistent with previous observations from argillaceous chalks (Baker *et al.*, 1980), and points to a buffering effect of the matrix clays on intensity of carbonates remobilization. Similar observations were also made in Kimmeridge Clay mudstones by Macquaker *et al.* (2014). They observed that reactive clays are dissolved upon presence of organic acids generated due to sulfate reduction, methanogenesis, and thermochemical decay of organic matter during burial, and hence act as efficient acid buffers. In this study we found a moderate positive correlation between the image porosity and calcite content in the dark lamina of the least mature shale, and no correlation in the strongly recrystallized fossiliferous aggregates (Figure 3.20b). Moreover, a detailed study showed that in the low maturity shale, pores < 300 nm contribute more porosity in the clay-material enriched dark laminae in comparison to horizons packed with the biogenic fossiliferous aggregates (Figure 3.17c). Different distribution of calcite pores in the clay-rich and faecal pellet rich laminae indicates that diagenetic redistribution of calcite modified pores size distribution of the calcite pores present, led to a selective growth of larger pores at the expense of smaller, and resulted in the local increase in recorded image porosity values (Figure 3.15f, Figure 3.20b). In both early oil window and gas window shale, despite the observed recrystallization features, total porosity is positively related to calcite content and no diagenetic pore volume loss can be inferred. We suggest that, analogous to chalks, such positive relationship is enhanced by the development of contact cement between calcite crystals, arresting compaction of the not-resolved matrix pores (Fabricius, 2003). Indeed, in the low maturity marlstone samples, we observed presence of pore throats that are even one order of magnitude higher than typical pore throats present in the calcareous shale (Figure 3.6a). Recrystallization of calcite without pore volume loss in Posidonia stands in contrast to pore-blocking effect of the calcite cement

often reducing porosities in shale reservoirs (Chalmers and Bustin, 2012). We attribute this lack of porosity loss to only limited calcite precipitation as encountered in muds that experienced stable low redox conditions in their pore waters, to the presence of clays alternating with the carbonate-rich matrix, and finally to the oil-coating of mineral grains.

High minus-bitumen porosities observed in SEM micrographs of the peak oil window shale indicate that, analogously to conventional carbonate and quartzose oil-filled reservoirs (Worden et al., 1998; Heasley et al., 2000; Scholle, 1977), diagenesis and cementation in Posidonia was retarded once bitumen filled inorganic pores. As showed by the identical distribution of pore throat sizes in the oil window marlstone and calcareous shale (Figure 3.6b), petroleum trapping controlled the maximum loss of pore throats, and limited the impact of both compaction and cementation. We suggest that total compaction was most effective in the most organic rich parts of the shale, and is reflected by a loss of the area occupied by image pores and organic phase between 0.53-0.89% Ro (Figure 3.21).

A regain in total, image and gas porosities in the gas window shows that organic occlusion is reversible and should be linked to processes of maturation of organic matter under increasing thermal stress. Moderate correlation between image porosity and calcite content implies that the major change in shale porosity takes places in pores < 50 nm. A large spread of porosities between the faecal pellets and the bulk shale matrix, with the former yielding values up to 7%, suggest that shale composition and texture control development and preservation of pores in the gas window.

Kerogen transformation, organic porosity loss and gain

Early oil window bitumen

Total porosity of Posidonia Shale bottoms out at oil window maturities, and shows no dependence on Total Organic Content (Figure 3.4, Figure 3.10). Considering consistent loss of organic carbon upon increasing thermal stress (Table 3.2, Table 3.6), this porosity - TOC relation cannot be fully explained without recognizing effects of kerogen transformation, here monitored by a significant drop in S1, S2, Hydrogen Index and the amount of soluble bitumen. A complex path of kerogen transformation was described by Behar *et al.*, (2008), and involved decomposition of kerogen into viscous liquid rich in NSO-compounds (nitrogen, oxygen ans sulphur), followed by decomposition of the last into more soluble non-hydrocarbon compounds and finally, cracking into hydrocarbons. Our experiments confirm the presence of a substantial amount of high density, non-volatile bitumen phase dominating

total extract of the low maturity Posidonia shale (Clementz, 1978; Wilhelms *et al.*, 1990). Presence of inorganic pores devoid of visible organic linings in the Wickensen sample and association of the majority of the extract with kerogen suggests that this early bitumen did not enter the mass migration stage and still occupies kerogen pores (Hwang *et al.*, 1998; Sandvik *et al.*, 1992).

Loss of porosity in the oil window

In the peak oil window shale, more than half of total porosity is lost (Figure 3.4), with solid bitumen blocking the inter- and intraparticle space (Figure 3.15g-j). Presence of the organic phase filling the pore space is responsible for the high slope of the line describing the fractal distribution of HAR pores, and a relatively small importance of pores > 400 nm (Figure 3.17a). Whilst we do not have information on the exact physiochemical nature of this pore filling solid organic residue, it is plausible that its precursor was a heavy, viscous polymer that developed more aromatic and condensed structure upon cracking into lighter hydrocarbons (Behar *et al.*, 1997; Curiale, 1986; Hill *et al.*, 2003; Horsfield *et al.*, 1992; Lewan 1997; Michelis *et al.*, 1996). Bitumen residing in the inter- and intraparticle spaces is non-extractable by organic solvents and therefore cannot account for a density increase of the bulk shale upon solvent washing (Table 2). This increase must be ascribed to a presence of lighter petroleum fraction, of which ca. 1/2-1/3 resides in pores as small as < 6 nm. High affinity for kerogen of the peak oil window oil, also recorded by Rexer *et al.* (2014), suggests that the residual oil must be absorbed onto organic matter, and therefore blocks its internal porosity (Sandvik *et al.*, 1992). Although the solvent soluble petroleum phase occupies ca. 50% of pore space of the peak oil window shale, we presume that its mobility in the finest pores was restricted. Limited motion and strong sorpion of oil in micropores is reflected by the presence of residual oil blocking < 6 nm pores in the gas window shale. High oil saturation of the organic matter in the oil window also implies that light oil might have been a driving force for petroleum migration, increasing mobility of the petroleum phase (Vanderbroucke *et al.*, 1993). Such hypothesis was also proposed by Lewan (1997) and was explained by the volume expansion following bitumen and oil generation.

Thermal conversion of kerogen and porosity gain

In the oil window Posidonia, not all porosity was lost due to oil and bitumen pore filling, and the SEM micrographs show presence of the interface pores between the organic phase and minerals. Although the appearance of the interface pores may have been induced by dessication, depressurization or post-coring phase alteration (Fishman *et al.*, 2012; Milliken *et al.*, 2013), it is not unreasonable to think of their origin as a product of in-situ interaction between diagenetically chaning carbonate phases and solidifying organic polymer. We have not found evidence for any visual post-coring alterations within analyzed Posidonia shale samples but we understand that the long storage of the Posidonia cores (> 20 years) may have depleted organic matter in the most volatile components and could have contributed to the loss of volume of the organic phase. On the other hand, the concept of porosity evolution in the oil window is supported by the reported loss of volume of the residual organic matter upon thermal conversion and expulsion of lighter hydrocarbons under oil generating conditions (Table 3.2, Figure 3.8) (Kanitpanyacharoen *et al.*, 2013). Because the organic-inorganic interface pores are primarily concentrated within rigid zones of the fossiliferous aggregates and pyrite framboids, such distribution emphasizes the role of the inorganic framework as controlling petroleum micromigration of the non-hydrocarbon polar and hydrocarbon fractions and its trapping away from the major expulsion conduits (Leythaeuser *et al.*, 1988; Pelet *et al.*, 1986). Such pore location also suggests that the presence of rigid zones is essential in order to arrest compaction and preserve organic porosity evolved due to conversion of kerogen and bitumen. Preferential location of porosity within rigid zones is especially visible in the gas window shale where 75% of image porosity (pores > 100 nm) is not directly in the OM but within faecal pellets and pyrite framboids. Because the combined area of the image pores and OM does not change between peak oil window and gas window shale (Figure 3.21), it stems that the porous fossiliferous zones act as microreservoirs for generated petroleum and are instrumental in contributing gas window porosity. Considering significant drop in the amount of the convertible organic carbon and residual oil content between 0.89-1.45% Ro, it is highly plausible that the evolution of the inorganic-hosted porosity is associated with the cracking of the residual bitumen saturated with oil.

Evolution of organic porosity in the gas window

In contrast to fossiliferous aggregates, due to shale framework compaction and bitumen escape, ductile clay-rich zones are less porous, wih the visible pores contained predominantly

within the organic matter. Although point-counted visibly porous organic matter grains are relatively rare (35%), they show fractal distribution and most likely host significant amount of porosity < 50 nm not resolved in images (Figure 3.19c, d). This is consistent with Rexer *et al.* (2014) who recorded increase in the sorption pore volume contained in the isolated kerogen from 69-87 mm^3/g at 0.9% Ro up to 104-113 mm^3/g at 1.4% Ro, and agrees with the increase of the bulk shale sorption porosity as recorded in this study (Table 4).

Although we do not know the composition of the organic particles hosting the intraorganic pores, Bernard *et al.* (2011) and Bernard *et al.* (2012), based on the synchrotron-based transmission spectromicroscopy, classified them as oil-spent pyrobitumen. The evolution of the intraorganic porosity is commonly linked to the secondary cracking of petroleum and the exsolution of thermogenic gas (Bernard *et al.*, 2012; Curtis *et al.*, 2010; Jarvie, 2007; Loucks *et al.*, 2009). Indeed, similarly to Curtis *et al.* (2012), Loucks *et al.* (2009), Milliken *et al.* (2013) and Milner *et al.* (2010), in this study the intraorganic pores appear only in the gas window sample. Lack of intraorganic pores at lower maturities also suggests that any gas generated was likely dissolved in the liquid phase (Pepper and Dodd, 1995; Schenk *et al.*, 1997; Tan et al., 2013; Waples, 2000). Co-existence of porous and non-porous organic areas in the gas window shale and different morphologies of the organic pores all point to the small-scale heterogeneity of the organic material in the shale matrix at the onset of cracking and emphasize that not all organic matter is prone for development of intraorganic porosity. Although the heterogeneity of the mature organic matter is typical for shales with type II kerogen (e.g. Curtis *et al.*, 2012; Milliken *et al.*, 2013; Milner *et al.*, 2010) its genesis is still not well understood. As various studies on coaking coal showed (Iglesias *et al.*, 2001, Kwiecinska *et al.*, 1992), the composition and density of the organic matter are crucial for development of gas vacuoles within the organic phase. For instance, high concentration of mobile phase (hydrogen) in coal favours mobility of the aromatic stacks (solvating fluid) and transfer of hydrogen to free radicals, thus inhibiting linkage and enabling subsequent nucleation and growth of gas vacuoles during the coaking stage. Past research also emphasizes the importance of hydrogen donor compounds such as asphaltenes or hydroaromatics as preventing cross-linking during cracking (Behar and Pelet, 1988; Michelis, 1996; Schenk *et al.*, 1997), delaying conversion and aromatization of the organic polymers (Lewan, 1997). If similar mechanisms acted during maturation of organic matter in the Posidonia shale, only those particles that retained enough mobile hydrogen would have been prone to devolatilization through bubble formation. Availability of hydrogen-rich compounds was ensured by the primarily algal composition of the Posidonia kerogen as a

precursor for the Posidonia bitumen and hydrocarbons, consistent with findings of Littke *et al.* (1988) and Littke *et al.* (1991). In more rigid, kerogen-like particles, with advanced cross-linking and most of the H immobilised in polycondensed aromatic molecules, any gas generated would have likely diffused through micropores (Vanderbroucke and Largeau, 2007). The lack of visible porosity in the gas mature kerogen was experimentally corroborated by Bernard *et al.* (2011) and is consistent with the high fraction (ca. 65%) of non-porous organic particles point counted in this study.

We found positive relation between OM volume and image resolved intraorganic porosity, with no difference in absolute porosity values between faecal and matrix domains but with stronger covariation outside the faecal pellet zones (Figure 3.20f). Such positive correlation stands in contrast to a negative relationship found between OM-hosted image pores and TOC as observed by Milliken *et al.* (2013) in the Marcellus Shale. We suggest that different association of the image porosity to the content of OM in shales is related to textural and compositional differences. In Posidonia, the presence of rigid, fossiliferous zones favoured entrapment of oil-saturated bitumen, and was followed by its efficient degasification. Such conditions may have been less operative in shale composed primarily of the extrabasinal siliciclastic debris (Milliken *et al.*, 2013).

Porosity balance. Compaction, bitumen entrapment and cracking

The potential amount of organic porosity evolved due to thermogenic loss of organic carbon can be estimated for shales of any maturity if the original TOC, HI and the extent of thermal transformation of kerogen are known or can be restored (Jarvie *et al.*, 2007; Modica and Lapierre, 2012). Moreover, for any stage of thermal degradation of kerogen, potential total porosity can be calculated if information about the initial porosity is accessible. In Posidonia, despite the evidence of thermal degradation of kerogen with increasing thermal stress (Table 3.2), the estimated theoretical total porosity does not match the measured values at any stage (Figure 3.8c). The porosity balance shows that from the total porosity loss between 0.53-0.89% Ro, only 30-40% of the observed decrease can be easily accounted for by the retention of the liquid oil. Total difference between potential and measured porosity in the peak oil window shale can be explained only when including compaction and/or bitumen retention as other porosity reducing mechanisms. Although not measured directly, the minimum porosity lost due to compaction in the oil window Posidonia can be estimated after subtracting the amount of porosity occluded by oil from the total increase in the potential

organic porosity between 0.53-0.89% Ro. In our samples, such estimated loss amounts to ca. 4.5% of the bulk rock, and accounts for only 35% of the estimated total porosity decrease between 0.53-0.89% Ro.

Although our porosity balance does not yield the amount of solid bitumen occluding pores, its content can be evaluated while examining further porosity change at higher levels of thermal conversion. For instance, we noticed that only 40% of the regain in measured porosity between 0.89-1.45% Ro is due to decrease in the oil content, with the majority of the measurable increase ascribed to the evolution of additional organic pores. The organic origin of this porosity is quantitatively reflected as the accordance between the measured increase in the oil-free total porosity and the estimated increase in the potential organic porosity due to thermal decomposition of the organic matter (Figure 3.8d). The 4% increase in the organic porosity between 0.89-1.45% follows the loss in the pyrolizable organic matter as measured by Rock-Eval (Table 3.2) and implies that in the oil window solid bitumen forms part of the S2 peak. Our porosity reconstructions show that although organic content is a good predictor for the amount of organic porosity evolved in the gas window Posidonia Shale, any predictions of porosity at lower levels of thermal maturity will not work without estimating the amount of residual bitumen trapped in the matrix.

Potential for gas storage and connectivity of the pore system

In Posidonia ca. 90% of porosity is in the meso- and micropore size range, and ca. 40% is contained within sorption pores < 6 nm. Such high contribution of meso- and micropores is significant from the shale gas production point of view, and will affect estimations of the shale gas storage capacity and gas flow efficiency (Ambrose *et al.*, 2010; Chalmers and Bustin, 2012). We found that in the gas window Posidonia shale, porosity < 6 nm is associated with the clay and organic domains (Figure 3.11), with radically different affinities for water and oil. Most certainly, any organic porosity is oil-wet as it evolved via cracking of the pore-filling bitumen and oil (Table 3.3). Moreover, retarded cementation of the fossiiferous zones suggests that fossil-hosted pores also became oil wet and thus form part of the oil-wet pore system. In contrast, clays are hydrophilic and may remain water-wet even at high maturities (Aplin and Macquaker, 2011). As in Posidonia clays are microporous, they may not participate in the gas transfer from the matrix to a fracture and a wellbore (Modica and Lapierre, 2012; Passey *et al.*, 2010).

Organic porosity in the gas mature Posidonia is highly heterogeneous, with pore sizes as small as < 6 nm, co-existing with micron-size pores hosted by fossiliferous aggregates and pyrite framboids. Such heterogeneiy of pores has consequences for the amount of gas stored in the free and adsorbed phase. While we did not measure the absolute gas capacity of the Posidonia shale, we can certainly argue that its volume is controlled by the amount of bitumen trapped in shale, and thus we expect the best microreservoir for free gas to be associated with the macroporous and rigid faecal pellet zones.

The approximation of total shale porosity by the combination of gas sorption and mercury injection techniques confirmed that those two pore systems are connected, and that the pore connectivity extends to pore bodies resolved in SEM micrographs (Figure 3.10, Figure 3.15). Consistently, high residual mercury saturation as encountered in the early oil window and gas window samples could be interpreted as reflecting high pore body/pore throat size ratio, leading to extensive snap-off of the mercury phase in throats over the entire range of the imbibition pressures before retraction from the pore bodies takes place (Figure 3.7) (Ioannidis *et al.*, 1991; Ioannidis *et al.*, 1993; Porcheron and Monson, 2004). An elevated ratio of pore body to throat sizes is in accordance with the lack of overlap between the mercury pore size distributions and the distribution of sizes of the image resolved pores (Figure 3.19a, b). However, we cannot exclude that alternatively, high residual mercury is induced by compressibility of the shale under high pressures and does not necessarily reflect the ratio of pore bodies to pore throats (Toda and Toyoda, 1972). Such interpretation stems from the very high percentage (ca. 90%) of total porosity that was not emptied from the receding mercury at the equivalent intrusion pressures and which was confirmed with the SEM studies (Figure 3.17b, c).

A microstructure composed of pore bodies connected through < 40 nm pore throats as present in Posidonia is typical for shales reported elsewhere (Nelson, 2009) and is believed to have a major control on gas flow efficiency through the matrix (Chalmers and Bustin, 2012; Rushing *et al.*, 2008). According to Chalmers and Bustin (2012) a more balanced ratio between micro-, meso- and macropores favours permeability of shales. In the water-free calcareous Posidonia shale from the early oil and gas window, a moderate porosity balance is attained at ca. 40-50-10% of total porosity contained in pores < 6 nm, 6-100 nm and >100 nm respectively. However, in a tight, clay-bearing shale with water-wet surfaces, this balance is likely disturbed as finer pores are lost.

Summary and Conclusions

A detailed analysis of the Posidonia shale revealed a heterogeneous rock with a micron-scale alternation of the carbonate-rich, clay-rich and organic-rich domains. The application of a range of different techniques measuring pores of various sizes allowed to identify factors controlling the change in shale porosities with maturity and between lihologies.

Posidonia Shale from the Hils Sincline shows a non-linear pattern of the porosity change with maturity. Total porosity is ca.10% at maturities of 0.6% Ro, but declines to ca. 4% at Ro = 0.9% as a result of compaction and pore-filling with bitumen. At Ro = 1.4%, porosities increase to values similar to those at 0.6% Ro, related to hydrocarbon generation from the residual bitumen. The initial retention of bitumen in the shale matrix indicates that the Transformation Ratio is of limited use when modelling the organic porosity evolution in the oil window shale. However, it becomes again a reliable measure of the porosity gain in the gas window. The Posidonia shale case study revealed the porosity of the overmature shales can be accurately estimated using the Leco TOC and Rock Eval data if only porosity of the oil window shale is known and its further compaction has been arrested.

A major consequence of the entrapment and thermal cracking of the hydrocarbon-prone bituminous phase is the appearance of organic pores. Image analysis revealed that although this porosity covaries positively with the content of the organic phase, it is not evenly distributed. In Posidonia, the preferential entrapment of bitumen occurred within faecal pellets, pyrite framboids and in the vicinities of the rigid mineral grains, showing the highest present day macroporosities. Such location of the petroleum traps is most likely related to their rigidity and the resistance against compaction. The visible macropores, although surrounded by the inorganic phase, are likely oil-wet and may potentially act as microreservoirs of gas.

The retention of bitumen in the shale matrix has major consequences for arresting compaction of carbonates. We showed that trapping of petroleum in the faecal pellets prevented chemical cementation of the fossiliferous aggregates and thus porosity loss. The concomitant recrystallization of the biogenic calcite not only did not reduce porosity, but plausibly strengthened the shale framework and induced growth of macropores. The loss of the pore volume was most effective in the clay- and organo-rich domains, and followed kerogen-to-bitumen transformation.

Our study showed that the pore network in Posidonia is connected at all maturities, and is composed of narrow pore throats (< 40 nm diameter) providing access to SEM resolved pore

bodies (> 50 nm). The pore size distribution is not uniform and is a function of both the maturity and the rock texture and composition. Both in the low maturity and in the overmature shale, wider pore throats are characteristic for the calcite-rich mudstone, with higher potential for fabric strengthening than the clay-rich shale. In the peak oil window it is the occlusion of porosity by oil that reduces the size of the pore throats, but is reversible with the onset of the oil-to-gas cracking. A major difference in porosities is seen between the fossiliferous and the clay rich zones, with the former arresting the loss of pores through compacion and enhancing development of macropores in the gas window, and the latter contributing microporosity. In the gas window shale, a fractal distribution of the intraorganic pores resolved in SEM images suggests that pore connectivity within the organic phase is at least partly attained.

This study showed that the multi-technique approach is essential for characterizing pores and pore connectivity in shales. We found that CO_2 gas sorption at 195K is a good indicator of micro- and fine mesoporosity, and when combined with the mercury porosimetry, it can approximate the connected porosity. Complementary to the bulk analyses is the SEM-BIB-FIB microscopy, offering unique approach for visualizing shale heterogeneity and identification of the hydrocarbon microreservoirs. When coupled with the quantitative image analysis, the high resolution microscopy provides the essential background for the understanding of the evolution of the shale microstructure on different scales. Despite the advantages of each technique alone, their limitations in describing the full range of pores place constraints on the interpretation of the data if not supported by other methods. In the case of the BIB-SEM microscopy, those limitations involve limited resolution of the microscropic micrographs, and large, over a centimetre-scale, lithological variations.

The last comment herein relates to the classification of shale pores. While we recognize that in the organic-rich, overmature shales the genetic classification of pores may be more appropriate, the grouping of pores on the basis of their spatial location is useful, and may facilitate the recognition of pathways of bitumen migration and entrapment in the oil window. The confusement in classifying shale pores may arise while realizing that many inorganic-hosted pores observed in the gas window maturity shale evolved due to thermal decomposition of the residual organic matter and are *de facto* of organic origin. This realization may however not be possible via the visual observations alone, and without the access to the geochemical data from a suite of samples covering a range of maturities. The possibility that many inorganic-hosted pores are of organic origin should lead to re-evaluation of pore network types in many shale plays.

References

AMBRAMOFF, M., MAGALHAES, P., RAM, S. 2004. Image processing with ImageJ. *Biophotonics International*, **11**, 36–42.

AMBROSE, R.J., HARTMAN, R.C., DIAZ-CAMPOS, M., AKKUTLU, I.Y., SONDERGELD, C.H. 2010. New pore-scale considerations for shale gas in place calculations. In: Proceedings, SPE Unconventional Gas Conference, SPE, 23–25 February 2010, Pittsburgh, Pennsylvania, USA.

ALEXANDER, T. 2011. Shale gas revolution. *Oilfield review*, **23**, 40-55.

BAKER, P.A., KASTNER, M., BYERLEE, J.D., LOCKNER, D.A., 1980. Pressure solution and hydrothermal recrystallization of carbonate sediments—an experimental study. *Marine Geology*, **38**, 185–203.

BEHAR, F., PELET, R. 1988. Hydrogen-Transfer Reactions in the Thermal Cracking of Asphaltenes. *Energy & Fuels*, **2**, 259-264.

BEHAR, F., VANDENBROUCKE, M., TANG, Y., MARQUIS, F., ESPITALIE, J. 1997. Thermal cracking of kerogen in open and closed systems: determination of kinetic parameters and stoichiometric coefficients for oil and gas generation. Organic Geochemistry, **26**, 321-339.

BEHAR, F., LORANT, F., LEWAN, M. 2008. Role of NSO compounds during primary cracking of a Type II kerogen and a Type III lignite. *Organic Geochemistry*, **39**, 1–22.

BERNAL, J.L.P., BELLO, M.A. 2001. Fractal geometry and mercury porosimetry. Comparison and application of proposed models on building stones. *Applied Surface Science*, **185**, 99-107.

BERNARD, S., HORSFIELD, B., SCHULTZ, H.M., WIRTH, R., SCHREIBER, A., SHERWOOD, N. 2011. Geochemical evolution of organic-rich shales with increasing maturity: A STXM and TEM study of the Posidonia Shale (Lower Toarcian, northern Germany). Marine and Petroleum Geology, **31**, 70-89.

BERNARD, S., WIRTH, R., SCHREIBER, A., SCHULZ, H.-M., HORSFIELD, B. 2012. Formation of nanoporous pyrobitumen residues during maturation of the Barnett Shale (Fort Worth Basin). *International Journal of Coal Geology*, **103**, 3–11.

BJØRLYKKE, K., HØEG, K. 1997. Effects of burial diagenesis on stresses, compaction and fluid flow in sedimentary basins. *Marine and Petroleum Geology*, **14**, 267 -276.

BUSTIN, R.M., BUSTIN, A.M.M., CIU, X., ROSS, D.J.K., MURPHY PATHI, V.S. 2008. Impact of shale properties on pore structure and storage characteristics. SPE Shale Gas Production Conference, 16-18 November 2008, Fort Worth, Texas, USA.

CHAIKA, C., DVORKIN, J. 2000. Porosity reduction during diagenesis of diatomaceous rocks. *American Association of Petroleum Geologists Bulletin*, **84**, 1173–1184.

CHALMERS, G.R.L., BUSTIN, R.M. 2007. On the effects of petrographic composition on coalbed methane sorption. *International Journal of Coal Geology*, **69**, 288–304.

CHALMERS, G.R.L., BUSTIN, R.M. 2012. Geological evaluation of Halfwaye-Doige-Montney hybrid gas shale-tight gas reservoir, northeastern British Columbia. *Marine and Petroleum Geology*, **38**, 53-72

CHALMERS, G.R.L., ROSS, D.J.K., BUSTIN, R.M. 2012. Geological controls on matrix permeability of Devonian Gas Shales in the Horn River and Liard basins, northeastern British Columbia, Canada. *International Journal of Coal Geology*, **103**, 120-131.

CLARKSON, C.R., SOLANO, N., BUSIN, R.M, BUSTIN, A.M.M., CHALMERS, G.R.L., HE, L., MELNICHENKO, Y.B., RADLINSKI, A.P., BLACH, T.P. 2013. Pore structure characterization of North American shale gas reservoirs using USANS/SANS, gas adsorption, and mercury intrusion. *Fuel*, **103**, 606–616.

CLEMENTZ, D.M. 1978. Effect of oil and bitumen saturation on source-rock pyrolysis. *American Association of Petroleum Geologists Bulletin*, **63**, 2227-2232.

COMISKY, J.T., SANTIAGO, M., McCOLLOM, B., BUDDHALA, A., NEWSHAM, K.E. 2011. Sample size effects on the application of mercury injection capillary pressure for determining the storage capacity of tight gas and oil shales. SPE Canadian Unconventional Resources Conference, 15–17 November 2011, Calgary, Alberta, Canada.

COSKEY, R.J. 2001. Bakken and Niobrara plays. A geologic comparison. Tight Oil from Shale Plays World Congress, 31 January – 1 February 2011 (Online).

CURIALE, J.A. 1986. Origin of solid bitumens, with emphasis on biological marker results. *Organic Geochemistry*, **10**, 559-580.

CURTIS, C.D. 1995. Post-depositional evolution of mudstones l: early days and parental influences. *Journal of the Geological Society*, **152**, 577-586.

CURTIS, M.E., AMBROSE, R.J., SONDERGELD, C.H., RAI, C.S. 2010. Structural Characterization of Gas Shales on the Micro- and Nano-Scales. SPE Canadian Unconventional Resources and International Petroleum Conference, 19-21 October 2010, Calgary, Alberta, Canada.

CURTIS, M.E., AMBROSE, R.J., SONDEGELD, C.H., RAI, C.S. 2011. Investigation of the relationship between organic porosity and thermal maturity in the Marcellus Shale. SPE North American Unconventional Gas Conference and Exhibition, 14-16 June 2011, The Woodlands, Texas, USA.

CURTIS, M.E., SONDERGELD, C.H., AMBROSE, R.J., RAI, C.S. 2012. Microstructural investigation of gas shales in two and three dimensions using nanometer-scale resolution imaging. *American Association of Petroleum Geologists Bulletin*, **96**, 665-677.

CURTIS, M.E., SONDERGELD, C.H., RAI, C.S. 2013. Relationship between organic shale microstructure and hydrocarbon generation. SPE Unconventional Resources Conference-USA, 10-12 April 2013, The Woodlands, Texas, USA.

ESPITALIE, J., LAPORTE, J.L., MADEC, M., MARQUIS, F., LEPLAT, P., PAULET J., BOUTEFEU, A. 1977. Methode rapide de characterisation des roches meres, de leur potential petrolier et de leur degree d'evolution, *Rev. Inst. Franc. Pétrole.*, **32**, 23-42.

FABRICIUS, I.L. 2003. How burial diagenesis of chalk sediments controls sonic velocity and porosity. *American Association of Petroleum Geologists Bulletin*, **87**, 1755 – 1778.

FISHMAN, N.S., HACKLEY, P.C., LOWERS, H.A., HILL, R.J., EGENHOFF, S.O., EBERL, D.D., BLUM, A.E. 2012. The nature of porosity in organic-rich mudstones of the

Upper Jurassic Kimmeridge Clay Formation, North Sea, offshore United Kingdom. *International Journal of Coal Geology*, **103**, 32–50.

FURMANN, A. MASTALERZ, M., SCHIMMELMANN, A., PEDERSEN, P.K., BISH, D. 2014. Relationships between porosity, organic matter, and mineral matter in mature organic-rich marine mudstones of the Belle Fourche and Second White Specks Formations in Alberta, Canada. *Marine and Petroleum Geology*, **54**, 65-81.

GIESCHE, H. 2006. Mercury porosimetry: A general (practical) overview. *Part. Part. Syst. Charact.*, **23**, 9–19.

HEASLEY, E.C., WORDEN, R.H., HENDRY, J.P. 2000. Cement distribution in a carbonate reservoir: Recognition of a paleo-oil–water contact and its relationship to reservoir quality in the Humbly Grove field, onshore, United Kingdom. *Marine and Petroleum Geology*, **17**, 639–654.

HILL, R.J., TANG, Y., KAPLAN, I.R. 2003. Insights into oil cracking based on laboratory experiments. *Organic Geochemistry*, **34**, 1651–1672.

HORSFIELD, B., SCHENK, H.J., MILLS, N., WELTE, D.H. 1992. An investigation of the in-reservoir conversion of oil to gas: compositional and kinetic findings from closed-system programmed-temperature pyrolysis. *Organic Geochemistry*, **19**, 191-204.

HORSFIELD, B., LITTKE, R., MANN, U., BERNARD, S., TIEM, A.T.V., Di PRIMIO, R., SCHULZ, H.-M. 2010. Shale Gas in the Posidonia Shale, Hils Area, Germany. American Association of Petroleum Geologists Annual Convention, April 11-14, 2010, New Orleans, LA, USA.

HOUBEN, M.E., DESBOIS, G., URAI, J.L. 2013. Pore morphology and distribution in the Shaly facies of Opalinus Clay (Mont Terri, Switzerland): Insights from representative 2D BIB-SEM investigations on mm to nm scale. *Applied Clay Science*, **71**, 82-97.

HWANG, R.J., TEERMAN, S.C., CARLSON, R.M. 1998. Geochemical comparison of reservoir solid bitumens with diverse origins. *Organic Geochemistry*, **29**, 505-517.

IGLESIAS, M.J., CUESTA, M.J., LAGGOUN-DEFARGE, F., SUAREZ-RUIZ, I. 2001. The influence of impregnation by hydrocarbons on coal structure during its thermal evolution. *Journal of Analytical and Applied Pyrolysis*, **58 – 59**, 841– 871.

IOANNIDIS, M.A., CHATZIS, I., PAYATAKES, A.C. 1991. A mercury porosimeter for investigating capillary phenomena and microdisplacement mechanisms in capillary networks. *Journal of Colloid and Interface Science*, **143**, 22-36.

IOANNIDIS, M.A., CHATZIS, I. 1993. A mixed-percolation model of capillary hysteresis and entrapment in mercury porosimetry. *Journal of Colloid and Interface Science*, **161**, 278-291.

JARVIE, D.M., HILL, R.J., RUBLE, T.E., POLLASTRO, R.M., 2007. Unconventional shale-gas systems: the Mississippian Barnett Shale of north-central Texas as one model for thermogenic shale gas assessment. *American Association of Petroleum Geologists Bulletin*, **91**, 475–499.

JUSTWAN, H., DAHL, B. 2005. Quantitative hydrocarbon potential mapping and organofacies study in the Greater Balder Area, Norwegian North Sea. *Petroleum Geology Conference series*, **6**, 1317-1329.

KANITPANYACHAROEN, W., VANORIO, T., LIU, Y., XIAO, X., BENMORE, C. 2013. Evolution of mineral fabrics and microstructures in Kimmeridge Shale upon kerogen maturation. Second International Workshop on Rock Physics, 4-9 August 2013, Southampton.

KLAVER, J., DESBOIS, G., URAI, J.L., LITTKE, R. 2012. BIB-SEM study of the pore space morphology in early mature Posidonia Shale from the Hils area, Germany. *International Journal of Coal Geology*, **103**, 12-25.

KUILA, U., PRASAD, M. 2013. Specific surface area and pore-size distribution in clays and shales, *Geophysical Prospecting*, **61**, 341–362.

KWIECINSKA, B.K., HAMBURG, G., VLEESKENS, J.M. 1992. Formation temperatures of natural coke in the lower Silesian coal basin, Poland. Evidence from pyrite and clays by SEM-EDX. *International Journal of Coal Geology*, **21**, 217-235.

LEWAN, M.D., 1997. Experiments on the role of water in petroleum formation. *Geochimica et Cosmochirnica Acta*, **61**, 3691-3723.

LEYTHAEUSER, D., LITTKE, R., RADKE, M., SCHAEFER, R.G. 1988. Geochemical effects of petroleum migration and expulsion from Toarcian source rocks in the Hils syncline area, NW-Germany. *Organic Geochemistry*, **13**, 489-502.

LITTKE, R., BAKER, D.R., LEYTHAEUSER, D., RULLKÖTTER, J. 1991. Keys to the depositional history of the Posidonia Shale (Toarcian) in the Hils Syncline, northern Germany. In: Tyson, R.V., Pearson, T.H. (Eds.) Modern and ancient continental shelf anoxia. *Geological Society Special Publication*, **58**, 311-333.

LOUCKS, R.G., REED, R.M., RUPPEL, S.C., JARVIE, D.M. 2009. Morphology, genesis and distribution of nanometer-scale pores in siliceous mudstones of the Mississippian Barnett Shale. *Journal of Sedimentary Research*, **79**, 848–861.

LOUCKS, R.G., REED, R.M., RUPPEL, S.C., HAMMES, U. 2012. Spectrum of pore types and networks in mudrocks and a descriptive classification for matrix-related mudrock pores. *American Association of Petroleum Geologists Bulletin*, **96**, 1071-1098.

MACQUAKER, J.H.S., ADAMS, A. 2003. Maximizing information from fine-grained sedimentary rocks: an inclusive nomenclature for mudstones. *Journal of Sedimentary Research*, **73**, 735-744.

MACQUAKER, J.H.S., TAYLOR, K.G., KELLER, M., POLYA, D. 2014. Compositional controls on early diagenetic pathways in fine-grained sedimentary rocks: Implications for predicting unconventional reservoir attributes of mudstones. *American Association of Petroleum Geologists Bulletin*, **98**, 587–603.

MANN, U., MÜLLER, P.J. 1988. Source rock evaluation by well log analysis (Lower Toarcian, Hils syncllne). *Organic Geochemistry*, **13**, 109-119.

MASTALERZ, M., SCHIMMELMANN, A., DROBNIAK, A., CHEN, Y. 2013. Porosity of Devonian and Mississippian New Albany Shale across a maturation gradient: Insights from organic petrology, gas adsorption, and mercury intrusion. *Association of Petroleum Geologists Bulletin*, **97**, 1621-1643.

MICHELIS, R., LANGLOIS, E., RUAU, O., MANSUY, L., ELIE, M., LANDAIS, P. 1996. Evolution of asphaltenes during artificial maturation: A record of the chemical processes. *Energy & Fuels*, **10**, 39-48.

MILLIKEN, K.L., RUDNICKI, M., AWWILER, D.N., ZHANG, T. 2013. Organic matter–hosted pore system, Marcellus Formation (Devonian), Pennsylvania. *American Association of Petroleum Geologists Bulletin*, **97**, 177-200.

MILNER, M., MCLIN, R., PETRIELLO, J., TEK, T. 2010. SPE Canadian Unconventional Resources and International Petroleum Conference, 19-21 October 2010, Calgary, Alberta, Canada.

MODICA, C.J., LAPIERRE, S.G. 2012. Estimation of kerogen porosity in source rocks as a function of thermal transformation: Example from the Mowry Shale in the Powder River Basin of Wyoming. *Association of Petroleum Geologists Bulletin*, **96**, 87-108.

NELSON, P.H. 2009. Pore-throat sizes in sandstones, tight sandstones, and shales. *American Association of Petroleum Geologists Bulletin*, **93**, 329–340.

PADHY, G.S., LEMAIRE, C., AMIRHARAJ, E.S., IOANNIDIS, M.A. 2007. Pore size distribution in multiscale porous media as revealed by DDIF–NMR, mercury porosimetry and statistical image analysis. *Colloids and Surfaces A: Physicochemical Engineering Aspects*, **300**, 222–234.

PASSEY, Q. R., BOHACS, K. M., ESCH, W. L., KLIMENTIDISS, R., SINHA, S. 2010. From Oil-Prone Source Rock to Gas-Producing Shale Reservoir – Geologic and petrophysical characterization of unconventional shale-gas reservoirs. *Proceedings of the North American Unconventional Gas Conference and Exhibition. Society of Petroleum Engineers*, Paper 131350, 29p.

PELET, R., BEHAR, F., MONIN, J.C. 1986. Resins and asphaltenes in the generation and migration of petroleum. *Organic Geochemistry*, **10**, 481-498.

PEPPER, A.S., DODD, T.A. 1995. Simple kinetic models of petroleum formation. Part II: oil-gas cracking. *Marine and Petroleum Geology*, **12**, *321-340*.

PORCHERON, F., MONSON, P.A. 2004. Modeling mercury porosimetry using statistical mechanics. *Langmuir*, **20**, 6482-6489.

RAISWELL, R., BERNER, R.A. 1987. Organic carbon losses during burial and thermal maturation of normal marine shales. *Geology*, **15**, 853-856.

REXER, T.F., MATHIA, E.J., APLIN, A.C., THOMAS, K.M. 2014. High-Pressure Methane Adsorption and Characterization of Pores in Posidonia Shales and Isolated Kerogens. *Energy & Fuels*, **28**, 2886-2901.

RODUIT. 2008. JMicroVision: Image analysis toolbox for measuring and quantifying components of high-definition images. Version 1.2.7. Software available for free download at http://www.jmicrovision.com/ accessed August, 2011.

ROSS, D.J.K, BUSTIN, R.M. 2009. The importance of shale composition and pore structure upon gas storage potential of shale gas reservoirs. *Marine and Petroleum Geology*, **26**, 916–927.

RUSHING, J.A., NEWSHAM, K.E., BLASINGAME, T.A. 2008. Rock typing —keys to understanding productivity in tight gas sands. SPE Unconventional Reservoirs Conference, 10-12 February 2008, Keystone, Colorado, USA.

SANDVIK, E.I., YOUNG, W.A., CURRY, D.J. 1992. Expulsion from hydrocarbon sources: the role of organic absorption. *Organic Geochemistry*, **19**, 77-87.

SCHENK, H.J., DI PRIMIO, R., HORSFIELD, B. 1997. The conversion of oil into gas in petroleum reservoirs. Part 1: Comparative kinetic investigation of gas generation from crude oils of lacustrine, marine and fluviodeltaic origin by programmed-temperature closed-system pyrolysis. *Organic Geochemistry*, **26**, 467-481.

SCHIEBER, J. 2011. Shale microfabrics and pore development – an overview with emphasis on the importance of depositional processes. In: Gas Shale of the Horn River basin, D.A. Leckie and J.E. Barclay (Eds.), Canadian Society of Petroleum Geologists, Calgary, p. 115-119.

SCHMITT, M., FERNANDES, C.P., DA CUNHA NETO, J.A.B., WOLF, F.G. DOS SANTOS, V.S.S. 2013. Characterization of pore systems in seal rocks using Nitrogen Gas Adsorption combined with Mercury Injection Capillary Pressure techniques. *Marine and Petroleum Geology*, **39**, 138-149.

SCHOLLE, P. A. 1977. Chalk diagenesis and its relation to petroleum exploration: oil from chalks, a modern miracle? *American Association of Petroleum Geologists Bulletin*, **61**, 982-1009.

SING, K.S.W., EVERETT, D.H., HAUL, R.A.W., MOSCOU, L., PIEROTTI, R.A., ROUQUEROL, J. 1985. Reporting physisorption data for gas/solid systems. Spetial reference to the determination of surface area and porosity. *Pure and Applied Chemistry*, **57**, 603-619.

SLATT, R.M., O'BRIEN, N.R. 2011. Pore types in the Barnett and Woodford gas shales: Contribution to understanding gas storage and migration pathways in fine-grained rocks. *American Association of Petroleum Geologists Bulletin*, **95**, 2017–2030.

STRAPOC, D., MASTALERZ, M., SCHIMMELMANN, A., DROBNIAK, A., HASENMUELLER, N.R. 2010. Geochemical constraints on the origin and volume of gas in the New Albany Shale (Devonian–Mississippian), eastern Illinois Basin. *American Association of Petroleum Geologists Bulletin*, **94**, 1713-1740.

TAN, J., HORSFIELD, B., MAHLSTEDT, N., ZHANG, J., DI PRIMIO, R., TIEM, T.A., BOREHAM, C.J., Van GRAAS, G., TOCHER, B.A. 2013. Physical properties of petroleum formed during maturation of Lower Cambrian shale in the upper Yangtze Platform, South China, as inferred from PhaseKinetics modelling. *Marine and Petroleum Geology*, **48**, 47-56.

TAO, S., WANG, Y., TANG, D., WU, D., XU, H., HE, W. 2012. Organic petrology of Fukang Permian Lucaogou Formation oil shales at the northern foot of Bogda Mountain, Junggar Basin, China. *International Journal of Coal Geology*, **99**, 27–34.

TODA, Y., TOYODA, S. 1972. Application of mercury porosimetry to coal. *Fuel*, **51**, 199-201.

VANDENBROUCKE, M.., BEHAR, F., SAN TORCUATO, A., RULLKÖTER, J. 1993. Kerogen maturation in a reference kerogen Type II series: the Toarcian shales of the Hils syncline, NW Germany. *Organic Geochemistry*, **20**, 961-972.

VANDENBROUCKE, M.., LARGEAU, C. 2007. Kerogen origin, evolution and structure. *Organic Geochemistry*, **38**, 719–833.

VANDENBYGAART, A.J., PROTZ, R. 1999. The representative elementary area REA in studies of quantitative soil micromorphology. *Geoderma*, **89**, 333–346.

WAPLES, D.W. 2000. The kinetics of in-reservoir oil destruction and gas formation: constraints from experimental and empirical data, and from thermodynamics. *Organic Geochemistry*, **31**, 553-575.

WASHBURN, E.W. 1921.The Dynamics of Capillary Flow, *Phys. Rev*., **17**, 273 – 283.

WILHELMS, A., LARTER, S.R., LEYTHAEUSER, D., DYPVIK, H. 1990. Recognition and quantification of the effects of primary migration in a Jurassic clastic source-rock from the Norwegian. *Organic Geochemistry*, **16**, 103-113.

WORDEN, R.H., OXTOBY, N.H., SMALLEY, P.C. 1998. Can oil emplacement prevent quartz cementation in sandstones? *Petroleum Geoscience*, **4**, 129–137.

Chapter 4: Microscopic, petrophysical and geochemical characterization of the Wealden Shale of Northwest Germany – implications for porosity development in the heterogeneous shale gas reservoir

Introduction

The successful exploration of shale gas in the US sparked an interest in shale formations in Europe and induced research into finding potential targets for domestic European shale gas exploration. One of the sedimentary sequences that attracted the attention of the industry is the Lower Cretaceous Wealden Shale from the Lower Saxony Basin in Northwest Germany. Preliminary assessment of the German Wealden was conducted through the Isteberg 1001 drilling in the west of the basin and discovered an oil-prone rock with a lacustine Type I kerogen, but with a variable input of terrestrial (type III) and marine (type II) organics (Berner *et al.*, 2010). A recent geochemical study by Rippen *et al.* (2013) on 3 cores retrieved from the Hannover area, and also used in this study, confirmed the predominantly lacustrine character of the organic matter with a lateral gradient in maturation from the early oil window, to postmature and overmature. In the central part of the basin the Wealden is dominated by clay-rich mudstones intercalated with limestones (Mutterlose and Bornemann, 2000), and thus differs in composition from mostly siliceous US shale gas plays (Curtis, 2002). It is expected that despite the high hydrocarbon potential of the accumulated organic matter, such clay-rich lithologies may negatively affect the producibility of gas (Jarvie *et al.*, 2007).

The efficiency of gas flow through the matrix to naturally occurring and artificially induced fractures depends also on the nature of the pore systems, and its vertical change in rocks of varied lithology. It has been recognized that the nature of matrix pores influence the permeability and wettability of shale reservoirs and thus their long-term production profiles (Aplin and Macquaker, 2011; Chalmers *et al.*, 2012; Soeder, 1988). The volume and type of matrix pores constitute also a major input into estimations of the adsorbed and free gas storage capacities of shale reservoirs (Ambrose *et al.*, 2010). A range of pore types have been documented, including pores hosted by organic phases (Bernard *et al.*, 2010; Bernard *et al.*, 2011; Curtis *et al.*, 2010; Desbois *et al.*, 2009; Loucks *et al.*, 2009; Milner *et al.*, 2010; Passey *et al.*, 2010; Schieber, 2010; Sisk *et al.*, 2010; Lu *et al.*, 2011; Slatt and O'Brien, 2011). The importance of organic porosity for gas storage and its flow to a wellbore is critical

as indicated by the presence of a broad positive relationship between total porosity and organic carbon (Passey *et al.*, 2010). The formation of the organic pores is recognized to be secondary, related to the maturation of organic matter and thus in theory its occurrence should be predicted by kinetic models (Jarvie *et al.*, 2007). To date, several attempts have been made to predict the formation of organic pores (Jarvie *et al.*, 2007; Loucks et al., 2012; Modica and Lapierre, 2012), all of them stressing bitumen formation and entrapment as a factor inhibiting development of organic porosity in the oil window.

Numerous studies have documented that pores in shales are connected. The presence of the open porosity in the clay phase was documented via a selection of gas adsorption, mercury porosimetry, metal injection and imaging techniques in studies performed by e.g. Curtis *et al.*, 2010, Hildenbrand and Urai, 2003; Kuila *et al.*, 2013, Sondergeld *et al.*, 2010. Likewise, high resolution 3D image visualizations methods have demonstrated pore connectivity within the organic phase. Despite such promising results, it is recognized that the effective pore connectivity in the subsurface is significantly lower, negatively affected by the presence of water and oil molecules (Aplin and Macquaker, 2011, Kuila *et al.*, 2013; Modica and Lapierre, 2012).

Vertical and lateral heterogeneity of the pore systems encountered in shales cannot be fully predicted without recognition of depositional environments and diagenetic changes within muds (Macquaker *et al.*, 2014). Such spatial variation is especially important in shales with large vertical and lateral heterogeneity in the sedimentary facies. The resolution of the well logging methods may not be sufficient to resolve original heterogeneity of the shale formations, and its direct estimation requires extensive work and excellent sampling strategy. Such work is also useful from the academic standpoint and may contribute significantly to understanding relationships between different aspects of mudstone deposition and its physical attributes. In this study, an attempt to perform such work has been undertaken. Both petrophysical and geochemical investigations were carried out on three cores of the German Wealden, retrieved by ExxonMobil Production Deutschland and made available for scientific investigations. The bulk measurements were supplemented by analysis of microtextures both in the petrographic and scanning electron microscope micrographs, followed by an analysis of pore systems using highly polished thin sections. The main aim of our work was to address the issue of small-scale variation of the lithologically heterogeneous clay- and carbonate-rich units, and its effect on the porosity evolution in shales of radically different maturity. Moreover, in the gas window maturity rocks, we paid special attention to development and

connectivity of organic pores as potential sites for storage of free gas and the most likely permeability pathways of gas flow in the context of shale gas exploration.

Samples and Methodologies

292 samples retrieved from cores at a distance ca. 1 m apart were analysed for TOC and Rock Eval hydrocarbon potential by Applied Petroleum Technology AS, Norway. Rock-Eval was performed according to Espitalié *et al.* (1977) using a Vinci RE-6 Standard instrument. To correct for an oil-in-kerogen peak, 4 shale samples were solvent extracted with a mixture of dichloromethane (93%) and methanol (7%) and subsequently analysed for its remaining hydrocarbon potential.

The X-ray diffraction was performed by Macaulay Scientific Consulting Ltd. The bulk samples were wet ground (in ethanol) in a McCrone mill and spray dried to produce random powders. X-ray powder diffraction (XRPD) patterns were recorded from 2-75°2θ using Cobalt Kα radiation. Quantitative analysis was done by a normalised full pattern reference intensity ratio (RIR) method. Expanded uncertainty using a coverage factor of 2, i.e. 95% confidence, is given by $\pm X^{0.35}$, where X = concentration in wt.%, e.g. 30 wt.% ±3.3.

Shale grain density was measured on samples dried at 105°C using the "Small Pyknometer Method", yielding density values within an error ± 0.02 g/cm^3. Mercury injection data was collected on Micrometrics Autopore II on samples freeze-dried at -50°C and evacuated to 10^{-4} psia. Total shale porosity was determined from grain density and bulk density of samples immersed in mercury at the pressure of 25 psia. The mercury was intruded to a maximum pressure 41,000 psia, followed by a pressure drop to 25 psia. The pressure and intrusion data were converted to a pore size distribution using the Washburn equation (Washburn, 1921), with the input parameters as followes: an advancing contact angle of 141°, a receding contact angle 140° and surface tension 485dyn/cm.

Low pressure sorption experiments were performed on an Intelligent Gravimetric Analyzer (IGA), supplied by Hiden Isochema Ltd., Warrington, UK, on shales dried at 110°C for 4 hours under vacuum. CO_2 was injected stepwise up to a pressure of 1 bar at a constant temperature of 195K (dry ice/acetone bath). All isotherms were run twice to ensure experimental repeatability. Sorption pore volumes (SPV) were calculated from the maximum uptake at 1 mbar assuming a density of CO_2 equal to 1.177 g/cm^3. Corresponding sorption porosities were determined using the pycnometer shale grain density.

For microscopic studies, 20 highly-polished thin sections and 5 Araldite resin covered blocks, all cut perpendicular to bedding, were prepared. Thin sections were first scanned using an Epson Perfection V500 scanner with 9600 dpi resolution. Subsequently, each thin section was examined with a Nikon Eclipse LV100 POL transmitted light petrographic microscope with an attached Nikon Digital Sight DS-U3 camera. Polished blocks were examined in the reflected and UV light using an Oil Zeiss Immersol 518N oil immersion microscope. The fluorescence of organic matter was determined qualitatively using the UV light with an HXP 120C accessory. The vitrinite reflectance (VR) measurements were made on randomly selected particles using a Zeiss Axio Imager M2m microscope at x50 magnification with a 546 nm interference filter. The standard used for calibration was Yttrium-Aluminium-Garnet with a refractive index of 0.889. The VR of OM particles was recorded in a digital mode using Fossil 3.0 software.

For high resolution imaging, one thin section of low maturity shale and two sections of gas mature shale of varied carbonate content were selected, milled and polished perpendicular to the bedding plane with a Gallium (Ga) focused ion beam (FIB) in a FEI Helios Nanolab 600 with FEG source. Trenches 15 µm x 5 µm were cut using a 1-30kV accelerating voltage and 3.3nA beam current. Samples were viewed in the BSE Immersion or secondary electron mode with the following conditions: 4.1 mm WD, 1.5-3.0 kV accelerating voltage, 2-4 nA beam current, using through-the-lens detector for better spatial resolution. The images were captured at magnifications between 10,000-200,000x, corresponding to pixel sizes 25-1.2 nm respectively.

Twenty carbon-coated polished thin sections were examined using a Hitachi SU-70 High Resolution Analytical SEM, equipped with an Oxford Instrument Energy Dispersive X-ray microanalysis system (INCA Energy 700). Samples were viewed in the Back Scattered Electron (BSE) mode using the YAG detector with the following conditions: 15-8 mm WD, 15keV accelerating voltage, 2-4 nA filament current. To reduce the shale topography, prior to the SEM imaging, selected samples were polished with an argon broad ion beam (BIB) in the GATAN 691 Precision Ion Polishing System (PIPS^{TM}). In order to fit into the PIPS^{TM} chamber, the sample size was reduced to a 3 mm in diameter disc with GATAN 601 Ultrasound Disc Cutter using water emulsion of boron nitrate powder as a saw. The prepared discs were bombarded with Ar ions in a vacuum (10^{-2} Pa) for 6 hours (angle 3°, 5kV, 1-20 µA). The images of shale porosity were captured in the Secondary Electron (SE) mode using a through-the-lens detector (TLD) at magnifications of 600 x (pixel size 100 nm), 6,000 x (pixel size 15 nm) and 10,000 x, (pixel size 6 nm) using the Automate mosaic building option.

For selected areas, an Energy Dispersive X-ray (EDX) mode was implemented, generating maps of elemental and phase distribution. Microanalysis settings for the EDX collection were set at 300 µm dwell time, 15kV accelerating voltage and 4 nA filament current. The areas covered by EDX mapping varied between 5424 and 77741 μm^2. The phase extraction procedure involved conversion of each X-ray map into an RGB colour mode map, its binarization and quantification of areas in the ImageJ 1.44 software (Abramoff *et al.*, 2004). Additionally, for selected samples the BSE generated images were used to estimate distributions of grain sizes with diameters > 2 µm. Areas used for the grain size analysis were captured at a magnification of 500 x, covering 48387 μm^2 each. Grains outlines were digitized in Adobe Photoshop 8.0 and were quantified in ImageJ software.

To determine a Representative Elementary Area for estimations of image porosity, a modified box counting method described in Houben *et al.* (2013) was applied. With this method, continuous variations of any given property can be established by gradually increasing an area of investigation in a two-dimensional space. The box counting was proceeded for 4 groups of minerals: phyllosilicates, quartz and feldspar, carbonates and pyrite. The phases were extracted from a mix of RGB-converted EDX elemental maps. For the purpose of this study an area was selected as representative if the measurements of the content of an individual phase in boxes of an increasing size did not change by more than +/- 10% relative to the previous area.

For each representative mosaic, total image porosity was quantified by digitization of pore areas manually outlined in Adobe Photoshop 8.0. The digitization was followed by binarization and quantification proceeded in the image analysis software ImageJ 1.44 (Abramoff, 2004). Further statistical analysis was performed using statistical and mathematical software: Minitab 15 and Excel 2010. For two gas window samples, pores were also point counted (150 counts) and classified into types in the image analysis software JMicroVision 1.2.7. (Roduit, 2008). The same software was used to quantify organic matter in the images. At least 300 counts were made, until no significant change in the OM percentage was observed. Additionally, for one gas window sample, a fraction of the area occupied by porous and non-porous particles was point-counted with the 300 counts limit.

As a result of the limited image resolution at any magnification, not all pores could be fully visualized in BIB image mosaics. To determine the minimum fully resolved pore size in BIB mosaics, a method described in Houben *et al.* (2013) and Klaver *et al.* (2012), based on a concept of a fractal dimension was implemented. According to this method, all pore areas were grouped in bins with subsequent bins increased by a power of two and subsequently, the

number of pores were counted and varied as a power of the corresponding pore area. The unique power law equation was determined for fully resolved pore sizes and graphically represented by a linear regression line(s) defined by a specific slope (D) and interception with the *y* axis (C). The minimum pore size fully resolved in images was determined as the one corresponding to the minimum pore area that does not deviate from the calculated regression line.

Depositional setting

The German Wealden is a term describing predominantly regressive, continental, limnic to brackish siliciclastic deposits of the early Cretaceous in northwestern Germany (Figure 4.1). Historically, the German Wealden is divided into the Obernkirchen Member (W1-W4) and Osterwald Member (W5-W6) (Elstner and Mutterlose 1996; Wolburg, 1949), and belongs to the Bückeburg Formation deposited through middle Berriasian to early Valanginian times in the Lower Saxony Basin. Being part of the Central European Basin System (CEBS), the evolution of the Lower Saxony sub-basin in the middle Jurassic was a result of intensive rifting in the Central Atlantic, resulting in the establishment of a system of deeply subsiding graben structures and strike-slip faults (Bachmann *et al.*, 2008). As a result of rapid burial during the Early Cretaceous, in the central part of the basin (Hannover-Minden-Braunschweig shaded area in Figure 4.1) the Berriasian sediments currently attain thicknesses up to 700 m, with up to 300 m of overlying Valanginian (Mutterlose and Bornemann, 2000). Although the predominant lithologies are siltstones and mudstones, occasionally interbedded with mollusc (gastropods, bivalves) coquinas, the character of the sediments changes laterally, with coaly layers of backswamp environments and sandstones/siltstones related to fluvial transport in the southeast (Peltzer et al., 1992). The lithological heterogeneity of the Wealden shows that it was deposited in a series of sequence-stratigraphically linked environments, embracing flood plain, littoral, sublittoral and deep lacustrine settings, controlled by base level variations (Table 4.1) (Berner *et al.*, 2011; Mutterlose and Bornemann, 2000; Stollhofen *et al.*, 2008). The transgressive-regressive periods were oscillatory, with several short-lived marine incursions during the W2 interval, increasing marine influence on the deposition above W3, and a fully developed marine realm in the lower Valanginian (Casey *et al.*, 1975; Stollhofen *et al.*, 2008). The influence of the sea level variations, local base level oscillations, changes in the oxygen content and intensity of sedimentation led to overall overfilling of the lake with sediments and resulted in the small-

scale variation in facies seen in the character of the cores used in this study (Table 4.1). The changing hydrological conditions are indicated by the faunal assemblages (molluscs, ostracods), mainly of limnic nature but shifting towards brackish and normal saline at the end of Berriasian and in the Valanginian (Elstner and Mutterlose, 1996). Similarly, the change in salinity is indicated by the character of the organic matter, mainly brackish lacustrine but with a marine overprint towards the top of the Berriasian interval (Berner, 2011; Rippen *et al.*, 2013).

The maturity of the German Wealden is not uniform and varies laterally across the basin (Bruns *et al.*, 2013). As established by Rippen *et al.* (2013), well A sediments from the northern margin of the Berriasian basin show maturities of Ro 0.5-0.6% within the interval sampled in this study (932-1058 m). This is slightly less than the Ro values reported by the Egs-ploration (unpublished) (up to 0.7% Ro) (Table 4.1). Southwest of well A, at the location of the C well, Wealden Shale exhibits wet gas window maturity, with VR increasing from 1.5 to 1.9% between 609-921 m. In the most central part of the basin (well B), and also over the largest interval studied (981-1578 m), the vitrinite reflectance shows the highest values, between 2.2-2.4%, placing the accumulated organic matter in the dry gas window. For the last well, the vitrinite reflectance measured by Rippen *et al.* (2013) deviates from the measurements by Littke (2008, unpublished), reporting Ro values between 1.6-2.4% over the studied interval. Due to uncertainties regarding the correct maturity of the C sediments, we use the extended maturity values by Littke (2008, unpublished) in this study.

Table 4. 1. *Information about depth, geological age, facies and maturity of three cores of German Wealden: A, B and C.*

Well	Depth (m)	Interval*	Depositional setting*	Maturity Ro(%)
A	832-850	Lachmoeve	Deep marine	0.5-0.7
	910-928	Brachvogel B	Sublittoral	
	967-998	Austernfischer	Deep lacustrine	
	1029-1058	Unnamed	Deep lacustrine	
B	604-617	Lachmoeve	Marine influenced deep lacustrine	1.6 -2.4
	709-728	Brachvogel A	Marine influenced deep lacustrine	
	828-890	Austernfischer	Deep lacustrine	
	920-942	Unnamed	Lake plain	
C	981-1003	Lachmoeve	Marine influenced deep lacustrine	1.5-1.9
	1006-1016	Unnamed	Undefined	
	1150-1186	Brachvogel A	Deep lacustrine	
	1285-1350	Austernfischer	Deep lacustrine	
	1563-1578	Eiderente	Deep lacustrine	

***After ExxonMobil (unpublished)**
****After Egs-ploration (unpublished), Littke (2008, unpublished) and Rippen *et al.* (2013)**

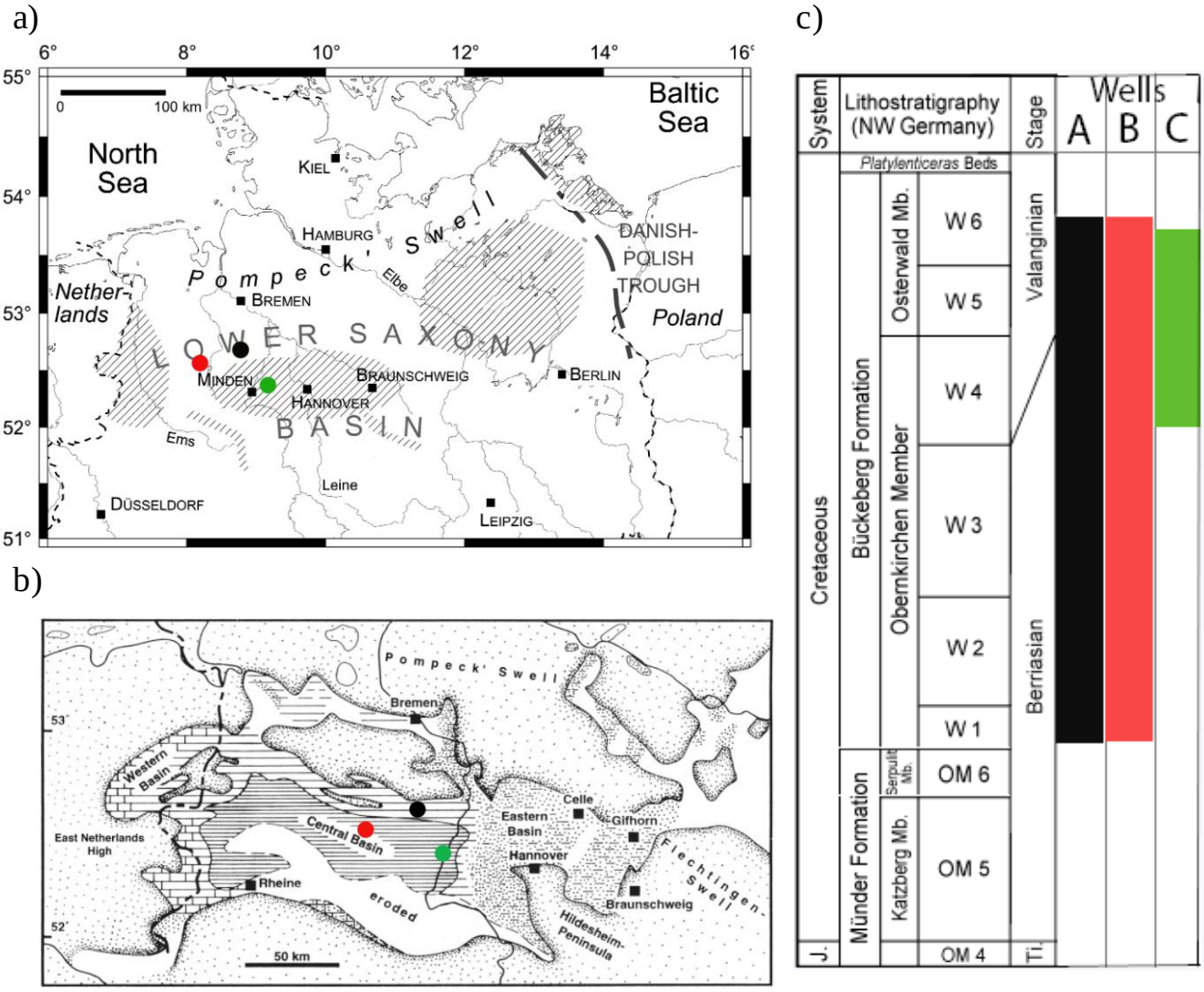

Figure 4. 1. *Regional units of the Lower Cretaceous German Wealden (shaded area) in Northern Germany (after Mutterlose and Bornemann (2000) and Stollhofen et al. (2008)). The three boreholes: A (R_o 0.5-0.6%), B (2.2-2.4%) and C (1.5-1.9%) are marked with black, red and green circles respectively b) Palaeogeography of the Lower Saxony Basin in Berriasian times (after Elstner and Mutterlose, 1996) with the current location of the three boreholes. c) Lithostratigraphy of the Berriasian and lower Valanginian of the northwest Germany (after Elstner and Mutterlose, 1996, modified). Colour bars show top and bottom of the cored interval for each of the wells.*

Results

Mineralogy and textural features from XRD, EDX and petrographic analysis

Wealden shale is not a homogeneous rock but encompasses a variety of interlayered and interbedded rock types of both argillaceous and carbonate nature (Fig. 4.2). Five main sublithofacies were distinguished in all three cores through the analysis of thin sections and RGB-colour converted EDX maps: clay-rich siliciclastic mudstone, clay-rich siliclastic mudstone with physical or biogenic sedimentary structures, clay-bearing fossiliferous mudstone, limestone (mollusc- or ostracod-rich packstone or grainstone) often forming shell pavements and carbonate concretions (Figure 4.2 and Figure 4.3). The allochtonous components consist of detrital clays, quartz and terrigenous organic matter. The autochtonous components consist of biogenic carbonate and algal organic matter. The diagenetic components include pyrite, principally magnesium and ferroan diagenetic dolomite/ankerite, diagenetic clays (illite, kaolinite) and solid bitumen.

The low maturity Wealden shale from the A borehole (Ro = 0.5-0.7%) is a greenish grey rock, either homogeneous and visibly bioturbated (Figure 4.3a), non-laminated with an undisturbed fabric (Figure 4.3b, 4.3 f-h), or exhibiting visible, subcentimetric lamination. In the visibly laminate shale the altermating laminae often constitute of grains of different size (Figure 4.3c, d), or alternatively show varied abundance of the fossil component (Figure 4.3e). The bulk mineralogy (Table 4.2, Figure 4.7) shows an inversely correlated proportion of both calcite and clays, with the relative amount of each depending on the content of the microfossils (foraminifers, molluscs, ostracods). Clay-rich mudstone shows elevated proportion of clays (55-66%), mostly illite and illite - smectite, and kaolinite, and only <1-2% to 10% carbonates. In contrast, mollusc, foraminifera and clay bearing mudstone (sample A10326) has 40% carbonates and only ca. 30% clays. Such heterogeneity reflects changes in depositional paleoenvironments between supralittotal, littoral, sublittoral and distal basinal settings and the associated, varied supply of clastic and biogenic material (Mutterlose and Bornemann, 2000).

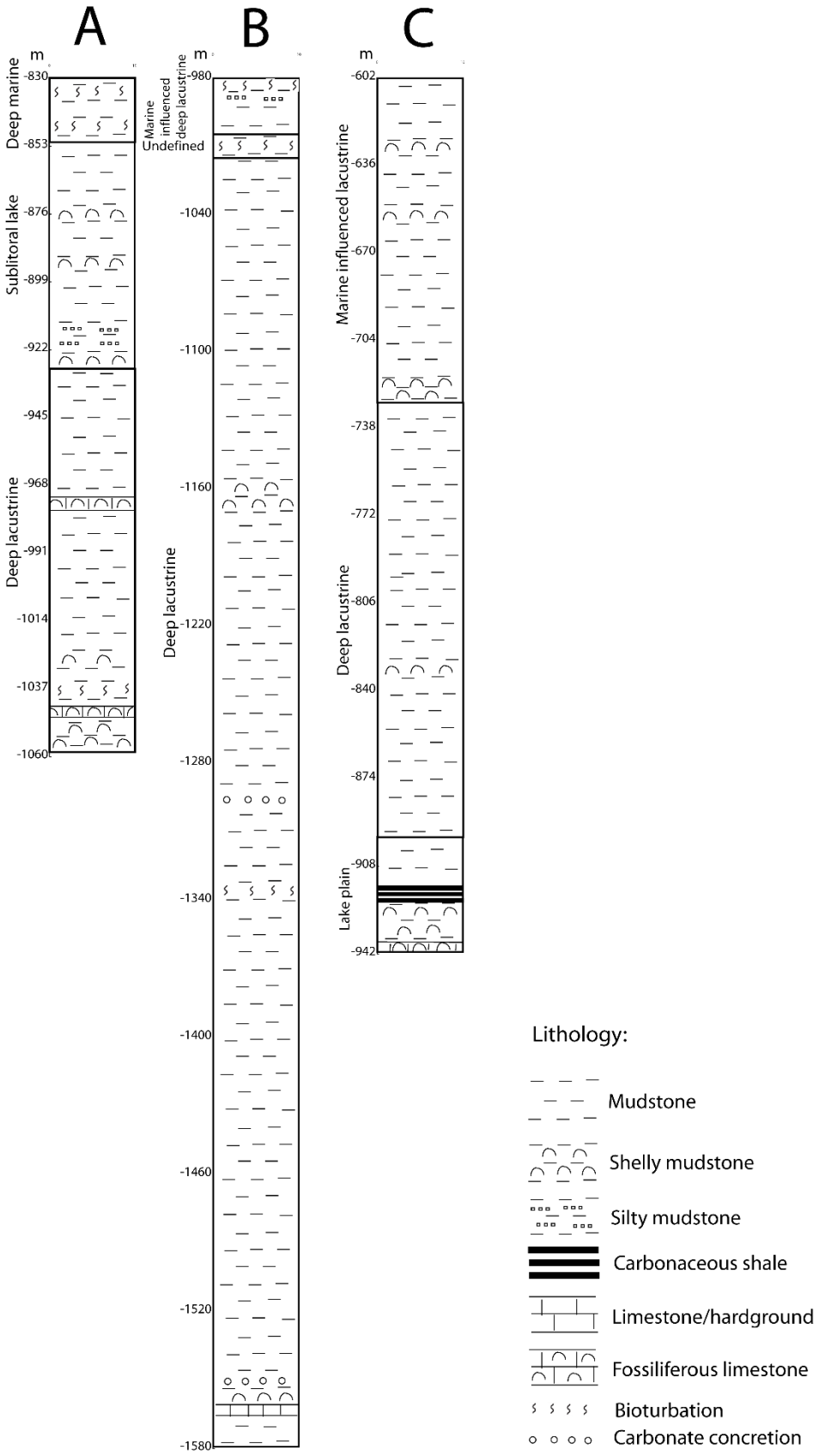

Figure 4. 2. *Lithological logs for cores retrieved from A, B and C boreholes. The TVD (true vertical depth) scale is in metres. The basic depositional environment of the each sediment interval is provided left to each log.*

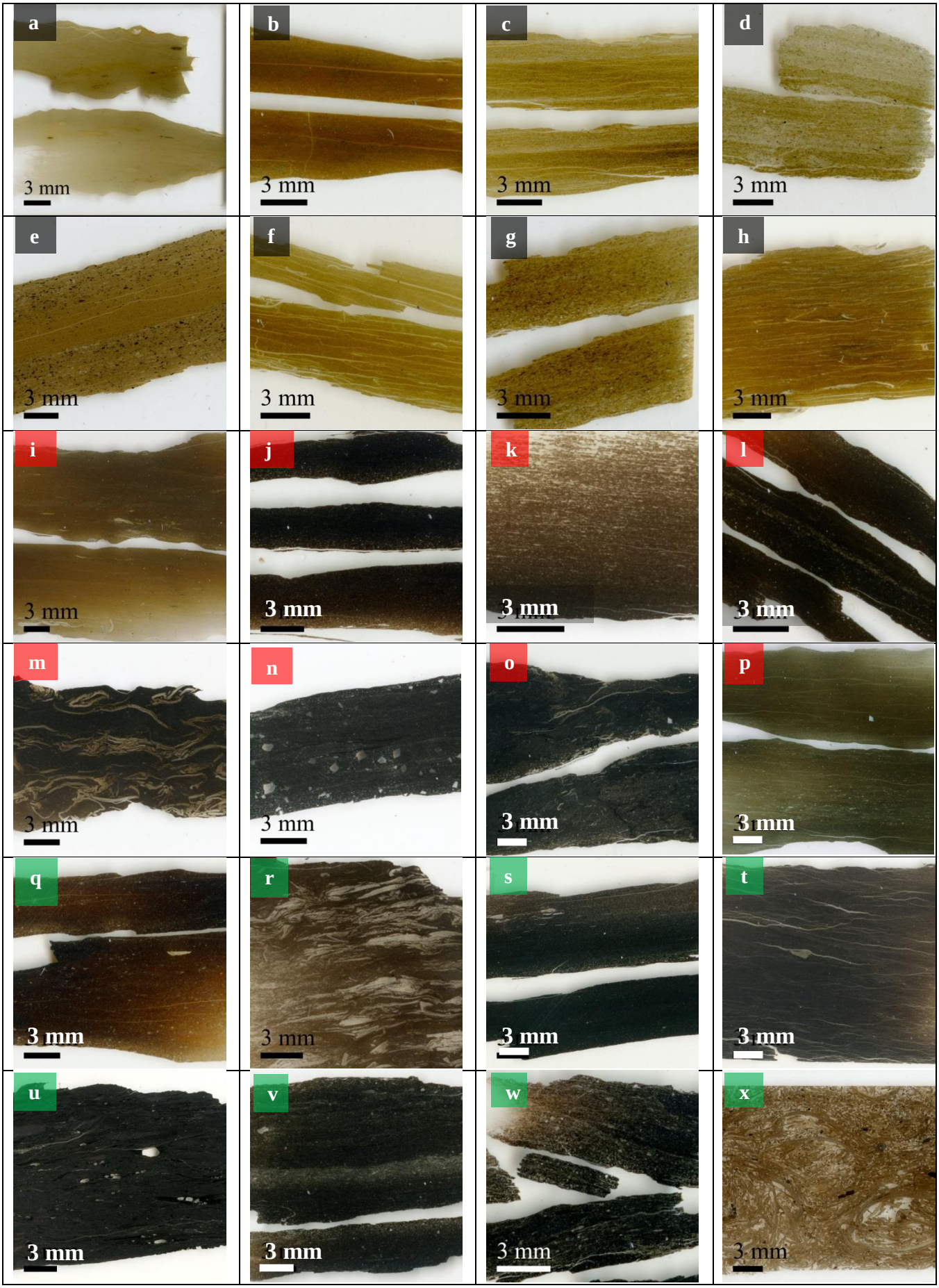
a
3 mm
b
3 mm
c
3 mm
d
3 mm
e
3 mm
f
3 mm
g
3 mm
h
3 mm
i
3 mm
j
3 mm
k
3 mm
l
3 mm
m
3 mm
n
3 mm
o
3 mm
p
3 mm
q
3 mm
r
3 mm
s
3 mm
t
3 mm
u
3 mm
v
3 mm
w
3 mm
x
3 mm

Figure 4. 3. *Scan micrographs of the selected Wealden Shale samples. In each well, samples originate from a number of different depositional settings. a) A10278: Deep marine, clay-rich siliclastic mudstone with biogenic sedimentary structures. Visible burrows are differentiated by their darker shades and flat, enlogated shapes. b) A10282: Deep marine, clay-rich siliciclastic mudstone. The shale fabric is homogeneous and lacks any biogenic structures. c) A10289: Visibly laminated clay-rich siliciclastic mudstone from the sublittoral lake setting. The lighter laminae are composed of silt-sized quartz grains and alternate with darker laminae dominated by the unresolved, fine-grained mineral matrix. d) A10299: Clay-rich siliciclastic mudstone from the sublittoral lake setting. The mudstone shows abundant silt-bearing laminae (light coloured). e) A10305: Clay-bearing fossiliferous mudstone from the sublittoral lake setting. Distinct lamination is a result of varied content of structured organic matter (black). f) A10320: Deep lacustrine, clay-rich siliciclastic mudstone. The shale fabric is fine-grained and homogeneous. g) A10326: Deep lacustrine, clay-bearing mudstone with abundant microfossils. h) A10342: Deep lacustrine, clay-rich siliciclastic mudstone with homogeneous fabric. i) B10444: Marine influenced, deep lacustrine, clay-rich siliclastic mudstone with biogenic sedimentary structures. The burrows are differentiated by their lighter colours and elongated shapes. j) B10455: Marine influenced, deep lacustrine, clay-rich siliciclastic mudstone. The shale fabric is homogeneous with the predominance of fine-grained constituents. k) B10458: Marine influenced, deep lacustrine, clay-rich siliciclastic mudstone with very scarce silt-sized grains. l) B10482: Deep lacustrine, clay-rich siliciclastic mudstone. A visible fossil-rich (light) lamina in the centre. m) B10494: Deep lacustrine, clay-bearing fossiliferous mudstone. Macro-sized fossils are embedded in the clay-rich matrix, forming distinct laminae. n) B10525: Deep lacustrine, clay-rich siliciclastic mudstone with abundant silt-size carbonate crystals (light). o) B10547: Deep lacustrine, clay-rich siliciclastic mudstone. The matrix is visibly diagenetically altered. p) B10562: Deep lacustrine, clay-rich siliciclastic mudstone with abundant pyrite (light lamina at the bottom). q) C10371: Marine influenced, lacustrine, clay-rich siliciclastic mudstone with visible silt-sized components (light). r) C10388: Marine influenced, lacustrine, clay-bearing fossiliferous mudstone. Macro-sized shells are embedded in the fine-grained matrix. s) C10397: Deep lacustrine, clay-rich siliciclastic mudstone. Macro-sized fossils* ***ARE*** *visible at the top. t) C10401: Deep lacustrine, clay-rich siliciclastic mudstone. u) C10418: Lake plain, clay-rich siliciclastic mudstone with sand-sized quartz grains. v) C10426: Lake plain, clay-rich siliciclastic mudstone interbedde with shell layers (light). w) C10432: Lake plain, clay-rich siliciclastic mudstone. The matrix is diagenetically altered. x) C10438: Lake plain, mollusc-packed grainstone. The interstices between the shell detritus are infilled with cement.*

Table 4. 2. *The TOC-normalized XRD mineralogical composition of selected Wealden shale samples in wt.% for wells A (0.5-0.7% Ro), B (1.6-2.4% Ro) and C (1.5-1.9% Ro). The TOC content (in wt.%) was determined with LECO.*

	A10282	A10305	A10320	A10326	A10342	C10388	C10401	C10418	C10426	B10458	B10482	B10533	B10547
Quartz	19.7	17.4	15.6	10.7	18.1	19.4	14.4	6.5	20.5	20.2	20.0	20.5	21.0
Plagioclase	0.7	0.7	0.3	0.9	0.0	1.1	1.2	1.0	1.7	0.8	0.2	0.8	1.9
K-Feldspar	0.5	0.9	0.0	0.5	0.0	0.4	1.5	2.5	1.9	0.4	0.0	0.0	0.4
Calcite	0.2	7.0	0.5	42.9	0.9	22.6	3.1	0.2	2.7	0.1	0.5	0.3	6.1
Dolomite	0.0	0.9	0.0	1.3	0.7	8.7	9.5	0.4	1.7	3.6	5.7	2.2	4.5
Siderite/ Ankerite	0.1	0.2	0.0	0.8	0.3	0.2	0.6	0.1	4.7	0.1	8.7	6.0	6.9
Pyrite	6.5	2.2	4.2	1.8	4.4	4.0	1.9	1.4	5.1	6.0	4.4	6.4	2.5
Marcasite	nd	0.2	nd	nd	nd	0.0	0.3	0.1	nd	0.6	nd	nd	nd
Anatase	0.4	0.4	0.3	0.1	0.1	0.5	0.5	0.7	0.5	0.7	0.6	0.6	0.5
Muscovite	5.0	2.8	4.6	1.1	2.4	4.4	6.6	3.5	8.3	5.9	7.0	3.8	4.4
Illite + I/S	42.0	39.7	44.4	24.4	46.8	29.5	36.2	44.5	42.5	42.4	42.1	49.8	40.5
Kaolinite	15.9	13.1	14.8	4.9	7.7	4.5	9.6	20.3	4.2	13.8	5.9	4.5	1.2
Chlorite	1.8	0.0	1.8	1.2	2.2	2.6	3.7	0.0	0.0	1.3	0.8	0.5	1.3
Gypsium	0.8	1.0	0.9	2.6	0.1	0.0	4.9	0.7	0.6	0.0	0.0	0.0	2.9
Halite	0.4	0.6	0.3	0.5	0.5	0.0	0.0	0.2	0.2	0.0	0.2	0.1	0.5
Bassanite	0.1	1.2	0.5	2.3	0.2	0.0	0.0	0.6	0.4	0.0	0.2	0.5	1.6
TOC	5.8	11.8	11.4	4.1	15.3	1.9	6.2	17.4	5.1	4.2	3.8	4.1	3.9
Total	100	100	100	100	100	100	100	100	100	100	100	100	100

The top marine mudstone is either visibly bioturbated, with silty burrows arranged in layers or lenses and occasional wood fragments (Figure 4.3a), or alternatively organic- and clay-rich with no biogenic sedimentary structures (Figure 4.3b; Fig 4.4a, b). The middle sublittoral lake shale (Figure 4.3c-e; Figure 4.4c, d) is on average more abundant in fossil debris and may show interlamination of clay-rich and silt-rich laminae (Figure 4.3c, d). Finally, the bottom, deep lacustrine shale shows the highest variability, and is represented by non-laminated, clay-rich siliciclastic mudstone (Figure 4.3f, h, Figure 4.4e, f, Figure 4.4i, j), bioturbated, silt-bearing, clay-rich mudstone, foraminifera and mollusc-, clay- and silt-bearing mudstone (Figure 4.3g, Figure 4.4g, h), and finally interbedded shelly limestone.

The size of the shell fraction varies across the A core, and is much coarser in the fossil-bearing mudstone (or wackstone) (> 0.5 mm), packstone and grainstone (> 3 mm) in comparison to the clay-rich mudstone (<0.3 mm). Calcite cement is more common in fossiliferous layers, and may infill intergranular porosity. Other types of cements sporadically present include replacement siderite/ankerite and kaolinite. Quartz is present in all rock types, with the content varying between ca. 10-20% in the samples analyzed. It forms angular, subangular or rounded grains from > 100 µm down to < 5 µm, either disseminated in the

matrix, concentrated in laminae or infilling burrows. Occasionally, silica cement infills porosity in carbonate-rich intervals. Finally, pyrite is present either as euhedral crystals < 5 µm, pyrite framboids > 30 µm, or infilling algal cysts. Pyrite is 2-7 wt.% and is less abundant in the fossil-rich shale.

The original heterogeneity of the Wealden Shale is still observable in the high maturity rocks, although often masked in thin sections by the dark colour of the shale matrix imparted by mature organic matter. In the marine-influenced, deep lacustrine shale interval from the top of the B core, the mudrock matrix may be partly homogenized, showing the presence of silty burrows (Figure 4.3i), or may alternatively have an undisturbed fabric (Figure 4.3j, k, Figure 4.5a-d). The bottom, deep lacustrine shale is more heterogeneous in terms of its composition and texture, but still with only rare biogenic material. If present, fossil debris is disseminated in the clay matrix (Figure 4.3m), or densely packed and cemented forming a hardground bed. Clay-rich mudstone is usually organic-rich (TOC > 2 wt.%), either non-laminated (Figure 4.5g, h, l) or finely laminated (Figure 4.3n, p, Figure 4.5e, f), with occasional cement or microfossils (Figure 4.3o, Figure 4.5i, j).

The C core shale shows similar variations, with the top, marine-influenced lacustrine shale showing a varied abundance of micro- and macrofossil debris (Figure 4.3q, r; Figure 4.6a, b). The middle, deep lacustrine shale is usually clay- and organic-rich (Figure 4.3s, t; Figure 4.6c-f). The highest variability in the shale composition and texture was encountered in the bottom, lake plain deposits represented by clay-rich siliciclastic mudstone (Figure 4.3w), often intebedded with shelly (Figure 4.3v; Figure 4.6i, j) or coaly layers (Figure 4.3u; Figure 4.6g, h) and finally, by carbonate-dominated and clay-poor grainstone (Figure 4.3x).

In contrast to most of the investigated low maturity shale samples from well A, in both high maturity cores the original variation of shale components is overprinted by advanced diagenetic processes. This means that while in the siliciclastic mudstone samples the clay content still varies between 41-68% (Table 4.2), the carbonate content is controlled not only by the amount of shell debris, but also the presence of diagenetic ferroan dolomite. This is concentrated in shell beds, either as inter- and intraparticle cement, or as discrete, replacement dolomite-siderite rhomboids. Dolomite-replacement rhomboids are also common in the clay-rich matrix, with sizes between <5 µm to over 500 µm. Other diagenetic features include calcite cement, especially abundant in fossil-rich laminae and beds and irregular silica patches. Overall, the total content of carbonates in the analyzed high maturity shale samples varies between < 1% up to > 30%, with the most carbonate-rich rocks showing the highest fossil abundance.

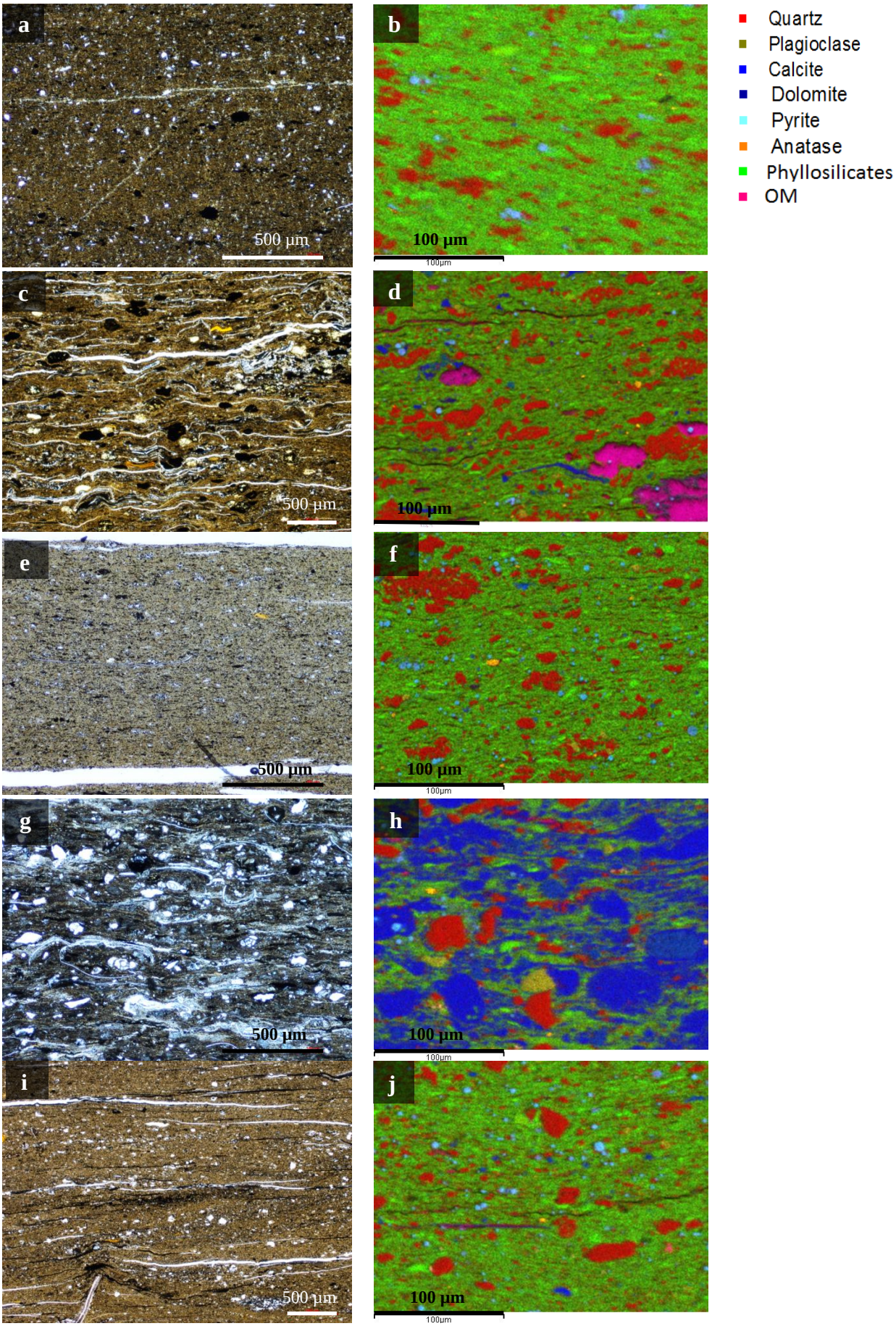
a
500 µm
b
100 µm
c
500 µm
d
100 µm
e
500 µm
f
100 µm
g
500 µm
h
100 µm
i
500 µm
j
100 µm
Quartz
Plagioclase
Calcite
Dolomite
Pyrite
Anatase
Phyllosilicates
OM

Figure 4. 4. *Transmitted light micrographs (left) and RGB colour mode EDX maps (right) displaying textural features of the Wealden Shale from the immature/early mature well A, a, b): A10282 deep marine, clay-rich siliciclastic mudstone; c, d): A 10305 sublittoral lake, clay-rich siliciclastic mudstone; e, f): A10320 deep lacustrine, clay-rich siliciclastic mudstone; g, h): A10326 deep lacustrine, clay-bearing fossiliferous mudstone; i, j): A10342 deep lacustrine, clay-rich siliciclastic mudstone. In the transmitted light micrographs black colour denotes pyrite or pyritized algae bodies (c), white – fossils (c, g) or quartz grains (i), brown – clay matrix. White elongated features are fractures.*

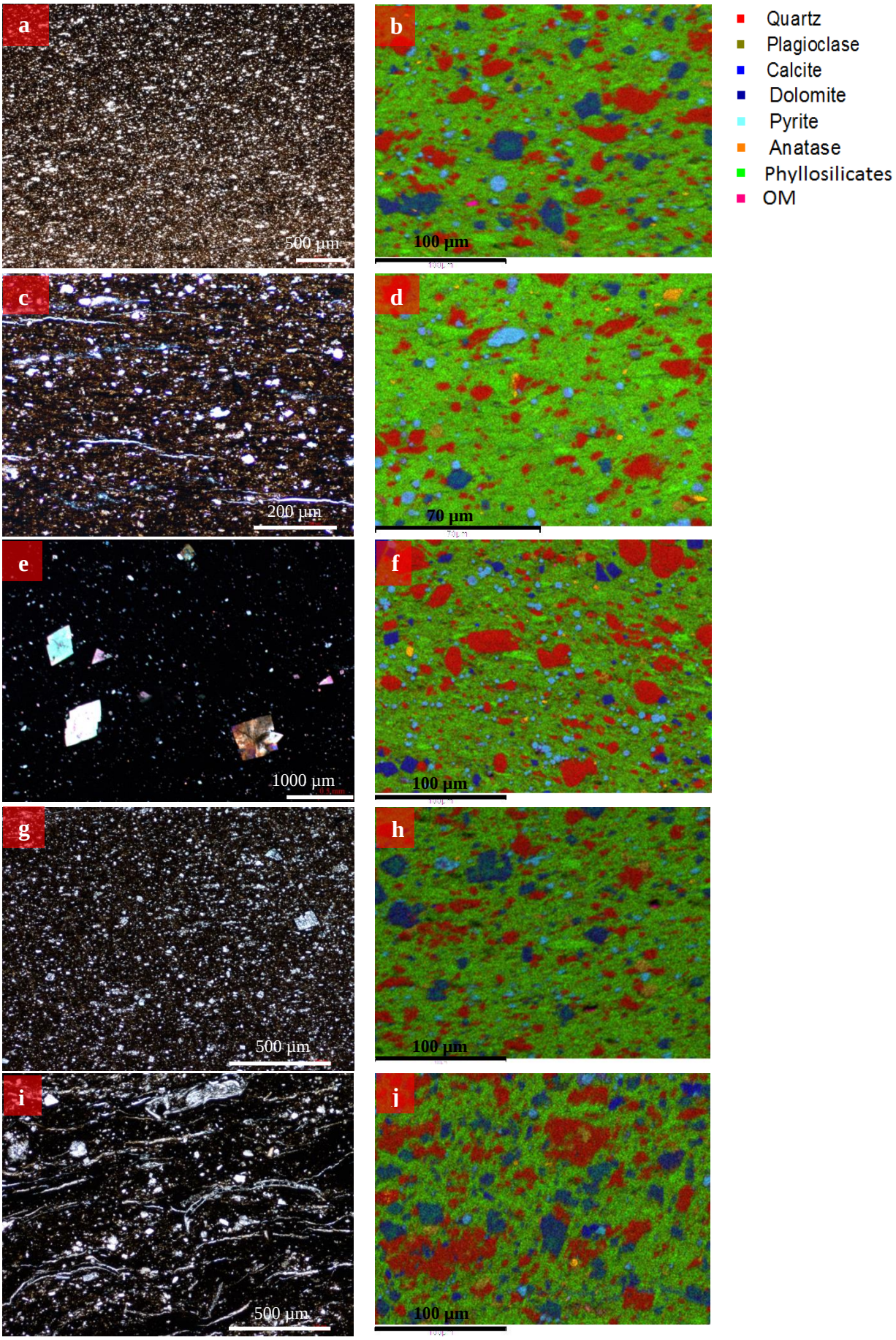
a
500 µm
b
100 µm
Quartz
Plagioclase
Calcite
Dolomite
Pyrite
Anatase
Phyllosilicates
OM
c
200 µm
d
70 µm
e
1000 µm
f
100 µm
g
500 µm
h
100 µm
i
500 µm
j
100 µm

Figure 4. 5. *Transmitted light micrographs (left) and RGB colour mode EDX maps (right) of the Wealden Shale from the overmature well B. a, b): B10455 marine influenced, deep lacustrine, clay-rich siliciclastic mudstone; c, d): B10458 marine influenced deep lacustrine, clay-rich siliciclastic mudstone; e, f): B10525 deep lacustrine, clay-rich siliciclastic mudstone; g, h): B10533 deep lacustrine, clay-rich siliciclastic mudstone; i, j): B10547 deep lacustrine, clay-rich siliciclastic mudstone. In the transmitted light micrographs brown and dark brown colour denotes clay-rich matrix, white – quartz and diagenetic carbonates, or fossils (i). White elongated features in c) are fractures.*

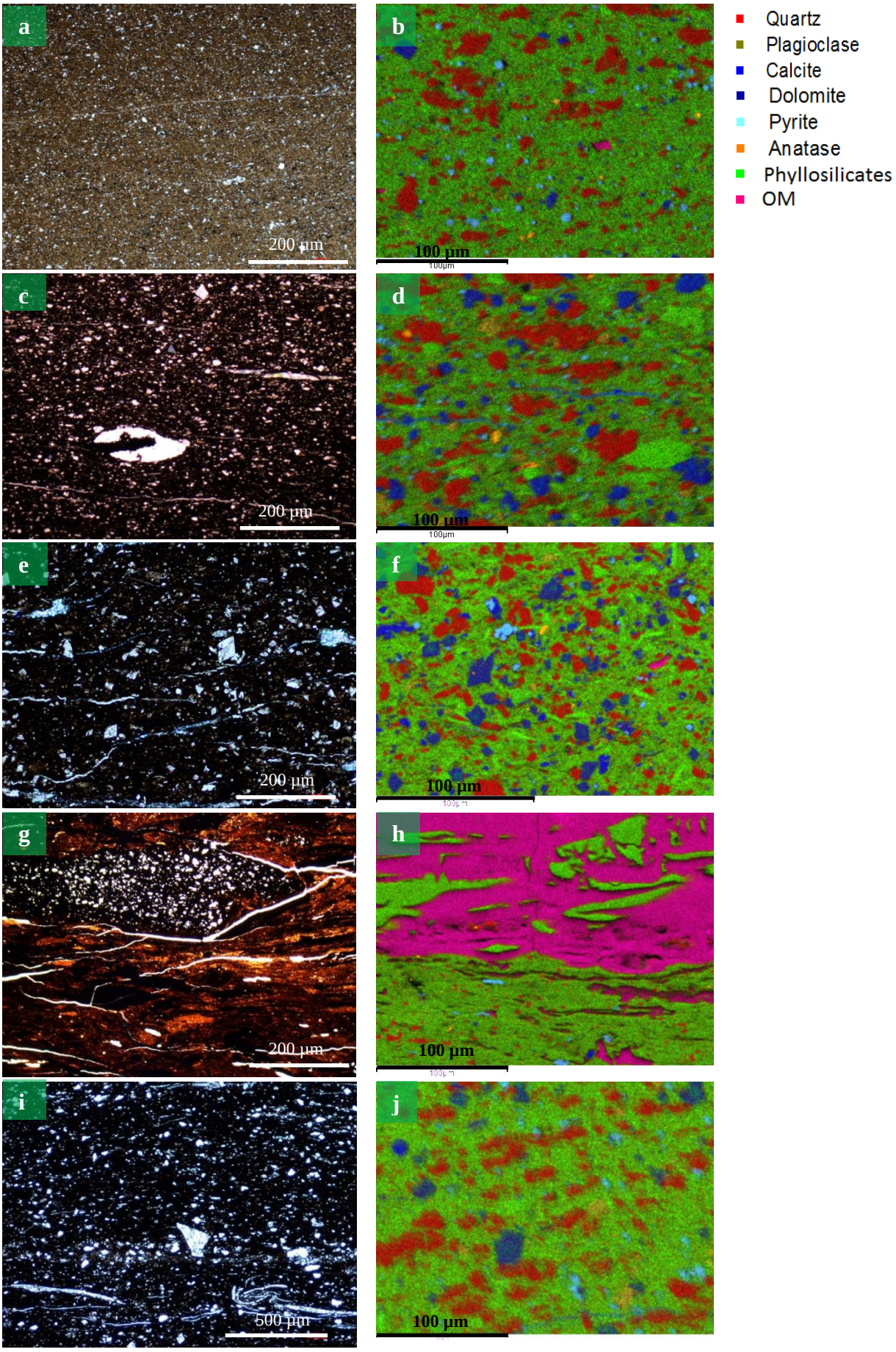
a
200 µm
b
100 µm
c
200 µm
d
100 µm
e
200 µm
f
100 µm
g
200 µm
h
100 µm
i
500 µm
j
100 µm
Quartz
Plagioclase
Calcite
Dolomite
Pyrite
Anatase
Phyllosilicates
OM

Figure 4. 6. *Transmitted light micrographs (left) and RGB colour mode EDX maps (right) of the Wealden Shale from the overmature well C. a, b): C10371 marine influenced lacustrine, clay-rich siliciclastic mudstone; c, d): C10397 deep lacustrine, clay-rich siliciclastic mudstone; e, f): C10401 deep lacustrine, clay-rich siliciclastic mudstone; g, h): C10418 lake plain, clay-rich siliciclastic mudstone; i, j): C10426 lake plain, clay-rich siliciclastic mudstone. In the transmitted light micrographs brown and dark brown colour denotes clay-rich matrix, white – quartz and diagenetic carbonates, or fossils (i). White elongated features in e) and g) are fractures.*

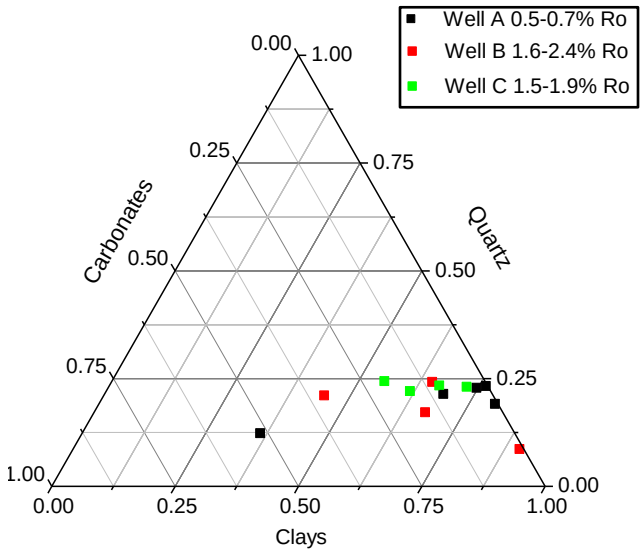

Figure 4. 7. *Ternary diagram showing the basic mineralogy of the Wealden shale suite. Samples taken from three cores: A (Ro 0.5-0.7%), B (Ro 1.6-2.4%) and C (Ro 1.5-1.9%). German Wealden consists of a lithologically diverse group of rocks including mudstones and limestones. Note a negative correlation between a proportion of clays and carbonates implying, that those are the main components building the shale framework.*

In shales of all maturities we recorded the presence of horizontal fractures sealed with gypsum/bassanite, and in high maturity rocks occasionally with pyrite. The presence of pyrite-sealed fractures suggests that those are naturally occurring in the subsurface. On the other hand, the genesis of sulfate minerals may be related to the reaction of calcium carbonate present in shales with acid sulfate from the oxidative weathering of pyrite (Burkart *et al.*, 2004).

Organic matter variation as a function of maturity and depositional setting

We recorded a significant drop of Hydrogen Index from the mean value 591 to 30 and 40 mg/g between the well A and wells B and C (Table 4.3, Table 4.A1). This drop is associated with a decrease in the S2 hydrocarbon potential but no change in the S1 content. The low S1 content of the A well shale succession suggests it has not yet started generating hydrocarbons. Despite a presumed drop of the carbon content between early oil window and gas window maturities (Jarvie *et al.*, 2007), the mean organic carbon is not significantly different between low and high maturity wells, yielding average values 2.5% (1.8-3.8%), 2.4% (2.1-2.5%) and 2.1% (1.7-2.3%) in wells A, B and C respectively (Table 4.4). In contrast, there is a higher contribution of TOC-rich samples (> 2 wt.%) in the gas window shale, and a higher

abundance of shales with TOC < 2% in the least mature well (Figure 4.8). This distribution of organic content reflects the different palaeogeographic position of the three sampled cores in the basin and the different amount of organic matter originally buried in sediments (Figure 4.1b).

Table 4. 3. *Rock-Eval data statistics (median and 95% confidence interval) for Wealden shale, samples taken every 1 m, wells A (0.5-0.7% Ro), B (1.6-2.4% Ro) and C (1.5-1.9% Ro).*

Sample	Depth (m)	S1 (mgHC/g)	S2 (mgHC/g)	S3 (mgHC/g)	HI (mgHC/gTOC)	OI (mgHC/gTOC)	Tmax
Well A	832-1056	0.2 (0.1-0.3)	15.8 (9.4-27.0)	1.0 (0.9-1.2)	591 (493-637)	38 (34-50)	438 (437-439)
Well B	981-1578	0.1 (0.1-0.1)	0.6 (0.6-0.7)	0.6 (0.5-0.7)	30 (26-38)	27 (23-33)	462 (372-485)
Well C	604-942	0.3 (0.2-0.5)	0.9 (0.8-1.2)	0.8 (0.7-1.0)	40 (37-76)	35 (29-46)	472 (463-497)

Table 4. 4. *TOC and HI data statistics (median and 95% confidence interval) for Wealden shale, samples taken every 1 m, wells A (0.5-0.7% Ro), B (1.6-2.4% Ro) and C (1.5-1.9% Ro). Samples originate from core intervals assigned to different depositional settings (ExxonMobil, unpublished).*

Sample	Depth (m)	TOC (%)	95% CI	HI	95% CI
Well A	**832-1056**	**2.5**	**1.8-3.8**	**591**	**493-637**
Deep marine	832-850	1.8	1.0-4.3	203	132-499
Sublittoral lake	910-928	3.8	2.4-5.4	704	581-770
Deep lacustrine	966-1056	2.2	1.6-3.8	604	491-669
Well B	**981-1578**	**2.4**	**2.1-2.5**	**30**	**26-38**
Marine influenced deep lacustrine	981-1003	2.1	1.2-3.6	67	61-84
Undefined	1006-1016	0.8	0.6-0.9	62	60-70
Deep lacustrine	1150-1578	2.5	2.2-2.7	25	21-28
Well C	**604-942**	**2.1**	**1.7-2.3**	**40**	**37-76**
Marine influenced deep lacustrine	604-728	1.9	1.3-2.2	147	130-166
Deep lacustrine	828-890	2.5	2.0-3.2	37	33-28
Lake plain	920-942	1.3	1.0-4.0	29	22-32

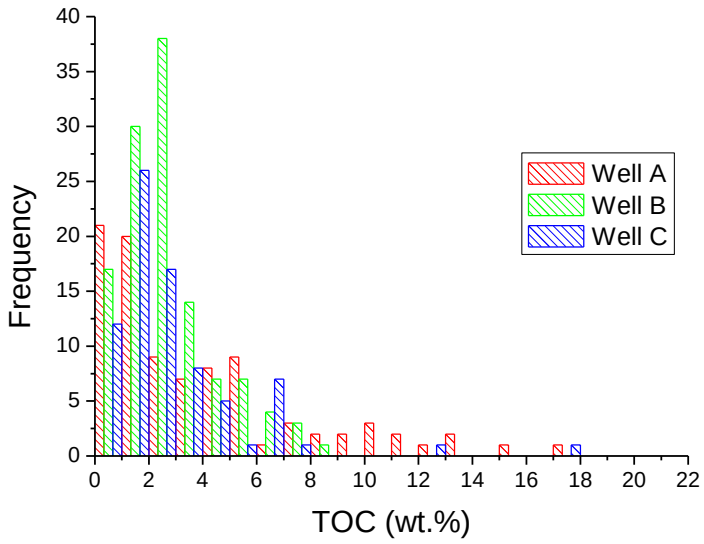

Figure 4. 8. *Histogram of Total Organic Carbon of the Wealden Shale. Measurements were taken every 1 m from each available core and thus represent a true distribution of TOC.*

Following the lateral heterogeneity, Wealden organofacies are not homogeneous within single wells, but instead show interbedding of kerogen Type I with kerogen Types II and III (Figure 4.9). The TOC variation is depth and time dependent (Table 4.4, Table 4.A1) and thus reflects fluctuations in the base level of the Cretaceous lake. For instance, in well A, a significant input of Type II and III kerogen coincides with increased marine influence on sedimentation after the W3 interval, resulting in the lowest mean HI of 203 mg/g. The TOC variation is large, between 0.3-17.5%, with both low and high values found in the deep marine, sublittoral lake and deep lacustrine shale. The highest mean TOC value is characteristic of the sublittoral lake shale (3.8%), followed by the deep lacustrine shale (2.2%), and the deep marine shale (1.8%). High TOC (> 3%) shales are also hydrogen rich (HI > 500 mg/g) and have well preserved kerogen Type I or II (Figure 4.3b-h). In contrast, low TOC (< 1%) shales are low in hydrogen (HI < 500 mg/g), have kerogen Type II or III and are typically associated with visibly bioturbated shales (Figure 4.3a). Shales with intermediate organic contents (1-3%) can be either hydrogen rich (HI > 500 mg/g), but with organic matter diluted by a fossil debris, or depleted of hydrogen (HI<500 mg/g), partly bioturbated, enriched in macrofossils, or more resistant terrestrial organic matter, implying a more proximal location at the time of deposition. In general, as supported by the petrographic evidence, depletion in hydrogen in the A well is a function of poor preservation rather than increased input of terrestrial organic macerals.

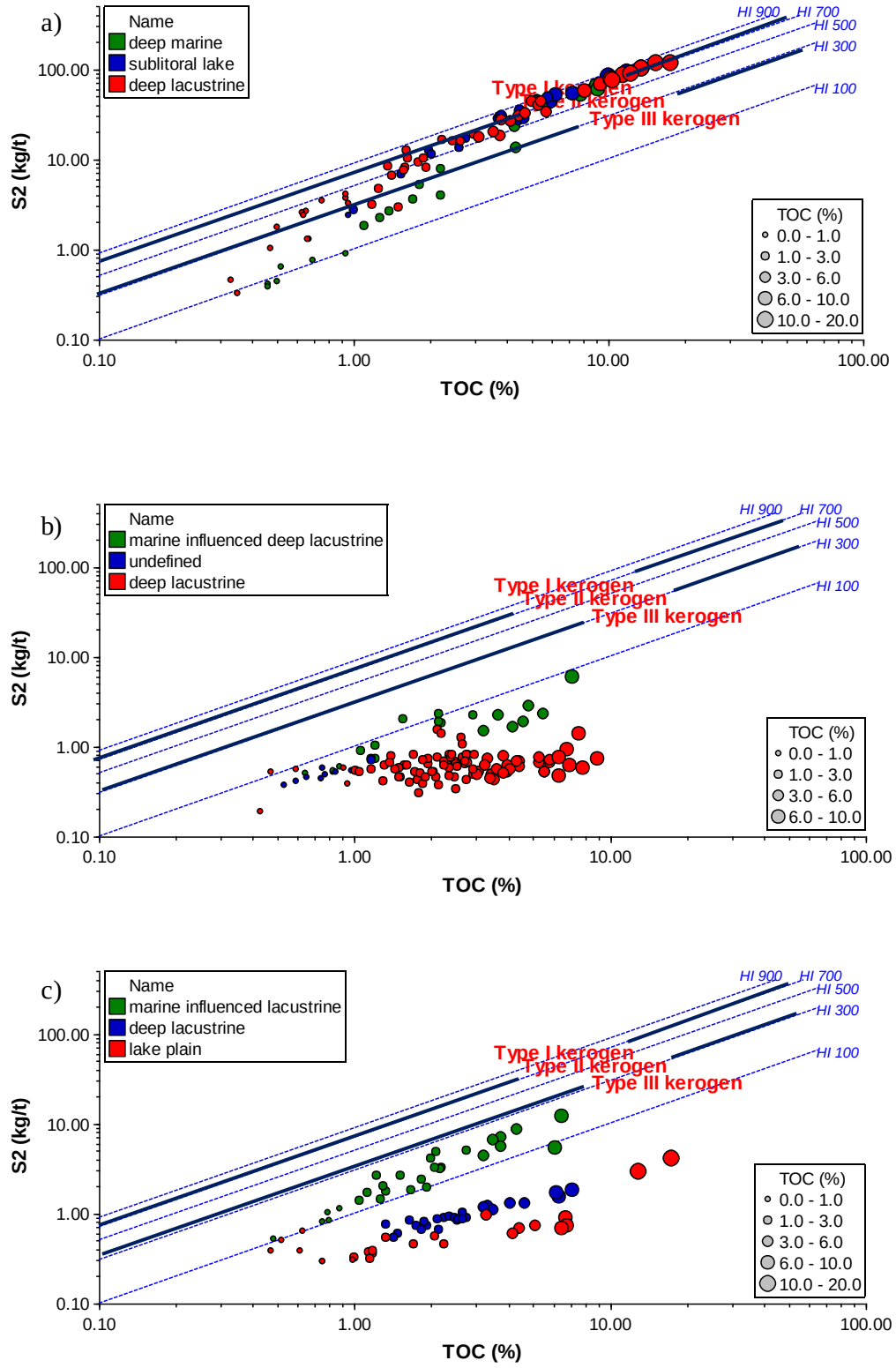

Figure 4. 9. *Kerogen type and depositional setting of the Wealden Shale from wells a) A, Ro 0.5-0.7%), b) B, Ro 1.6-2.4% and c) C, Ro 1.5-1.9%.*

At higher stages of maturity, remaining hydrocarbon potential is no longer an indicator of the kerogen type, and all shales plot within the field of kerogen type III (Figure 4.9b, c). In contrast to the low maturity shale, the most organic-rich shales are not always the most hydrogen-rich due to differences in both kerogen type and maturity (Table 4.4, Table 4. A1). For instance in the C well, shallower in the core shales from the marine-influenced lacustrine setting have higher HI values (mean 147 mg/g) but lower TOC (mean 1.9%) than deeper-buried shales from the deep lacustrine setting (means 37 mg/g and 2.5% respectively). Similarly in the well B, deep lacustrine shale with a marine influence from the top of the core shows a higher hydrogen index (mean 67 mg/g) but similar TOC compared to deep lacustrine shale from the bottom of the core (mean 25 mg/g and 2.5% respectively).

In both B and C shale, the organic richness variation is significant, with TOC values ranging between 0.4-9% in well B and 0.5-17% in well C. The lowest organic content values were recorded in shales showing the presence of bioturbation, macrofossils, or silt laminae, all implying poorer preservation and/or dilution of organic matter (Figure 4.3i, x). Such observations are consistent with the lowest recorded mean TOC (1.3%) in the C core in shale from the lake plain setting. Significantly higher TOC values are encountered in the deep lacustrine shale from both overmature wells, with a mean TOC of 2.5%. The highest measured TOC values (> 10%) are associated with coaly organic matter found in the lake plain setting shales from the C core (Figure 4.3u).

Vitrinite reflectance measurements on selected samples confirm different maturities of the shale from well A (Ro = 0.7% on 1 sample) and from wells B and C (1.6-1.9% on 3 samples) (Table 4.5). The marginally higher reflectance of the least mature sample and significantly lower reflectance of the sample from the B well, as compared to Rippen *et al.* (2013), likely results from inaccuracies of the vitrinite reflectance method in mudrocks with only scarce vitrinite. However, our measurements of the VR in the A and B wells are consistent with those reported elsewhere (Egs-ploration, unpublished; Littke, 2008, unpublished) and therefore are assumed to be valid for this section.

Table 4. 5. *Mean vitrinite reflectance values at random vitrinite particles in selected samples from the cores A, B and C.*

Sample	Depth (m)	No. of measurements	Mean (%)	Standard deviation (%)
A10305	924	19	0.7*	0.1
B10458	1001	59	1.9*	0.2
C10388	721	122	1.6	0.2
C10401	857	75	1.9	0.1

*Please note that the value deviates from those reported by Rippen *et al.* (2013).

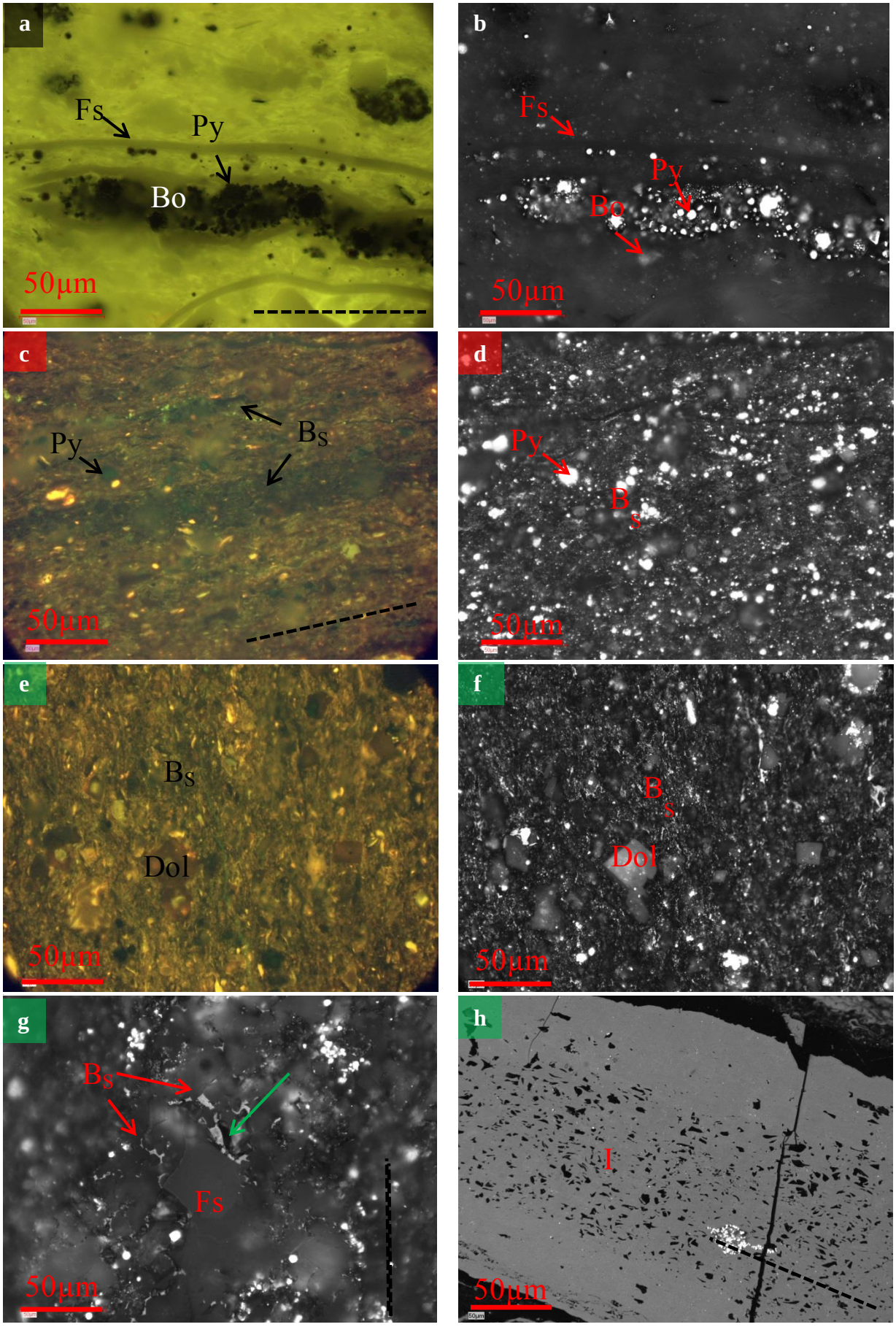
a
Fs
Py
Bo
50µm
b
Fs
Py
Bo
50µm
c
Py
Bs
50µm
d
Py
Bs
50µm
e
Bs
Dol
50µm
f
Bs
Dol
50µm
g
Bs
Fs
50µm
h
I
50µm

Figure 4. 10. *Oil immersion micrographs of Wealden Shale. Horizontal scale bars denote 50 µm. Dashed lines indicate direction of a bedding plane. a) (A10305): Fluorescence mode micrograph of sublittoral lake, clay-rich siliciclastic shale of measured maturity Ro 0.7%. Strong fluorescence of the matrix is due to the presence of the algal material. b) Normal incident light micrograph of the same field as a). Structured algal liptinite is common, forming well-preserved bodies of Botryococcus (Bo). c) (B10458): Fluorescence mode micrograph of marine influenced deep lacustrine, clay-rich siliciclastic mudstone of measured maturity Ro 1.9%. The bituminous groundmass exhibits no fluorescence and no structured algal liptinite is present. d) Normal incident light micrograph of the same field as c). Solid bitumen (B_S) is present, concentrating in microfractures. e) (C10401): Fluorescence mode micrograph of deep lacustrine, clay-rich siliciclastic mudstone of measured maturity Ro 1.9%. The bituminous groundmass exhibits only very weak fluorescence. f) Normal incident light micrograph of the same field as e). A tight network of irregularly-shaped solid bitumen fills the intergranular space within the clay matrix, and concentrates in compaction shadows of mineral grains. g) (C10388): Normal incident light micrograph of marine influenced lacustrine, clay-bearing fossiliferous mudstone of measured maturity Ro 1.6%. Solid bitumen phase is highly concentrated, filling intra- and intergranular space within disseminated fossil fragments. h) (C10418): Normal incident light micrograph of lake plain, clay-rich siliciclastic mudstone (no maturity measured). Semifusinite and fusinite constitute principal macerals. Bo – Botryococcus, Bs – solid bitumen, I – inertinite, Dol – dolomite, Fs – fossil, Py – pyrite.*

As a consequence of maturity changes, the maceral types found in shales of different maturities show a gradual change in type, volume and colour. For instance, in the least mature sublitoral lake A10305 shale, structured algal liptinite is common, forming well-preserved or selectively pyritized bodies of Botryococcus, and co-exists with thin, flat and fluorescent lamellar alginate interlayered with clay laminae and the so-called matrix bituminite (Tao *et al.*, 2012) (Figure 4.10a, b). Terrestrial macerals, including vitrinite and inertinite, are dispersed and are present in very low abundance. At the gas window maturity (Ro > 1.9%; samples B10458 and C10401), the groundmass organic matter exhibits only very weak fluorescence and no structured algal liptinite is present (Figure 4.10c-f). Instead, a tight network of irregularly-shaped solid bitumen fills the intergranular space, both within the clay matrix, and especially in compaction shadows of mineral grains. The bitumen phase is a visually dominant organic component of the overmature shale. In a shell detritus-bearing mudstone at Ro 1.6% maturity, the solid bitumen phase is even more concentrated, filling intra- and intergranular space within disseminated fossil fragments (Figure 4.10g). No bitumen was noted in an organic-rich mudstone from the lake plain setting with semifusinite, fusinite and vitrinite as principal macerals (Figure 4.10h).

Grain density, total and mercury porosity, and pore throat size distribution

Grain density

The average density of the mineral matrix shows significant variation between samples within and between wells (Table 4.6 and Figure 4.11a) and is influenced by the variation in the mineralogical composition (Figure 4.11b). For the three wells, density values exhibit a single mode between 2.6-2.8 g/cm3, with a higher frequency of lower density samples in the least mature well and a larger frequency of samples with higher density in the overmature shale. This distribution implies the primary role of maturity inducing a change in the density of the organic component and of the bulk shale (Okiongbo *et al.*, 2005). In the least mature A samples, grain density varies between 2.1 and 3.0 g/cm^3 and decreases significantly with an increasing content of organic carbon (Figure 4.11c). Although a similar variation, from 2.2 to 2.9 g/cm^3, is observed in the shale from the C well, the density of the organic-rich rocks (TOC > 5%) is always higher in the mature shale. For shales with organic carbon contents < 5%, due to elevated content of high grain density carbonate component in the A shale, densities of the A and C shale overlap. In the investigated sample suite from the C well, the

lowest density shale, 2.2-2.3 g/cm^3, shows the lowest pyrite content and the highest TOC and contains predominantly type III kerogen. The highest densities, > 2.7 g/cm^3, occur where there are interbedded carbonate microconcretions. In the B well, the spread in shale grain density is the lowest, between 2.5-3.1 g/cm^3, and coincides with the smallest variation in the organic content.

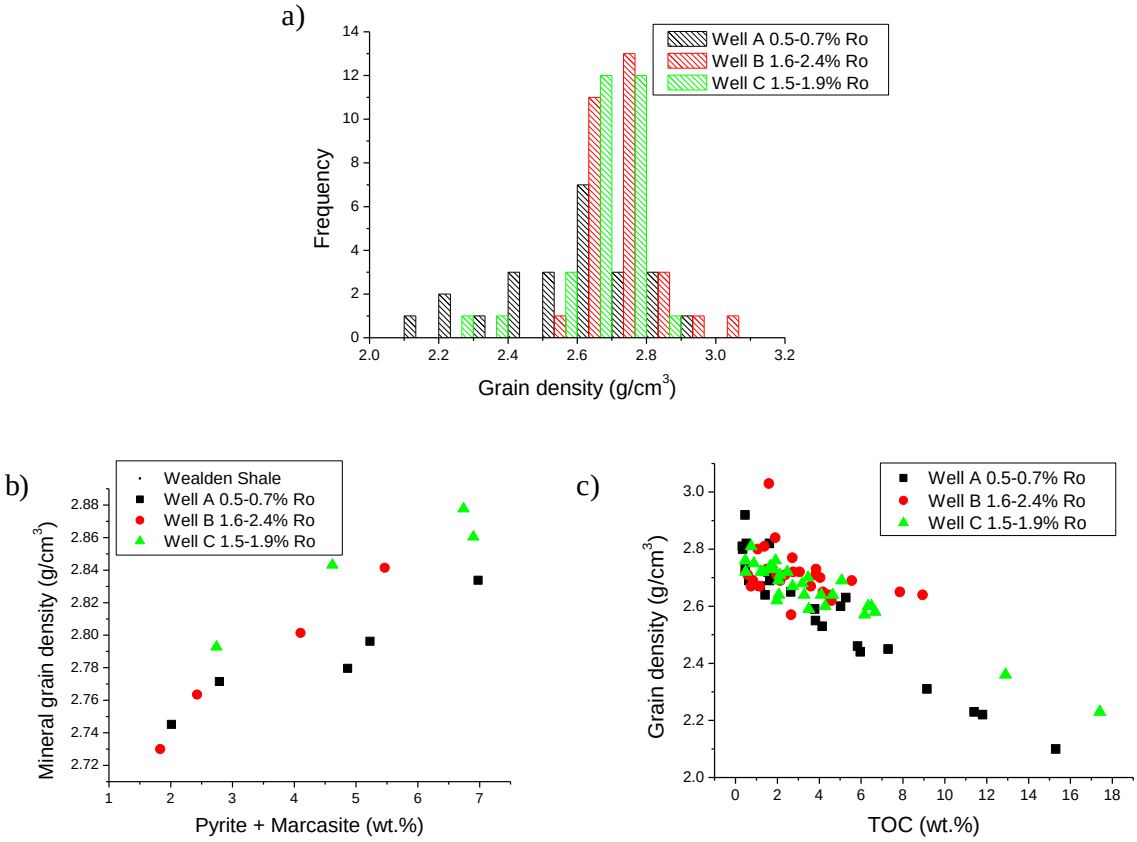

Figure 4. 11. *Grain density variation in shale of different maturity. a) Histogram of grain density distribution of Wealden shale from wells A, B and C. Density values exhibit a mode between 2.6-2.8 g/cm^3, with higher frequency of lower density samples in the least mature well and larger frequency of samples exhibiting higher density in the overmature shale. b) At all maturities grain density is influenced by the mineralogical composition, with a strong positive influence of the pyrite content. c) Organic content has a negative influence on grain density values. In the most organic rich shale (TOC > 5%) at any given content of organic carbon, density values of the overmature shale exceed those measured in the least mature shale.*

Table 4. 6. *Statistics for grain density and porosity data obtained with different techniques for selected Wealden shale samples, wells A (0.5-0.7% Ro), B (1.6-2.4% Ro) and C (1.5-1.9% Ro). For the porosity data, average values and standard deviation are provided, while for the remaining data, median and 95% confidence interval.*

Well	Number of samples	Total porosity (%)	Hg porosity (%)	Porosity < 5.6 nm (%)	Hg access radius (nm)	Grain density (g/cm^3)
Well A	24	9.8 +/-4.4	7.6 +/-3.8	2.2 +/-1.7	19.0 (11.3-25.9)	2.64 (2.52-2.70)
Well B	30	7.6 +/- 2.5	5.3 +/-1.7	2.3 +/-1.6	8.3 (7.6-9.2)	2.71 (2.69-2.73)
Well C	30	7.6 +/-2.9	5.4 +/-2.2	2.1 +/-1.4	9.1 (8.0-10.8)	2.69 (2.64-2.72)

Total porosity

Measurement of grain densities enables the estimation of total porosities of a lithologically varied suite of shale samples. Experimentally obtained raw total porosity was corrected for pores intersected by the sample surface (conformance correction), responsible for an increase in the volume of mercury at the very start of the injection experiment (Figure 4.12b) (Comisky *et al.*, 2011). The conformance error occurs when mercury does not fill the whole empty space around the sample in a penetrometer due to the sample roughness, until higher pressures are applied (Sigal, 2009). In order to estimate a true radius of the onset of Hg intrusion into a porous network within each sample, cumulative mercury volume data were compared with distribution of pore throats as calculated with the Washburn equation (Washburn, 1921) (Figure 4.12a). To make a comparison more effective, calculated areas of pore throats cross-sectioned by a theoretical plane were grouped in bins of an increasing size and plotted as a function of pore volume intruded by mercury (Bernal and Bello, 2001; Houben *et al.*, 2013). The resulting fractal distribution of pore throats was fitted with 2-3 linear regression lines (Figure 4.12c), with the line of the smallest slope (typically < 1.0) describing the largest pores interpreted as an artifact, created due to intersection of pores by the sample surface. The true injection of Hg to pore bodies is described by a regression line with a slope usually > 2, and corresponds to a rise in the pore volume density beyond the background values. Consistent with Comisky *et al.* (2011), the estimated true radius of intrusion is up to 3 orders of magnitude lower than the apparent radius derived from the raw data.

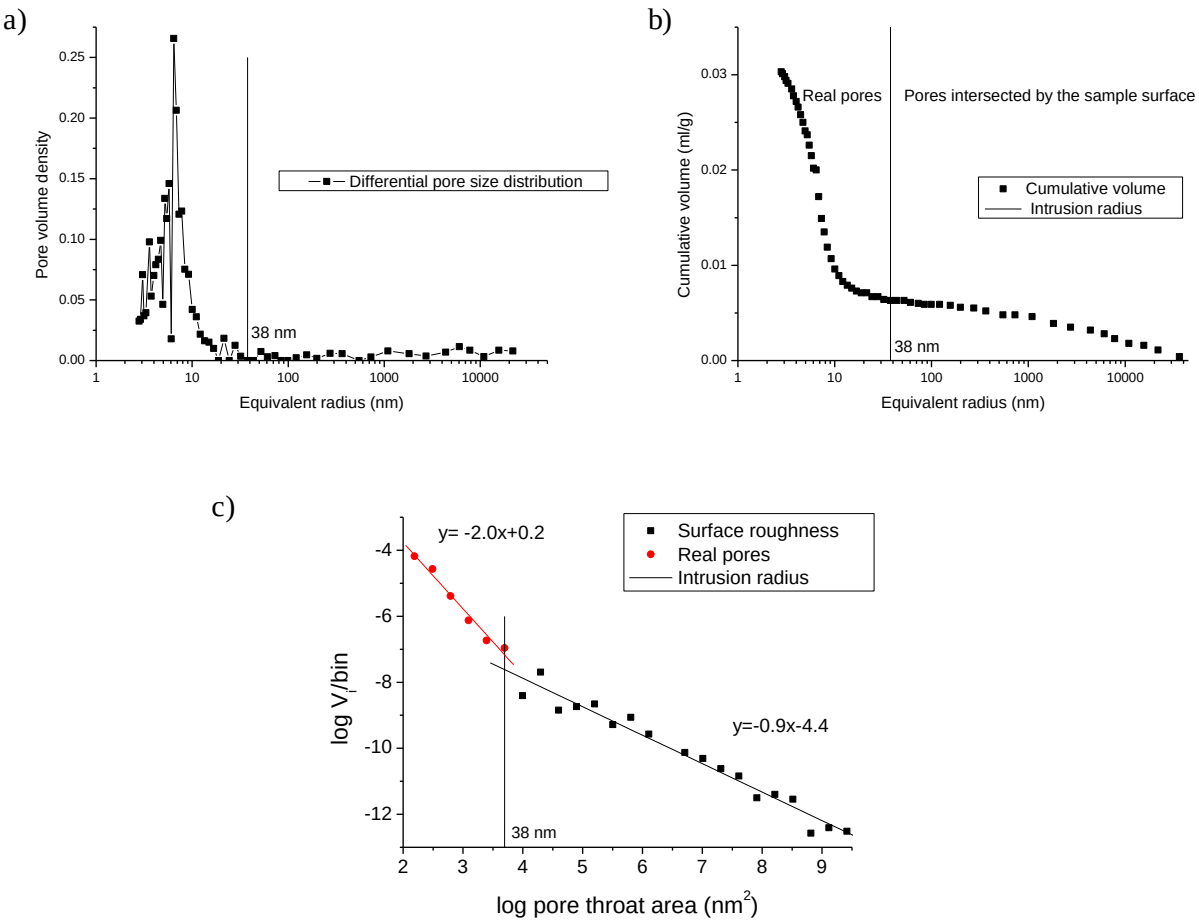

Figure 4. 12. *a) Pore volume density, b) cumulative volume of intruded mercury and c) fractal distribution of pores in the B10482 sample. Pores exhibit non-uniform fractal distribution with pores > 38 nm (slope -0.9) interpreted as those intersected by the sample surface (surface roughness) and pores < 38 nm (slope -2.0) interpreted as pores accessed through corresponding throats.*

Measured total porosities show a large range in shales of both low and high maturity (Table 4.6, Table 4.A2 and Figure 4.13a). At Ro = 0.5-0.6% porosities vary between 1.9-18.3%, with an average value of 9.8 +/-4.5%. In the high maturity wells, porosities show a higher range of values, varying from 1.6 to 12.5% and 1.1 to 12.4% in wells B and C respectively. In the overmature shales, the average total porosities are also lower than in the early mature well, amounting to 7.6 +/-2.5% and 7.6 +/-2.9% in the B and C wells respectively.

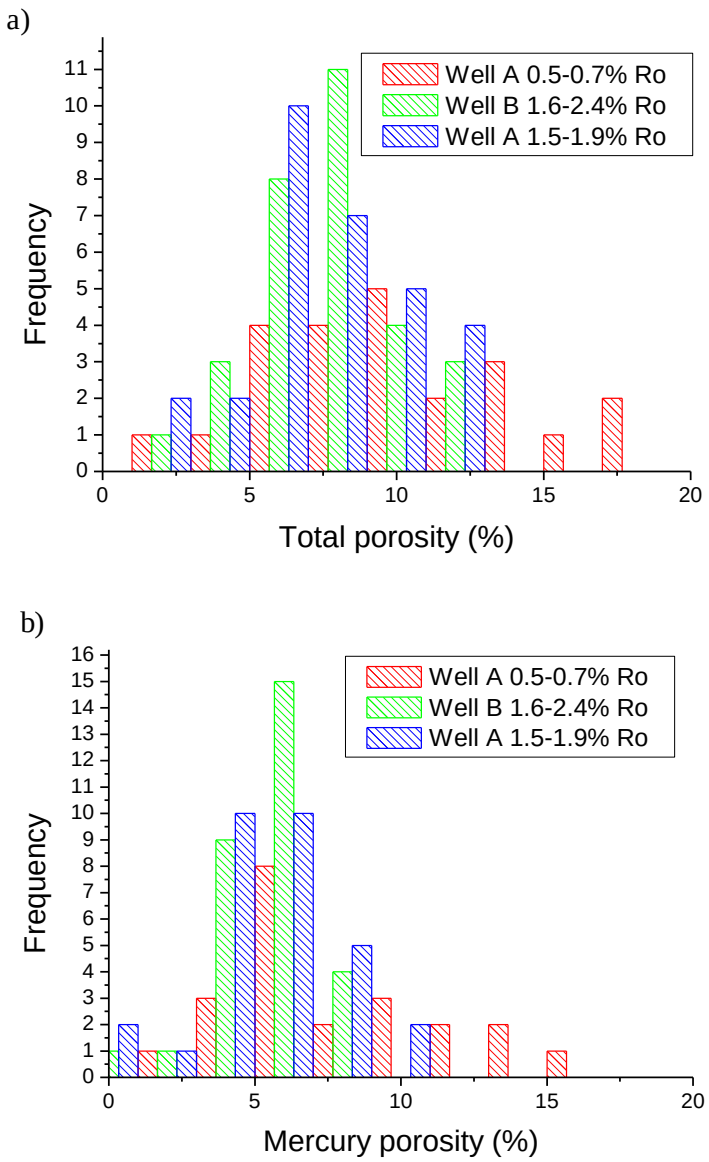

Figure 4. 13. *Histogram of porosity distribution in samples from wells A, B and C. a) Total porosity. b) Mercury injection porosity.*

Mercury porosity and pore size distribution

Mercury porosities show a lower spread than total porosities, varying between 0.6-15.2% in well A, 0.4-8.5% in well B and 0.7-9.2 % in well C (Figure 4.13b). For the least mature shale the average mercury porosity is higher, amounting to 7.6 +/-3.8%, in comparison to 5.3 +/-1.7% from the B and 5.4 +/-2.2% from the C gas mature shale.

For ca. 95% of the investigated shale samples the threshold aperture, defined as the aperture providing access to > 10% of porosity, does not exceed 50 nm diameter (Table 4.6, Table 4.A2). In the low maturity well, despite the prevalence of < 50 nm apertures (median = 38 nm), wider pore size distributions were encountered in a few fossiliferous mudstones and

limestones. Within the mudstone group only, fossil-bearing mudstones show higher threshold apertures (> 35 nm) in comparison to fossil-depleted siliciclastic equivalents. Moreover, higher pore apertures coincide with coarser grain sizes of the silt fraction as retrieved from SEM images (Figure 4.14). For 6 samples for which grain size distribution was determined, two with the coarsest grains across the full size range have higher Hg apertures (40 nm and 2000 nm) than samples with finer silt fractions. At the same time, 3 samples with the densest population of grains with the size in a range 2-500 nm have higher apertures (> 35 nm) than 3 much finer samples (aperture < 22 nm). In the overmature shale, the threshold aperture is smaller than in the less mature equivalent, with a median value of 16 nm, 98% of samples with apertures < 50 nm and 70% of samples with apertures < 20 nm. Although slightly higher apertures were found in the shale from the lake plain setting (median 22 nm), they are not significantly different in comparison to the remaining sample set (median 16 nm). Overall, the width of the threshold apertures of the overmature shales have a smaller range than in the early mature shale, varying between 12-24 nm and 14-36 nm for the B and C well respectively.

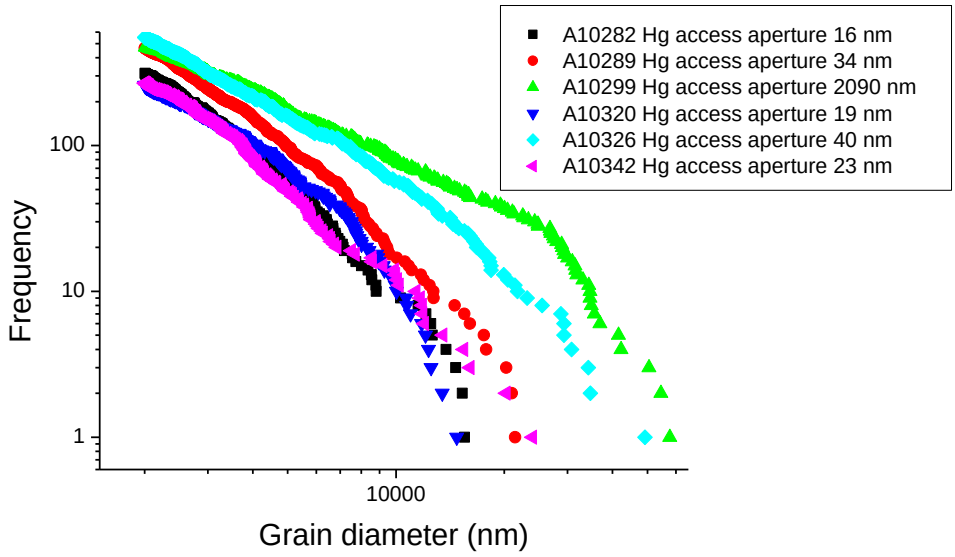

Figure 4. 14. *Grain size distribution for the silt fraction in selected samples from the A well. Samples A10299 and A10326 show much coarser grains across the full size range. Additionally, along with the sample A10289 they show significantly denser population in the size < 500 nm.*

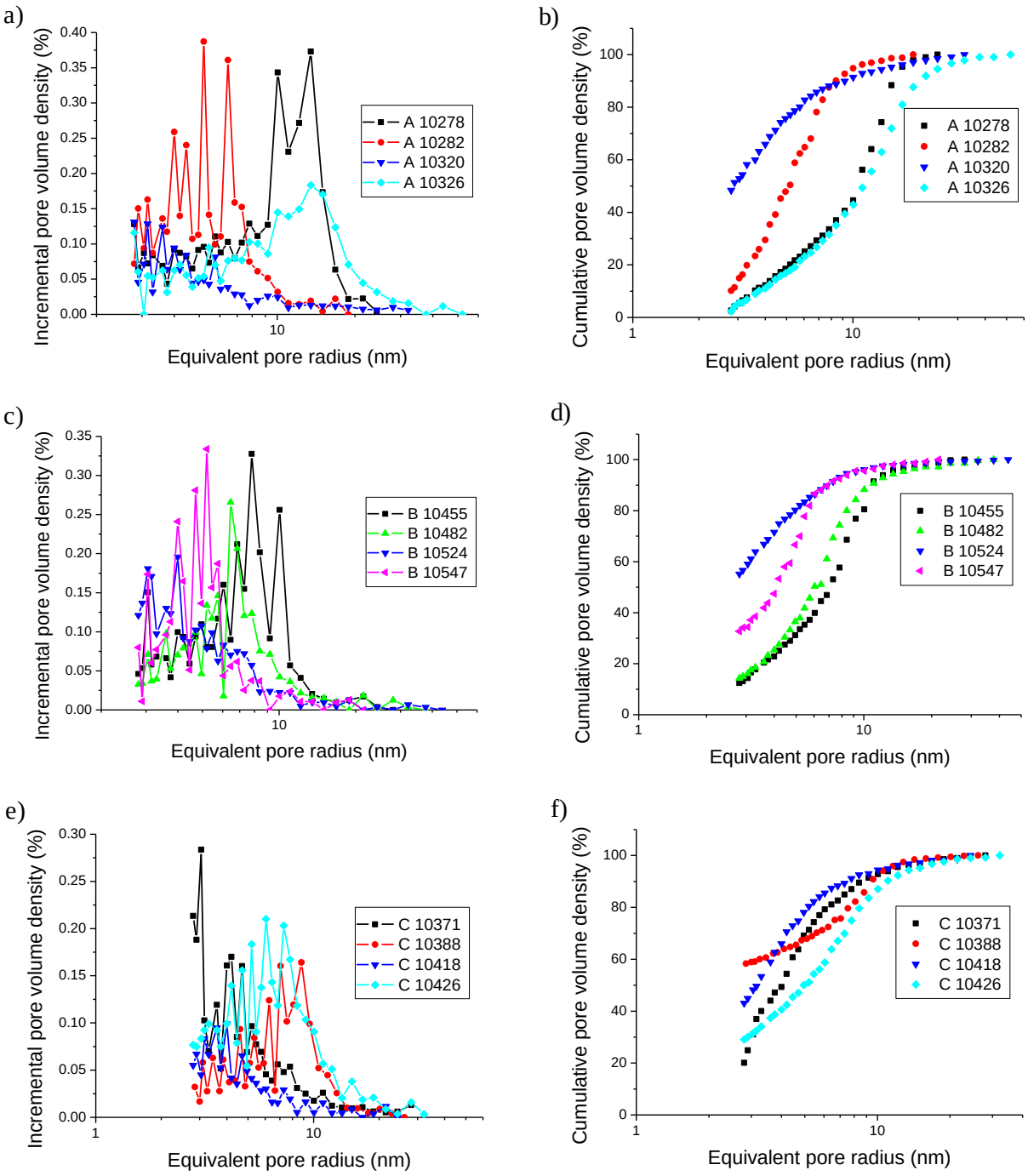

Figure 4. 15. *Incremental (left column) and cumulative (right column) pore volume density of selected Wealden samples, wells: a, b) A (Ro 0.5-0.7%), c, d) B (Ro 1.6-2.4) and e, f) C (Ro 1.5-1.9%). The mercury data was cut off at a radius interpreted as a true onset of the mercury intrusion into a pore network. In the immature and early mature shale, pore throat distributions are predominantly unimodal with the peak between 10-40 nm. A larger spread of pore throat sizes is characteristic for mudstones enriched in a shell detritus (A10326) or burrows filling silt fraction (A10278). In the overmature wells B and C, distribution of pore throat sizes is unimodal with the highest pore volume density between 10-20 nm. In shales enriched in the shell detritus (C10388, C104260) distribution is skewed towards higher values (10-20 nm) in comparison to clay-rich mudstones (< 10 nm).*

Similarly to the value of the threshold aperture, pore size distributions show variations within and between wells, reflecting the spread of pore throat sizes and different amounts of porosity contained both in mercury pores (> 5.6 nm in diameter) and pores with a diameter < 5.6 nm (Figure 4.15). In the A well, distributions are predominantly unimodal, with a peak between 10-40 nm. A larger spread of pore throat sizes, and modal peaks shifted towards larger pores is characteristic for mudstones enriched in shell detritus (A10326) or burrows lined with quartz silt (A10278) (Figure 4.15a, b). For a few fossil-rich limestones as well as silt-laminated mudstones, the distribution is bimodal, with peaks at < 20 nm and ca. 60-200 nm (not shown). In the overmature wells B and C, the distribution of pore throat sizes is unimodal with the highest pore volume density between 10-20 nm (Figure 4.15c-f). In shales enriched in the shell detritus (C10388, C10426), pore size distributions are skewed towards higher values (10-20 nm) in comparison to clay-rich mudstones (< 10 nm).

While the size and distribution of pore throats control intrusion of mercury during the drainage stage of the mercury injection experiment, the extrusion process is controlled by the pore body/pore throat ratio (Webb, 2001). In general, an increase in this ratio leads to the entrapment of mercury in pore cavities, leading to the development of hysteresis (Figure 4.16a, c, e) and causing some pores to empty at capillary pressures lower than corresponding to their size as estimated from the Washburn equation (Padhy *et al.*, 2007). As shown by the curves plotting the difference between porosity intruded and emptied during intrusion-extrusion experiments at equivalent pressures (Figure 4.16b, d, f), in all samples the absolute amount of trapped mercury that is not released during the imbibition at the intrusion pressure initially increases. When a threshold diameter is reached, the rate of extrusion exceeds the rate of intrusion at an equivalent pressure, and mercury starts to recede from pores that could not be emptied before. The maximum fraction of porosity occluded by trapped mercury that cannot be emptied before the pressure equivalent to the threshold diameter is reached, varies between 0.62-0.99 across samples and, regardless of the maturity, is strongly related to the content of organic carbon. The maximum percentage of porosity occluded by mercury that was not released from the sample at the equivalent intrusion pressure is encountered in the least organic rich shales and decreases linearly with increasing TOC (Figure 4.17). This relation indicates that little, if any, retraction occurs from inorganic pores at the start of the imbibition and that considerable compression of the shale structure may take place upon pressures exerted by mercury in the most organic rich shales (Friesen and Mikula, 1988).

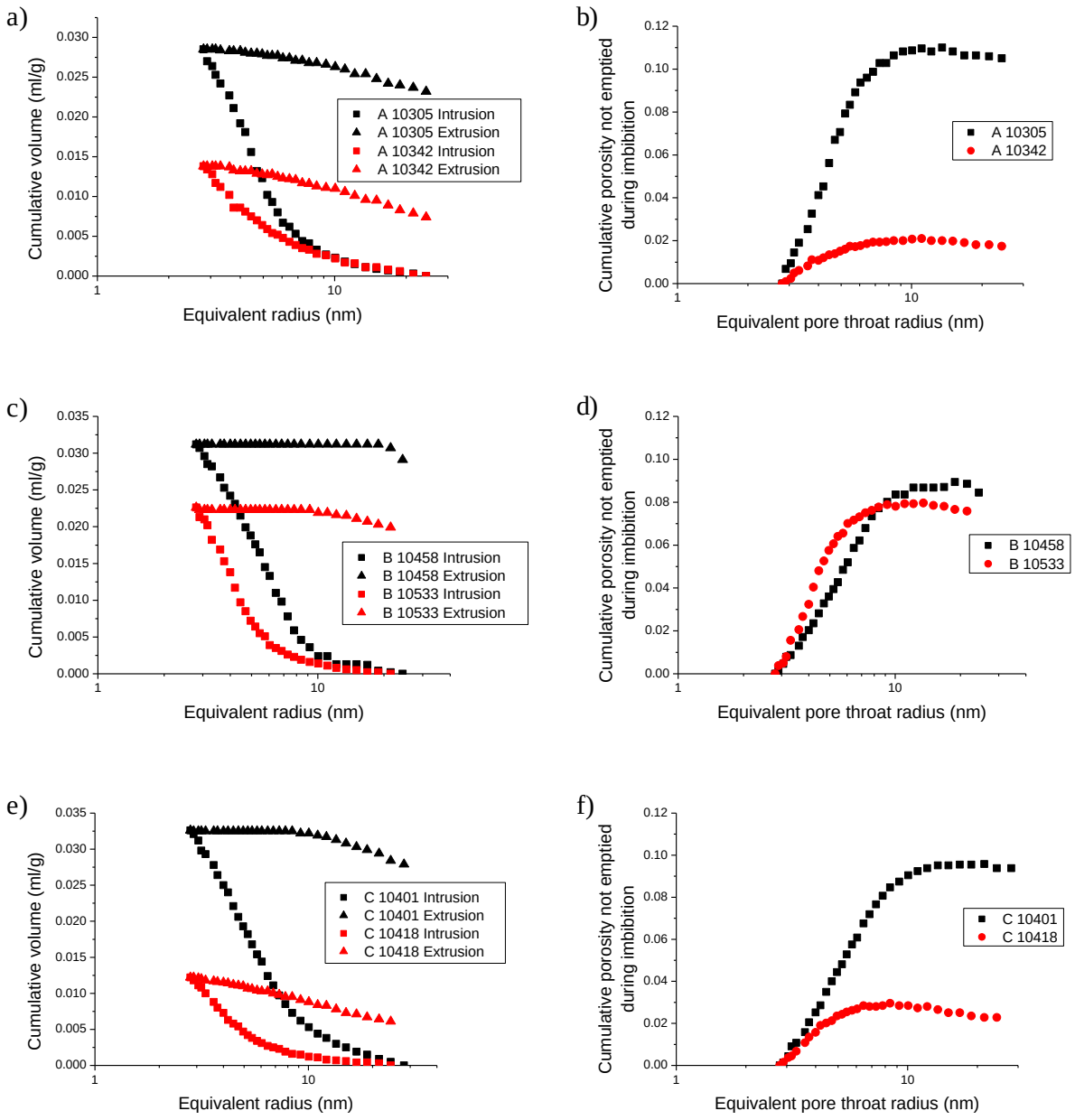

Figure 4. 16. *Cumulative intrusion (squares) and extrusion (triangles) of mercury for selected Wealden shale samples from wells a) A, c) B and e) C. The mercury data were normalized to the true volume of intrusion after cutting off the pore volume data interpreted as representing surface roughness. b) A, d) B and f) C shale. Cumulative porosity that is not emptied from mercury during the imbibition. The curves plot cumulative difference between porosity intruded and emptied during the intrusion-extrusion experiments at equivalent pressures as % of a rock. Note that in all samples during the imbibition process the absolute amount of mercury that is not released at the intrusion pressure initially increases.*

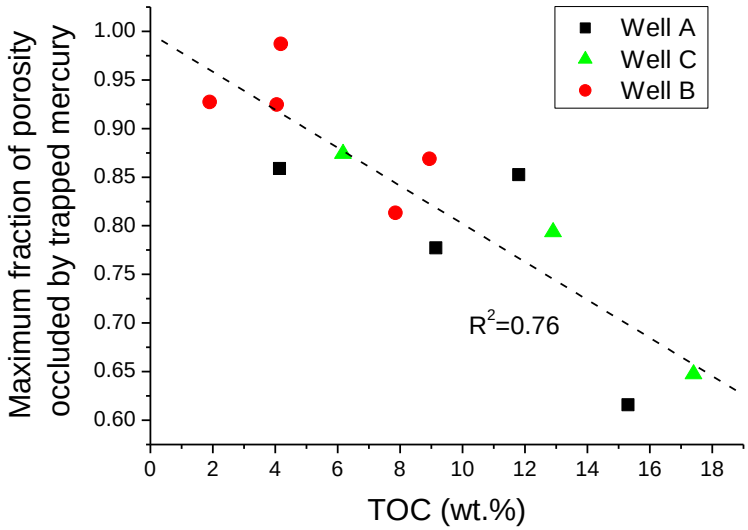

Figure 4. 17. *Maximum fraction of total porosity trapped by mercury during the imbibition experiment for selected Wealden shale samples from the A (black squares), B (red circles) and C (green triangles) wells. The fraction occluded by mercury shows a strong negative relation with the content of organic carbon.*

Rock classification based on factor analysis

In order to explain variability in measured porosity values between different shale samples and give them geological meaning, a factor analysis was employed. The 10 variables included in the multivariate statistical analysis included geochemical data (TOC, HI, S1, S2, S3) and petrophysical data (total porosity, mercury porosity, ratio of mercury to total porosity, maximum access radius for injected mercury and grain density). For the early mature shale from the A well, the first three factors explain 84% of the total variance. These factors group samples with high TOC, HI, S2 and low grain density (Factor 1), low total porosity, mercury porosity and S3 (Factor 2) and low S1 and maximum access radius for mercury (Factor 3) (Figure 4.18). The factor analysis revealed 3 groups of samples and 2 main trends in terms of porosity variability across the measured TOC range (Figure 4.20a). Group 1 includes samples with high average porosity (7.9 +/-3.1%), low organic content (1.8 +/-1.3%), varied grain density (2.53-2.82 g/cm^3), and varied extent of preservation of organic matter (generative potential), from highly oxidized (poor) to well preserved (very good). Samples distinguished for this group are quite heterogeneous but embrace mostly deep lacustrine shelly bed deposits, fossil-bearing mudstones and carbonate concretions (Figure 4.3d, g). In combination, these samples show a positive correlation between total porosity, organic content, and the preservation of organic matter.

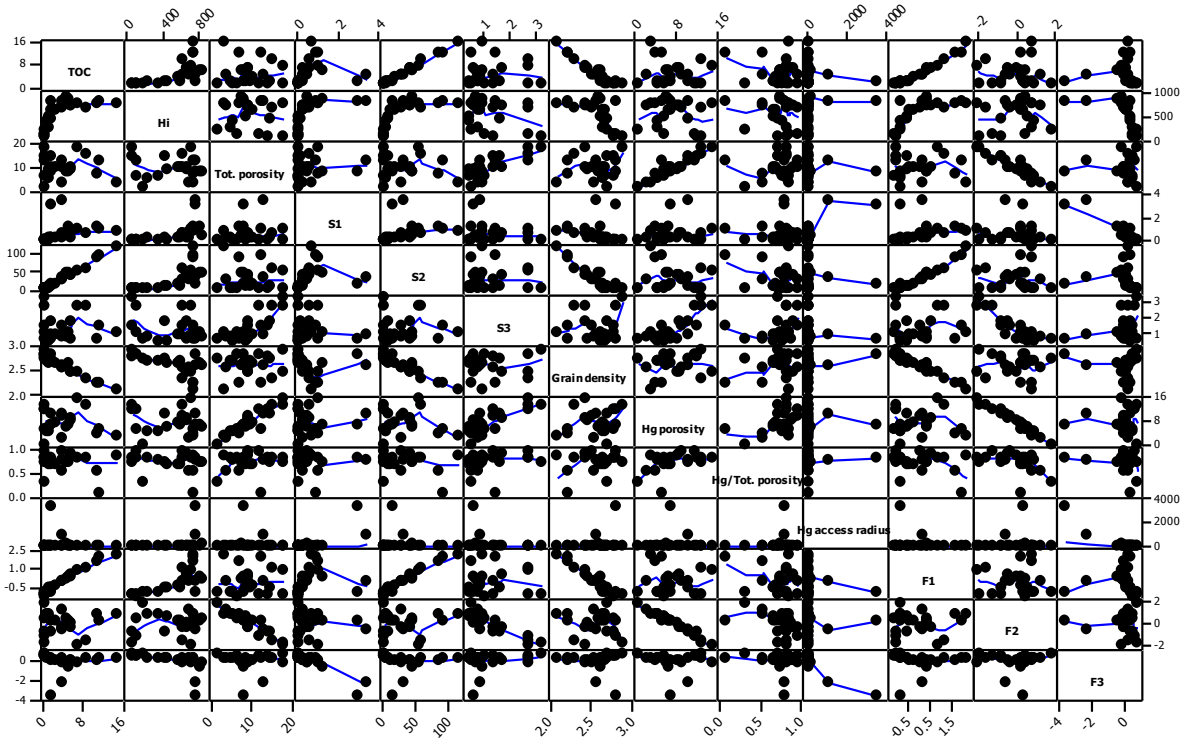

Figure 4. 18. *Matrix scatterplot of the early mature well A Wealden Shale samples showing variation of 10 variables and 3 factors extracted during the factor analysis. Factor 1 correlates positively with TOC, HI, S2 rather than grain density. A negative correlation is observed between Factor 2 and total porosity, mercury porosity and S3. Factor 3 is inversely correlated with S1 and maximum access radius for mercury.*

The second group of samples selected through the factor analysis includes clay-rich mudstones with total porosity ranging from very high to very low (3-18%, average 5.2 +/-5.0) over the range of TOC values ranging from < 0.5 to > 15.0% (average 10.5 +/-4.4). The strong negative correlation between total organic content and total porosity of this sample set is associated with a decrease in grain density from 2.9 to 2.1 g/cm^3, coinciding with a varied abundance of early diagenetic cement, and an increase in the generative potential from poor to very good. Characteristically for this group of rocks, higher porosities coincide with the presence of silt-filled biogenic sedimentary structures encountered in the marine shale (Figure 4.3a), and decline rapidly in silt- and TOC-poor mudstones (e.g. siliciclastic mudstone with clay-filled burrows). In comparison, with TOC contents above 2-4%, characteristic of shales with no sedimentary structures and good quality organic matter (Figure 4.3b, c, f, h), porosities decline at a moderate rate.

The last group of samples distinguished through the factor analysis includes samples with both high porosity (average 15.6 +/-2.7%) and organic content (average 9.4 +/-2.3%), low

grain density (2.2-2.4 g/cm^3), and consistently high preservation and high generative potential of the organic matter. Because the samples are both clay-rich and show the presence of fossiliferous debris, they could be classified as those with intermediate lithologies between high generative potential fossiliferous shale from group 1 and clay-rich mudstone from the group 3 (Figure 4.3e).

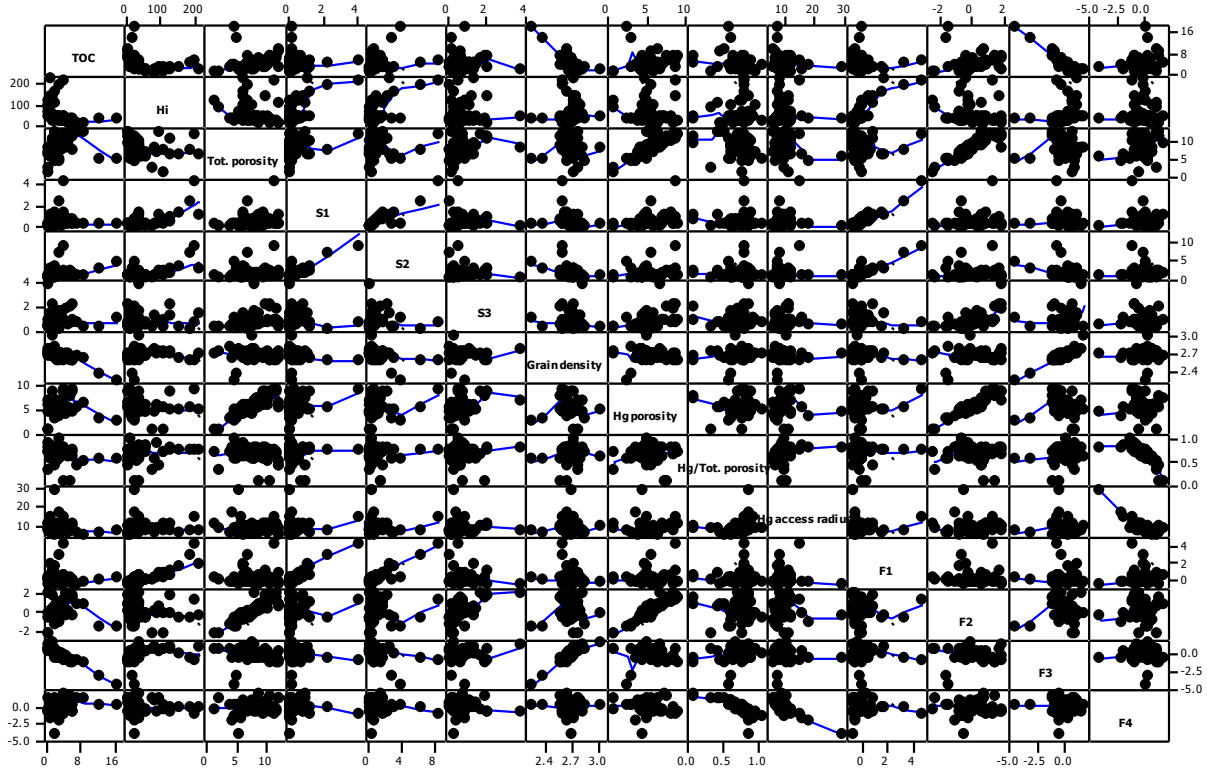

Figure 4. 19. *Matrix scatterplot of the gas window Wealden Shale samples (well B, C) showing variation of 10 variables and 4 factors extracted during the factor analysis. Factor 1 correlates positively with HI, S1 and S2. A good positive correlation is observed between Factor 2 and total porosity, Hg porosity and S3. Factor 3 correlates positively with grain density rather than TOC. Factor 4 is inversely correlated with the maximum access radius for mercury and ratio of mercury to total porosity.*

For the gas window mature shales, the factor analysis was performed for the samples from wells B and C combined. The first 4 factors extracted explain 85% of the total variance and group samples based on high HI, S1 and S2 (Factor 1), high total porosity, Hg porosity and S3 (Factor 2), high grain density rather than TOC (Factor 3), and low maximum access radius to mercury and low ratio of mercury to total porosity (Factor 4) (Figure 4.19). The analysis of the four factors reveals four groups of samples and two different trends of total porosity variation in relation to the content of organic carbon (Figure 4.20b). The first sample subset

includes samples with low TOC (0.6-2.7%, average 1.3 +/-0.7%) and unusually high grain densities for a given content of the organic carbon. Total porosity for this group rises from 1-12% (average 7.0 +/-3.2%) with increasing carbon content, with a variable ratio of mercury to total porosity. Samples selected in this group are fossil-bearing, imparting higher grain density to the bulk shale and come from both deep lacustrine and lake plain settings (Figure 4.3m, r, x).

The second group consists of samples with total porosity values ranging from moderate to very high (4-12%, average 7.8 +/-2.0%) over a wide range of TOC between 0.7 to 8.9% (average 3.4 +/-1.9%). What is characteristic is a low average maximum access radius to mercury as well as a low ratio of mercury to total porosity. Samples within this group are classified as deep lacustrine, clay-rich mudstones, with the porosity positively correlated with the amount and the extent of preservation of organic carbon in the sediment (Figure 4.3j-l, n-q, s-r). Importantly, this group embraces both organic- and carbonate poor mudstones with sedimentary structures such as current features, as well as laminated organic-rich mudstones with undisturbed clay-rich fabrics.

The next sample group consists of samples with both higher than average maximum access radius to mercury and fractions of total porosity accessible to mercury. In this group, the TOC variability is moderate, (1.3-6.7%, average 4.2 +/-2.1%), followed by positive change in total porosities from 4 to 12% (average 8.8 +/-3.4%). As both the mercury:total porosity ratio and access radius correlate with the fourth factor explaining only 12% of variance, the porosity and TOC values of these samples do not deviate from those characteristic for the second group of samples. Lithologically, this third group includes clay-rich and fossil-bearing mudstones deposited exclusively in the lake plain setting (Figure 4.3v, w).

The last sample subset extracted through the factor analysis consists of only two samples, with very high organic contents (12.9 and 17.4%), relatively low grain densities (2.23 and 2.36 g/cm^3) and low total porosity (5.0 and 4.6%). This group includes carbonaceous mudstones with terrestrial organic matter concentrated in coaly laminae (Figure 4.3u).

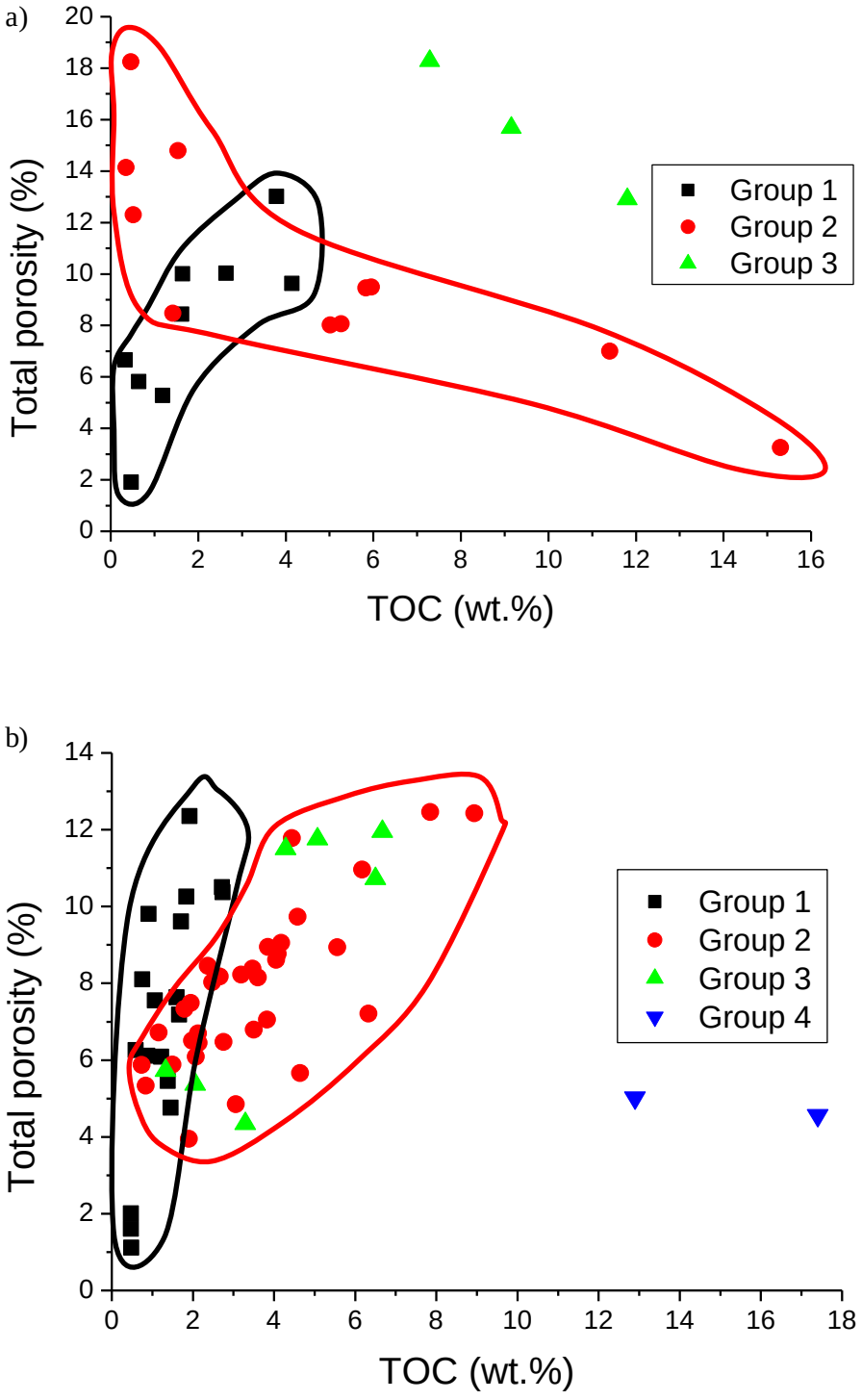

Figure 4. 20. *Variation of total porosity as a function of maturity and organic carbon content. a) Well A (0.5-0.7% Ro). Group 1:* fossil-bearing mudstone, shelly bed deposits and carbonate concretions; *Group 2:* clay-rich mudstones; *Group 3:* clay-rich mudstone with fossil debris. *b) Wells B and C (Ro 1.6-2.4% and 1.5-1.9% respectively).* Group 1: fossil-bearing mudstone, limestone and carbonate concretions; Group 2: clay-rich mudstone; Group 3: clay-rich and fossil-bearing mudstone deposited in the lake plain setting; *Group 4:* carbonaceous mudstone with terrigenous organic matter. *For details see text.*

Micro- and mesoporosity

A fraction of porosity, due to pores either being blind, finer than 5.6 nm or hidden below < 5.6 nm constrictions, was not detected by mercury. In the low maturity well, this porosity (1-MICP) varies between 0.2-7.4% with an average value 2.2 +/-1.7% (Table 4.6, Table 4.A2). Similar porosities were measured in the gas window shale samples, showing both equal spread, from < 0.1 to 6.8% and 0.3-7.1% in the B and C well respectively, and average values (2.3 +/-1.6% and 2.1 +/-1.4% for B and C sample subsets). In the low maturity well, 1-MICP porosity, unlike in the gas window shales, does not show a correlation with the organic content for any of the sample groups distinguished (Figure 4.21a). At high maturities, 1-MICP is positively correlated with the organic carbon content for all main sample groups 1 to 3 (Figure 4.21b).

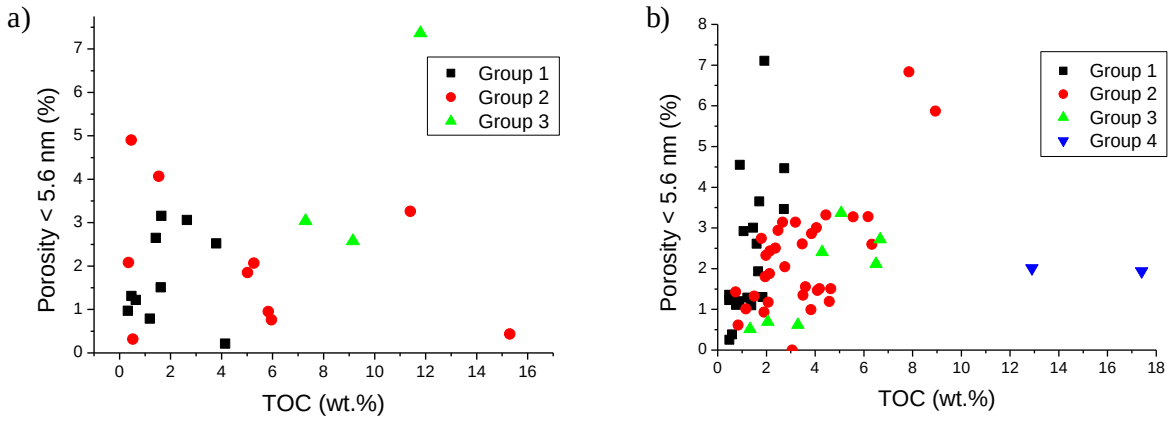

Figure 4. 21. *Variation of porosity not penetrated by mercury during mercury porosimetry as a function of maturity and organic carbon content. a) Well A (0.5-0.7% Ro). b) Wells B and C (1.5-2.4% Ro). For group description see Figure 4.20.*

High entry pressure, compressible samples can yield reduced MICP porosities due to compressibility of the shale and thus overestimate the content of small or inaccessible pores (Shafer *et al.*, 2000) Hence, in order to investigate the amount of the < 5.6 nm pores (Rexer *et al.*, 2014), porosities for 3 selected organic-rich shale samples of different maturities were measured with low pressure CO_2 195K gas sorption. All CO_2 isotherms are type I (Sing *et al.*, 1985), and demonstrate evidence of the presence of microporosity filled at the lowest pressures (Figure 4.22). Sorption pore volumes measured at 1 mbar do not differ significantly and amount to 0.018-0.022 cm^3/g in all shale samples investigated (Table 4.7). Similarly, corresponding sorption porosities (SP) vary only insignificantly, yielding 4.4% for both the early mature A10305 and overmature B10458 shale, and 5.2% for the C10401 shale sample from the overmature well C. After solvent extraction, performed for 2 overmature shales,

total sorption increased, leading to an increase in the calculated sorption porosities to 5.0% and 5.5% in the B 10458 and C 10401 samples respectively (Table 4.4, Figure 4.17). Such small porosity increase indicates that extractable bitumen at high maturities occupies only small fraction of bitumen free sorption porosities (5 and 12% in B and C sample respectively).

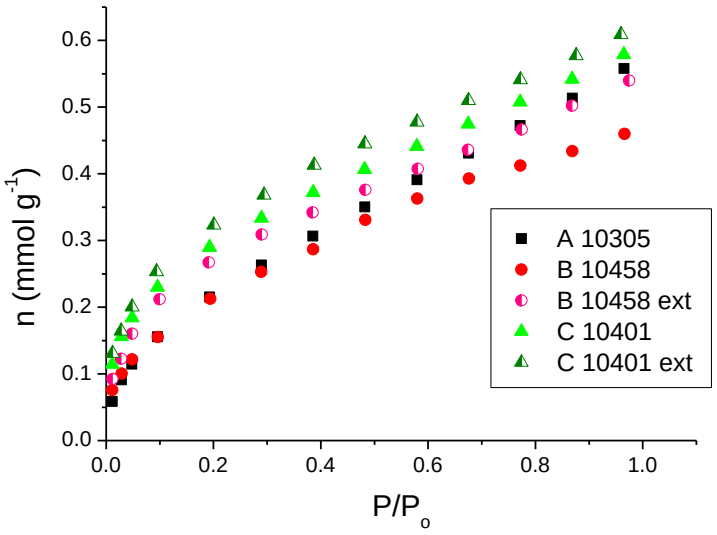

Figure 4. 22. *195K CO_2 isotherms for selected Wealden shale samples, A10305 (Ro 0.7%), B10458 (Ro 1.9%) and C10401 (Ro 1.9%). Samples with a solid symbol were not solvent extracted, while those marked with a semi-solid symbols were solvent extracted (ext) prior to the analysis.*

Table 4. 7. *Porosities and pore parameters measured with different techniques for selected Wealden samples, wells A (0.7% Ro), B (1.9% Ro) and C (1.9% Ro).*

Sample	Total porosity (%)	Mercury Injection			CO_2 195K				
		Hg porosity (%)	Hg access radius (nm)	Porosity < 5.6 nm (%)	Sorption porosity (%)		Sorption pore volume (cm^3/g)		Extract. bitumen in sorption pores (%)*
					Pre-ext.	Post-ext.	Pre-ext.	Post-ext.	
A10305	12.91	5.59	6.2	7.31	4.42	nd	0.021	nd	nd
C10401	10.96	7.68	10.6	3.28	5.24	5.50	0.022	0.023	0.25
B10458	9.06	7.55	8.9	1.51	4.44	5.02	0.018	0.020	0.58

* The amount of bitumen occupying sorption pores was estimated as a difference between sorption porosity of a pre-extracted shale (pre-ext.) and shale extracted with organic solvents (post-ext.).

Due to a small number of measurements, it was not possible to determine the relation between sorption porosity and shale composition. However, including a sample set measured on the Lower Jurassic, calcareous Posidonia Shale of maturities Ro 0.53% and 1.45% (Chapter 3), a positive trend between sorption porosity and the combined content of clays (including muscovite) and TOC emerged (Figure 4.23).

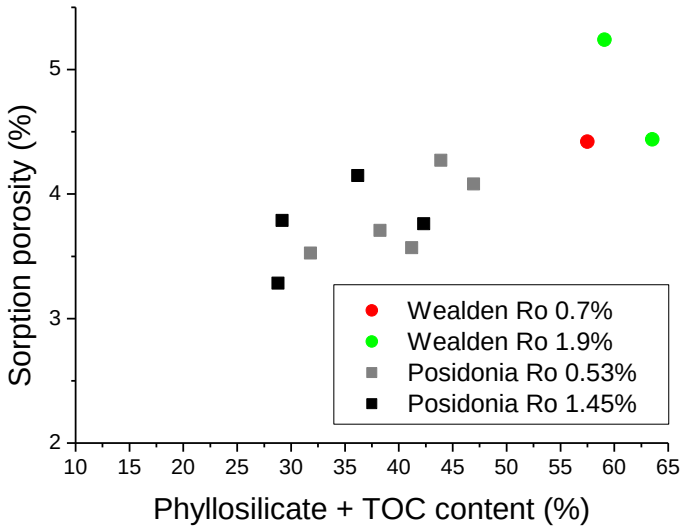

Figure 4. 23. *Relationship between the combined content of phyllosilicate minerals and TOC against 195K CO_2 sorption porosity. Wealden data points refer to samples of maturities 0.7% (green) and 1.9% (red). The Wealden shale data were plotted against data acquired on Posidonia Shale, referring to samples of maturities 0.5% (grey) and 1.4% (black).*

Meso and macroporosity in FIB- and BIB-SEM images

SEM observation of Meso and Macroporosity

Three samples, one from the early mature well (A 10305) and two from the overmature wells (B10458, C10401) were selected for image porosity analysis. All shale samples are classified as silt-bearing, clay-rich mudstones, with abundant organic matter (Figure 4.10, Figure 4.24). In the low maturity shale, the organic phase forms pyritized algal bodies intermixed with flat, lamellar algal wisps and a poorly-defined organic groundmass (Figure 4.24a, b). In the higher maturity shale, organic matter is dispersed in a tight clay matrix and concentrated in compaction shadows of mineral grains (Figure 4.24d, f). The nature of the carbonate phase varies between samples and maturities, with carbonates dominated by fossil debris in the low mature shale (Figure 4.24a), and by diagenetic ferroan dolomite at higher maturities (Figure 4.24c, e). Within the gas window maturity shales, there is more

pronounced preferred orientation of grains in the B10458 sample, reflected by the planar arrangement of clay laths and organic particles. The organic phase is represented both by fracture filling bitumen and less defined organic wisps and blobs filling spaces between various grains (Figure 4.24c, d). In contrast, in the C10401 shale, the clay matrix is less visibly aligned and random orientations of clay laths and associated organics are not uncommon (Figure 4.24e, f).

Based on the spatial relation of pores with respect to mineral phases and organic matter, pores were classified using the general classification of Loucks *et al.* (2012) into interparticle, intraparticle and organic. The following definitions of different pore types were adapted for this study:

- Interparticle: 1) pores between detrital grains, authigenic minerals, nannofossils and clay platelets, occasionally partly filled with authigenic cement; 2) pores (in 2D or 3D space) associated with the interface of organic matter and mineral matrix that visibly do not extend into an organic particle;
- Intraparticle: 1) pores within fossils or fossil assemblages; 2) pores within pyrite framboids; 3) pores along cleavage planes of phyllosilicate minerals; 4) moldic pores formed due to dissolution of mineral phases; 5) pores at the interface of inorganic matrix and organic macerals that do not visibly extend into an organic particle, contained within a fossil body, or pyrite framboid;
- Organic: 1) pores within immature algal bodies; 2) discrete, round, bubble-like pores in the organic matter; 3) sponge-like pores within the organic matter, often interconnected and grouped; 4) highly irregular pores, usually at the interface of organic matter and mineral matrix, but visibly extending into the organic particle mass; 5) visible cracks within OM particles, often with jagged edges and extending into the particle edge.

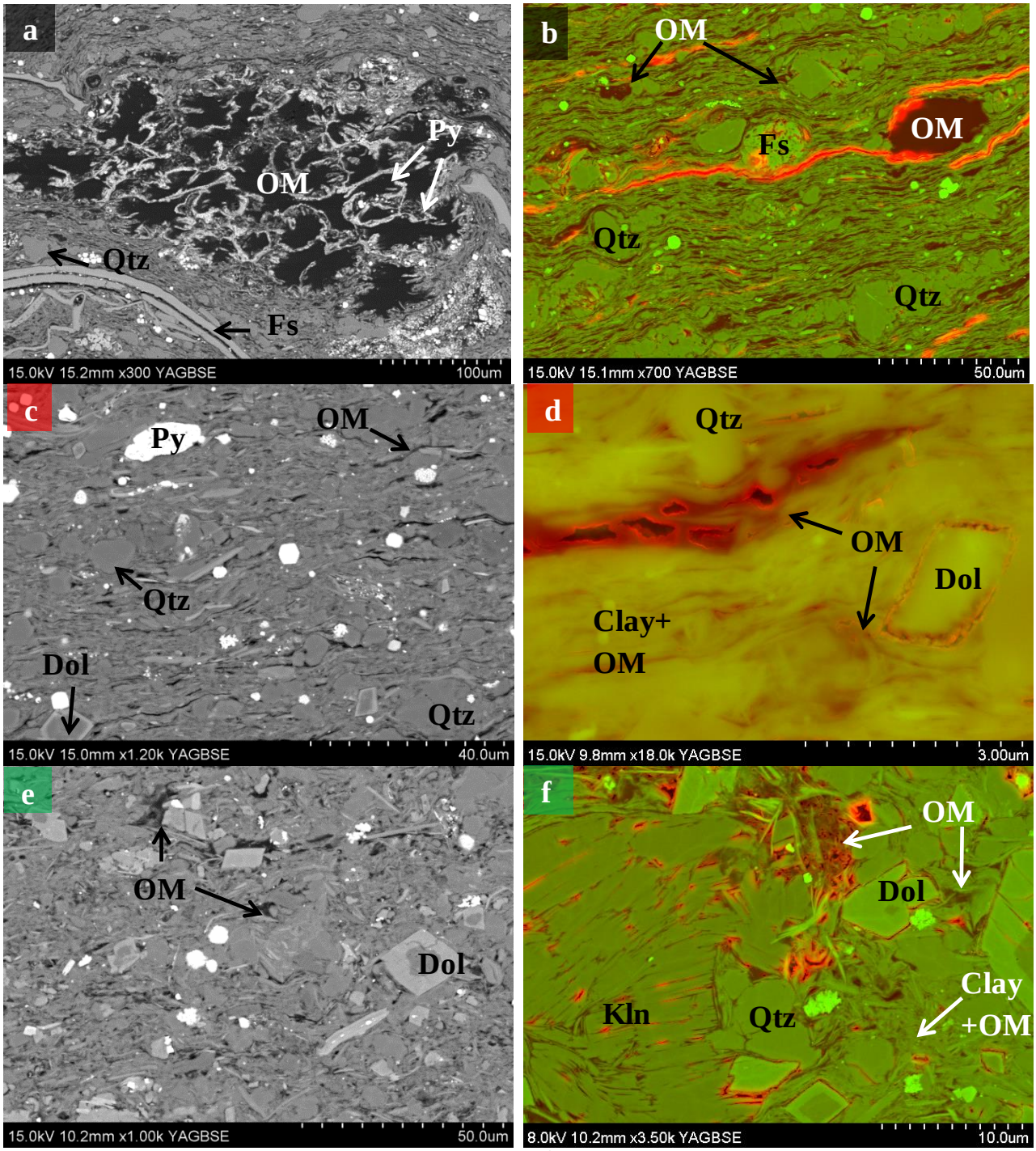

Figure 4. 24. *Backscattered electron micrographs of mudstone samples polished with BIB. In all images the bedding plane is horizontal. Sample A10305: a) Organic phase forms pyritized algal bodies intermixed with less defined organic groundmass. Highly dispersed carbonate phase is represented by calcitic fossil remains. b) Quartz occurs predominantly as horizontal pods aligned according to the bedding plane. Sample B10458: c) The silt fraction is represented by quartz grains and diagenetic dolomite. d) Organic phase is aligned horizontally, and is strongly intermixed with the clay-rich matrix. e) Sample C10401: Diagenetic dolomite is abundant, disseminated in the clay-rich matrix. f) Organic phase is intermixed with clays and concentrated in compaction shadows of mineral grains.*

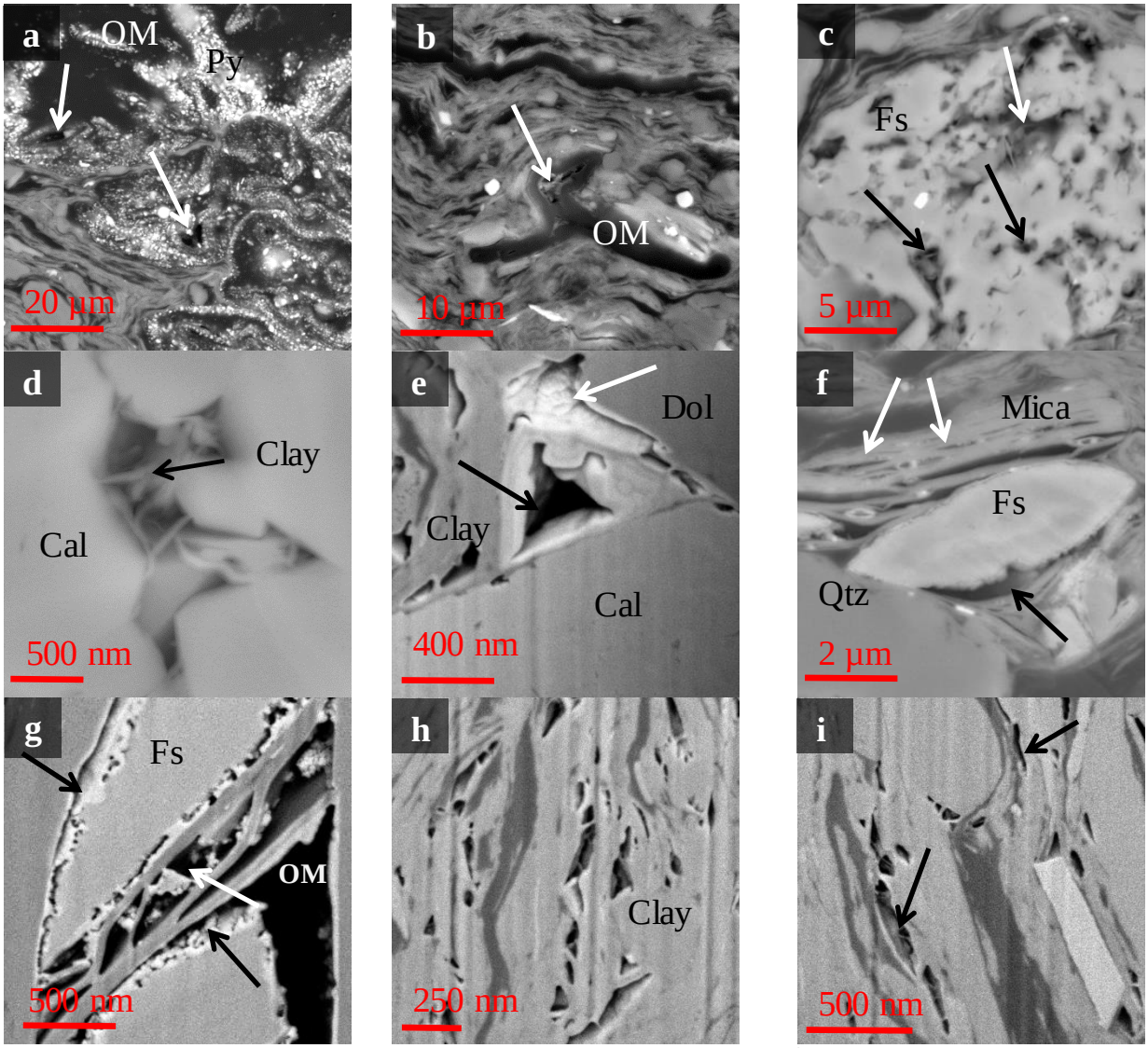

Figure 4. 25. *FIB-SEM and BIB-SEM micrographs (BSE mode) of an early mature shale sample A10305. a) Organic pores within an algal cyst (arrows). b) Pore between walls of a partly compacted algal cyst (arrow). c) Intraparticle pores in a fossil (black arrows); Note intraorganic pores developed in kerogen lining the fossil interstices (white arrow). d) Intraparticle pores in a recrystallizaed fossil partly filled with authigenic clays. e) Interparticle pore in a compaction shadow of a dolomite crystal (black arrow). Note presence of a dissolution pore within adjacent calcite grain (black arrow). f) Interparticle pores rimming a foraminifera test (black arrow). The overlying mica group mineral grain contains numerous cleavage associated intraparticle pores (white arrows). g) Intraorganic pores formed due to dissolution of a calcareous foraminifera test (black arrows). Interparticle pores between platelets of a phyllosilicate phase are partly filled with calcite cement (white arrow). A large interparticle pore adjacent to a fossil clast is filled with the bituminous phase. h) Interparticle pores between folded clay platelets. Pores may represent space between not fully compacted clay floccules. i) Interparticle pores adjacent to kerogen particles (arrows). Fs- fossil, Cal – calcite, Dol – dolomite, Py – pyrite, OM – organic matter.*

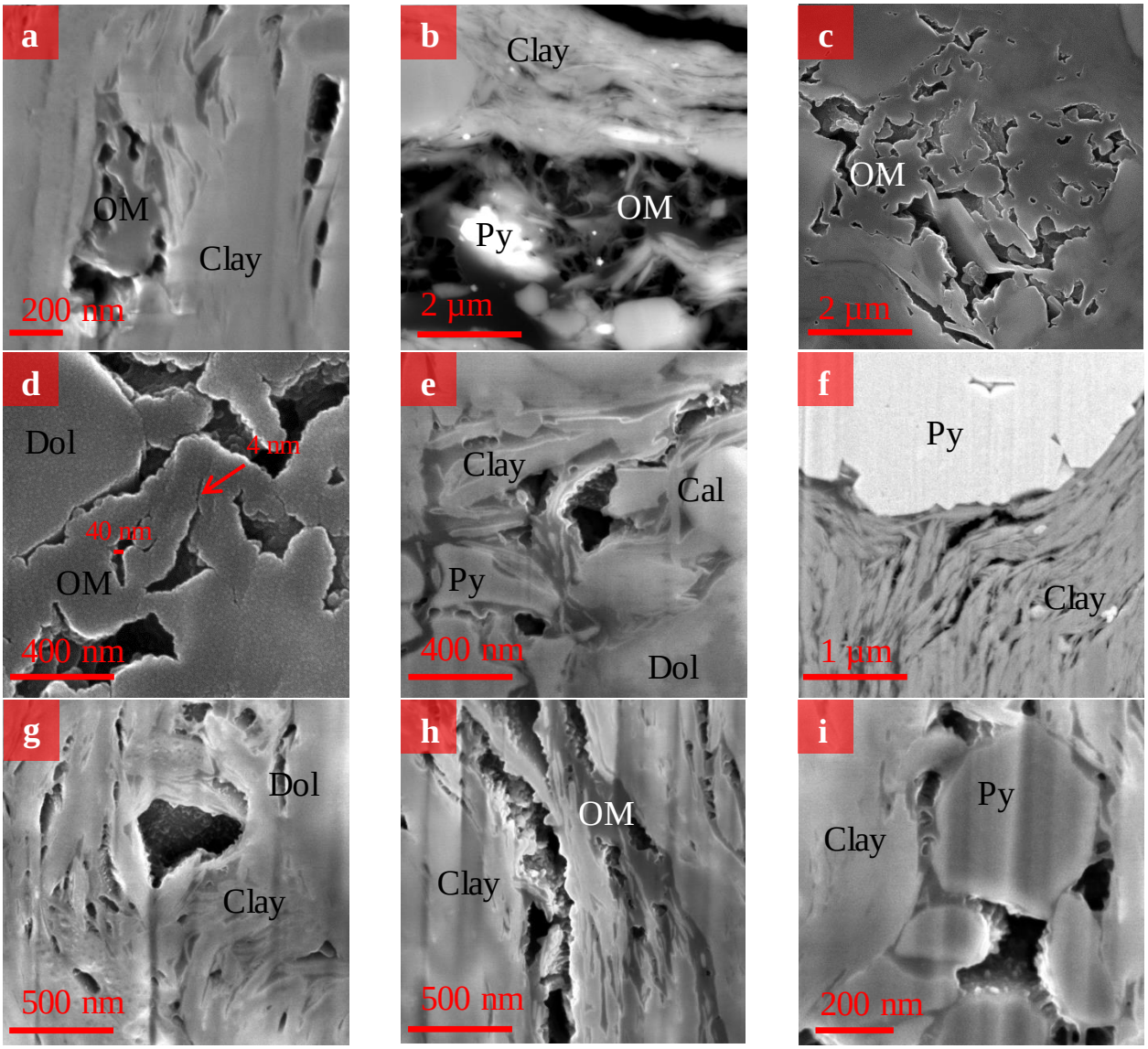

Figure 4. 26. *FIB-SEM and BIB-SEM micrographs (BSE and SE mode) of an overmature shale sample B10458. a) Interconnected spongy organic pores grow into a large pore located the particle margin. b) Spongy organic pores within an organic grains. c) Organic pores interconnect with each other, and grow into a large pore located at the margin of the organic grain. d) The visible connections between organic pore bodies may be as small as 4 nm. e) Large pores located at the margin of an organic particle, and in the compaction shadow of surrounding mineral grains. Organic pores show a characteristic fibrous internal structure on its walls. f) Interparticle pores located between clay platelets, in a compaction shadow of a pyrite framboid. Pores have jagged margins suggesting that they de facto developed in the organic mass that had previosuly filled the pore space. g) Interparticle pores between folded clays. h) Interparticle pores between clay platelets (left) show identical internal structure of its walls as organic pores (right). i) Intraparticle pores within a pyrite framboid. Fs- fossil, Cal – calcite, Dol – dolomite, Py – pyrite, OM – organic matter.*

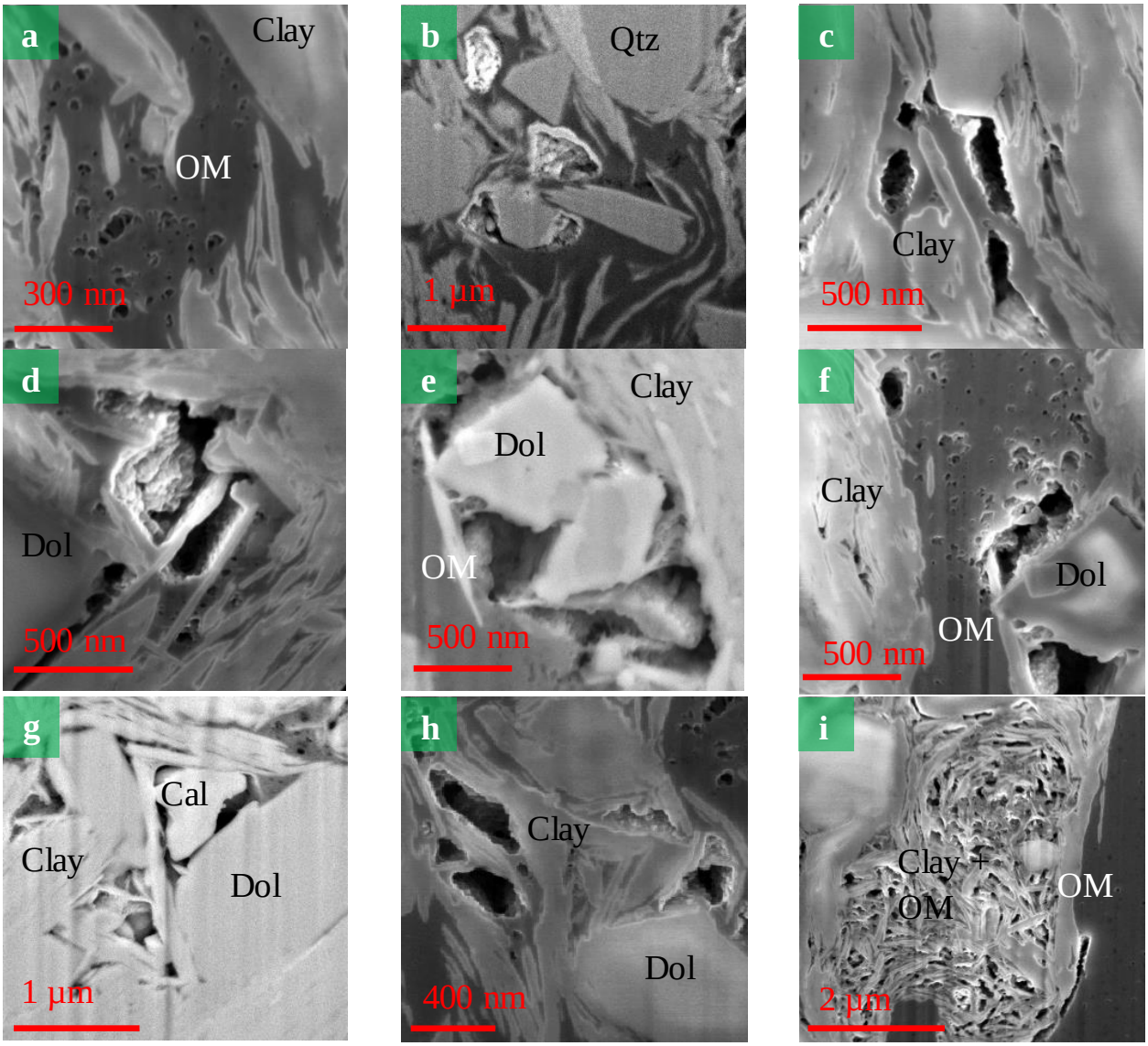

Figure 4. 27. *FIB-SEM and BIB-SEM micrographs (BSE and SE mode) of an overmature shale sample C10401. a) Discrete, bubble-like and partly interconnected spongy pores within an organic particle. Note close association of porous and non-porous organic regions. b) Large intraorganic pores, partly located at the margins of adjacent dolomite crystals. c) Intraorganic (left) and interparticle pores (right) developed in the organic matter mass located in the compaction shadow of a calcite grain (bottom). d) Complex organic pore located in a compaction shadow of a dolomite crystal (left). Note the rough surface of a pore wall. e) Organic pores developed in the vicinity of dolomite crystals (centre). f) Discrete, spongy and large complex organic pores developed in the organic matter grain in the vicinity of a dolomite crystal (right). g) Interparticle pores between folded clays and dolomite (bottom right). h) Interparticle pores between clay platelets. Note jagged edges of the pore walls characteristic for pores of an organic origin. i) Intraparticle pores in a faecal pellet. Intraparticle pores within a pyrite framboid. Fs- fossil, Cal – calcite, Dol – dolomite, Py – pyrite, Qtz – quartz, OM – organic matter.*

In the least mature sample, visible pores are associated with the inorganic and, to a lesser extent, organic phase. Despite the predominantly visibly non-porous nature of the bulk organic matter, organic pores are represented by up to 1 μm in diameter, round or oval pores located in Botryococcus bodies (Figure 4.25a), and more irregular, remnant pores between walls of partly compacted algal cysts (Figure 4.25b). Also, a few intraorganic pores are developed in the organic material lining and filling interstices within fossil aggregates (Figure 4.25c). Inorganic porosity, at the scale of BIB-SEM images, is found predominantly within sparsely disseminated, recrystallized biogenic calcite forming small (<50 μm) faecal pellets (Figure 4.25c, d) and occasionally in compaction shadows of mineral grains and fossils (Figure 4.25e, f). Depending on the size of the mineral or fossil grain, the size of the neighbouring pores may span between 1 μm down to 100 nm. Inorganic pores may be left intact, partially filled with authigenic clay (Figure 4.25d) or calcite (Figure 4.25g). Some intraparticle pores formed due to dissolution of calcite (Figure 4.25e, g).

Although in the BIB-SEM micrographs clay porosity remains unresolved, higher magnification FIB-SEM images revealed the presence of pores along cleavage planes of mica group minerals (Figure 4.25f) and between clay platelets (Figure 4.25h, i). Some pores associated with clay platelets may be up to 1-2 μm long and 400 nm wide, often adjacent to kerogen particles (Figure 25i) and occasionally lined with authigenic calcite (Figure 4.25g). Clay-related pores sometimes show signs of distortion by compaction and represent remnant open space within compacted clay floccules (Figure 4.25h).

In both overmature shales, the character of porosity changes, with new types of pores found within dispersed bitumen. The porosity of organic grains is variable - organic pores can occupy either the whole particle, or a fraction of a particle, or can be concentrated at particle margins. Also, the size of organic pores varies, with the diameter of the smallest pores below 50 nm and the largest ones exceeding 500 nm. The smallest are isolated, bubble-like pores (Figure 4.27a, f), often co-existing with clusters of partly interconnected spongy pores (Figure 4.26a, b). 3D Slice and View images show that organic pores branch out and interconnect with each other, and may grow into large (up to 500 nm), complex pores (Figure 4.26c, d). These can be located directly within an organic particle (Figure 4.27b, c) or, most commonly, at particle margins, often within compaction shadows of mineral grains (Figure 4.26b, Figure 4.27b-f). Organic pores, if large enough, show a characteristic jagged wall structure (Figure 4.27d). Similar jagged structures occur in pores that do not visibly penetrate the organic mass but occur at the interface of organic and inorganic phases (Figure 4.26e). This observation suggests that those are *de facto* organic in origin, and likely represent the

thermogenic loss of the organic mass (Figure 4.26h, Figure 4.27h). Depending on their relation to the surrounding inorganic phases, such inorganic-hosted pores can be classified either as interparticle or intraparticle. The interparticle pores are most commonly found in compaction shadows of mineral grains (Figure 4.26e, f; Figure 4.27g), between folded clays and partly compacted clay floccules (Figure 4.26g) or between horizontal clay platelets, often following the elongation of the associated organic phase (Figure 4.26h). The intraparticle pores are present within pyrite framboids (Figure 4.26i), faecal pellets (Figure 4.27i) or along cleavage planes of mica group minerals.

Mineralogical composition from SEM images. Estimation of the Representative Elementary Area

To determine the Representative Elementary Area that could yield representative porosity values and its distribution in the shale matrix, a mix of EDX maps was used. The box counting was performed once for each sample and proceeded until measurements made on a particular parameter did not change by more than 10% relative to the previous area (Figure 4.28) (VandenBygaart and Protz, 1999). The estimation of the REA did not include organic matter grains which remained largely unresolved in the EDX maps. The counting showed that in all shales, the scale of a change in the content of each mineral phase depends on both the abundance and spatial distribution of the measured components. For instance, we noticed only a small change in variance of the most abundant phyllosilicate phase, with values below 10% for areas above 1100 μm^2 (Table 4.8). Much larger areas were required to obtain a representative area for less abundant and more dispersed quartz and feldspar (5985 μm^2 for the B10458 and 4397 μm^2 for the C10401 sample), and carbonates (5985 μm^2 in the shale from well C). Within the overmature shale, only for the sparse carbonates from the B well sample as well as pyrite in the C well shale did the change remain significant for much larger areas – up to 7818 μm^2 and 20644 μm^2 respectively. In contrast, in the early mature shale, box counting did not yield representative values for most of the phases until the area up to 7818 μm^2 for quartz and feldspar, 39577 μm^2 for carbonates and 59121 μm^2 for pyrite. For the purpose of this paper, 5985 μm^2 area was established as representative for both overmature shales. The mineral phases that are not representative for the samples on such a limited area are spatially scarce and therefore their impact on the estimation of the REA may be neglected. In the early mature shale, the established representative area is larger: 7818 μm^2 and is limited to areas that are scarce in fossil fragments.

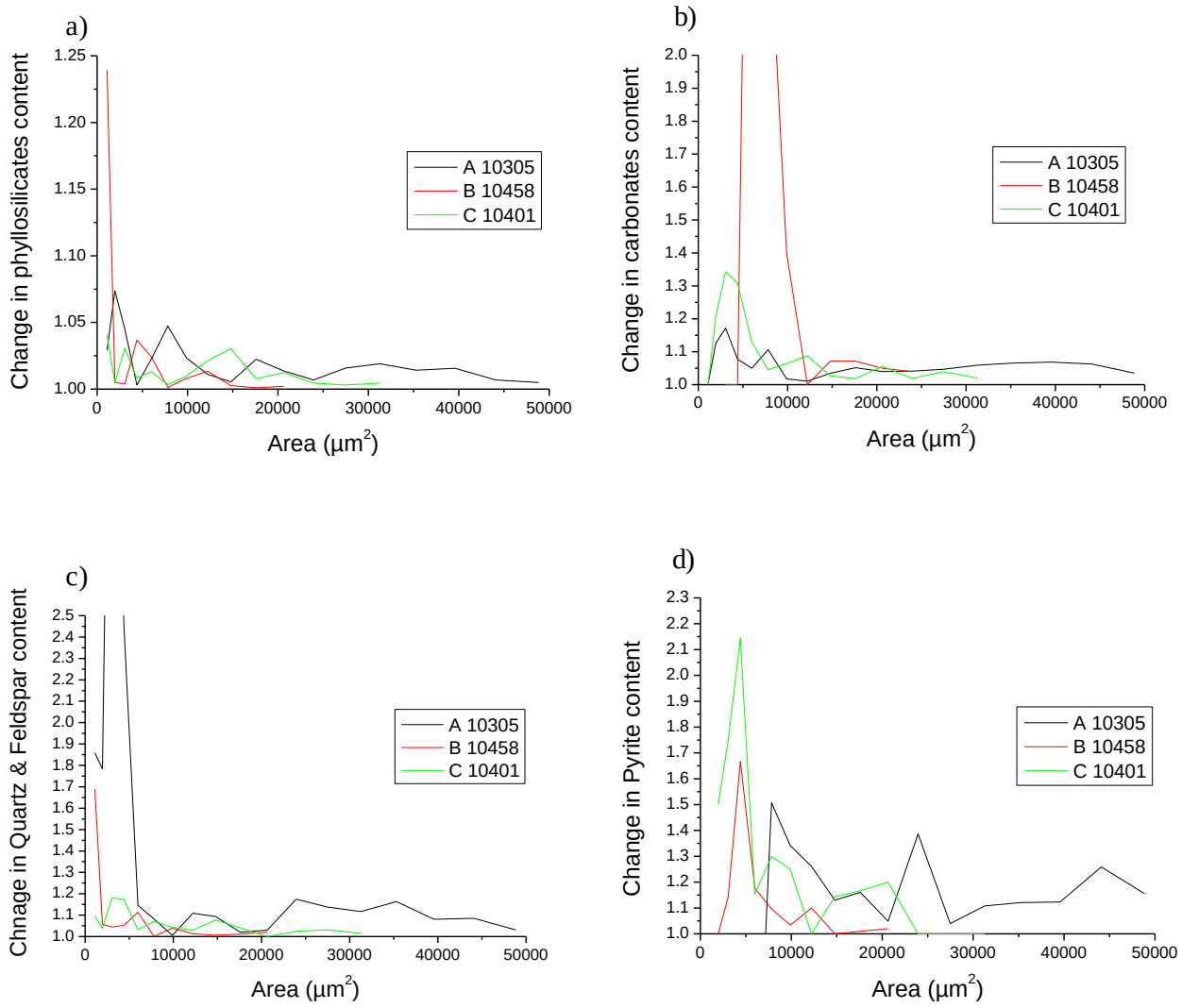

Figure 4. 28. *Change of the mineralogical composition within areas of progressively increasing size as retrieved from EDX maps of three selected shale samples. Measurements reflect % change of a parameter between two successive areas. Phases investigated include phyllosilicates (a), carbonates (b), quartz and feldspar (c) and pyrite (d).*

Table 4. 8. *Minimum area for which a change in the mineralogical composition does not exceed 10%, estimated for four mineral groups: phyllosilicates, carbonates, quartz + feldspar, and pyrite. Samples investigated include A10305 (0.7% Ro), B 10458 (1.9% Ro) and C 10401 (1.9% Ro).*

Sample	Area (µm²) for < 10% change in the phase content			
	Phyllosilicates	Carbonates	Quartz + Feldspar	Pyrite
A10305	1099	39577	7818	59121
B10458	1099	7818	5985	5985
C10401	1099	5985	4397	20644

Despite the fact that the representative area could be graphically determined for all shale samples, its average EDX composition does not always agree with the volume converted XRD mineralogical content (Table 4.9). For instance, the estimated content of the

phyllosilicate phase in all shales is significantly higher than determined by XRD, yet shows only small scatter when calculated for different areas of the same sample. This indicates that due to the limited resolution of EDX maps when captured on large areas, a graphical way of mineral quantification is not a valid method and may lead to overestimation of mineral phases that remain either intermixed with organic phases or which are internally porous. Similarly, mineral phases may be either under- or overestimated if large scale sample heterogeneity introduces significant variation in the content of minerals or fossils over large areas (e.g. large shell fragments in sample A10305).

Table 4. 9. *Comparison of EDX Representative Elementary Area phase composition and bulk mineralogical composition retrieved from XRD. XRD mineral contents were converted to vol.% of rock using standard grain densities of composite minerals. Numbers in brackets show standard deviation for EDX mineral content estimation.*

Phase	Phyllo-silicates (vol.%)		Qtz+Fsp (vol.%)		Carbo-nates (vol.%)		Pyrite (vol.%)	
Method	EDX	XRD	EDX	XRD	EDX	XRD	EDX	XRD
A10305	67.6 (+/-13.9)	42.0	8.7 (+/-5.4)	14.7	13.2 (+/-15.7)	6.0	0.2 (+/-0.1)	1.0
B10458	70.5 (+/-5.4)	56.6	16.1 (+/-1.2)	19.3	0.9 (+/-0.1)	3.2	5.0 (+/-2.3)	3.2
C10401	63.5 (+/-2.9)	49.5	13.5 (+/-0.9)	15.3	12.9 (+/-0.8)	10.9	0.8 (+/-0.6)	1.0

Quantification of BIB-SEM porosity. Pore size distribution of meso- and macropores.

The quantitative assessment of SEM porosity was performed on BIB-polished thin sections on a pre-determined, representative elementary area. As a compromise between the number of images and their resolution, for the two overmature shales the image mosaics were acquired at a magnification of 6,000 x (pixel size 15 nm), covering an area of 6871 µm^2. For the early mature shale, due to a large scatter in the distribution of the visible algal bodies and a significantly smaller number of pores per unit area, the mosaic was acquired at a significantly lower magnification of 600 x (pixel size 100 nm), and covering a total area of 306602 µm^2. Additionally, for each of the shale samples, < REA 1-2 mosaics were acquired at 10,000 x magnification (pixel size 6 nm), covering an area of 3665 µm^2 each.

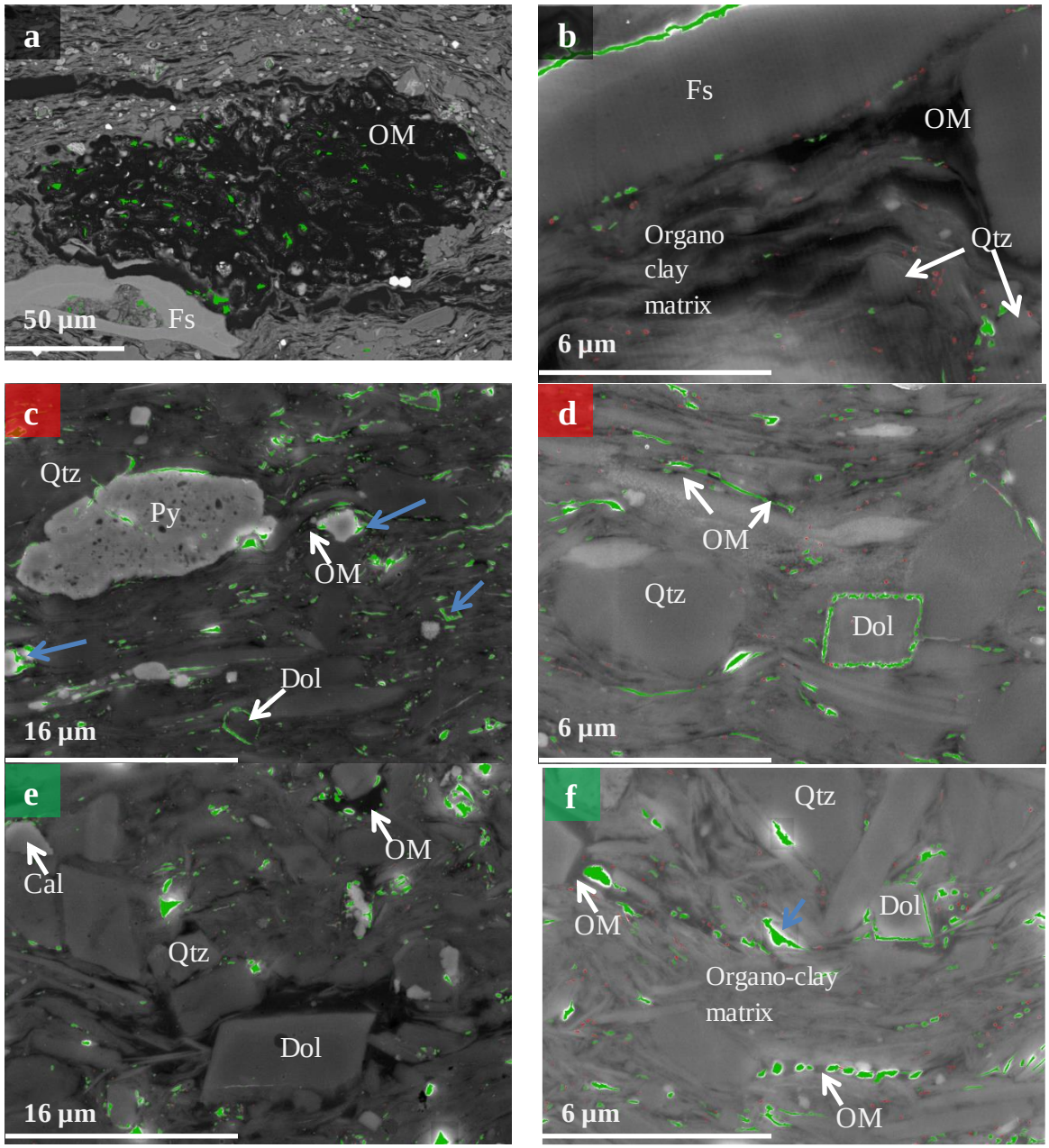

Figure 4. 29. *BIB-SEM images as part of the image mosaics showing distribution of pores. Green denotes pores that are not directly connected, and red, pores which size is equal to or smaller than the maximum "real"pore throat size penetrated by mercury (see text). A10305: a) Mag. 600 x; Although the groundmass organic matter is not internally porous, pores commonly populate Bottryococcus bodies. b) Mag. 10,000 x; Inorganic pores rim fossil assemblages and concentrate around quartz grains, with only a small proportion of much finer pores visible in the organo-clay matrix. B10458: c) Mag. 6,000 x; Pores rim dolomite rhomboids and concentrate in compaction shadows of mineral grains, often in association with residual organic matter (blue arrows). d) Mag. 10,000 x; Pores visible in the organo-clay matrix are predominantly associated with organic matter squeezed between horizontally aligned clays and/or grains, and may follow elongation of the organic particles. C10401: e) Mag. 6,000 x; Pores developed mostly in vicinity of mineral grains disseminated in the shale matrix, often within accumulated organic matter. f) Mag. 10,000 x; Pores are present directly in the clay matrix between folded clays (blue arrow), and in accumulated organic matter. Note that not all organic matter is visibly porous. Fs- fossil, Cal – calcite, Dol – dolomite, Py – pyrite, Qtz – quartz, OM – organic matter.*

In all shales, visible pores are found predominantly in compaction shadows of mineral grains, and within organic matter; clay porosity is unresolved at all magnifications (Figure 4.29). In the A10305 shale, although the groundmass organic matter is not internally porous, pores commonly occur in Botryococcus bodies (Figure 4.29a). Moreover, inorganic pores rim fossil assemblages and concentrate around quartz grains, with only a small proportion of much finer pores visible in the organo-clay matrix (Figure 4.29b). In the B10458 shale mosaic, pores rim dolomite rhomboids and are concentrated in compaction shadows of pyrite crystallites and quartz, often in association with residual organic matter (Figure 4.29c). Pores visible in the organo-clay matrix are predominantly associated with the organic matter squeezed between horizontally aligned clays and/or grains, and may follow elongation of the organic particles (Figure 4.29d). Finally, in the C10401 shale, pores are developed mostly in the vicinity of pyrite and dolomite crystals, either at the margins of mineral grains, or within accumulated organic matter (Figure 4.29e, f). More commonly than in the B10458 shale, pores are present between folded clays, interpreted as incompletely compacted clay floccules (Loucks *et al.*, 2012). In both overmature shales, even at the high magnification of 10,000 x, only 30% of point counted organic grains bear visible pores, with most of the organic matter remaining visibly non-porous.

To compare porosity and the distribution of pores sizes between representative areas of different samples, only fully resolved pores were taken into account. Their minimum size was estimated after grouping all pore areas into bins of an increasing size and plotting them as a function of pore numbers (Figure 4.30) (Houben *et al.*, 2013; Klaver *et al.*, 2012). At all maturities, a fractal distribution of fully resolved pores was approximated by one linear regression line, with slopes of -2.21 in A10305, -2.36 in B10458 and -2.19 in C10401 shale (Figure 4.31a). For the two overmature shales from wells B and C, pores smaller than 100 nm could not be linearly fitted, and this diameter is interpreted as the minimum pore diameter fully resolved in the REA images. For the A shale, due to the lower resolution of images, the minimum fully resolved pore size is larger – 280 nm.

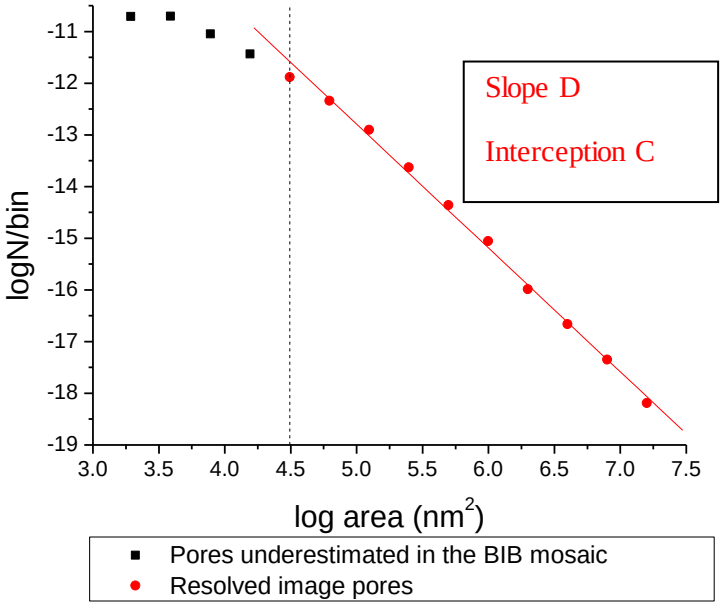

Figure 4. 30. *Typical distribution of pores from BIB-SEM mosaics of the Wealden shale samples. An area of investigation covers the size of an estimated Representative Elementary Area. Fully resolved pores (red circles) are fitted with a linear regression line defined by a slope (D) and a point of interception with the y axis (C). Pores not fully resolved in mosaics (black squares) deviate from the linear regression line estimated for the fully resolved pores.*

Table 4. 10. *Binarized BIB/SEM image porosities and point-counted relative contribution of different pore types of selected Wealden shales samples: A10305 (Ro 0.7%) B10458 (Ro 1.9%) and C10401 (Ro 1.9%). The minimum fully resolved pore size is 100 nm, except for the sample A 10305, 280 nm.*

Sample	Area (µm²)	BIB image porosity > 100 nm (%)	BIB image porosity as fraction of total porosity	BIB image porosity > 280nm (%)	BIB image porosity as fraction of total porosity	% of organic, inter-, intraparticle pores
A 10305	638x479	nd	nd	0.2	0.01	nd
B 10458	96x70	1.7	0.19	1.0	0.12	46-52-2
C 10401	96x70	1.1	0.10	0.7	0.07	52-43-5

The resolved image porosity of the two overmature shales amounted to 1.7 and 1.1% in the B and C samples respectively (Table 4.10). In the A shale, at a lower resolution of the image mosaic, the porosity amounted to 0.2%. For comparison, in the two higher maturity shales, if only pores > 280 nm are taken into account, the porosity is much higher than in the low maturity shale, reaching 1.0% in the B10458 and 0.7% in the C10401 sample. For all shale samples, a differential distribution of pore sizes shows a single maximum located between 400-560 nm in B and C and 560-800 nm in the A shale (Figure 4.31b). In the two overmature shales, due to the greater resolved porosity, the maximum is more pronounced, and corresponds to the onset of a decrease in the density of pores with a diameter < 400 nm.

The median diameter of fully resolved pores from all samples investigated is the highest in the low maturity shale, 438 nm (Table 4.11). When taking into account the equivalent pore size range in the overmature shale samples, this diameter is only 378 and 390 nm for the B and C shale respectively. The higher median diameter in the A well shale indicates that at the lower maturity, larger pores are more abundant and contribute more porosity than equivalent pores in the overmature shale (Figure 4.31c). The most elongated pores with a median aspect ratio of 3.5 were found in the overmature B shale, consistent with its highly aligned fabric (Table 4.11 and Figure 4.31d). In two other shales, the aspect ratio of pores > 280 nm is much lower, only 2.2 and 2.0 in the A10305 and C10401 sample respectively.

Table 4. 11. *Median size and aspect ratio of pores which diameter exceeds 280 nm diameter resolved in BIB-SEM image mosaics of the A10305 (0.7% Ro), B10458 (1.9% Ro) and C10401 (1.9% Ro) shale.*

Sample	Median equivalent diameter (nm)	Median aspect ratio
A 10305	438	2.2
B 10458	378	3.5
C 10401	390	2.0

At the magnifications (6,000 x) used in this study, fully resolved image porosities contained in pores > 100 nm constitute only 19 and 10% of the physically measured total porosity for the investigated B10458 and C10401 samples, respectively (Table 4.10). When taking into account fully resolved pores > 280 nm characteristic for mosaics taken at a magnification of 600 x, the fraction of total porosity resolved in images of the two shales is even lower, only 12 and 7%. At the similar magnification in the low maturity sample, fully resolved pores (> 280 nm) constitute only 1% of the total porosity, the lowest value in all samples investigated. A comparison of image and mercury injection derived cumulative and incremental porosity curves show that > 100 nm and > 280 nm image pore bodies are 1-3 orders of magnitude larger than pore throats 'seen' by the mercury injection experiments, and thus they are not directly connected at the image scale (Figure 4.29a, c, e; Figure 4.32a, b). This lack of connectivity is consistent with the differential distribution of image resolved pores, showing decreasing contributions to porosity towards smaller pores (Figure 4.31b). In all investigated shales, pores of a size of mercury apertures (< 75 nm, 48 and 56 nm in A10305, B10458 and C10401 shales respectively) are poorly resolved even in mosaics captured at a magnification of 10,000 x. These pores are located primarily in the poorly-resolved organo-clay matrix, and in the case of the overmature samples, directly in the organic matter (Figure 4.29).

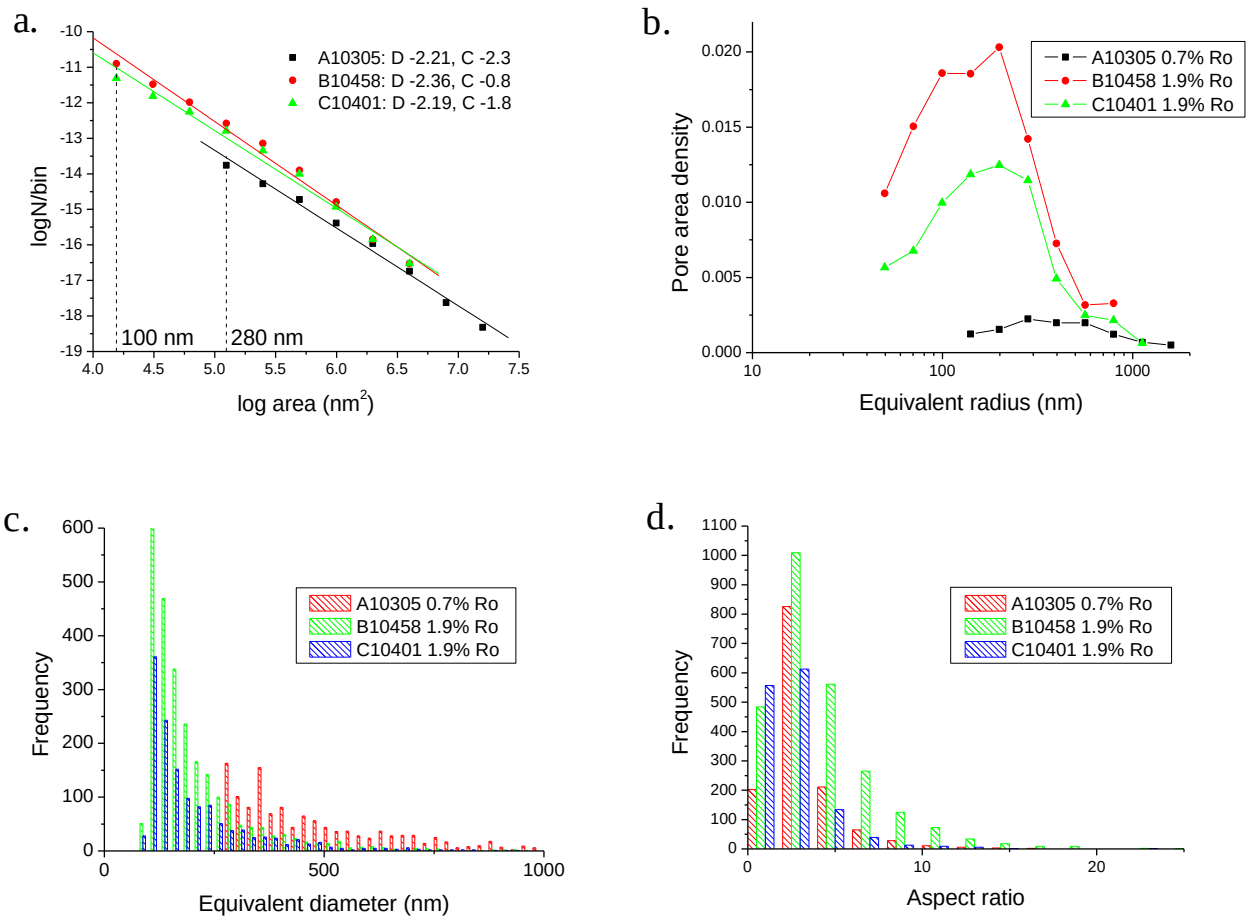

Figure 4. 31. *Distribution of pore sizes, equivalent diameters and aspect ratios of BIB-SEM fully resolved pores for the three samples: A10305 (0.7% Ro), B10458 (1.9% Ro) and C10401 (1.9% Ro). Images were captured at the magnification 6,000x (B10458, C10401) and x600 (A10305). a) Fractal distribution of pores > 100 nm (B10458, C10401) and > 280 nm (A10305) with the line of the best linear fit described by a slope (D) and intercept with the y axis (C). b) Differential pore size distribution as a function of an equivalent radius shows a single maximum located between 400-560 nm in B and C and 560-800 nm in the A shale. Note sharp decrease in the pore area density of pores with a diameter below < 400 nm in the overmature shale samples. c) Size distribution of image pores as a function of pore number. For the early mature shale, contribution of pores with a diameter > 250 nm is approximately twice as much as in the overmature shale. d) Aspect ratio of image pores for samples described in d).*

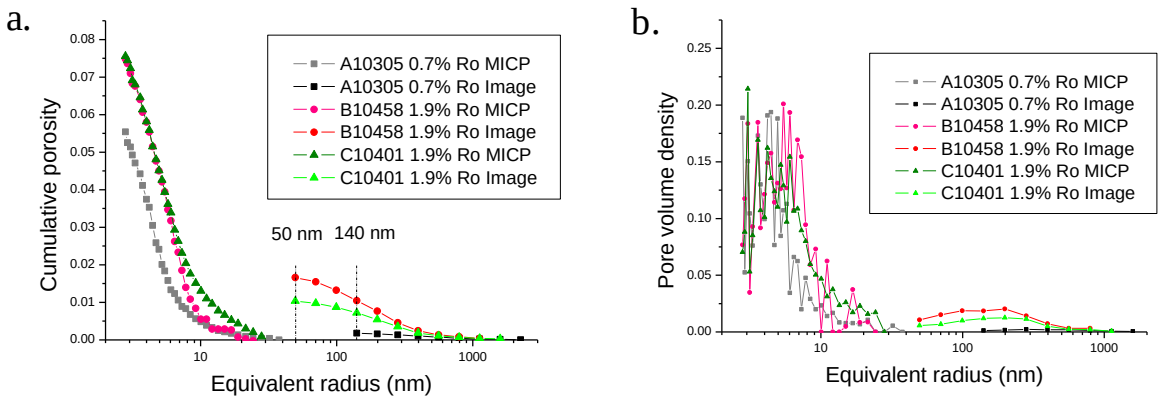

Figure 4. 32. *Comparison of cumulative porosity (a) and pore size distribution (b) obtained from mercury injection (> 5.6 nm) and image analysis of pores for three samples: A10305, B 10458 and C 10401. The analysis of image pores included only fully resolved pores in respected mosaics: > 140 nm radius in the A shale, and > 50 nm radius in both B and C shales.*

Distribution of image pores in shale domains

Quantification of image pores in relation to the content of mineral phases was performed on < REA mosaics acquired at a magnification of 10,000 x (practical minimum pore diameter 50 nm). For each mosaic, extracted porosity was superimposed on the EDX-derived mineralogical composition corrected for the point counted content of organic matter. All areas selected for the analysis are clay-rich except for the C10401 mosaic, with < 50 vol.% of clays and > 10 vol.% of carbonates (Table 4.12).

Table 4. 12. *Porosity and phase composition of BIB-SEM mosaics selected for the porosity-mineralogy quantification.*

Sample	Area (μm^2)	Porosity (%)	OM (%)	Phyllosilicates (vol.%)	Qtz+Fsp (vol.%)	Carbonates (vol.%)	Pyrite (vol.%)
A10305	77x48	0.4	23.8	57.1	11.1	8.8	0.2
B10458	64x48	0.8	11.8	63.4	16.8	1.1	6.1
B10458	64x48	2.1	23.1	56.9	14.1	2.8	0.8
C10401	77x48	3.6	24.4	43.6	16.0	10.6	2.6

At the scale of the BIB-SEM mosaics, clay packages are not visibly porous at any maturity (Figure 4.33), and thus no correlation was encountered between EDX-derived phyllosilicate content and image macroporosity (Figure 4.33a, b). Likewise, no correlation was found for image porosity and the content of carbonates, all showing scatter over a large range of values (Figure 4.33c, d). Despite this lack of a distinct trend, in both the A10305 and C10401 mosaics carbonate-rich areas have higher porosity values than carbonate-depleted

domains. For instance, in the C10401 mosaic, the image porosity of areas with > 5 vol.% carbonate shows the highest spread and the porosity values (1-9%) are higher than in areas with carbonate contents < 5 vol.% (0.5-5.5%). Similarly, in the low maturity A10305 mosaic, areas for which the carbonate content exceeds 40 vol.% show higher porosity values (0.4-2.0%) than areas with carbonate contents below 20 vol.% (0.1-1.1%). No such pattern exists in the B10458 mosaic, where no difference between the porosity of the carbonate-rich and carbonate-poor areas was found; this may be related to the low overall carbonate content (Table 4.12, Figure 4.33d).

In all shales, image porosity is more strongly related to the volume of point counted organic matter than to the amount of any mineralogical phase. In the low maturity shale, this relation is negative, with the most organic-rich areas (ca. > 60%) showing low porosities (< 0.5%) (Figure 4.33e). In contrast, a positive correlation is encountered both in the gas-mature, carbonate-poor B 10458 shale and as well as in carbonate-poor areas within the gas-mature C10401 mosaic (Figure 4.33f). For these samples, porosity increases from 0.4 to 5.5% as organic matter content increases from 5 to 40%. The image porosities of areas rich in carbonates (> 5%) are less related to the content of organic matter and show significant variations over a small range of the OM abundance (Figure 4.33f). To highlight the positive effect of organic matter on image porosity within the C 10401 mosaic, we extracted intraorganic pores and excluded porosity concentrated in compaction shadows of mineral grains. The resulting relation is positive, with porosities varying between 0.2-1.3% over the 19-40% organic matter variation (Figure 4.33g). This result also shows that absolute image porosities contained directly in the organic matter are smaller than porosities spatially associated with the inorganic grains.

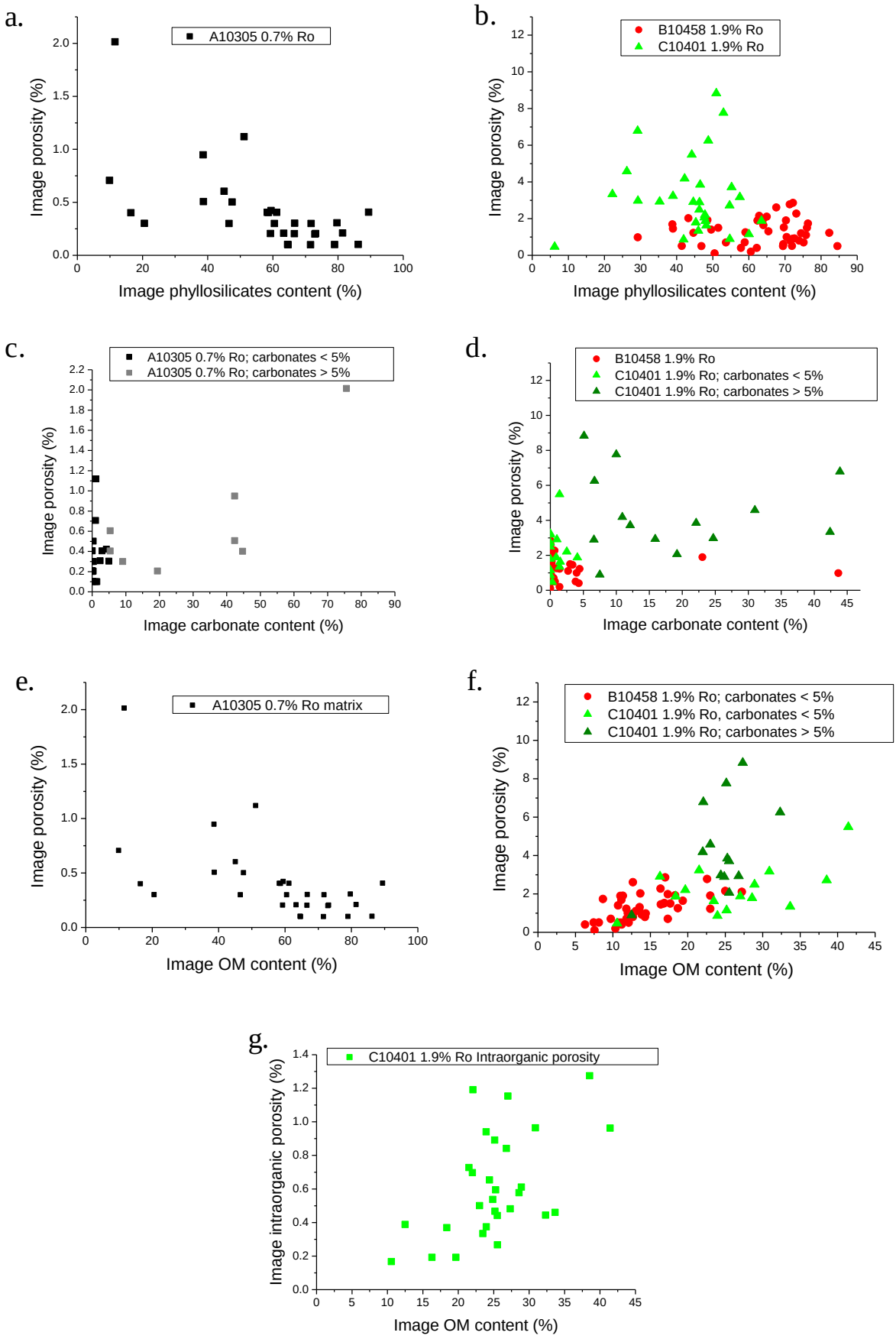

Figure 4. 33. *Covariation of image porosity with phyllosilicate, carbonate and OM content. Each data point represents one BIB-SEM image captured at mag. 10,000 x.*

Discussion

Depositional environment and facies variation

The stratigraphy of all three sections comprises < 1 m alternations of organic-rich and organic-lean facies composed of siliciclastic and fossiliferous mudstones, mud-depleted limestones and concretionary carbonates. This lithological variability extends to a centimetre and sub-centimetre scale with adjacent beds or laminae showing varied abundances of autochtonous, allochtonous and diagenetic components. According to Mutterlose and Borneann (2000), the distribution of facies within Lower Creatceous sediments in the Lower Saxony Basin is related to differential subsidence, local tectonics and sea level changes. At the locations of the cores investigated in this study, these changes resulted in the alternating deposition of the lake plain, distal delta front and basinal muds, as well as supralittoral, littoral and sublittoral bioclastic beds (ExxonMobil, unpublished).

The varied character of deposition of the German Wealden and its dependence on the supply of siliciclastic and biogenic material is reflected in the petrography and organic geochemistry of shales. Thin sections show that the biogenic input was dominated by the shelly detritus organized into millimeter-scale laminations (Figure 4.3m, r), typical for storm and turbidite deposits of littoral and sublittoral zones (Brett and Allison, 1998), with foraminifera-rich beds marking the high productivity regime (Figure 4.4g, h) (Berner, 2011). Biogenic sedimentary structures are scarce and mostly limited to transgressive sediments deposited in the marine realm in the top parts of the core sections (Figure 4.3a, Figure 4.4a). In all cores, the strongly siliciclastic and basinal character of the sediments dominates (Figure 4.4, 4.5, 4.6), pointing to allochtonous terrigeneous input as the primary source of the sediment (Figure 4.3h, Figure 4.4a, Figure 4.5g, Figure 4.6e).

The analysis of the Wealden sections reveals a link between the shale lithofacies, depositional environment, and the organofacies type. The TOC screening showed there is a higher frequency of organically leaner rocks in the more proximal A core in comparison to the more basinal located cores B and C. As the organic richness is a function of production, dilution, preservation and nutrient recycling, without elemental analyses it is difficult to determine the contribution of each of these factors on the observed pattern (Bohacs *et al.*, 2005; Sageman *et al.*, 2013; Werne *et al.*, 2002). In shale gas plays across the world, e.g. the Marcellus Shale, the organic enrichment in aquatic kerogen coincides with periods of low dilution by biogenic debris and excellent preservation in anoxic or euxinic conditions (Werne

et al., 2002). In the Wealden, we found that in all sections, the most TOC-rich intervals are associated with siliciclastic shales deposited away from terrigenous sediment sources and with limited biogenic input (Figure 4.4c, Figure 4.5e). The only exception is coaly mudstones found in the C core, where high present-day concentrations of organic carbon resulted from deposition of land plant type III kerogen on a lake plain (Figure 4.6g). Lower organic contents in the Wealden sediments coincide with the presence of macrofossil debris, biogenic sedimentary structures and carbonate cements. As the organic-lean shales have predominantly low HI (HI < 400), and there is no petrographic evidence for the increased input of terrestrial macerals, we interpret this as a result of limited preservation of aquatic kerogen (Canfield, 1993; Curtis, 1995; Irwin *et al.*, 1977; Kidwell, 1989; Schutter, 1998). Because carbonates tend to dilute organic matter in siliciclastic sequences (Werne *et al.*, 2002), we presume that organic carbon concentrations are dilution-limited in carbonate-rich intervals in the Wealden. This is supported by the up to four times lower TOC contents as compared to siliciclastic mudstone at similar HI values (> 700). The distribution of organofacies observed in the German Wealden is typical for sediments deposited in overfilled lakes, for example the Luman Tongue member of the Green River Formation (Bohacs, 1998).

Porosity distribution and its relation to lithology, organic content and maturity

Early oil window maturity shale

A detailed analysis of different rock types shows that total porosities vary within and between maturities (Figure 4.13). In relatively immature Wealden shales (Ro 0.5-0.6%) with visibly non-porous organic matter, porosities range from 1-17%. The potential factors that could cause this porosity difference include: effective stress, lithology differences, and cementation (Bjørlykke, 1999). Here, with the restricted depth range of the studied interval effective stress cannot explain the observed porosity variation (Table 4.A2). Instead, our results show that total porosity of the immature Wealden shale is strongly controlled by the organic matter content and lithological variations, where lithology is defined by the content and arrangement of the clay, carbonate and silt particles. To be precise, we found that the relation between total porosity and organic content in the carbonate facies (including microfossil-bearing mudstones, macroshell laminated mudstones, fossiliferous limestones, and concretionary carbonates) is opposite to that in siliciclastic shales (both biologically reworked and fabric-intact organic-rich mudstones; Figure 4.20a).

For the carbonate-rich facies, the relationship is positive and, as supported by the petrographic micrographs, it is controlled by the extent of cementation, most pervasive in the leanest rocks (Figure 4.3c). Consistently, the lowest porosities are in rocks with TOC < 1.5 wt.%, in which organic matter is dominated by degraded kerogen (bottom left on Figure 4.9a). While we do not have information regarding the timing or nature of the cements, we presume that the positive correlation between organic carbon and total porosity reflects a depositional link between the intensity of microbial oxidation, the degree of diagenetic cementation and the extent of preservation of organic matter (Bohacs *et al.*, 2005; Curtis *et al.*, 1995; Lash and Engelder, 2011; Macquaker and Gawthorpe, 1993; Raiswell and Fisher, 2000). In the investigated samples the amount of cement visible in thin sections decreased and porosity increased in the order: carbonate concretion - fossiliferous limestones - macroshell laminated mudstones - microfossil-bearing mudstones. This order agrees with Schutter's (1998) observation that clays arrest cementation and thus porosity loss by inhibiting transfer of solutes to the precipitation sites.

In the clay-rich siliciclastic shales, the relation between porosity and organic content is negative and, as discussed below, strongly controlled by the shale composition and arrangement of the silt particles. The two shale end members distinguished within this group are (a) organic-lean, visibly bioturbated mudstones with silt-lined burrow structures and (b) organic-rich mudstones with very well preserved organic material and intact fabric (bottom left and top right in Figure 4.9a respectively). Porosity data, supported by petrographic micrographs, show that porosities halve from 18% to 9% when moving from the organic-lean shale rich in silt-lined biogenic structures (Figure 4.3a) to the bioturbated shale devoid of silt linings. In the more organic-rich shales, the porosity decrease is less sharp, and bottoms out at 4% in the most organic-rich shale (TOC 15 wt.%) (Figure 4.3f). Although we cannot fully explain the above relationships without a representative set of grain-size data, our mercury injection porosity curves imply that the occurrence of tens of micrometer size quartz grains packed in discrete aggregates plays an important role in resisting compaction and enhancing porosities, at least on a local scale. This presumption stems from the presence of the bimodal pore size distribution within the silt-burrowed shales, with a considerable amount of porosity accessed through pore throats 50-100 nm (Table 4.6).

We cannot be conclusive about the reason for a consistent drop in porosities in the organic-rich siliciclastic shale. It is plausible that the observed trend reflects the ratio of the porosity held by kerogen as compared to the bulk inorganic matrix. In our study, both clays and kerogen are mostly microporous (Figure 4.22, Figure 4.33a, e), and when combined with

the Posidonia Shale data set (Figure 4.23), they show a positive relation with the 195K CO_2 sorption porosity which is believed to be mainly in < 6 nm pores (Rexer *et al.*, 2014). Although Rexer *et al.* (2014) showed that at low maturities kerogen contributes half the total pore volume in sorption pores, those experiments did not account for the pore space contained in larger mesopores (Kuila *et al.*, 2013; Schieber *et al.*, 2010). Therefore we presume that the fraction of porosity held by the inorganic pores exceeds that indicated by Rexer *et al.* (2014) and could explain the relatively lower porosities of the most organic rich clays.

Gas window maturity shale

At higher maturities (Ro 1.5-2.4%), total porosities of shales show a somewhat smaller spread as compared to their low maturity counterparts, spanning between 2-12%. The loss of porosity is consistent with higher effective stress and greater compaction usually experienced by deeper buried rocks (Bjørlykke, 1999; Bjørlykke and Høeg, 1997; Connell-Madore and Katsube, 2006; Van de Kamp, 2008), and reflected here by the decrease in the mean Hg access radius (Table 4.6). The evidence of compaction is readily seen in connection to the disappearance of algal cysts (Figure 4.10), often associated by the collapse of the shale structure (see Chapter 3). Moreover, diagenetic features, such as irregular patches of silica, rhomboids of diagenetic dolomite, and carbonates locally filling interstices between fossil fragments (Figure 4.5e, i, Figure 4.6c, e) are consistent with typical features of chemical compaction occurring in shales (Laughrey *et al.*, 2011; Peltonen *et al.*, 2009). Although we cannot provide details of the timing of the cementation events, at least the first two types of cements occur predominantly within the high maturity Wealden shale and are mostly absent from low maturity counterparts.

The second evidence of the loss of porosity in the overmature Wealden shale is the presence of solid bitumen. As inferred from the oil immersion and SEM micrographs (Figure 4.10), solid bitumen represents in-situ generated or migrated bitumen that remained trapped in the rock and filled up potential pore space (Curiale, 1986). Although in this study we did not have any samples of oil window maturity, from the Posidonia shale study (Chapter 3) it is known that at the peak oil generation, pore-filling bitumen is visibly non-porous. In the overmature Wealden, bitumen contains visible pores (Figure 4.26 and 4.27), explaining the positive relationship between organic carbon content and total porosity encountered in both fossiliferous and siliciclastic shales (Figure 4.20b). The presence of secondary organic pores

also implies that the loss of porosity due to compaction and bitumen filling was higher than that directly inferred from the difference between the present day porosity values.

The control of organic matter on total porosity in the gas window shale is less clear in the fossil-bearing rocks than in the siliciclastic shales (Figure 4.20b). With the help of the petrographic and SEM micrographs (Figure 4.10g), we interpret a different slope of the porosity-TOC relation as related to the variable abundance of non-organic pores. As already shown in the low maturity shale, porosity in the organic-lean fossiliferous rocks is affected by cementation, with more pervasive cements in the relatively leaner rocks. The presence of inorganic pores in these rocks at higher maturities implies that either compaction was arrested or secondary porosity developed due to dissolution of inorganic phases (Loucks *et al.*, 2012; Schieber, 2010). The first hypothesis is supported by the presence of migrabitumen in the shelter porosity of the organic-lean but highly porous fossiliferous mudstone. The abundance of this bituminous phase suggests that the rock was sufficiently porous to allow migration of the bitumen phase, likely generated in more organic-rich intervals and contributing to the "carryover" effect of S1 into the S2 peak (and thus high HI values, Table 4.A1) in the top section of our C core (Rippen *et al.*, 2013). As presence of oil was previously reported to retard compaction in quartzose and carbonate oil filled reservoirs (e.g. Worden et al., 1998; Heasley et al., 2000; Scholle, 1977), it is possible that in the fossiliferous Wealden Shale, carbonate surfaces became oil-wet, inhibiting pore cementation (van Duin and Larter, 2001; Aplin and Larter, 2005). Still, given the etched-like character of many carbonate surfaces (Pudlo *et al.*, 2012), we cannot preclude the possibility that the inorganic porosity partly filled by the migrating bitumen is secondary, evolved under the action of carboxylic and phenolic acids released from the kerogen at elevated temperatures (Crossey, 1991; Schieber *et al.*, 2010).

In comparison to fossiliferous shales, siliciclastic mudstones show a wider variation of the total porosity over a large range of organic carbon contents, proving the dominant control of organic matter abundance on porosity in clay-rich shales. The maximum contribution of inorganic pores may be estimated from the imaginary intercept of the TOC-porosity relation with the *y* axis, here corresponding to ca. 4-6% of the bulk rock (Figure 4.20). Similarly to the low maturity Wealden, this porosity is held predominantly by pores not visible in the SEM, and certainly not quantifiable with microscopic methods. Indeed, sorption experiments showed that approximately 30-50% of total porosity is held by micro- and fine mesopores (< 6 nm), equivalent to 4-5% of the bulk rock, probably with at least half of the volume outside the organic matter (Rexer *et al.*, 2014). In contrast, image mosaics (practical resolution 240

nm) showed that only fraction of the porosity (0.5% of the bulk volume) is contained in inorganic pores large enough to be quantified with microscopic methods.

Total porosities measured in the overmature siliciclastic shales are independent of the size of the pore throat apertures (Groups 2 and 3 in Figure 4.20b), consistent with the secondary nature of the organic porosity. In contrast, high resolution images showed that macroporosity is strongly controlled by the mineralogical composition. As shown in Chapter II, biogenic debris may create traps for the generated bitumen, which when exposed to higher temperatures will exsolve gaseous phases, leading to the formation of secondary porosity (e.g. Bernard *et al.*, 2012; Chalmers *et al.*, 2009; Curtis *et al.*, 2010; Jarvie, 2007; Loucks *et al.*, 2009; Milner *et al.*, 2010). In the clay-rich Wealden Shale, a similar role is played by authigenic carbonates, providing compaction shadows for bitumen accumulation and secondary porosity development (Figure 4.26d, Figure 4.27d). We found that despite much scatter in the macroporosity data, there is significantly more pore space associated with compaction shadows of the carbonate grains and crystals rather than present within clay-rich domains (Figure 4.33d). Interestingly, there is no quantitative evidence for quartz grains displaying a similar association with porosity, despite the high content and scattered nature of the quartz grains. Precipitation of diagenetic carbonates during post-burial diagenesis is driven by pore water alkalinity and partial pressure of CO_2 and thus at increased temperatures organic reactions may favour precipitation of dolomite cement (Davies, 1979; MacGowan, 1990). However, the same factors will control dissolution of carbonates, promoting appearance of dissolution rims around dolomite grains and partly dissolved crystals (Figure 4.24d). Hence, it is suggested that the mutual effect of the grain dissolution and bitumen entrapment, followed by secondary porosity development, led to increased porosities of the carbonate-rich microdomains as compared to quartz-rich domains. The positive effect of carbonate content on image porosity enhancement is in contrast to reports of bulk porosity decrease with high calcite cement abundance (Lu *et al.*, 2011). This highlights the importance of petrographic validation of the bulk porosity and XRD results by establishing the genesis of carbonates and comparing porosities from an equivalent pore size range.

Evolution of organic porosity in the gas window

The positive relation between total porosity and TOC found in the overmature Wealden shale is a common feature of multiple shale gas plays (Passey *et al.*, 2010). Hence, in order to build quantitative models of organic matter and total porosity change with maturity, there is a

need for a better understanding of the evolution of organic pores. To date, the most urgent questions to be answered involve: the role of organic matter type in the development of organic pores, mechanisms that lead to the formation of pores, the maturity at which this formation occurs, and the range of pores sizes.

The presence of two distinct organic pore type end members, and the visibly heterogeneous nature of organic pores (Figure 4.26, 4.27) imply that, similar to the Posidonia shale (Chapter 2), the evolution of porosity in the overmature Wealden is at least partly controlled by the composition of the organic material. The first pore type end member distinguished in this study embraces highly irregular, up to > 500 nm in size pores with a characteristic jagged wall structure, visibly penetrating the solid bituminous mass (Figure 4.26i, Figure 4.27d, h). The second end member includes discrete, fine organic pores, disconnected from each other on the scale of the SEM imaging (Figure 4.27a). Because the full spectrum of organic pore types is much wider and only bracketed by these two end members, it is reasonable to assume that there is a related compositional spectrum of organic matter particles, which evolve during maturation and oil cracking. Such an assumption is consistent with kinetic schemes of petroleum generation, involving the thermal decomposition of high molecular weight polar compounds and their successive cracking into lighter hydrocarbons with a solid residue remaining in the form of char (Behar *et al.*, 2008a, b). Therefore, we link the variation in the morphology of organic pores observed in this study to the concept of successive steps in hydrocarbon generation. In this light, pores found in compaction shadows of mineral grains are likely to represent the initial step in the cracking of hydrocarbons physically trapped in the shale matrix, experiencing a phase change and substantial volume loss. Consequently, the appearance of discrete organic pores likely reflects the onset of the gas exsolution stage from already partly polycondensed aromatic molecules (Tiem *et al.*, 2008). Similar bubble-like pores are typical for cokes, in which the formation of porosity follows the onset of a densification stage of the carbon residue (Loison *et al.*, 1989). Hence, comparably to cokes, we presume that the formation of discrete organic pores in shales is linked to densification processes within the residual bitumen, arresting release of the pressure build up during gas generation, and coinciding with limited diffusion of gas on a relevant time scale.

Identical pore types distinguished in the type I kerogen dominated Wealden shale and type II kerogen Posidonia shale (Chapter 2) point to similarities between these two kerogen types in terms of organic porosity development. This uniformity is best observed on a TOC - total porosity binary plot, with the calcareous Posidonia shale and siliciclastic Wealden shale

plotting within the same field (Figure 4.34). Although we cannot be sure about the reasons for the observed similarties, it is likely the consequence of a similar mechanism of pore development through the intermediate, solid bituminuous phase present in both shales (Figure 4.10). Within the Wealden data set, the only group of samples that did not fall onto distinct TOC – total porosity trends are samples with abundant type III/IV kerogen (Figure 4.10h). The relatively lower porosities of the coaly shales, along with the evidence of the absence of solid bitumen in their matrix, once again indicates that organic pores in gas window shales are associated with the thermal maturation of exclusively oil-prone macerals (Curtis *et al.*, 2012; Loucks *et al.*, 2009; Milliken *et al.*, 2013). Consequently, the evaluation of the genesis and preservation of those pores need to be decoupled from the evaluation of mechanisms controlling the fate of micropores encountered in coals and coaly kerogen (Green *et al.*, 2011; Loison *et al.*, 1989).

The positive relation between total porosity and organic carbon content in the overmature siliciclastic shale with the predominant genetic type I kerogen is valid for samples with a broad range of maturities between Ro 1.5 to 2.4% (Figure 4.20). A lot of attention has been given to maturity as a potential factor controlling the development of pores in gas window shales, with very promising results obtained via the combination of pyrolysis and diamondoid geochemistry (Dahl *et al.*, 2012). Here, based on total porosity measurements coupled with the petrographic characterization of rocks, we propose that maturity should not be treated as a single factor controlling porosity in gas window shales. Similar observations of a lack of relationship between image porosity and maturity were made by Curtis *et al.* (2012) on Late Devonian-Early Mississippian Woodford Shale with marine kerogen. In our study, marine Posidonia and lacustrine Wealden samples plot within the same TOC-porosity trend, and thus we exclude compositional difference between the two oil-prone kerogen types (type I and II) as a potential factor influencing the above relationship (Figure 4.20b). Similarly, we found no significant amount of residual oil that could block porosities at the gas window maturity and thus influence measured porosity values (Table 4.7). A lack of correlation between shale porosity and thermal maturity at Ro > 1.5% suggests that organic porosity evolution in Wealden was active only below that maturity level. Observing that the porosity of shales that have not experienced oil cracking is lower in comparison to their postmature and overmature counterparts (Chapter 2 and 3), we suggest that the most likely timing for the development of organic pores is the wet gas stage. Interestingly, these findings are consistent with Dahl *et al.* (2012) who noticed the maximum increase in the image organic porosity in shales that were artificially heated up to wet gas window temperatures. The lack of evidence for a further

increase in porosity in the most mature shales, despite the measured hydrogen loss (Table 4.3) suggests that the late gas generation did not produce significant volume of microcavities or alternatively, that this porosity was prone to destruction (Loison *et al.*, 1989). Consequently, our findings do not support the models of continuous organic porosity development based on the increasing transformation ratio and hydrogen loss (Romero-Sarmiento *et al.*, 2013).

To fully understand the control of organic matter on the evolution of porosity, it is necessary to recognize the range of pore sizes that control the above relationship. In this study we implemented gas sorption techniques to measure the smallest pores not recognized in SEM images. Based on the similarity between the summed sorption and mercury injection porosities compared to total porosity in a suite of Posidonia shale samples, Rexer *et al.* (2014) concluded that 195K CO_2 gas sorption mainly quantifies < 6 nm pores. For the three samples investigated here, the maximum difference between the MICP-1 <5.6 nm porosity and sorption porosity is equivalent to 3% of the bulk rock and thus raises questions about the validity of the 6 nm threshold (Table 4.7). Those differences may however be compromised by the fact that mercury porosities are prone to being overestimated due to the elastic deformation of the organic matter induced by mercury penetration under elevated pressures, expressed as a strong covariation between mercury retraction and the content of organic matter already known from coals (Toda and Toyoda, 1972) (Figure 4.17).

Based on the strong positive relationship between the wt.% sum of the phyllosilicate and organic carbon vs sorption porosity (Figure 4.23), we conclude that the amount of < 6 nm porosity is only partly controlled by the content of organic matter. Consequently, the remaining sorption porosity is likely to occur within non-visibly porous clays (Figure 4.33a, b) (Kuila and Prasad, 2013). Again, this is consistent with Rexer *et al.* (2014) who discovered that within the Jurassic Posidonia shale, at all maturities, approximately half of the sorption porosity is contained within organic matter, with the other half contained in clays and at inorganic-organic interfaces. A positive relationship between clay and organic content vs sorption porosity found for two sets of shales with varying kerogen type emphasizes a lack of difference between evolution of micropores in lacustrine and marine shales. However, as this relationship was constructed only on a limited number of samples, the above conclusion should be treated as tentative.

Similarly to < 6 nm pores, we showed that porosity resolved by SEM images is only broadly connected to the volume of organic matter (Figure 4.33). Moreover this correlation is absent for the visibly non-porous, low maturity organic matter. The lack of a clear relation between macroporosity and the content of organic matter at gas window maturities is

certainly distorted by the presence of pores encountered at the interface with the inorganic matrix. Those pores, not located directly in the residual organic matter, likely reflect thermally induced volume loss of the organic particles and very much resemble pores reported by Curtis *et al.* (2012) in the Woodford Shale or Milner *et al.* (2010) in the Marcellus Shale. The dominant contribution of macropores, with only minor amounts of visible porosity held by intraorganic pores, supports the idea that most of the intraorganic pores reported here - and in other studies (Curtis *et al.*, 2012; Loucks *et al.*, 2009; Milliken *et al.*, 2013; Milner *et al.*, 2010) - cannot be seen with microscopic methods. Yet, it is these pores that exhibit a strong positive correlation with the content of organic matter within the macropore size range (Figure 4.33g), and thus most likely control the experimentally measured total porosity-TOC relationship at diameters < 50 nm.

Potential shale gas production from German Wealden

The heterogeneity of the Wealden Shale has important implications for the economic evaluation of this potential shale gas reservoir and the related production of hydrocarbons. As already shown, the observed alternation between fossil-poor and fossil-rich lithologies is a key control on the variability of total porosity of adjacent beds and laminae on a millimetre and centimetre scale. Such variability may pose a challenge when building reservoir models of hydrocarbon exploration, including gas in place estimations and fluid flow prediction within shale packages (Ambrose *et al.*, 2010; Bowker, 2007; Bustin and Bustin, 2012; Clarkson *et al.*, 2012). Recognizing the need to better constrain the mudrock properties on a small scale, we found that the bulk shale porosities are predictable on a centimetre scale when the organic content is known, with half of the porosity associated with the organic phase in siliciclastic mudrocks with TOC contents > 10 wt.%. Interestingly, the slope of the porosity - organic content relationship differs between lithologies, and is higher in the fossil debris bearing mudstones than in the siliciclastic shales. We presume that due to the high porosities of some of the fossiliferous rocks, with the evidence of past bitumen migration to macropores, the carbonate surfaces became hydrophobic, giving rise to additional hydrocarbon storage space within inorganic calcite pores. If similar variations of the TOC-total porosity correlations exist in other shale gas plays, as e.g. those reported by Passey *et al.* (2010), it follows that the amount of effective porosity is controlled not only by the organic content, but also lithology and diagenetic history. This is important for gas-in-place estimations, since a significant proportion of total gas appears to be associated not only with large, inter-

connected nano-pores within the organic material (Ambrose *et al.*, 2010), but also large, inorganic-hosted macropores.

The results reported here support the division between marine and terrestrial organic matter as being of utmost importance when assessing the potential for the development of organic pores and in-situ gas storage sites (Schieber, 2010). In our work, we showed that kerogen type III/IV does not produce recognizable organic porosity upon maturation, and therefore its abundance is secondary to total gas-in-place predictions as compared to kerogen type I or II. Although we cannot be conclusive about the reasons for the limited porosity and thus gas potential of terrestrial macerals, Erdmann and Horsfield (2006) argue that with a high input of terrestrial organic matter, recombination reactions between kerogen and generated hydrocarbon moieties inhibit the release of hydrocarbons until higher temperatures in a source rock are attained. In this case, analogous to coals, kerogen type III/IV is at best microporous (Bustin and Clarkson, 1998; Clarkson and Bustin, 1997; Griffin *et al.*, 2013; Mastalerz *et al.*, 2008), so that gas is mainly physisorbed within organic particles (Ambrose *et al.*, 2010; Bustin and Clarkson, 1998). In contrast to oil-prone shales, the transport of this gas may be additionally hindered due to the lack of a recognizable network of porous, solid bitumen.

Both pore throat apertures and the percentage of open porosity are recognized as primary factors controlling the permeability of shales (Clarkson *et al.*, 2012). In the Wealden, at least half of the pore space is associated with inorganic pores, with a considerable fraction water-bearing due to the high content of microporous clays. These inorganic pores are the dominant pore system in organic-lean beds (Figure 4.20) and, coupled to their narrow pore throat apertures, may not be part of the effective porosity, posing barriers for the flow of gas (Passey *et al.*, 2010). If so, generated gas would preferentially accumulate in microreservoirs of porous fossilifeous mudstones that experienced limited cementation as well as in the organic-rich layers with abundant intraorganic porosity and macropores located in compaction shadows. Analogous microreservoirs were found in the calcareous Posidonia Shale rich in recrystallized faecal pellets (Chapter 3), and are a substantial part of the gas-producible porosity encountered in interlayered faecal pellet and silt-rich laminae of the Eagle Ford Shale (Schieber *et al.*, 2012).

Apart from the lake plain deposits, we did not find evidence of a substantially different distribution of mercury pore sizes in gas mature, fossil-bearing shales in comparison to their clay-rich equivalents. Likewise, we did not find differences in porosities other than resulting from the varied organic content between organic-lean siliciclastic shales with distinct

physical and biogenic sedimentary structures and often laminated, organic-rich mudstones. Therefore, unlike in the immature Wealden, we recognize that the impact of the original shale texture on the total porosity and mercury pore apertures at high maturities is obliterated by diagenesis and hydrocarbon generation. Even with similar mercury pore size distributions, shale fabric continues to keep a strong hold on the alignment of pores. In this study, higher aspect ratio pores were found in the aligned, clay-rich, organic-rich mudstone as compared to a mudstone with more randomly-oriented clay platelets (Figure 4.24). The origin of the less oriented shale with more chaotic orientation of the clay sheets could not be determined from the thin section, but such a clay arrangement is often found in rapidly resedimentated muds. The significance of the clay orientation was demonstrated by Lash and Engelder (2005) who showed that shales with planar arrangements of clay grains are more prone to developing horizontal fractures related to stresses active during kerogen-to-bitumen conversion. In this study, this mechanism could have contributed to the formation of the microscopically distinguishable horizontal, bitumen-filled microcracks in the B10458 shale (Figure 4.10) and thus explain the horizontal arrangement of many organic pores found therein (Figure 4.24c, d). Another implication of a pore system composed of the preferably aligned pores is a potentially less tortuous path for the hydrocarbon flow within an unfractured reservoir (Chalmers *et al.*, 2008; Soedrer, 1988; Thomas and Clouse, 1990). As the alignment of clays in poorly aligned shales controls the distribution and alignment of the dispersed bitumen (Figure 4.24e, f), such an arrangement is likely to slow the gas diffusion rate to a fracture and a wellbore and thus limit its final production.

Summary and Conclusions

In this study, an attempt was undertaken to classify shales based on selected petrophysical and geochemical attributes and provide a practical meaning to the lithological variability as observed in core and thin sections. The shale samples were initially characterized in terms of the mineralogical composition, texture, presence of sedimentary structures, organic content, kerogen type and maturity. The subsequent experimental setup involved the determination of a range of porosities using different techniques, each probing pores of different sizes and selectively differentiating between the size of pore throats and bodies. The visual heterogeneity of the German Wealden was captured at the thin section scale, and led to the differentiation of microlithofacies within the sequence of

stratigraphically linked deposits (Bohacs, 1998). Image analysis of thin sections revealed that even such sharply defined intervals are highly heterogeneous on a submillimetre and micrometre scale and thus their experimentally defined bulk properties represent average values. All measurements were conducted at two levels of thermal maturation, corresponding to early oil window and gas window, and when coupled with petrographic evidence, allowed a direct comparison of shales differentiated by the level of thermal maturity. This approach provided promising results in terms of screening for the abundance of organic and inorganic pores and pointing out locations of potential microreservoirs of gas. As changes in observed shale properties parallel changes in their lithological characteristics, we believe that our results can be easily validated or at least compared to additional studies of shales with similar, or conversely, distinct lithologies.

This study showed that lithological variability, and most notably clay and carbonate abundance, are primary factors in defining principal rock characteristics, such as porosity and organic carbon content, with a partial overlap of values between rocks of differing lithology (Figure 4.20). In the low maturity calcareous mudstones and limestones, a positive relation between total porosity and TOC exists, despite the variable nature of the carbonate component (carbonate concretion, shell debris, pelagic carbonates). Hence, we presume that different environmental conditions associated with the episodic precipitation of cements, deposition of the shell debris and the supply of pelagic carbonates are directly reflected in a variable but mutually linked preservation of both organic and inorganic pores. In siliciclastic mudstones devoid of carbonate, shale porosities are again dependent on the general texture, and are enhanced by the greater abundance of the silt fraction associated with sediment reworking, and possibly more oxygenated bottom waters (Figure 4.3i). In the most organic-rich, often laminated, siliciclastic sediments (>5 wt.% TOC) with well-preserved type I kerogen, total porosities reach a minimum, possibly controlled by the ratio of the porosity held by kerogen as compared to the bulk inorganic matrix.

At gas window maturities, the variation in total porosities within clay and carbonate enriched rocks is still notable, despite a diagenetic overprint within the carbonate and quartz phases. There is a strong, positive correlation between organic carbon content and total porosity within siliciclastic and fossiliferous mudstones and limestones, with two distinct slopes of the porosity-TOC relation in rocks of differing lithology. Different slopes between the two parameters in fossil-poor and fossil-enriched rocks indicate the important role of the inorganic framework in the preservation of inorganic pores and the trapping of generated hydrocarbons at oil window maturities (see Chapter 2). High porosities of the fossil-bearing

shales with TOC < 2 wt.% point to either dissolution of the shale framework or enhanced preservation of inter- and intrafossil porosity in mature rocks that underwent oil generation and/or migration. In contrast to the low maturity shale, siliciclastic mudstones do not show elevated porosities at low organic concentrations, suggesting framework compaction accompanying hydrocarbon generation.

The most notable result for the suite of the gas window shales analyzed in this study is a lack of influence of the level of maturity attained on the values of total porosity. We presume that this reflects the maturity range over which organic porosity is generated, constrained by the physiochemical properties of the organic phase, and mimicking similar observations in cokes (Loison, 1989). The specific timing of porosity evolution explains the location of the large, complex organic pores in the oil-saturated bitumen (see Chapter 3), preferentially trapped in the vicinity of mineral grains and crystals (Figure 4.24e), and co-existing with the bubble-like-shape intraorganic pores, the growth of which is inhibited by the solidification of the host organic polymer (Tiem *et al.*, 2008). If the varied pore morphologies reflect the diminishing potential for evolution of pores within the organic phase, any loss of hydrogen and exsolution of gas beyond the threshold maturity level continued only within the previously formed porous network and hence did not further affect the measurable porosity of the shale. The exact timing of organic porosity development could not be constrained due to a lack of samples with < Ro 1.5%, but it most likely corresponds to wet gas window maturities.

After examination of gas window maturity siliciclastic shales with high resolution SEM microscopy, we note that the best potential microreservoirs of gas are associated with compaction shadows of carbonate grains and crystals. This specific location of macropores is interpreted as a dual effect of carbonate dissolution in the volumes of active generation of hydrocarbons, as well as the subsequent decomposition of bitumen trapped in the vicinities of such grains. In contrast, no enhanced porosities and therefore no visible microreservoirs were encountered in kerogen type III/IV dominated shales. For these, different mechanisms and/or timing of gas exsolution are implied. We also showed that the shale composition and fabric has an impact on the arrangement of pores and pore body sizes, potentially varying at similar levels of organic carbon concentration. For instance, the presence of oriented clay flakes is reflected in pore size and orientation, with potential consequences for connectivity. Constraining this heterogeneity, potentially linked back to depositional mechanisms and environments, will have a direct impact on estimations of the efficiency of delivery of produced hydrocabons to the wellbore. Interestingly, despite the varied distribution of observed macropores in different shales, the total amount of porosity measured in high

maturity shales was found to be independent of the sizes of the pore apertures and thus may affect estimations of permeabilities when only pore size distribution is taken into account.

References

ALEXANDER, T. 2011. Shale gas revolution. *Oilfield review*, **23**, 40-55.

ABRAMOFF, M., MAGALHAES, P., RAM, S. 2004. Image processing with ImageJ. *Biophotonics International*, **11**, 36–42.

AMBROSE, R.J., HARTMAN, R.C., DIAZ-CAMPOS, M., AKKUTLU, I.Y., SONDERGELD, C.H. 2010. New pore-scale considerations for shale gas in place calculations. In: Proceedings, SPE Unconventional Gas Conference, SPE, 23–25 February 2010, Pittsburgh, Pennsylvania, USA.

APLIN, A.C., LARTER, S.R. 2005. Fluid Flow, Pore Pressure, Wettability, and Leakage in Mudstone Cap Rocks. AAPG Special Bulletin: ***AAPG Hedberg Series***, **2**, 1-12.

APLIN, A.C., MACQUAKER. H.S. 2011. Mudstone diversity: Origin and implications for source, seal, and reservoir properties in petroleum systems. *AAPG Bulletin*, **95**, 2031–2059.

BACHMANN, G.H., VOIGT, T., BAYER, U., VON EYNATTEN, H., LEGLER, B., LITTKE, R. (2008): Depositional history and sedimentary cycles in the Central European Basin System. In: Littke,R., Bayer, U., Gajewski, D., Nelskamp, S. (Eds), Dynamics of Complex Intracontinental Basins - The Central European Basin System, Springer-Verlag, Berlin-Heidelberg, pp. 155-169.

BEHAR, F., LORANT, F., LEWAN, M. 2008a. Role of NSO compounds during primary cracking of a Type II kerogen and a Type III lignite. *Organic Geochemistry*, **39**, 1–22.

BEHAR, F., LORANT, F., MAZEAS, L. 2008b. Elaboration of a new compositional kinetic schema for oil cracking. *Organic Geochemistry*, **39**, 764–782.

BERGINS, C., HULSTON, J., STRAUSS, K., CHAFFEE, A.L. 2007. Mechanical/thermal dewatering of lignite. Part 3: Physical properties and pore structure of MTE product coals. *Fuel*, **86**, 3–16.

BERNAL, J.L.P., BELLO, M.A. 2001. Fractal geometry and mercury porosimetry. Comparison and application of proposed models on building stones. *Applied Surface Science*, **185**, 99-107.

BERNARD, S., HORSFIELD, B., SCHULTZ, H.M., SCHREIBER, A., WIRTH, R., TIEM, T.A.V., PERSSEN, F., KÖNITZER, S, VOLK, H., SHERWOOD, N., FUENTES, D. 2010. Multi-scale detection of organic and inorganic signatures provides insights into gas shale properties and evolution. *Chemie der Erde*, **70**, 119-133.

BERNARD, S., HORSFIELD, B., SCHULTZ, H.M., WIRTH, R., SCHREIBER, A., SHERWOOD, N. 2011. Geochemical evolution of organic-rich shales with increasing maturity: A STXM and TEM study of the Posidonia Shale (Lower Toarcian, northern Germany). *Marine and Petroleum Geology*, **31**, 70-89.

BERNARD, S., WIRTH, R., SCHREIBER, A., SCHULZ, H.-M., HORSFIELD, B. 2012. Formation of nanoporous pyrobitumen residues during maturation of the Barnett Shale (Fort Worth Basin). *International Journal of Coal Geology*, **103**, 3–11.

BERNER, U. 2011. The German Wealden, an unconventional hydrocarbon play? *Erdöl Erdgas Kohle*, **127**, 1–5.

BERNER, U., KAHL, T., SCHEEDER, G., 2010. Hydrocarbon potential of sediments of the German Wealden Basin. *Oil Gas European Magazine*, **2**, 80–84.

BJØRLYKKE, K., HØEG, K. 1997. Effects of burial diagenesis on stresses, compaction and fluid flow in sedimentary basins. *Marine and Petroleum Geology*, **14**, 267 -276.

BJØRLYKKE, K. 1999. Principal aspects of compaction and fluid flow in mudstones. *Geological Society Special Publications*, **158**, 73-78.

BOHACS, K.M. 1998. Contrasting expressions of depositional sequences in mudstones from marine to non-marine environs. In: Schieber, J., Zimmerle, W., Sethi, P., eds., Shales and Mudstones, vol. 1, Stuttgart, Schweizerbart'sche Verlagsbuchhandlung, p. 32–77.

BOHACS, K.M., GRABOWSKI, G. J., CARROLL, A. R., MANKIEWICZ, P. J., MISKELL-GERHARDT, K. J., SCHWALBACH, J. R. 2005. Production, destruction, and dilution: The many paths to source rock development. In: HARRIS, N. B., (Ed.), The deposition of organic carbon-rich sediments: Models, mechanisms, and consequences: Society for Sedimentary Geology Special Publication **82**, 61–101.

BOWKER. K.A. 2007. Barnett Shale gas production, Fort Worth Basin: Issues and discussion. *American Association of Petroleum Geologists Bulletin*, **91**, 523-533.

BRETT, C.E., ALLISON, P.A. 1998. Paleontological approaches to the environmental interpretation of mudrocks. In: Schieber, J., Zimmerle, W., Sethi, P.S., eds., Shales and Mudstones, vol. 1, Stuttgart, Schweizerbart'sche Verlagsbuchhandlung, p. 301-349.

BRUNS, B., Di PRIMIO, R., BERNER, U., LITTKE, R., 2013. Petroleum system evolution in the inverted Lower Saxony Basin, northwest Germany: A 3D basin modeling study. *Geofluids*, **13**, 246-271.

BURKART, B., GROSS, G.C., KERN, J. 1999. The role of gypsum in production of sulfate-induced deformation of lime-stabilized soils. *Environmental and Engineering Geoscience*, **5**, 173-187.

BUSTIN, R.M., CLARKSON, C.R. 1998. Geological controls on coalbed methane reservoir capacity and gas content. *International Journal of Coal Geology*, **38**, 3–26.

BUSTIN, R.M., BUSTIN, A.M.M., CIU, X., ROSS, D.J.K., MURPHY PATHI, V.S. 2008. Impact of shale properties on pore structure and storage characteristics. SPE Shale Gas Production Conference, 16-18 November 2008, Fort Worth, Texas, USA.

BUSTIN, A.M.M., BUSTIN, R.M. 2012. Importance of rock properties on the producibility of gas shales. *International Journal of Coal Geology*, **103**, 132–147.

CANFIELD. D.E., THAMDRUP, B., HANSEN, J.W. 1993. The anaerobic degradation of organic matter in Danish coastal sediments: Iron reduction, manganese reduction, and sulfate reduction. *Geochimica et Cosmochimica Acta*, **57**, 3867-3883.

CASEY, R., ALLEN, P., DÖRHÖFER, G., GRAMANN, F., HUGHES, N.F., KEMPER, E., RAWSON, P.F., SURLYK, F. 1975. Stratigraphical subdivision of the Jurassic–Cretaceous boundary beds in NW Germany. *Newsletters on Stratigraphy*, **4**, 4-5.

CHALMERS, G., BUSTIN, R.M., POWER, I. 2009. A Pore by any other name would be as small: The importance of meso-and microporosity in shale gas capacity. American Association of Petroleum Geologists Annual Convention and Exhibition, 7-10 June, Denver, Colorado.

CHALMERS, G.R.L., BUSTIN, R.M. 2012. Geological evaluation of Halfwaye-Doige-Montney hybrid gas shale-tight gas reservoir, northeastern British Columbia. *Marine and Petroleum Geology*, **38**, 53-72

CHALMERS, G.R.L., ROSS, D.J.K., BUSTIN, R.M. 2012. Geological controls on matrix permeability of Devonian Gas Shales in the Horn River and Liard basins, northeastern British Columbia, Canada. *International Journal of Coal Geology*, **103**, 120-131.

CLARKSON, C.R., BUSTIN, R.M. 1997. Variation in permeability with lithotype and maceral composition of Cretaceous coals of the Canadian Cordillera. *International Journal of Coal Geology*, **33**, 135-151.

CLARKSON, C.R., JENSEN, J.L., PEDERSEN, P.K., FREEMAN, M. 2012. Innovative methods for flow-unit and pore-structure analyses in a tight siltstone and shale gas reservoir. *American Association of Petroleum Geologists Bulletin*, **96**, 355-374.

COMISKY, J.T., SANTIAGO, M., McCOLLOM, B., BUDDHALA, A., NEWSHAM, K.E. 2011. Sample size effects on the application of mercury injection capillary pressure for determining the storage capacity of tight gas and oil shales. SPE Canadian Unconventional Resources Conference, 15–17 November 2011,Calgary, Alberta, Canada.

CONNELL-MADORE, S., KATSUBE. T.J. 2006. Pore size distribution characteristics of Beaufort-Mackenzie Basin shale samples, Northwest Territories.In: Geological Survey of Canada, Current Research (Online) 2006-B1, pp. 13.

CROSSEY, L.J. 1991. The Thermal Stability of Organic Acids in Sedimentary Basins. AAPG Annual Convention Dallas, April 7-10, 1991, Texas, USA.

CURIALE, J.A. 1986. Origin of solid bitumens, with emphasis on biological marker results. *Organic Geochemistry*, **10**, 559-580.

CURTIS, C.D. 1995. Post-depositional evolution of mudstones l: early days and parental influences. *Journal of the Geological Society*, **152**, 577-586.

CURTIS, J. 2002. Fractured shale-gas systems. *American Association of Petroleum Geologists Bulletin*, **86**, 1921–1938.

CURTIS, M.E., AMBROSE, R.J., SONDERGELD, C.H., RAI, C.S. 2010. Structural Characterization of Gas Shales on the Micro- and Nano-Scales. SPE Canadian Unconventional Resources and International Petroleum Conference, 19-21 October 2010, Calgary, Alberta, Canada.

CURTIS, M.E., SONDERGELD, C.H., AMBROSE, R.J., RAI, C.S. 2012. Microstructural investigation of gas shales in two and three dimensions using nanometer-scale resolution imaging. *American Association of Petroleum Geologists Bulletin*, **96**, 665-677.

DAHL, J, MOLDOWAN, J.M., WALLS, J., NUR, A., DE VITO, J. Creation of porosity in tight shales during organic matter maturation. AAPG Annual Convention and Exhibition, April 22-25, Long Beach, California, USA.

DAVIES, G.R. 1979. Dolomite Reservoir Rocks: Processes, Controls, Porosity Development. In: Moore, C.H. (Organizer), Geology of carbonate porosity, American Association of Petroleum Geologists Continuous Education Course Note Series, **11**, C1-C17.

DESBOIS, G., URAI, J.L., KUKLA, P.A. 2009. Morphology of the pore space in claystones – evidence from BIB/FIB ion beam sectioning and cryo-SEM observations. *eEarth*, **4**, 15–22.

ELSTNER, F., MUTTERLOSE, J. 1996. The lower Cretaceous (Berriasian and Valanginian) in NW Germany. *Cretaceous Research*, **17**, 119–133.

ERDMANN, M., HORSFIELD, B. 2006. Enhanced late gas generation potential of petroleum source rocks via recombination reactions: Evidence from the Norwegian North Sea. *Geochimica et Cosmochimica Acta*, **70**, 3943–3956.

ESPITALIE, J., LAPORTE, J.L., MADEC, M., MARQUIS, F., LEPLAT, P., PAULET J., BOUTEFEU, A. 1977. Methode rapide de characterisation des roches meres, de leur potential petrolier et de leur degree d'evolution, *Rev. Inst. Franc. Pétrole.*, **32**, 23-42.

FRIESEN, W.I., MIKULA. R.J. 1988. Mercury porosimetry of coals: Pore volume distribution and compressibility. *Fuel*, **67**, 1516-1520.

GREEN, U., AIZENSTAT, Z., GIELDMEISTER, F., COHEN, H. CO_2 adsorption inside the pore structure of different rank coals during low temperature oxidation of open air coal stockpiles, *Energy Fuels*, **25**, 4211-4215.

GRIFFIN, S., LITKE, R., KLAVER, J., URAI, J.L. 2013. Application of BIB–SEM technology to characterize macropore morphology in coal. *International Journal of Coal Geology* (Online).

HEASLEY, E.C., WORDEN, R.H., HENDRY, J.P. 2000. Cement distribution in a carbonate reservoir: Recognition of a paleo-oil–water contact and its relationship to reservoir quality in the Humbly Grove field, onshore, United Kingdom. *Marine and Petroleum Geology*, **17**, 639–654.

HILDENBRAND, A., URAI, J.L. 2003. Investigation of the morphology of pore space in mudstones—first results. *Marine and Petroleum Geology*, **20**, 1185–1200.

HOUBEN, M.E., DESBOIS, G., URAI, J.L. 2013. Pore morphology and distribution in the Shaly facies of Opalinus Clay (Mont Terri, Switzerland): Insights from representative 2D BIB-SEM investigations on mm to nm scale. *Applied Clay Science*, **71**, 82-97.

IRWIN, H., CURTIS, C. 1977. Isotopic evidence for source of diagenetic carbonates formed during burial of organic-rich sediments. *Nature*, **269**, 209-213.

JARVIE, D.M., HILL, R.J., RUBLE, T.E., POLLASTRO, R.M., 2007. Unconventional shale-gas systems: the Mississippian Barnett Shale of north-central Texas as one model for thermogenic shale gas assessment. *American Association of Petroleum Geologists Bulletin*, **91**, 475–499.

KLAVER, J., DESBOIS, G., URAI, J.L., LITTKE, R. 2012. BIB-SEM study of the pore space morphology in early mature Posidonia Shale from the Hils area, Germany. *International Journal of Coal Geology*, **103**, 12-25.

KIDWELL, S.M. 1989. Stratigraphic condensation of marine transgressive records: origin of major shell deposits in the Miocene of Maryland. *Journal of Geology*, **97**, 1-24.

KUILA, U., PRASAD, M. 2013. Specific surface area and pore-size distribution in clays and shales, *Geophysical Prospecting*, **61**, 341–362.

LASH, G.G., ENGELDER, T. 2011. Thickness trends and sequence stratigraphy of the Middle Devonian Marcellus Formation, Appalachian Basin: Implications for Acadia. *American Association of Petroleum Geologists Bulletin*, **95**, 61–103.

LAUGHREY, C.D., RUBLE, T.E., LEMMENS, H., KOSTELNIK, J., BUTCHER, A.R., WALKER, G., KNOWLES, W. 2011. Black Shale Diagenesis: Insights from Integrated High-Definition Analyses of Post-Mature Marcellus Formation Rocks, Northeastern Pennsylvania. AAPG Annual Convention and Exhibition, April 10-13, 2011, .Houston, Texas, USA.

LOISON R., FOCH P., BOYER A., 1989. Coke: Quality and Production, Butterworths, London, pp. 353.

LOUCKS, R.G., REED, R.M., RUPPEL, S.C., JARVIE, D.M. 2009. Morphology, genesis and distribution of nanometer-scale pores in siliceous mudstones of the Mississippian Barnett Shale. *Journal of Sedimentary Research*, **79**, 848–861.

LOUCKS, R.G., REED, R.M., RUPPEL,S.C., HAMMES, U. 2012. Spectrum of pore types and networks in mudrocks and a descriptive classification for matrix-related mudrock pores. *American Association of Petroleum Geologists Bulletin*, **96**, 1071-1098.

LU, J., MILLIKEN, K., REED, R.M. 2011. Diagenesis and sealing capacity of the middle Tuscaloosa mudstone at the Cranfield carbon dioxide injection site, Mississippi, U.S.A. *Environmental Geosciences*, **18**, 35–53.

MACGOWAN, D.B., SURDAM, R.C. 1990. Carboxylic acid anions in formation waters, San Joaquin Basin and Louisiana Gulf Coast, U.S.A. - Implications for clastic diagenesis. *Applied Geochemistry*, **5**, 687-701.

MACQUAKER, J.H.S., GAWTHORPE, R.L. 1993. Mudstone lithofacies in the Kimmeridge Clay Formation, Wessex Basin, Southern England: Implications for the origin and controls of the distribution of mudstones. *Journal of Sedimentary Petrology*, **63**, 1129-1143.

MACQUAKER, J.H.S., TAYLOR, K.G., KELLER, M., POLYA, D. 2014. Compositional controls on early diagenetic pathways in fine-grained sedimentary rocks: Implications for predicting unconventional reservoir attributes of mudstones. *American Association of Petroleum Geologists Bulletin*, **98**, 587–603.

MASTALERZ, M., DROBNIAK, A., STRAPOC, D., ACOSTA, W.S., RUPP, J. 2008. Variations in pore characteristics in high volatile bituminous coals: Implications for coal bed gas content. *International Journal of Coal Geology*, **76**, 205–216.

MILLIKEN, K.L., RUDNICKI, M., AWWILER, D.N., ZHANG, T. 2013. Organic matter–hosted pore system, Marcellus Formation (Devonian), Pennsylvania. *American Association of Petroleum Geologists Bulletin*, **97**, 177-200.

MILNER, M., MCLIN, R., PETRIELLO, J., TEK, T. 2010. SPE Canadian Unconventional Resources and International Petroleum Conference, 19-21 October 2010, Calgary, Alberta, Canada.

MODICA, C.J., LAPIERRE, S.G. 2012. Estimation of kerogen porosity in source rocks as a function of thermal transformation: Example from the Mowry Shale in the Powder River Basin of Wyoming. *Association of Petroleum Geologists Bulletin*, **96**, 87-108.

MUTTERLOSE, J., BORNEMANN, A. 2000. Distribution and facies patterns of Lower Cretaceous sediments in northern Germany: a review. *Cretaceous Research*, **21**,733–759.

OKIONGBO, K.S., APLIN, A.C., LARTER, S.R. 2005. Changes in Type II Kerogen Density as a Function of Maturity: Evidence from the Kimmeridge Clay Formation. *Energy & Fuels*, **19**, 2495-2499.

PADHY, G.S., LEMAIRE, C., AMIRHARAJ, E.S., IOANNIDIS, M.A. 2007. Pore size distribution in multiscale porous media as revealed by DDIF–NMR, mercury porosimetry and statistical image analysis. *Colloids and Surfaces A: Physicochemical Engineering Aspects*, **300**, 222–234.

PASSEY, Q. R., BOHACS, K. M., ESCH, W. L., KLIMENTIDISS, R., SINHA, S. 2010. From Oil-Prone Source Rock to Gas-Producing Shale Reservoir – Geologic and petrophysical characterization of unconventional shale-gas reservoirs. *Proceedings of the North American Unconventional Gas Conference and Exhibition. Society of Petroleum Engineers*, Paper 131350, 29p.

PELTONEN, C., MARCUSSEN, Ø., BJØRLYKKE, K., JAHREN, J. 2009. Clay mineral diagenesis and quartz cementation in mudstones: The effects of smectite to illite reaction on rock properties. *Marine and Petroleum Geology*, **26**, 887–898.

PELZER, G., RIEGEL, W., and WILDE, V. 1992. Depositional controls on the Lower Cretaceous Wealden coals of northwest Germany. In Controls on the Distribution and Quality of Cretaceous Coals, eds. P.J. McCabe, and J.T. Parrish. *Geological Society of America, Special Paper*, **267**, 227–244.

PUDLO, D., REITENBACH, V., ALBRECHT, D., GANZER, L., GERNERT, U., WIENAND, J., KOHLHEPP, R., GAUPP, R. 2012. The impact of diagenetic fluid–rock reactions on Rotliegend sandstone composition and petrophysical properties (Altmark area, central Germany). *Environ mental Earth Science*, **67**, 369–384.

RAISWELL, R., FISHER, Q.J. 2000. Mudrock-hosted carbonate concretions: a review of growth mechanisms and their influence on chemical and isotopic composition. *Journal of Geological Society*, **157**, 239-251.

REXER, T.F., MATHIA, E.J., APLIN, A.C., THOMAS, K.M. 2014. High-Pressure Methane Adsorption and Characterization of Pores in Posidonia Shales and Isolated Kerogens. *Energy & Fuels*, **28**, 2886-2901.

RIPPEN, D., LITTKE, R., BRUNS, B., MAHLSTEDT, N. 2013. Organic geochemistry and petrography of Lower Cretaceous Wealden black shales of the Lower Saxony Basin: The transition from lacustrine oil shales to gas shales. *Organic Geochemistry*, **63**, 18-36.

RODUIT. 2008. JMicroVision: Image analysis toolbox for measuring and quantifying components of high-definition images. Version 1.2.7. Software available for free download at http://www.jmicrovision.com/ accessed August, 2011.

ROMERO-SARMIENTO, M.-F., DUCROS, M., CARPENTIER, B., LORANT, F., CACAS, M.-C., PEGAZ-FIORENT, S., WOLF, S., ROHAIS, S., MORETTI, I. 2013. Quantitative evaluation of TOC, organic porosity and gas retention distribution in a gas shale play using petroleum system modeling: Application to the Mississippian Barnett Shale. *Marine and Petroleum Geology*, **45**, 315-330.

SAGEMAN, B.B., MURPHY, A.E., WERNE, J.P., VER STRAETEN, C.A., HOLLANDER, D.J., LYONS, T.W. 2003. A tale of shales: the relative roles of production, decomposition, and dilution in the accumulation of organic-rich strata, Middle–Upper Devonian, Appalachian basin. *Chemical Geology*, **195**, 229-273.

SCHIEBER, J. 2010. Common Themes in the Formation and Preservation of Intrinsic Porosity in Shales and Mudstones - Illustrated with Examples Across the Phanerozoic. SPE Unconventional Gas Conference, 23-25 February 2010, Pittsburgh, Pennsylvania, USA.

SCHIEBER, J., REMUS, L., BOHACS, K., KLIMENTIDIS, R.E., OTMANN, J., DUMITRESCU, M. 2012. A Scanning Electron Microscope Study of Porosity in the Eagle Ford Shale of Texas. AAPG Annual Convention and Exhibition, April 22-25, 2012, Long Beach, California, USA.

SCHOLLE, P. A. 1977. Chalk diagenesis and its relation to petroleum exploration: oil from chalks, a modern miracle? *American Association of Petroleum Geologists Bulletin*, **61**, 982-1009.

SCHUTTER, S.R. 1998. Characteristics of shale deposition in relation to stratigraphic sequence system tracts. In: Schieber, J., Zimmerle, W., Sethi, P., eds., Shales and Mudstones, vol. 1, Stuttgart, Schweizerbart'sche Verlagsbuchhandlung, p. 79-108.

SHAFER, J., NEASHAM, J. 2000. Mercury porosimetry protocol for rapid determination of petrophysical and reservoir quality properties. International Symposium of the Society of Core Analysts, (2000) SCA 2021.

SIGAL, R.F. 2009. A methodology for blank and conformance corrections for high pressure mercury porosimetry. *Measurement Science and Technology*, **20**, 045108, 11pp.

SING, K.S.W., EVERETT, D.H., HAUL, R.A.W., MOSCOU, L., PIEROTTI, R.A., ROUQUEROL, J. 1985. Reporting physisorption data for gas/solid systems. Spetial reference to the determination of surface area and porosity. *Pure and Applied Chemistry*, **57**, 603-619.

SISK, C., DIAZ, E., WALLS, J., GRADER, A., SUHRER, M. 2010. SPE Annual Technical Conference and Exhibition held in Florence, Italy, 19–22 September 2010.

SLATT, R.M., O'BRIEN, N.R. 2011. Pore types in the Barnett and Woodford gas shales: Contribution to understanding gas storage and migration pathways in fine-grained rocks. *AAPG Bulletin*, **95**, 2017–2030.

SOEDER, D.J. 1988. Porosity and permeability of eastern Devonian gas shale. *Society of Petroleum Engineers Formation Evaluation*, **3**, 116-124.

SONDERGELD, C.H., AMBROSE, R.J., RAI, C.S., MONCRIEFF, J. 2010. Micro-Structural Studies of Gas Shales. Society of Petroleum Engineers Unconventional Gas Conference, 23-25 February 2010, Pittsburgh, Pennsylvania, USA.

STOLLHOFEN, H., BACHMANN, G.H., BARNASCH, J., BAYER, U., BEUTLER, G., FRANZ, M., KÄSTNER, M., LEGLER, B., MUTTERLOSE, J., RADIES, D. 2008. Upper Rotliegend to Early Cretaceous basin development. In: Littke, R, Bayer, U, Gajewski, D & Nelskamp, S, eds. Dynamics of Complex Intracontinental Basins - The Central European Basin System. Berlin Heidelberg: Springer; 2008. p. 181-221.

TAO, S., WANG, Y., TANG, D., WU, D., XU, H., HE, W. 2012. Organic petrology of Fukang Permian Lucaogou Formation oil shales at the northern foot of Bogda Mountain, Junggar Basin, China. *International Journal of Coal Geology*, **99**, 27–34.

THOMAS, M.M., CLOUSE, J.A. 1990. Primary migration by diffusion through kerogen: II. Hydrocarbon diffusivities in kerogen. *Geochimica et Cosmochimica Acta*, **54**, 2781-2792.

THOMAS, M.M., CLOUSE, J.A., LONGO, J.M. 1993. Adsorption of organic-compounds on carbonate minerals. 3. Influence on dissolution rates. *Chemical Geology*, **109**, 227–237.

TIEM, V.T., HORSFIELD, B., SYKES, R. 2008. Influence of in-situ bitumen on the generation of gas and oil in New Zealand coals. *Organic Geochemistry*, **39**, 1606–1619.

TODA, Y., TOYODA, S. 1972. Application of mercury porosimetry to coal. *Fuel*, **51**, 199-201.

VAN De KAMP. P.C. 2008. Smecite-illite-muscovite transformations, quartz dissolution, and silica release in shales. *Clays and Clay Minerals*, **56**, 66-81.

VANDENBYGAART, A.J., PROTZ, R. 1999. The representative elementary area REA in studies of quantitative soil micromorphology. *Geoderma*, **89**, 333–346.

VAN DUIN, A.C.T., LARTER, S.R. 2001. A computational chemical study of penetration and displacement of water films near mineral surfaces, Geochemical Transacions 6.

WASHBURN, E.W. 1921.The Dynamics of Capillary Flow, *Phys. Rev*., **17**, 273 – 283.

WEBB, P.A. 2001. An introduction to the physical characterization of materials by mercury intrusion porosimetry with emphasis on reduction and presentation of experimental data. Micromeritics Instrument Corp., Norcross, Georgia, pp. 23.

WERNE, J.P., SAGEMAN, B.B., LYONS, T.W., HOLLANDER, D.J. 2002. An integrated assessment of a "type euxinic" deposit: evidence for multiple controls on black shale deposition in the middle Devonian Oatka Creek Formation. *American Journal of Science*, **302**, 110-143.

WOLBURG, J. 1949. Ergebnisse der Biostratigraphie nach Ostracoden im Nordwestdeutschen Wealden - Erdöl und Tektonik, Sammelband vom Amt für Bodenforschung, p. 349-360, Hannover-Celle.

WORDEN, R.H., OXTOBY, N.H., SMALLEY, P.C. 1998. Can oil emplacement prevent quartz cementation in sandstones? *Petroleum Geoscience*, **4**, 129–137.

Chapter 5: Summary and conclusions

Key results

Determination of sample porosity and its pore size distribution in the shale successions is a first step towards understanding of the variability of physical properties on larger scales. However, due to a fine-grained nature of mudstones, the pure estimation of their porosities is not as straightforward and the results may differ depending on the technique used, the experimental conditions and the sample size. Our results showed that due to a small size of pores, often exceeding the resolution of the technique deployed, porosities of shales are not suitable for the analysis with traditional methods alone, such as mercury porosimetry. On the other hand, more sophisticated gas sorption techniques, despite being efficient in quantification of porosity held by the finest pores, do not measure macropores, or even larger mesopores. In this study, the size of pores encountered in the investigated shale samples spanned from > 6 nm to ~5 µm. Such broad pore size distribution is a diagnostic feature of shales and is the primary reason for the unsuitability of any single technique to yield descriptive statistical information about the full spectrum of pores. The limitations of each of the measuring techniques used should be thus bore in mind while interpreting and comparing porosities between different samples. To overcome those limitations, a multi-technique approach is preferably used. As shown in this study, the combination of the mercury and gas sorption methods was critical to show the connectivity of the shale pore system in samples of maturities ca. 0.5-1.9% Ro. As the injection of mercury under high pressures may introduce an effect comparable to a deformation of the shale framework and/or its organic component, the exact agreement between the two porosity values and the total porosity of the shale varies, and is likely controlled by the content of the organic matter. This control is expressed a strong dependence of the mercury retraction on the content of the organic carbon. One of the techniques often deployed to avoid the uncertainties related to the sample compression, and on the other hand, those related to always limited accuracy of models converting sorption or mercury pore volume to a specific diameter value, is a high resolution microscopy. In this study, the microscopic pore visualization and the image analysis have proved to be a useful complementary technique with a huge potential to quantify macroporosity that could not be directly quantified neither by the mercury porosimetry nor the sorption techniques. The main advantage of the image pore visualization was a direct grouping of pores into pore bodies and

pore throats with an accuracy not attained by the mercury porosimetry alone. Moreover, the image technique, especially when coupled with the low resolution petrographic analysis, was capable to provide a valid geological background and mineralogical context for the porosities measured experimentally. Still, during our analysis, we found that the experimental feasibility may pose constraints on the interpretation of the image analysis results, as the higher sample representativeness is often a compromise for the lower image resolution. The last may thus pose a problem in very heterogeneous shales with a strong variability on the > cm scale.

In this study, we analysed a centimetre-and micrometer scale mudstone samples that are small enough to avoid many issues of the larger scale mudstone heterogeneity and thus can be directly used to interpret the influence of diagenesis and organic matter maturation on the measured physical rock properties. The Posidonia case study showed that although the maturity of the organic matter is an important factor in interpreting the change in porosities in relatively homogeneous calcareous mudstone successions, the influence of the mechanical compaction and the high-temperature carbonate diagenesis should not be neglected. We demonstrated that the theoretical porosity gain due to the expulsion of hydrocarbons in the oil window is effectively counteracted by the shale framework collapse and occlusion of pores by the generated organic phase. Despite blocking pores, the retention of the petroleum phase generated in situ or migrated from adjacent beds has also a positive effect, as it arrests calcite cementation and therefore prevents further porosity loss. The net effect of the increasing thermal maturity on porosity is stepwise, and the initial loss of porosity and the decline in the size of the accessible pore apertures is arrested, and even reversed in the gas window. The porosity balance approach showed that this late porosity gain is primarily accounted for by the evolution of the secondary organic pores, interpreted as the result of cracking of the residual solid bitumen and oil retained in shale. By studying a large set of shale samples containing Type I (Wealden) and II kerogen (Posidonia) we showed that the organic porosity evolution is constraint to the early (wet) gas window conditions, at which point the compositional differences between different aquatic kerogens (marine vs lacustrine) are not significant. The specific but prolonged timing for pores evolution is most plausibly controlled by the physiochemical properties of the organic phase and its progressive conversion into light hydrocarbons and pyrobitumen. Such interpretation offers a plausible explanation for the heterogeneity of pore morphologies encountered in the studied shales, could account for the presence of large irregular pores developed in the oil-saturated bitumen trapped in the stress-protected vicinities of mineral grains and can explain the size distribution of the bubble-like-shape intraorganic pores.

The full realization of the porosity change within the heterogeneous shale successions cannot be achieved without constraining the lithological and mineralogical framework of the inorganic matrix. In this study the analysis of the heterogeneous succession of the German Wealden shale shed light onto the levels of such porosity variation between and within groups of the shale samples statistically differentiated with selected petrophysical and geochemical characteristics. We demonstrated that the clay-rich mudstones can be differentiated from the carbonate bearing-mudstones by a different covariation with the embedded organic matter at both low (early oil window) and high (gas window) levels of maturity. Within the two lithological groups, the variation of porosity is similarly strong and follows the change in the rock texture and composition. Our most significant observation showed that within the gas window maturity shale the total porosity-TOC covariation is positive for both clay-rich and calcareous lithologies. Moreover, while comparing the Wealden and Posidonia shale, the nanofossil-bearing calcareous shale bore more resemblance to the carbonate-poor siliciclastic shale than to the macroshell carbonate-bearing beds. In combination, these two observations stress not only the significance of the organic porosity in the gas mature shales but also a different supportive role in its evolution of the embedded carbonate phases.

The significance of the low scale heterogeneity as revealed within the analyzed shale sequences has major implications from the practical point of the shale gas exploration. This study unequivocally showed that the location of the potential microreservoirs of free gas is linked to the compaction shadows of the mineral grains, nannofossil aggregates, or even diagenetic dolomite grains. Although the shale pores are typically connected through pore throats < 20-40 nm, the alternation of the clay and organic rich layers with the macroporous and rigid laminae, such as those packed with faecal pellet aggregates, may be favourable from the production standpoint. As the clay-rich lithologies and the organic phase remain mostly meso- and microporous, those would offer more potential for the storage of the sorbed gas.

Future work

The successful study of the controls on porosity of mudstones depends on the proper design of the initial sampling strategies for the future geochemical, petrophysical and microscopic work. The consistent selection of samples is crucial for simplification of the shale work flow and reducing the number of variables between subsequent experimental set-ups. In other words, this must involve comparison of shale lithologies bearing similar maturities and kerogen types, or alternatively, those that vary in terms of the level of the thermal maturation but show no significant lithological variation.

In the light of this work, and to better understand the timing of the organic porosity generation, the future work should direct its focus onto the shale-rich lithologies representing the late oil window - wet gas window maturities. Such recommendation stems from the visual observations of pores and the experimentally measured porosity values in the type I and II shale investigated in this study. The significance of the organic porosity timing from the reservoir standpoint entails different exploration and production strategies.

In order to better place investigated mudstone samples in a broader stratigraphic framework, we see necessity in constraining its heterogeneity by higher resolution chemostratigraphic methods. The elemental data can be acquired using inductively coupled plasma spectrometry optical emission spectrometry (ICP OES) and inductively coupled plasma spectrometry mass spectrometry (ICP MS), following a Li-metaborate fusion preparation. The knowledge about the elemental distribution will enable to track lateral and vertical changes in physical properties of shales, determine the environmental conditions of its deposition with redox, and productivity proxies, and thus extend the interpretation of the porosity parameters into broader conext. Finally, we see opportunity in combination of the high resolution porosity and geochemical data in modelling the distribution of highly productive shales and the organic deposition.

Chapter 6: Appendices

Appendix A

Table A 1. *TOC and Rock-Eval data for the Wealden shale, samples taken every 1 m, wells A (0.5-0.7% Ro), B (1.6-2.4% Ro) and C (1.5-1.9% Ro).*

Sample	Depth (m)	TOC (%)	S1 (mgHC/g)	S2 (mgHC/g)	S3 (mgHC/g)	HI (mgHC/gTOC)	OI (mgHC/gTOC)	Tmax (°C)
G010269	831.5	0.50	0.01	0.44	0.19	89.0	38.0	424
G010270	832.1	0.46	0.02	0.41	3.30	90.0	724.0	430
G010271	832.3	0.46	0.02	0.38	1.06	82.0	229.0	424
G010272	833.3	1.72	0.06	3.64	1.06	212.0	62.0	428
G010273	834.7	1.10	0.04	1.85	0.91	168.0	83.0	430
G010274	835.1	1.38	0.05	2.67	0.63	193.0	46.0	427
G010275	836.0	1.82	0.06	5.15	1.12	283.0	62.0	427
G010276	836.6	4.27	0.21	23.21	1.45	544.0	34.0	429
G010277	837.4	7.25	0.20	53.68	0.95	740.0	13.0	439
G010278	838.1	0.52	0.03	0.63	2.75	121.0	529.0	437
G010279	838.7	0.69	0.03	0.75	0.28	108.0	40.0	430
G010280	839.2	1.27	0.04	2.27	1.52	179.0	120.0	432
G010281	840.8	8.99	0.30	64.74	0.64	720.0	7.0	443
G010282	842.9	5.83	0.24	40.53	0.64	695.0	11.0	438
G010283	847.3	9.15	0.55	58.27	2.76	637.0	30.0	429
G010284	847.8	0.93	0.04	0.91	0.49	98.0	53.0	426
G010285	848.9	2.19	0.10	7.70	1.43	352.0	65.0	436
G010286	849.3	7.77	0.23	51.00	0.73	656.0	9.0	440
G010287	850.2	4.33	0.19	13.60	1.56	314.0	36.0	424
G010288	850.4	2.19	0.08	3.99	1.03	182.0	47.0	425
G010289	909.5	5.96	0.62	41.96	1.73	704.0	29.0	437
G010290	910.2	10.00	1.01	82.15	2.17	822.0	22.0	444
G010291	911.1	3.73	0.89	28.61	1.03	767.0	28.0	441
G010292	911.7	4.46	0.81	27.02	1.64	606.0	37.0	438
G010293	912.5	4.52	0.78	34.73	1.66	768.0	37.0	441
G010294	913.5	6.20	1.19	51.99	1.50	839.0	24.0	441
G010295	913.9	5.27	1.23	44.81	1.01	850.0	19.0	443
G010296	914.5	2.76	1.11	17.20	1.39	623.0	50.0	435
G010297	915.9	1.98	0.31	12.43	1.46	628.0	74.0	438
G010298	916.5	3.80	0.33	28.98	1.34	763.0	35.0	440
G010299	917.0	3.79	3.53	30.33	0.89	800.0	23.0	438
G010300	918.0	7.29	1.01	53.44	2.79	733.0	38.0	432
G010301	918.9	2.03	0.10	11.14	1.33	549.0	66.0	440
G010302	919.3	4.68	0.43	27.89	1.79	596.0	38.0	433
G010303	920.4	1.54	0.14	6.74	1.69	438.0	110.0	438
G010304	923.5	5.81	0.28	48.34	1.18	832.0	20.0	442
G010305	923.7	11.80	0.93	91.48	1.47	775.0	12.0	446
G010306	925.9	2.61	0.27	13.24	2.06	507.0	79.0	430
G010307	926.4	1.00	0.08	2.71	2.27	271.0	227.0	433
G010308	927.3	0.96	0.06	2.43	2.32	252.0	241.0	433
G010309	928.3	0.67	0.04	1.29	1.95	193.0	292.0	438
G010310	966.4	0.93	0.04	3.68	2.35	394.0	252.0	444
G010311	967.3	2.46	0.11	15.61	1.02	635.0	41.0	439
G010312	967.8	1.64	0.24	10.13	0.79	618.0	48.0	434
G010313	968.8	5.28	0.39	43.21	1.38	818.0	26.0	443
G010314	969.8	3.76	0.49	18.46	0.68	491.0	18.0	436
G010315	970.3	1.62	3.02	12.70	0.61	784.0	38.0	435
G010316	972.6	13.50	1.17	102.90	1.68	762.0	12.0	449
G010317	972.8	9.28	1.22	67.73	1.50	730.0	16.0	437
G010318	974.4	1.37	1.77	8.43	1.10	615.0	80.0	435
G010319	974.6	8.07	1.10	57.82	1.44	716.0	18.0	440
G010320	992.3	11.40	1.07	86.84	0.52	762.0	5.0	448
G010321	994.1	5.02	0.44	43.46	0.71	866.0	14.0	446
G010322	994.9	4.45	0.33	29.79	0.78	669.0	18.0	437
G010323	996.4	2.96	0.18	18.58	0.90	628.0	30.0	436
G010324	997.3	3.56	0.26	20.15	1.16	566.0	33.0	433
G010325	997.8	1.79	0.12	9.36	1.25	523.0	70.0	437
G010326	1029.2	4.14	0.48	26.74	1.41	646.0	34.0	429

G010327	1029.7	1.59	0.06	8.09	1.22	509.0	77.0	444
G010329	1031.0	10.20	0.56	77.87	0.93	763.0	9.0	448
G010330	1031.7	0.50	0.03	1.74	0.82	347.0	163.0	440
G010331	1031.9	0.95	0.04	3.19	0.97	336.0	102.0	441
G010332	1032.6	13.50	0.87	101.07	1.05	749.0	8.0	449
G010333	1033.6	2.64	0.25	15.95	0.85	604.0	32.0	436
G010334	1034.5	0.66	0.03	1.29	1.29	196.0	196.0	436
G010335	1036.9	0.65	0.06	2.68	1.27	412.0	195.0	440
G010336	1037.3	3.11	0.16	17.35	2.06	558.0	66.0	438
G010337	1038.4	12.30	0.71	89.86	0.60	731.0	5.0	448
G010338	1039.2	1.26	0.06	4.76	0.74	378.0	59.0	440
G010339	1040.1	0.75	0.11	3.48	0.84	466.0	112.0	437
G010340	1040.8	4.71	0.65	32.25	1.37	685.0	29.0	429
G010341	1042.6	1.42	0.06	6.58	0.45	463.0	32.0	440
G010342	1043.5	15.30	0.74	115.84	0.99	757.0	6.0	453
G010343	1043.9	1.19	0.07	3.08	0.76	259.0	64.0	441
G010344	1044.6	0.93	0.04	4.08	0.76	441.0	82.0	441
G010345	1045.2	1.51	0.09	2.96	0.82	196.0	54.0	426
G010346	1045.6	5.72	0.51	33.51	1.14	586.0	20.0	423
G010347	1046.0	0.47	0.03	1.01	0.57	215.0	122.0	428
G010348	1046.4	1.89	0.15	10.22	0.72	541.0	38.0	435
G010349	1048.0	5.32	0.21	40.01	0.62	752.0	12.0	442
G010350	1048.5	0.33	0.02	0.45	1.07	135.0	320.0	442
G010351	1050.1	17.50	0.82	116.19	0.54	664.0	3.0	452
G010352	1051.3	0.53	0.23	28.18	0.72	5317.0	136.0	438
G010353	1051.7	3.82	0.22	27.35	0.77	716.0	20.0	439
G010354	1052.4	0.63	0.04	2.53	0.76	405.0	122.0	441
G010355	1053.6	0.35	0.02	0.32	1.38	91.0	391.0	433
G010356	1054.4	1.58	0.12	7.66	0.63	483.0	40.0	437
G010357	1055.0	5.44	0.34	43.16	0.45	793.0	8.0	440
G010358	1055.3	1.94	0.13	7.96	0.67	410.0	35.0	437
G010359	1055.8	0.64	0.03	2.39	0.46	371.0	71.0	439
G010360	1056.6	2.24	0.16	16.32	0.76	729.0	34.0	439
G010361	1058.0	10.40	0.74	75.68	0.91	728.0	9.0	446
G010362	604.3	1.98	1.21	4.17	0.36	211.0	18.0	408
G010363	608.8	3.72	2.54	7.01	0.47	188.0	13.0	444
G010364	609.9	2.76	2.06	5.07	0.85	184.0	31.0	441
G010365	610.4	3.21	1.81	4.34	0.61	135.0	19.0	453
G010366	610.8	3.74	2.95	5.58	0.27	149.0	7.0	447
G010367	611.5	1.05	0.58	1.37	2.37	130.0	226.0	451
G010368	611.6	2.19	1.31	3.29	0.51	150.0	23.0	449
G010369	613.1	6.45	4.85	12.20	0.44	189.0	7.0	449
G010370	613.4	0.79	0.23	1.01	0.15	128.0	19.0	383
G010371	614.6	3.50	2.38	6.63	0.17	189.0	5.0	443
G010372	615.8	0.75	0.17	0.81	0.16	109.0	21.0	430
G010373	616.4	0.80	0.18	0.84	0.20	106.0	25.0	448
G010374	617.0	1.66	0.65	1.82	0.94	110.0	57.0	453
G010375	708.9	0.88	0.41	1.14	1.30	130.0	148.0	417
G010376	709.4	1.32	0.61	1.74	0.67	132.0	51.0	425
G010377	709.8	2.16	1.26	3.10	0.63	144.0	29.0	428
G010378	710.6	4.29	4.29	8.72	0.66	203.0	15.0	440
G010379	711.5	1.12	0.65	1.69	0.44	151.0	39.0	378
G010380	712.7	1.52	1.08	2.64	0.83	174.0	55.0	419
G010381	713.2	1.30	0.79	2.02	0.49	155.0	38.0	406
G010382	715.0	1.22	1.13	2.65	1.41	217.0	116.0	418
G010383	715.9	2.09	2.48	4.83	2.53	231.0	121.0	425
G010384	716.7	0.48	0.09	0.53	0.33	111.0	69.0	453
G010385	717.8	2.07	1.21	3.23	0.37	156.0	18.0	413
G010386	718.3	1.84	0.82	2.39	2.11	130.0	115.0	429
G010387	719.1	1.26	0.48	1.45	1.12	115.0	89.0	415
G010388	720.8	1.92	0.97	1.92	0.71	100.0	37.0	464
G010389	728.0	6.13	3.07	5.46	2.15	89.0	35.0	472
G010390	827.8	4.09	0.82	1.31	0.77	32.0	19.0	466
G010391	828.0	1.32	0.26	0.77	0.93	58.0	70.0	465
G010392	829.3	3.34	0.61	1.22	0.43	37.0	13.0	461
G010393	831.2	4.64	0.55	1.29	0.62	28.0	13.0	474
G010394	831.4	2.73	0.45	0.91	0.65	33.0	24.0	463
G010395	833.3	2.23	0.38	0.89	1.33	40.0	60.0	471
G010396	834.9	3.47	0.55	1.10	1.14	32.0	33.0	470
G010397	854.3	6.33	0.62	1.52	0.69	24.0	11.0	489
G010398	854.9	1.91	0.22	0.72	1.03	38.0	54.0	446

G010399	855.8	7.14	1.12	1.82	0.61	25.0	9.0	472
G010400	856.2	1.64	0.31	0.85	0.60	52.0	37.0	505
G010401	857.2	6.17	0.72	1.71	1.97	28.0	32.0	520
G010402	858.3	2.64	0.43	1.01	2.12	38.0	80.0	501
G010403	877.1	2.34	0.35	0.92	1.08	39.0	46.0	506
G010404	877.8	2.48	0.34	0.90	0.59	36.0	24.0	505
G010405	878.3	2.51	0.32	0.84	0.67	33.0	27.0	470
G010406	878.5	2.57	0.39	0.88	0.73	34.0	28.0	465
G010407	880.4	2.65	0.35	0.87	0.76	33.0	29.0	473
G010408	881.2	1.74	0.23	0.74	1.53	43.0	88.0	508
G010409	882.1	2.12	0.35	0.86	0.83	41.0	39.0	475
G010410	883.3	3.19	0.55	1.19	1.57	37.0	49.0	508
G010411	884.6	1.82	0.18	0.67	1.22	37.0	67.0	514
G010412	885.7	1.48	0.14	0.60	1.85	41.0	125.0	509
G010413	887.2	1.87	0.20	0.80	4.28	43.0	229.0	442
G010414	888.3	1.43	0.11	0.54	1.03	38.0	72.0	517
G010415	889.7	2.13	0.17	0.66	0.78	31.0	37.0	482
G010416	919.9	12.90	0.14	2.90	0.31	22.0	2.0	541
G010417	920.8	3.29	0.11	0.95	0.54	29.0	16.0	532
G010418	921.2	17.40	0.24	4.13	1.00	24.0	6.0	554
G010419	922.1	1.00	0.02	0.32	0.28	32.0	28.0	533
G010420	923.1	0.75	0.02	0.29	7.48	39.0	995.0	548
G010421	924.0	2.06	0.06	0.55	0.43	27.0	21.0	546
G010422	924.8	0.61	0.05	0.39	9.27	64.0	1515.0	496
G010423	926.0	1.33	0.10	0.54	0.96	41.0	72.0	517
G010424	926.5	2.23	0.07	0.46	0.18	21.0	8.0	589
G010425	927.7	4.41	0.16	0.68	1.31	15.0	30.0	597
G010426	929.3	5.07	0.17	0.74	1.78	15.0	35.0	501
G010427	930.2	0.98	0.03	0.30	1.08	31.0	111.0	563
G010428	931.1	1.18	0.03	0.36	0.37	31.0	31.0	529
G010429	932.0	4.15	0.11	0.59	1.12	14.0	27.0	598
G010430	933.0	1.14	0.04	0.37	0.51	32.0	45.0	498
G010431	933.6	0.63	0.09	0.63	0.41	100.0	65.0	277
G010432	934.5	6.67	0.29	0.90	0.78	13.0	12.0	487
G010433	935.4	6.77	0.18	0.74	1.76	11.0	26.0	600
G010434	936.5	0.52	0.06	0.50	1.08	96.0	208.0	539
G010435	937.0	1.15	0.03	0.31	1.37	27.0	119.0	574
G010436	937.3	0.75	0.02	0.29	3.79	38.0	503.0	547
G010437	938.5	1.18	0.03	0.38	1.11	32.0	94.0	550
G010438	939.5	0.47	0.04	0.39	0.36	82.0	76.0	495
G010439	940.6	1.71	0.05	0.45	0.57	26.0	33.0	574
G010440	941.6	6.50	0.13	0.68	2.16	10.0	33.0	599
G010441	980.5	0.64	0.09	0.51	0.92	80.0	144.0	315
G010442	983.2	1.20	0.20	0.74	0.91	62.0	76.0	307
G010443	984.9	0.88	0.12	0.59	0.34	67.0	38.0	468
G010444	985.8	1.06	0.21	0.91	1.22	86.0	115.0	371
G010445	986.3	4.79	1.71	2.82	1.78	59.0	37.0	461
G010446	987.7	1.20	0.31	1.03	0.49	86.0	41.0	392
G010447	988.9	2.19	0.70	1.85	0.54	84.0	25.0	375
G010448	989.6	2.13	0.76	1.89	0.28	89.0	13.0	358
G010449	990.4	2.90	1.02	2.23	0.20	77.0	7.0	320
G010450	991.2	7.12	4.27	5.94	0.95	83.0	13.0	472
G010451	992.4	3.22	0.96	1.48	0.82	46.0	25.0	453
G010452	993.0	3.67	1.40	2.25	0.58	61.0	16.0	453
G010453	995.3	2.13	1.14	2.30	0.26	108.0	12.0	345
G010454	996.0	1.55	0.57	2.01	1.88	130.0	121.0	395
G010455	996.6	4.58	1.29	1.90	0.58	41.0	13.0	457
G010456	996.8	5.50	1.39	2.28	0.48	41.0	9.0	459
G010457	997.2	1.16	0.18	0.72	0.69	62.0	59.0	450
G010458	1000.6	4.18	1.05	1.64	0.82	39.0	20.0	460
G010459	1002.0	0.82	0.09	0.53	0.77	65.0	94.0	310
G010460	1002.9	0.82	0.10	0.54	0.81	66.0	99.0	486
G010461	1006.0	0.75	0.11	0.57	0.30	76.0	40.0	489
G010462	1007.1	0.65	0.06	0.45	0.60	69.0	92.0	491
G010463	1008.6	0.77	0.08	0.48	0.26	62.0	34.0	490
G010464	1009.1	0.74	0.07	0.44	0.44	60.0	60.0	492
G010465	1010.0	0.97	0.10	0.54	0.81	56.0	84.0	491
G010466	1010.9	1.16	0.16	0.70	1.25	61.0	108.0	504
G010467	1012.0	0.59	0.05	0.41	0.38	70.0	65.0	487
G010468	1013.5	0.53	0.04	0.37	0.36	70.0	68.0	490
G010469	1015.9	0.84	0.09	0.52	0.45	62.0	54.0	484

G010470	1150.1	2.12	0.26	0.76	0.60	36.0	28.0	489
G010471	1150.2	1.31	0.14	0.61	0.87	47.0	66.0	514
G010472	1152.4	1.56	0.14	0.61	0.93	39.0	60.0	530
G010473	1153.0	2.61	0.43	1.24	0.65	48.0	25.0	525
G010474	1154.4	5.82	0.17	0.66	1.65	11.0	28.0	491
G010475	1155.1	0.59	0.11	0.55	0.89	94.0	152.0	314
G010476	1155.7	2.10	0.66	1.55	1.19	74.0	57.0	528
G010477	1157.1	5.84	0.18	0.71	1.12	12.0	19.0	484
G010478	1157.4	2.36	0.30	0.82	0.80	35.0	34.0	488
G010479	1158.9	4.42	0.13	0.69	1.53	16.0	35.0	528
G010480	1159.7	1.16	0.11	0.56	1.31	48.0	113.0	525
G010481	1160.3	2.51	0.16	0.64	1.63	25.0	65.0	599
G010482	1160.9	3.83	0.28	0.78	0.91	20.0	24.0	300
G010483	1161.7	1.72	0.09	0.52	0.40	30.0	23.0	504
G010484	1162.4	2.40	0.17	0.66	0.79	27.0	33.0	492
G010485	1163.3	2.72	0.12	0.63	0.89	23.0	33.0	462
G010486	1164.1	1.01	0.10	0.54	0.60	53.0	59.0	321
G010487	1164.9	3.97	0.09	0.52	0.52	13.0	13.0	324
G010488	1165.9	2.03	0.08	0.53	2.97	26.0	146.0	551
G010489	1166.7	3.99	0.14	0.61	1.09	15.0	27.0	313
G010490	1167.3	2.47	0.17	0.69	1.09	28.0	44.0	310
G010491	1169.2	1.50	0.10	0.57	0.14	38.0	9.0	319
G010492	1170.5	7.53	0.38	1.37	0.64	18.0	8.0	533
G010493	1171.4	1.52	0.07	0.45	0.48	30.0	32.0	511
G010494	1172.8	1.50	0.07	0.45	0.37	30.0	25.0	501
G010495	1173.7	2.90	0.08	0.49	1.06	17.0	37.0	482
G010496	1174.5	2.20	0.32	1.41	2.14	64.0	97.0	582
G010497	1175.6	0.94	0.02	0.38	0.86	40.0	92.0	483
G010498	1176.7	3.45	0.08	0.49	0.63	14.0	18.0	321
G010499	1176.3	2.79	0.10	0.66	0.19	24.0	7.0	597
G010500	1177.6	2.09	0.06	0.46	0.58	22.0	28.0	485
G010501	1178.4	2.37	0.27	0.77	0.50	32.0	21.0	475
G010502	1179.4	1.77	0.05	0.42	0.88	24.0	50.0	490
G010503	1180.4	1.85	0.05	0.39	0.43	21.0	23.0	581
G010504	1182.1	2.47	0.07	0.46	0.54	19.0	22.0	482
G010505	1183.1	2.40	0.30	0.80	0.95	33.0	40.0	478
G010506	1183.6	2.35	0.07	0.47	0.90	20.0	38.0	490
G010507	1184.8	1.95	0.15	0.64	0.47	33.0	24.0	484
G010508	1185.6	1.30	0.04	0.41	0.95	32.0	73.0	489
G010509	1285.3	2.66	0.51	1.07	0.49	40.0	18.0	600
G010510	1286.0	1.81	0.08	0.50	0.77	28.0	43.0	296
G010511	1287.0	2.65	0.26	0.76	0.70	29.0	26.0	601
G010512	1288.0	2.23	0.12	0.68	0.27	30.0	12.0	315
G010513	1289.3	1.70	0.32	0.81	0.76	48.0	45.0	315
G010514	1289.9	4.44	0.09	0.59	0.85	13.0	19.0	600
G010515	1296.6	2.53	0.13	0.61	1.28	24.0	51.0	280
G010516	1297.4	5.56	0.08	0.52	0.62	9.0	11.0	600
G010517	1298.7	3.60	0.10	0.55	0.50	15.0	14.0	316
G010518	1299.1	1.95	0.23	0.73	0.32	38.0	16.0	283
G010519	1299.5	0.43	0.01	0.19	0.29	44.0	67.0	593
G010520	1300.0	2.01	0.09	0.52	0.43	26.0	21.0	308
G010521	1301.0	2.49	0.17	0.65	0.40	26.0	16.0	291
G010522	1301.7	3.54	0.06	0.43	2.25	12.0	64.0	601
G010523	1302.1	0.91	0.07	0.57	0.76	63.0	83.0	297
G010524	1332.3	7.85	0.11	0.57	0.70	7.0	9.0	600
G010525	1332.7	8.94	0.22	0.73	0.32	8.0	4.0	600
G010526	1333.0	2.77	0.29	0.82	0.13	30.0	5.0	286
G010527	1333.3	2.50	0.04	0.34	0.31	14.0	12.0	599
G010528	1334.0	6.75	0.38	0.93	0.83	14.0	12.0	279
G010529	1334.5	1.60	0.14	0.61	0.35	38.0	22.0	322
G010530	1335.2	2.14	0.04	0.37	0.29	17.0	14.0	599
G010531	1336.0	6.35	0.22	0.76	0.14	12.0	2.0	284
G010532	1336.9	2.96	0.29	0.81	0.51	27.0	17.0	300
G010533	1337.8	4.05	0.11	0.55	1.24	14.0	31.0	304
G010534	1338.3	6.35	0.07	0.47	0.41	7.0	6.0	600
G010535	1339.9	6.91	0.13	0.61	0.41	9.0	6.0	298
G010536	1340.2	2.34	0.12	0.58	0.32	25.0	14.0	277
G010537	1340.9	2.76	0.32	0.82	0.70	30.0	25.0	290
G010538	1341.4	1.40	0.24	0.78	0.46	56.0	33.0	596
G010539	1344.4	5.31	0.18	0.67	0.21	13.0	4.0	289
G010540	1346.4	1.85	0.20	0.70	0.29	38.0	16.0	293

G010541	1347.8	3.34	0.22	0.72	0.54	22.0	16.0	280
G010542	1348.6	2.72	0.18	0.68	0.97	25.0	36.0	598
G010543	1349.6	1.79	0.03	0.30	0.15	17.0	8.0	597
G010544	1560.4	1.45	0.07	0.55	0.41	38.0	28.0	307
G010545	1561.4	5.31	0.23	0.75	0.28	14.0	5.0	299
G010547	1564.0	3.85	0.07	0.51	1.42	13.0	37.0	601
G010548	1564.8	3.39	0.05	0.44	0.45	13.0	13.0	598
G010549	1565.6	0.47	0.03	0.53	0.69	113.0	147.0	308
G010550	1565.7	4.32	0.16	0.68	0.95	16.0	22.0	255
G010551	1566.6	5.56	0.09	0.52	0.44	9.0	8.0	309
G010552	1567.7	1.64	0.04	0.40	0.67	24.0	41.0	513
G010553	1568.5	1.38	0.12	0.67	0.41	49.0	30.0	254
G010554	1569.4	3.06	0.09	0.52	0.63	17.0	21.0	284
G010555	1570.5	2.76	0.05	0.42	0.66	15.0	24.0	314
G010556	1570.9	2.25	0.13	0.61	0.81	27.0	36.0	281
G010557	1572.5	3.01	0.08	0.48	0.81	16.0	27.0	600
G010558	1573.5	1.05	0.06	0.52	0.79	50.0	75.0	277
G010559	1574.2	3.24	0.14	0.62	0.21	19.0	6.0	277
G010560	1574.6	2.93	0.11	0.56	0.30	19.0	10.0	281
G010561	1577.3	2.53	0.12	0.59	0.26	23.0	10.0	317
G010562	1577.9	1.90	0.07	0.46	0.19	24.0	10.0	309

Table A 2. *Porosities measured with different techniques for investigated Wealden shale samples, wells A (0.5-0.7% Ro), B (1.6-2.4% Ro) and C (1.5-1.9% Ro).*

Sample	Total porosity (%)	Hg porosity (%)	Porosity < 5.6 nm (%)	Hg access radius (nm)	Grain density (g/cm^3)
EX-B 010444	7.62	4.70	2.92	7.2	2.80
EX-B 010455	9.73	8.54	1.19	11.8	2.62
EX-B 010457	6.72	5.71	1.01	8.3	2.67
EX-B 010458	9.06	7.55	1.51	8.9	2.65
EX-B 010464	5.87	4.44	1.43	11.9	2.67
EX-B 010469	5.33	4.72	0.61	9.2	2.69
EX-B 010475	6.36	5.97	0.38	9.2	2.71
EX-B 010482	7.05	6.06	0.99	10.6	2.71
EX-B 010485	10.57	7.11	3.46	12.1	2.77
EX-B 010494	5.96	4.63	1.32	8.1	2.73
EX-B 010501	8.54	6.04	2.51	8.1	2.71
EX-B 010509	8.23	5.05	3.14	8.9	2.57
EX-B 010514	11.78	8.56	3.32	8.3	2.64
EX-B 010517	8.29	6.64	1.55	7.7	2.67
EX-B 010518	7.48	5.68	1.80	7.3	2.71
EX-B 010524	12.46	5.62	6.84	6.9	2.65
EX-B 010525	12.43	6.56	5.87	5.8	2.64
EX-B 010529	7.63	5.02	2.61	10.3	3.03
EX-B 010530	6.45	4.01	2.44	5.9	2.69
EX-B 010533	8.61	5.61	3.00	6.5	2.70
EX-B 010537	6.47	4.43	2.05	7.6	2.72
EX-B 010543	7.38	4.63	2.75	8.0	2.73
EX-B 010547	8.94	6.08	2.86	6.9	2.73
EX-B 010551	8.94	5.67	3.27	7.0	2.69
EX-B 010553	5.46	4.36	1.10	8.4	2.81
EX-B 010554	4.85	5.10	0.25	9.7	2.72
EX-B 010562	3.95	3.01	0.93	7.0	2.84
EX-B 010544	4.76	1.75	3.01	20.9	2.80
EX-B 010523	9.81	5.26	4.55	9.8	2.78
EX-B 010549	1.60	0.38	1.23	6.3	2.91
EX-C 010362	6.51	4.18	2.33	8.0	2.62
EX-C 010371	7.01	5.66	1.35	8.5	2.59
EX-C 010374	7.19	5.25	1.93	7.9	2.74
EX-C 010375	6.11	4.91	1.20	8.0	2.75
EX-C 010378	11.50	9.09	2.41	14.6	2.60
EX-C 010382	6.09	4.80	1.29	8.0	2.72
EX-C 010385	6.18	5.01	1.18	7.2	2.64
EX-C 010386	10.26	8.96	1.30	11.0	2.73
EX-C 010388	12.35	5.25	7.10	9.6	2.76
EX-C 010390	8.74	7.28	1.47	10.3	2.64
EX-C 010394	10.37	5.90	4.47	7.2	2.67
EX-C 010396	8.38	5.78	2.61	7.9	2.70
EX-C 010397	7.20	4.61	2.60	7.9	2.60
EX-C 010401	10.96	7.68	3.28	10.6	2.57
EX-C 010404	8.03	5.08	2.94	8.5	2.72
EX-C 010410	8.23	5.08	3.14	7.4	2.68
EX-C 010415	6.69	4.81	1.88	9.6	2.71
EX-C 010416	5.02	3.01	2.01	7.1	2.36
EX-C 010417	4.34	3.72	0.62	18.0	2.64

EX-C 010418	4.56	2.62	1.94	7.6	2.23
EX-C 010421	5.36	4.67	0.69	29.4	2.69
EX-C 010423	5.77	5.26	0.52	15.5	2.72
EX-C 010426	11.94	8.58	3.36	10.9	2.69
EX-C 010432	11.95	9.23	2.72	11.9	2.58
EX-C 010440	10.72	8.60	2.12	10.9	2.60
EX-C 010393	7.68	4.27	1.51	11.8	2.64
EX-C 010384	1.12	0.86	0.25	11.0	2.72
EX-C 010436	8.10	6.99	1.11	8.4	2.81
EX-C 010438	2.05	0.70	1.36	9.6	2.76
EX-C 010439	9.61	5.96	3.65	8.3	2.73
EX-A 010270	18.32	13.42	4.90	26.0	2.92
EX-A 010278	12.41	12.09	0.32	15.3	2.82
EX-A 010282	9.46	8.50	0.95	8.2	2.46
EX-A 010283	15.69	13.11	2.58	18.2	2.31
EX-A 010289	9.59	8.83	0.76	17.1	2.44
EX-A 010295	8.57	6.51	2.07	56.1	2.63
EX-A 010300	18.28	15.24	3.04	21.3	2.45
EX-A 010299	13.01	10.49	2.52	1045.3	2.59
EX-A 010303	14.79	10.72	4.34	19.7	2.72
EX-A 010305	12.91	5.54	7.36	6.2	2.22
EX-A 010312	10.01	6.85	3.16	25.9	2.69
EX-A 010315	8.43	6.92	1.51	3511.6	2.82
EX-A 010320	7.38	4.12	3.26	9.3	2.23
EX-A 010321	8.02	6.17	1.85	118.9	2.60
EX-A 010326	9.63	9.42	0.21	19.9	2.53
EX-A 010333	10.37	7.31	3.06	7.1	2.65
EX-A 010341	8.65	6.00	2.65	6.5	2.64
EX-A 010342	3.45	3.01	0.43	11.7	2.10
EX-A 010343	5.28	4.49	0.79	13.8	2.67
EX-A 010355	14.24	12.16	2.08	33.0	2.80
EX-A 010347	1.91	0.60	1.31	9.4	2.73
EX-A 010350	6.66	5.69	0.97	19.7	2.81
EX-A 010353	3.86	2.20	1.66	7.3	2.55
EX-A 010359	5.82	4.60	1.22	35.0	2.69